MICROWAVE IMAGING FOR EARLY STAGE BREAST TUMOR DETECTION AND DISCRIMINATION VIA COMPLEX NATURAL RESONANCES

By

Fan Yang

A Thesis Submitted for the Degree of

Doctor of Philosophy

Faculty of Engineering & Information Technology,
University of Technology, Sydney

March 2014

CERTIFICATION

I certify that this thesis has not already been submitted for any degree and is not being submitted as part of candidature for any other degree.

I also certify that this thesis has been written by me and that any help that I have received in my research work, preparing this thesis, and all sources used, have been acknowledged in this thesis. In addition, I certify that all information sources and literature used are indicated in the thesis.

Signature of Candidate

Production Note:
Signature removed prior to publication.

_____

(Fan Yang)

In loving memory of my father, Zengke Yang (1951-2013)

ACKNOWLEDGEMENTS

First and foremost, I am grateful for the supervision and encouragement from my supervisor, Associate Professor Dr. Ananda Mohan Sanagavarapu who offered me with every bit of guidance and expertise. The professional skills and enthusiasm that I learned from him will be invaluable in my life. His tireless pursuits in excellent research and fruitful thoughts, advice and valuable feedback have helped me to achieve many research goals, even during in tough times during PhD work. My thesis is part of an ARC Discovery grant obtained by my supervisor.

Secondly, I am particularly thankful to my alternative supervisor Professor Hung Nguyen, who offered me the Top-up scholarship to support me to study in Centre of Health Technologies at UTS and consistently provided me advice and encouragement. I feel extremely privileged to have been his student.

In particular, I extend my gratitude to Dr. Steven Su and Dr. Li Li at UTS, for providing me with valuable advices. I am also grateful to Professor Michael Cortie and Dr. Ronald Shimmon at Faculty of Science in UTS, for supporting me work in their wonderful lab. I would also like to acknowledge my erstwhile colleague and friend Dr. Mohammed Jainul Abedin for his constructive advice and collaboration that have contributed immensely to my personal and professional time at UTS as well as my other colleagues and friends Mr. Md Delwar Hossain, Dr. Mohd Yazed Ahmad and Mr. Md Masud Rana for all the great times that we have shared. I am especially grateful to Mr. Rifai Chai, who is a source of inspiration and technical skills that help me for my measurement work.

I am deeply thankful to my family for their love, support and sacrifices. For my parents whose love and boundless backing supported me in all my pursuits. For my loving, patient and unconditional supportive wife Xiuzhi whose faithful support during my PhD pursuit is deeply appreciated. Without them, this thesis work would never have been

finished. I dedicate this thesis to the memory of my beloved father Zengke Yang, whose role in my life was, and remains immense.

I owe a great debt of gratitude to Faculty of Engineering and IT, and Graduate School at UTS for providing me with IRS scholarship to study at UTS.

Lastly, I would like to thank our faculty's administrative officer, Rosa Tay, Phyllis Agius and Craig Shuard for their administrative support that kept us organized and were always ready to help.

ABSTRACT

In this thesis, a new microwave imaging technique for early stage breast cancer detection is developed to achieve two key aims: (i) to reconstruct the radar image of the suspicious region within the breast and (ii) to decide whether a suspicious region has malignant or benign tumors by differentiating their morphological features in terms of their complex natural resonances.

For our investigations we employ both numerical and chemical tissue mimicking breast phantoms. The breast phantom is illuminated by UWB pulses radiated from antenna elements arranged in a multistate configuration surrounding the breast. An efficient pre-processing technique is proposed to process the received pulses for the removal of early-time artifacts. To reduce the interferences of the background tissue clutter in inhomogeneous breast environment, a new time-of-arrival (TOA) auto-calibration is presented to estimate accurate TOA for confocal imaging. For determining the suspicious region within the breast, a novel and efficient data independent beam former known as Modified Weighted Delay and Sum (MWDAS) algorithm has been proposed. Once the suspicious region is localized by MWDAS method, the waveform of late-time backscattered field will be estimated using a proposed two-stage waveform estimation method. The accuracy of the waveform improves the extraction of complex natural resonances (CNR) that will be used to discriminate of whether a suspicious tissue is malignant or benign. Basing on radar target discrimination, we propose that the CNRs extracted from the late-time resonant tumor response can be closely related their morphological properties: spiculated lesion has CNR poles that differ from CNR poles of a smooth lesion. To validate our proposal, we perform FDTD simulations on 2D and 3D numerical breast phantoms that have been developed based on MRI-derived tissue dielectric properties. These simulations have revealed that the CNRs from malignant tumors have significant lower damping factors than the benign ones. These simulation

results helped to reconfirm that it is possible to distinguish malignant and benign breast tumors based on their CNRs.

To validate the proposed method of tissue discrimination, we have developed an experimental UWB imaging prototype using novel UWB sensors and tissue mimicking chemical breast phantoms to carry out preliminary preclinical experiments. Three novel end-fire compact sized UWB antennas have been proposed. After thoroughly investigating their characteristics, a novel UWB horn antenna known as BAHA that offered superior UWB performance is chosen, fabricated and measured to confirm its characteristics. A prototype experimental imaging system that incorporates 32 BAHA antenna elements forming a hemispherical UWB array is fabricated and tested using a vector network analyzer. Tissues mimicking chemical phantoms with dielectric properties similar to human breasts have been manufactured to have both adipose-tissue dominated homogeneous phantom with a dielectric contrast of 4:1 and a low-adipose in-homogeneously dense phantom with dielectric contrast of 1.7:1. Experimental results obtained using the hemispherical array prototype and phantoms have shown that dielectric inserts (12mm diameter) that mimic malignant and benign lesions can be successfully detected from both high and low dielectric contrast scenarios. Tumor mimicking lossy dielectric inserts with both irregular and smooth patterns have also been fabricated using chemicals to represent malignant and benign tumors respectively.

Finally, measured data from experimental prototype have demonstrated that tissue shape can be discriminated via CNRs. The experimental results confirmed that the proposed UWB antenna array is capable of picking up undistorted late-time signals from embedded tumor-mimicking dielectric inserts with different morphological profiles to offer reliable CNR extraction. Matrix Pencil Method is employed to extract CNRs from late time responses. Our investigations have confirmed that damping factors of the extracted CNRs from both spiculated and smooth inserts can be used to

differentiate their shapes which are quite promising for early stage breast cancer detection.

Contents

List of Tables

List of Figures

List of Symbols

$E_{i,j}(t)$	Received raw data between *i*th to *j*th antennas
$\|\cdot\|$	Euclidean norm
$\boldsymbol{r}$	Confocal point used in confocal microwave imaging
H	Complex conjugate transpose
W_{BF}	Beamforming weight
dia	diameter
Δt	Time interval used in FDTD simulation
$\mathbf{a}(\theta)$	Steering vector of a narrow band signal
θ	The angle at which an incident narrow band signal arrive at antenna array
λ	wavelength
ε_r	permittivity
σ	conductivity
E	Expectation
G	Array gain
σ^2	Signal power
$\mathbf{R}$	Cross-spectral density matrix
∂	constraint parameter on steering vector
$\prod_{i=1}^{M} x_i$	Product over x_i from *i* to *M*
S_m	*m*th s-plane CNR pole
Z_m	*m*th z-plane CNR pole
α_m	*m*th damping factor of CNR
f_m	*m*th resonant frequency of CNR
C_m	*m*th complex amplitude of CNR
std(·)	Calculate the standard deviation of focused region
μ	TOA compensation factor
ρ	Constrain parameter to terminate the process of TOA autocalibration
β_{MMSE}	Scaling parameter used in minimum mean-square-error beamforming
n_{norm}	Normalized CNR error
$\mathbf{F}$	Antenna fidelity
S11	Reflection coefficients
S21	Transmission coefficients
$\boldsymbol{e_c}$	Antenna coupling efficiency

List of Abbreviations

BAHA	Balanced antipodal horn antenna
BAVA	Balanced antipodal Vivaldi antenna
CMI	Confocal microwave imaging
CNR	Complex natural resonances
CPML	Convolutional perfectly matched layer
DAS	Delay-and-sum
DCIS	Ductal carcinoma in situ
DFT	Discrete Fourier transform
DMAS	Delay-multiply-and-sum
FDTD	Finite-Difference Time-Domain
GPR	Ground penetrating radar
iFFT	inverse Fast Fourier Transform
IDAS	Improved delay-and-sum
LCIS	Lobular carcinoma in situ
MAMI	Multistatic adaptive microwave imaging
MIST	Microwave-imaging-via-space-time
MWDAS	Modified-weighted-delay-and-sum
MMSE	Minimum mean-square-error
MPM	Matrix pencil method
MVDR	Minimum variance distortionless beamformer
NFD	Near field directivity
NCR	Normalized CNR error
PEC	Perfect electric conducting
PML	Perfectly matched layer
RCB	Robust capon beamforming
RCS	Radar cross section
RMSE	Root-mean-square-error
SCB	Standard capon beamforming
SEM	Singularity expansion method
SNR	Signal-to-noise ratio
SCR	Signal-to-clutter ratio
TOA	Time-of-arrival
TG-RCB	Transmitter grouping robust capon beamforming
TSAR	Tissue sensing adaptive radar

UWB	Ultra-wideband
UWCEM	University of Wisconsin Computational Electromagnetics Laboratory
VNA	Vector network analyzer

Chapter 1
Introduction

1.1 What is breast cancer?

Breasts are made up of lobules and ducts, surrounded by fatty and connective tissues. Early stage breast cancer is usually to start in the ducts and lobules of the breast as shown in Figure 1.1[1]. Once the cancer cells spread outside the ducts or lobules and into the breast tissues, they may form a lump called “invasive breast cancer”. Breast cancer is the most common non-skin malignancies in women and the second leading cause of female cancer mortality [2]. In Australia, 1 in 8 women and 1 in 688 men will be diagnosed with breast cancer before the age of 85 years [3]. On the other hand, non-invasive breast cancer such as ductal carcinoma in situ (DCIS) and lobular carcinoma in situ (LCIS) are confined to in the ducts and lobules. Although in the non-invasive stage breast cancer may not spread into other tissues, it increases the risk of developing an invasive breast cancer later on.

One of the strategies for increasing the likelihood of successful treatment and long-term survival is the detection of breast tumors at an early stage. For women with small cancers (10mm or less in diameter), 5-year survival is almost as high as that for women without breast cancer [3].

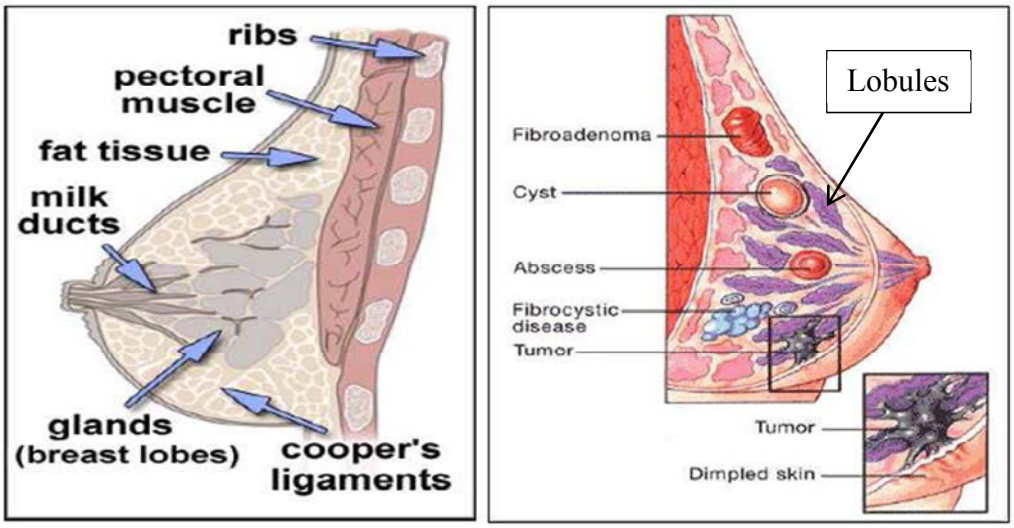

Figure 1.1 Breast structure [1]

1.2 The existing screening tools for breast cancer detection

The gold standard method for breast cancer imaging is the X-ray mammography. Although mammography used currently has undergone several improvements, it is still difficult to accurately predict as to which tissue abnormalities are cancerous or not without additional imaging or biopsy. Also, mammography has a significant false-negative detection rate from 4% to 34% [4] and it is difficult to image 25% of women who have dense breasts [5]. In addition, breast compression in mammography will make many patients feel uncomfortable and even painful. Also, X-rays provide ionizing radiation and hence are not advisable for longtime exposure.

Other medical imaging modalities such as ultrasound has been used clinically to determine whether a lesion detected by a mammogram is a liquid cyst or a solid tumor [5]. However, ultrasound is limited by its lower resolution. The acoustic waves occur around between 2-18MHz. Also, ultrasound is considered to be too operator-dependent. Magnetic resonance imaging (MRI) is another useful screening tool for breast tumor

detection. MRI can produce images of high resolution and provides much greater contrast between the different soft tissues within the body. However, it is very expensive to use for early stage screening [5].

1.3 Microwave Imaging

The concerns related to the above mentioned screening tools have generated interests in researchers of exploring alternative approaches for breast cancer screening. Microwave imaging, appeared as a promising technique, have been extensively investigated [6-15]. Although microwave technology does not have the same high spatial resolution of X-rays, however, it does offer exceptionally high contrast with respect to physical or physiological factors of clinical interest, such as water content, vascularization/angiogenesis, blood-flow rate, and temperate [16]. Furthermore, microwave attenuation in normal breast tissue is low enough to make signal propagation through even large breast volumes quite feasible. For these reasons, microwave breast imaging has the potential to overcome some of the limitations of conventional breast cancer screening modalities. Also, it can work as a complimentary modality to improve the prediction capability[17, 18].

Various techniques using microwave imaging have been explored for breast cancer detection including passive, hybrid and active methods. Passive methods use radiometers to measure the temperature differences between tumor and normal tissues [14, 19, 20]. Hybrid methods use microwave energy to heat the tumor followed by detection of ultrasound waves that are generated by the expansion of the heated tissues [21, 22].

In active microwave imaging methods, breast is illuminated by microwaves and the backscattered microwave signals are collected. Of interest in this thesis are active imaging approaches, which may be broadly classified as tomography and radar based

confocal microwave imaging (CMI). Tomographic image reconstruction methods commonly produce a series of sliced images of the permittivity and conductivity for the imaged region. [6, 23-26]. The challenge of microwave tomography, however, is that it involves the solution of an ill-conditioned nonlinear inverse scattering problem. Furthermore, the inverse-scattering problem requires image reconstruction algorithms that may be computational intensive. However, recent investigations using tomographic imaging have reported promising results [27-30].

Unlike tomographic microwave imaging, confocal microwave imaging (CMI) uses radar principle to focus backscattered signals into the breast to create images that indicate regions of significant scatterings[16, 17, 31-48]. The breast cancer detection using CMI method is based the difference of dielectric properties between malignant tumors (high-water content) and healthy breast tissues (low water content). CMI avoids nonlinear inverse scattering and only identifies regions of strong scatterers that arise due to content in dielectric property. To acquire the data for CMI, multistatic configuration is preferred to obtain spatial selectivity. The breast is illuminated with an ultra-wideband pulse from one antenna, and other antennas collect the backscattered waves. A time-delay-and-sum algorithm is used to obtain the synthetically focused intensity at a given focal point within the domain of interest. Then this focal point is scanned to a new location within the breast and this synthetic process is repeated to cover the entire breast region. Signals from the target are summed coherently, whereas signals from other locations add incoherently, then suppressing the effects from clutters[5]. Thus, this spatial focusing overcomes the challenges of breast heterogeneity, and is possible to detect and localize millimeter-sized tumors using CMI [16].

Safety assessments using specific absorption rate (SAR) are evaluated on realistic 3D breast phantoms prior to clinical implementation. Time-domain SAR evaluations have been reported in [49-51]. These evaluations have demonstrated that EM energy

absorptions using microwave are very small for breast cancer detection over ultrawideband frequencies. And the power was one or two orders of magnitude below that used by any cell phone. Hence, we feel that the safety in this case is not a major concern.

1.4 Breast tissues and dielectric properties

Breast is an inhomogeneous structure composed of multilayers of different types of tissues. Two main types can be categorized: adipose tissues and glandular tissues which reside inside lobules and ducts. At microwave frequencies, biological tissue interactions with the fields are defined by their complex permittivity, which consists of the dielectric constant ε', and the loss factor ε''. The dielectric constant determines the ability of the material to store the electric field energy, while the loss factor indicates how much of that energy is converted into heat and dissipated. Since biological tissues have frequency dependent dielectric constant and loss factor, they are dispersive over frequency. In order to assess the dielectric properties of healthy tissues and malignant tissues as well as benign tissues for microwave imaging application, a large-scale study was conducted based on surgical data [52, 53]. In these studies, three groups of breast tissues have been formed based on percentages of adipose, fibroconnective, and glandular tissues: 1) group-1 contains 0-30% adipose tissue (high water-content); 2) group-2 contains 31-84% adipose tissue; 3) group-3 contains 85-100% adipose tissues (low water-content).

The dielectric properties corresponding to the three types of breast tissues have been experimentally obtained by Lazebnik et al [52] and can be represented by Cole-Cole models. Cole-Cole model is commonly used as physics-based compact representations of wideband frequency-dependent dielectric properties[54]. Alternatively, a simpler one or two pole Debye models [55] can also be used to characterize the frequency-

dependent dielectric properties over ultrawideband (0.5-20GHz). The reported one and two-pole Debye models are sufficient to fit well with the experimental data from cancer surgeries and have close agreement with the computational complex Cole-Cole models [52, 55, 56]. Also the experimental study by Lazebnik et al [52] has revealed that heterogeneity of the dielectric properties is larger than that suggested by earlier studies, and the dielectric properties of healthy breast tissues are much higher than previously reported. This makes malignant tissue detection difficult in heterogeneously dense breast because a large amount of glandular tissues are present in dense breast.

Two-pole Debye model is defined by[55]:

$$\varepsilon(\omega) = \varepsilon_{\infty} + \sum_{n=1}^{N} \frac{\Delta\varepsilon_n}{1+j\omega\tau_n} + \frac{\sigma_s}{j\omega\varepsilon_0} \tag{1.1}$$

The parameters of the two-pole Debye model are shown in Table 1.1 [55]. The parameters of Debye model shown in Table 1.1 are frequency dependent. For frequencies up to 20GHz, these parameters provide close comparison with Cole-Cole model for the breast tissue dielectric properties. Hence, these Debye parameters given in Table 1.1 can model the dielectric properties of a breast tissue at any frequency below 20GHz

Table 1.1 Dielectric Properties of Tumor and Normal Breast Tissues in [55]

Parameter	High Adipose	Medium Adipose	Low Adipose	Malignant
$\Delta\varepsilon_1$	0.58	19.64	20.81	25.61
$\Delta\varepsilon_2$	1.09	14.23	20.22	23.91
$\tau_1\, ps$	8.07	5.81	7.39	7.22
$\tau_2\, ps$	19.25	16.49	15.18	15.30
ε_{∞}	3.14	5.57	7.82	6.75
σ_sS/m	0.036	0.52	0.71	0.79

1.5 Test beds using numerical and experimental breast phantoms

1.5.1 Numerical breast phantom

Research on both diagnostic and therapeutic microwave techniques benefits from anatomically realistic numerical breast phantoms that mimic breast structural complexities, tissue heterogeneity, and dispersive dielectric properties [57]. These realistic phantoms have been provided by the University of Wisconsin Computational Electromagnetics Laboratory's (UWCEM) breast phantom repository[57]. The numerical phantoms are derived from MRIs data collected from patients. The American College of Radiology defines four classes of breast composition according to the radiographic density of the breast: 1) almost entirely fat (C1); 2) scattered fibroglandular (C2); 3) heterogeneously dense (C3) and 4) extremely dense (C4). The four numerical phantoms C1, C2, C3 and C4 available from UWCEM phantom repository therefore correspond to the four types of breast classes and are obtained from MRI data for patients [57]. A sagittal slice of C3 heterogeneously dense breast can be seen in Figure 1.2. Blue color within the breast indicates the region of glandular tissues and red color denotes fatty tissues.

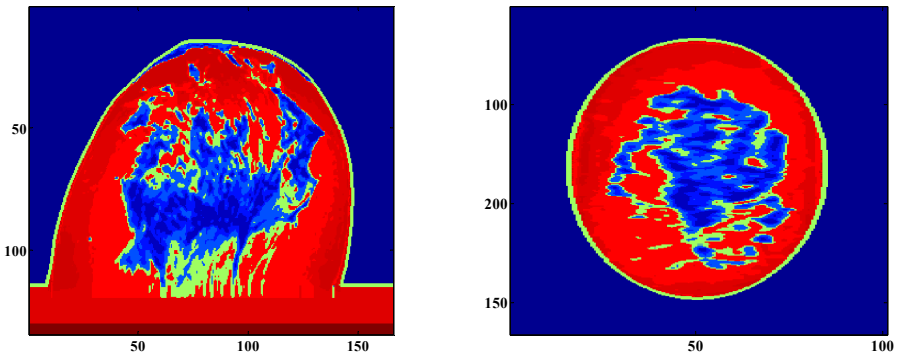

Figure 1. 2 MRI-derived 2D breast image.

1.5.2 Tissue mimicking breast phantoms

Since it is difficult to get clinical clearance to test any of the experimental imaging methods directly on human models, many investigators used tissue mimicking phantoms that are formed using chemicals, oil etc. An initial experiment using simple high dielectric tumor was reported in [40]. The tumor model has ε_r=43.7, $\sigma = 6.94$ at 4GHz which was fabricated by mixing Alginate powder, water and salt. Breast phantom was represented by a 10cm dia plastic cylinder having 30cm height, which is filled with fatty tissue phantom made by mixing flour, canola oil and 0.9% saline. This mixture has dielectric property of $\varepsilon_r = 4.2$, $\sigma = 0.16$ at 4GHz[40]. More advanced phantoms including homogeneous and inhomogeneous dense breast phantoms were also reported in literature [45], in which dielectric constant of mimicking materials ranging from 10 to 30 represented adipose and glandular tissues respectively. Those tissue phantoms were fabricated by mixing different portions of TX151 and polythene powder and water. A 2mm thick skin layer was formed and directly supported by a curved ceramic shell with dielectric constant of 2, and the tumor phantom had dielectric constant $\varepsilon_r = 50$.

Improved method of making phantoms was later reported recently [58] [59] using oil-gelatin mixture to make tissue mimicking breast phantoms. The phantoms were made by mixing gelatin and oil (50% safflower oil and 50% kerosene) as well as four other ingredients with different concentrations. Following this method, skin, fatty and glandular tissues and tumor can be fabricated and solidified using a custom defined mold. Although the measured dielectric properties did not match closely with the actual measured values for tissues as reported by Zastrow et al [57], but it was mentioned that the differences were tolerable, since the tissue properties usually vary widely between different patients. Using this method, fabrication of realistic breast phantom [60] and conical heterogeneous glandular tissues [61] also has been reported.

1.6 Existing confocal microwave imaging and challenges

1.6.1 Data-independent beamforming

Beamforming is a signal processing technique that is used coherently to enhance signal from the target of interest while suppressing the signals from other sources. Originally, delay-and-sum (DAS) beamforming was employed for confocal microwave imaging for breast cancer detection [31, 32]. DAS is one of the data-independent beamformers that form a beamforming weight without the knowledge of array response and requires low computational load for implementation. Later, an improved data-independent beamformer, known as microwave-imaging-via-space-time (MIST) beamforming was reported by Bond et al [34]. The MIST algorithm uses a least-square technique to design the weights of the beamformer so that it allows tumor response to pass through with unit gain but signals from other surrounding region are attenuated.

Another variant of DAS beamformer, known as delay-multiply-and-sum (DMAS) was proposed by Lim et al [46], where multiple pair signals are multiplied to increase the intensity of tumor response. Simulated results using FDTD have shown robust detection performance using this algorithm. Another method, known as Improved-DAS (IDAS) was also proposed in which a weighting factor was multiplied at each confocal point [41]. The main idea behind the IDAS is that the weighting factor increases the intensity of signal of interest adaptively and reduces the normalized signal value from other surrounding regions within the breast. The IDAS was demonstrated experimentally to localize tumors of size 7mm and 10mm (dia) in which 16 stacked-patch antenna elements were employed to examine a chemical breast phantom that has 5:1 dielectric contrast between tumor and background tissues and performed over a band of 3GHz to 10GHz.

Performances between conventional DAS, DMAS and IDAS have been compared by Byrne et al [62] by using FDTD simulations using realistic MRI-derived numerical breast models provided by UWCEM breast phantom repository [63]. It was demonstrated that the performances degraded significantly as the dielectric contrast varies from homogeneous to inhomogeneous phantoms, because of the assumption of constant dielectric breast properties for calculating the propagation velocity. Their results revealed that DAS is more robust compared to DMAS and IDAS [62].

1.6.2 Data-dependent beamforming

In contrast to data-independent beamforming, data-dependent beamforming was proposed using robust capon beamforming (RCB) initially by Li et al [47, 64, 65]. It was well acknowledged that multistatic adaptive microwave imaging (MAMI) method using RCB proposed by Li et al [47] showed superior performances than data-independent beamformers on image resolution and clutter rejection[42, 47]. In MAMI, a two-stage RCB was employed to detect 4mm (dia) tumor using 3D numerical breast phantom and obtained much higher resolution than DAS. Although MAMI introduced efficient RCB beamforming for CMI method, the phantom adopted in MAMI had unrealistic dielectric contrast between tumor and surrounding glandular tissues [66-69].

An improved robust capon beamforming using transmitter grouping (TG-RCB) [70] was proposed to obtain better accuracy of reconstruction and tested on realistic MRI-derived FDTD breast models by Zastrow et al [63]. Unlike the two-stage RCB proposed by Xie et al [47], TG-RCB focused energy at each step of RCB [70]. Simulations indicated that TG-RCB presented enhanced tumor images than MAMI in heterogeneous numerical breast phantoms that contains large amounts of glandular tissues.

Recent large scale studies on dielectric properties [52, 53] have revealed that the dielectric contrast between malignant tumor to glandular tissues could be as small as 1.1:1, which makes the microwave imaging very challenging for the detection of malignant lesions in dense breast [52, 53, 55]. Although confocal microwave imaging methods have demonstrated detection of small sized tumors in simple fatty tissue dominant breast phantoms, they cannot detect small sized lesions in dense breast phantom. Detection in dense phantoms is important for early stage detection, since breasts of younger adults are relatively denser [71]. Further, any detection method that is based on the strength of backscattered energy [31, 42, 47, 72] cannot differentiate the malignant lesion and benign glandular tissues, since the backscattering strength depends on the dielectric contrast. Hence, there is a need to investigate alternate methods of differentiating the tissues.

1.6.3 Experimental microwave imaging systems

Many experimental microwave imaging systems viz., pulsed radar system [32, 33] tissue sensing adaptive radar system (TSAR) [39] etc were reported in the literature to demonstrate the applicability of the confocal microwave imaging techniques for breast cancer detection. In these systems, simple antennas such as resistively loaded bowtie and monopole antennas were employed as the UWB sensors to illuminate UWB pulse into breast tissues. All time-domain "measured" waveforms have been generated synthetically using the vector network analyzer (VNA) in a swept frequency mode. Frequency domain data was scaled by the spectrum of the desired UWB input pulse and converted to the time domain using an inverse discrete Fourier transform (DFT)[31].

Another simple experimental investigation was reported in [73], where a simple dielectric rod was immersed in a water filled glass tank to mimic a tumor. Signals were obtained synthetically by frequency swept from 0.5 to 3GHz. Also, many radar imaging

systems for breast cancer detection have been reported. A microwave imaging system was designed and built with 31 wide-slot antennas [44, 45]. Instead of immersing the antennas in coupling liquid, the authors[44] used ceramic shell as the medium between antennas and phantom, and deployed multiple RF switches to switch between antenna elements and high-performance vector network analyzer. Similar to other frequency-domain measurements, measured time domain waveforms were obtained synthetically by frequency swept from 3GHz to 10GHz. It was reported that a full multistatic scan takes only 80 seconds to complete, and modified DAS algorithm was employed to reconstruct tumor image [44, 45] to successfully detect a 7mm tumor in both high dielectric contrast (5:1 at 3GHz) and low (1.67:1 at 3GHz) dielectric contrast phantoms.

The experimental methods that used DAS beamforming reported that DAS could achieve good image resolution and clutter rejection if it is combined with proper weight factors. Moreover, it was suggested that simple mechanical array rotation to remove early-time artifacts such as antenna excitation and skin reflection will be sufficient to obtain a good later-time response. An antenna system with 64 elements using a larger RF switch matrix to form multistatic configuration was also reported [43].

Despite the superior performances reported by many researchers [42, 44], some aspects of their measurement systems require a closer look. The wide-slot antenna when used to immerse in the coupling liquid did not obtain high magnitudes of S21 for backscattered field over full band for 100mm antenna separation. The magnitude of S21 of backscattered field strength was -30dB only at single frequency 4.5GHz but later significantly dropped to -60dB at 10GHz, which indicates that the reported wide-slot cannot cover sufficient bandwidth as well as at larger separation between antennas when immersed in coupling liquid. Also, the measurement of fidelity was made only between two antennas separated by small angles. Further, the significantly dropped magnitudes of S21 indicate that the fidelity of wide-slot antennas may be low.

A monostatic prototype was developed by Bourqui et al [74]. In their system, a cylindrical tank was filled with canola oil as coupling liquid for the immersion of phantom and antenna. Balanced antipodal Vivaldi antenna with dielectric director was employed to focus the beam into the breast phantom and used VNA with frequency sweep from 50MHz to 15GHz. A laser scanner was also mounted for estimating phantom outline. For each trial, 200 antenna locations were scanned within 30 minutes. The advantage of the system [75] is that the antennas were moving over many positions forming a synthetic array which reduced the cost of array fabrication. However, their system requires complex positioning method.

1.6.4 Design of UWB antenna elements for radar based microwave breast imaging

In the first reported experiment on radar based microwave breast imaging, a loaded Wu-King monopole antenna [76] was used. This monopole radiated within the band of 7GHz to 10GHz when immersed in coupling liquid having $\varepsilon_r = 3$. Unlike monopole or dipole antennas, end-fire antennas have attracted attentions because they can radiate more energy into the imaged region with focused beam. Most end-fire designs used the metallic cavities or absorbing material to force the radiated energy to focus into the breast. For example, a 16 element hemispherical array using a UWB patch antenna with small ground plane of $23\text{mm} \times 29\text{mm}$ was reported by Nilavalan et al [77], to work between 4.5GHz and 10GHz. Subsequently, an improved wide slot antenna was proposed with much smaller ground plane of $13\text{mm} \times 14\text{mm}$ so that a larger array surrounding the outer breast surface can be formed [78].

Most reported antennas for breast imaging were immersed in coupling liquid to reduce reflections. A modified pyramidal horn antenna was reported to work in both air

and coupling liquid [79]. It uses a curved metallic launching plane terminated by two resistors, and operates between 1 to 11GHz.

A new method to enhance the energy radiation into breast medium was reported in[80], in which the balanced antipodal Vivaldi antenna (BAVA) was coupled with a high dielectric director. This director will focus the radiated energy better into the imaged region and provide higher fidelity. Furthermore, numerical results have indicated that the dielectric director could receive the backscattered signal better than simple BAVA [80].

A new TEM horn antenna with aperture $19\text{mm} \times 30\text{mm}$ was proposed by Amineh et al [81] where the antenna touched breast surface directly without using coupling liquid. However this antenna has low coupling efficiency (37%) and the fidelity reduced with increased antenna separation. Hence, use of this antenna may require small amounts of breast compression. Later, this TEM horn was modified to improve the coupling efficiency higher than 80% [82]. A new antipodal tapered slot antenna with edge corrugations was proposed by Mohammed et al [83] which was used to form a 6×12 array for breast imaging to operate between 3.1 and 10.6GHz band when immersed in coupling liquid having $\varepsilon_r = 10.4, \sigma = 1.98$.

1.7 Methods to discriminate malignant tissues from benign tumors

An important objective for breast cancer detection is to discriminate malignant and benign lesions using microwave backscatters from the breast lesions. A microwave technique that could discriminate breast malignancy has potential to help mammography to reduce the false negative in clinical diagnosis. This motived us to use late-time target response to extract CNRs and use them to discriminate breast lesions.

1.7.1 Tumor morphologies

Mammographic and MR image analysis [4, 84-87] have shown that a blurred periphery, with radiating pattern on its surface also known as "spicules" is highly suggestive of tissue malignancy. On the contrary, the benign tumors are often well-circumscribed, compact and roughly elliptical with smooth periphery as shown in Figure 1.3 that are taken from X-ray mammography [87]. Computer-aided detection analysis indicated the shape of the mass as shown in green contours in Figure 1.3. Figure 1.3(a) gives a smooth boundary that highly corresponds to a benign tumor. Figure 1.3(b) shows a spiculated periphery which is considered to be malignant lesion [87]. Figure 1.4 shows the MRI breast images taken from two different patients [86]. The presence of irregularity or spiculation is highly sensitive and predictive of malignancy. While the presence of smooth or lobulated borders are highly predictive of benign tumor[86].

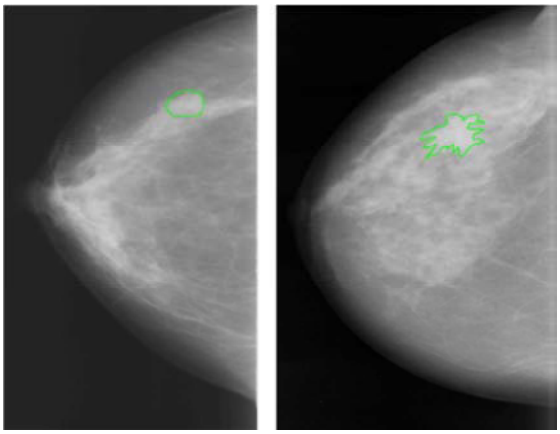

(a) (b)

Figure 1.3 Mammographic images of breast lesions (a) Lesion with oval well-circumscribed margin is highly predictive of benign. (b) Lesion with irregular or spiculated border is highly predictive of malignant.

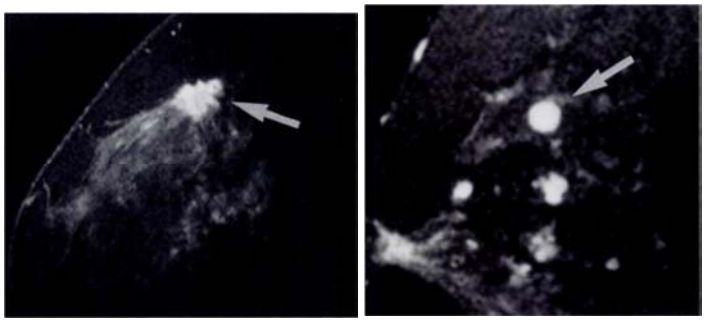

(a) (b)

Figure 1.4 MR image of breast lesions (a) spiculated and irregular shapes indicate a malignant lesion (arrow) (b) smooth borders indicates a benign lesion.

1.7.2 Breast tumor discrimination based on microwave signatures

The literature on radar [88-93] has shown that an embedded target can be discriminated based on complex natural resonances (CNRs) which are calculated from backscattered microwave late-time response if the target is excited by a short duration electromagnetic pulse. CNR signatures are independent of ambient medium and antenna locations but only dependent to the dielectric properties and shape of the target [89, 93]. For a target embedded in lossy medium, only a few studies have been conducted mainly for landmine detection [94-96]. Recently, CNR signatures have been used for breast cancer detection [97-101]. Therefore, CNR can be used to potentially discriminate embedded tumor within breast medium, since malignant tumor has high probability of having random irregular shape as compared to benign tumor [4, 86, 87].

In a simple FDTD based numerical study [97], an ellipsoidal tumor was examined when immersed in dielectric medium with increasing conductivity and fixed permittivity. The target was illuminated by Gaussian modulated pulse up to 12.5GHz. Extracted CNRs indicated that the damping factor increases as the conductivity increases and CNR poles can be discriminated on the plane of resonant frequency-damping factor as shown in Figure 1.5.

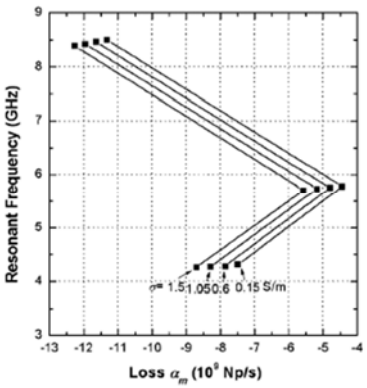

Figure 1.5 CNR poles for ellipsoidal tumor with different conductivity reported in [97].

The resonance spectra of backscattered response using radar cross section (RCS) were examined for breast tumor. RCS is related to CNR signature for a given resonant frequency and damping factor. On the RCS versus frequency plane, location of the peak of RCS corresponds to resonant frequency in CNR. On the other hand, the width of the RCS peak is associated to damping factor of CNR [94]. The numerical results have shown that RCS signatures are independent of orientation, incident polarization, or scattering directions [98]. As expected, RCS values were closely associated with tumor shape and dielectric properties. The study by El-Shenawee also indicated that spherical tumor and prolate spheroidal tumor can be differentiable between their RCS as shown in Figure 1.6[98].

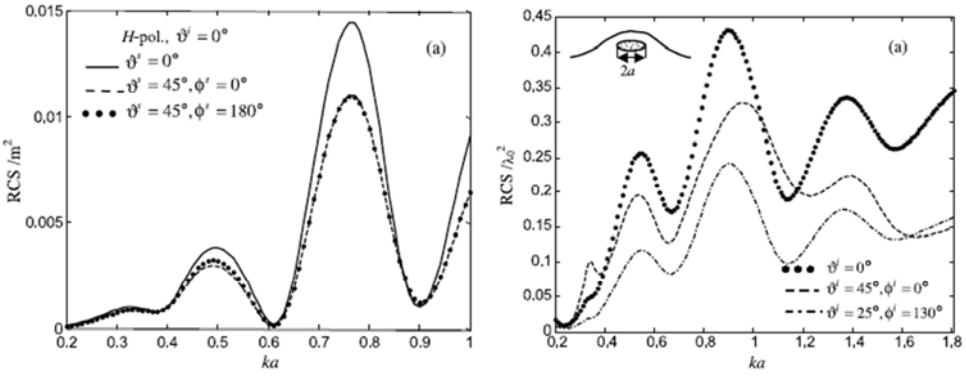

(a) (b)

Figure 1.6 RCS versus normalized radius of tumor. (a)for spherical tumor (b) for prolate spheroid tumor (right) as reported in [98]

Chen et al made comprehensive investigation for breast tumor discrimination via CNR [99] and its lesion classification [100]. In their study, 2D breast lesions with spiculated and smooth profiles were examined in both clutter-free breast as well as highly dense breast model with low dielectric contrast between tumor and normal tissues. Their results showed that it is possible to discriminate lesions from very smooth to highly spiculated lesions. Their numerical results were the first to establish the potentials for use of CNRs to differentiate lesion morphologies even in dense breasts. Interestingly, in a simulated study, Chen et al [99] have also indicated that performance of CNR discrimination is affected by antenna location and suggested that multistatic configuration may be a good way to obtain better CNR separation than just monostatic illumination.

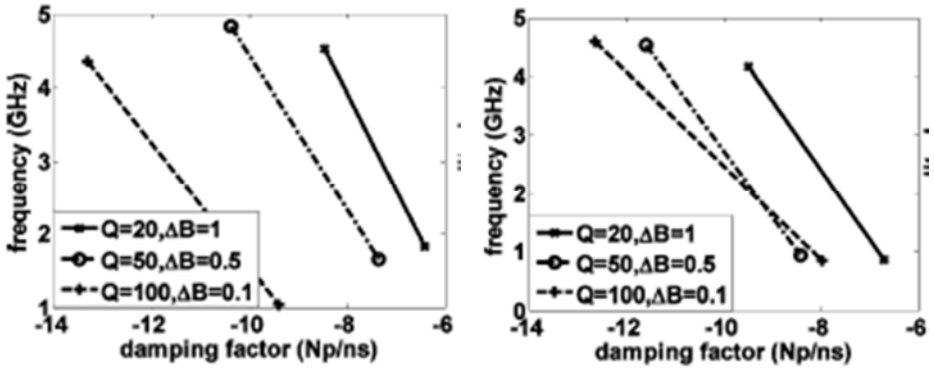

(a) (b)

Figure 1.7 (a)CNR poles in adipose-dominated homogeneous phantom and (b) low-adipose-content heterogeneous phantom reported in [99]. Q=20 , $\Delta\mathbf{B} = \mathbf{1}$ represents highly spiculation. Q=50,$\Delta\mathbf{B} = \mathbf{0.5}$ represents medium spiculation. Q=100,$\Delta\mathbf{B} = \mathbf{0.1}$ represents smooth lesion.

However, CNRs from 3D spiculated or smooth lesions have not been investigated either in realistic numerical phantoms or experimental chemical phantoms. For 3D simulation or experiment dealing with CNR extraction from complex shaped dielectric objects, a good reconstruction technique is required to obtain an accurate late-time time-domain waveform. A good experimental microwave imaging system is also required so

that UWB pulses can be received with minimal pulse distortion. These challenges have motivated our studies reported in this thesis.

1.8 Aims and Objectives of the thesis:

The aim of this thesis is to develop a new microwave imaging technique to accurately and efficiently localize the suspicious region within breast and extract complex natural resonances to discriminate whether the suspicious region is due to malignant lesion or benign tumor. To achieve this aim, we focus on the following objectives:

i. Develop a novel beamforming technique to localize the suspicious region within the breast that can provide the location of the lesion with high resolution and clutter rejection.

ii. Develop a novel adaptive waveform estimation method that can estimate accurately the time-domain signal from the suspicious region within the breast for use with CNR extraction

iii. Investigate techniques to overcome the effects from breast heterogeneity which will reduce the accuracy of localization of suspicious region.

iv. Investigate methods to suppress spurious CNRs extracted from time-domain signal, since early-time artifacts, antenna ringing and clutter interferences all can contribute to spurious CNRs.

v. Propose a novel UWB antenna for microwave breast imaging as well as tumor discrimination using complex natural resonances.

vi. Fabricate a realistic tissue mimicking phantom to test the proposed imaging techniques and experimental system.

vii. Demonstrate the proposed imaging and tumor discrimination strategy using proposed experimental microwave imaging system.

1.9 Brief description of methodology

We propose a technique to localize and discriminate breast tumor. We achieve this by localizing the suspicious region within breast phantoms using a novel data-independent array beamforming technique followed by a two-stage waveform estimation to extract CNRs which are used to discriminate tumors with different morphological features. To guarantee an accurate localization of suspicious region, a novel time-of-arrival auto-calibration and a generalized pre-processing are used to compensate the uneven propagation velocities within the heterogeneous breast environment and remove the early-time artifacts, respectively. To overcome the effects of spurious CNRs, dominant fundamental resonances are utilized to suppress the non-resonant signals and obtain the starting time period of late-time resonant signal from which CNRs can be extracted. The proposed technique is implemented by designing an experimental microwave imaging system prototype employing a novel horn antenna (BAHA) array with 32 elements. This system coupled with reconstruction technique could provide accurate localization of suspicious region which has been verified through experiments. Our experiments demonstrated that we can identify small tumors in both high dielectric contrast (4:1) and low dielectric contrast (1.7:1) chemical breast phantoms. By measuring the UWB backscattering signals from various tumor mimicking dielectric inserts with different shapes (malignant and benign lesions) embedded within the chemical breast phantoms, we extract CNRs and compare their damping factors to discriminate the shapes of inserts.

1.10 Organization of this thesis

This thesis is organized as follows:

Chapter 1: This chapter introduces motivations of the work in this thesis and briefly reviews the existing microwave imaging techniques for breast cancer detection. It highlights the challenges faced by current radar-based microwave imaging and reviews the available techniques for lesion discrimination.

Chapter 2: A novel data-independent beamforming technique is presented in this chapter. This chapter starts with an introduction of a simple beamforming method for microwave breast imaging and then discusses the proposed image reconstruction method for localizing suspicious region of breast cancer at early stage. The proposed method is then demonstrated using numerical phantom and FDTD simulations.

Chapter 3: This chapter proposes a technique for localizing the suspicious region and discriminating malignant and benign lesions within the breast. To efficiently and accurately localize the suspicious region, a new concept of pre-processing technique and a novel method for calibrating the propagation velocity are discussed. The waveform of backscattered field at the position of the suspicious region is estimated by using the proposed two-stage waveform estimation method. This two-stage waveform estimation method helps to obtain accurate extraction of associated CNR signatures of tumor combined with various techniques. Details of the technique will be presented in chapter 3. This chapter ends by showing that malignant and benign lesions within a MRI-derived numerical dense breast phantom can be accurately localized and discriminated.

Chapter 4: This chapter investigates three different end-fire ultra-wideband antennas with novel designs. Based on a set criterion, all three designs were compared and only one was selected which offers superior performance that was confirmed by

measured results. Antenna effects on CNR extraction have also been investigated by both simulation and measurement which have demonstrated that the proposed BAHA antenna can be used in the experimental microwave imaging system prototype for breast cancer detection.

Chapter 5: This chapter reports the first attempt of experimentally demonstrating the feasibility of discriminating breast lesions in chemical phantoms. It starts with the development of proposed experimental microwave imaging system prototype using the BAHA antenna element proposed in chapter 4. Next, the proposed reconstruction methods and breast lesion discrimination technique have been implemented by experiments based on chemical breast phantoms. Promising experimental results have shown that with good reconstruction method and sophisticated imaging system, it is possible to discriminate malignant and benign lesions, using complex natural resonances.

Chapter 6: This chapter summarizes the overall contributions made by the thesis and also scope for future work.

1.11 Publications arising from this research

[1] F. Yang, and A. S. Mohan, 'Microwave Imaging for Breast Cancer Detection using Vivaldi Antenna Array', 2012 International Symposium on Antennas and Propagation (ISAP2012) in Nagoya, Japan, on Oct.29-Nov.2, 2012

[2] F. Yang and A. S. Mohan, ' Complex Natural Resonances of Dielectric Objects Embedded in Inhomogeneous Breast Models ', IEEE Antennas and Propagation Society International Symposium *(APSURSI)*, Chicago, USA, July 8-14, 2012 in *Antennas and Propagation Society International Symposium*, 2012.

[3] F. Yang and A. S. Mohan, ' Complex Natural Resonances for Breast Tissues with Complex Morphology ', IEEE Antennas and Propagation Society International Symposium *(APSURSI)*, Washington, USA, July 3-8, 2011 in *Antennas and Propagation Society International Symposium*, 2011.

[4] F. Yang and A. S. Mohan, 'Time-of-Arrival Calibration for Improving the Microwave Breast Cancer Imaging', IEEE Topical Meeting on Biomedical Radio and Wireless Technologies, Networks, and Sensing Systems, Jan. 16-20 in Phoenix, AZ, USA, 2011.

[5] F. Yang and A. S. Mohan, 'Breast Cancer Detection: Comparison of Data-Dependent and Data-independent Approaches', Asia Pacific Microwave Conference, Melbourne, Australia, Yokohama, Japan, December 2010 in *Porceedings of the Asia Pacific Microwave Conference (APMC)* , 2010.

[6] F. Yang and A. S. Mohan, 'Breast Cancer Imaging Techniques using UWB Microwave Imaging', International Conference on Electromagnetics in Advanced Applications, ICEAA'10, September 20-24 in Sydney, Australia, 2010.

[7] F. Yang and A. S. Mohan, 'EM Techniques for the Detection of Breast Cancer', 2010 IEEE AP-S International Symposium on Antennas and Propagation and 2010 IEEE USNC/CNC/URSI Meeting in Toronto, ON, Canada, on July 11-17, 2010

A few journal papers are under preparation and will be submitted soon.

Chapter 2
Array Beamforming for Localizing the Suspicious Regions within Breast Phantoms

2.1 Introduction

Breast cancer detection using microwave imaging [27, 34, 44, 74] is based on contrast in the electrical properties between fatty, fibroglandular tissues and malignant tumors [52, 53]. Radar based active microwave imaging method [31, 34, 44, 47] generally uses ultra-wideband signals so as to obtain a good compromise between resolution and depth of penetration into tissues.

For radar-based microwave imaging, multiple antennas are employed which are positioned at multiple locations surrounding the breast and close to the skin to form a multistatic configuration[44, 47]. For this, at any time instant, one antenna transmits a short pulse of microwaves into the breast, and all other antennas receive the

reflected/backscattered signals. Thus different antennas cover different angular regions of the breast so that the backscattered signals from all parts of the breast can be potentially captured for further processing. The received backscattered fields after pre-processing to remove un-desirable signal reflections may be focused using various beamforming methods [34, 41, 46, 65] to form an image that can potentially indicate the locations of strongly scattering objects. The locations of the strongly scattering objects may not correspond to the actual locations of the tumor due to various dispersive effects and clutter interference as well as due to the presence of benign tumors. However, they can be used as suspicious regions within the breast at which the possibility of the presence of malignant lesion is high. Hence, it is important to improve the accuracy of localizing the suspicious regions so that it can help with improving the efficiencies of further processing to accurately find the presence of the tumor and reject the effects due to benign tissues[99]. Hence, in this chapter, we describe novel beamforming methods to efficiently and accurately localize suspicious region within the breast.

Performing signal processing operations on received scattered UWB signals at different receiving antennas to determine the presence and location of a tumor is riddled with number of uncertainties. As the breast tissue medium is frequency dispersive, the shape of the transmitted ultrawideband pulses and the shape of received pulses can differ significantly[102]. In addition, when the breast tissue composition is dominated by dense fibroglandular and fibroconnective tissues, they can act as benign tumors and sometimes may hide the presence of malignant lesions. This is because of the existence of low dielectric contrast [52, 53]. The dielectric contrast between malignant lesions and fatty healthy tissues can be high, but the dielectric contrast between malignant and glandular tissues can be as low as 1.1:1 [52, 53]. Hence localization of suspicious regions inside a dense breast requires complex signal processing. In this chapter, we investigate efficient methods of localizing suspicious region within homogeneous and heterogeneous numerical breast phantoms. We also investigate both data-independent

and data-dependent beamforming approaches for the reconstruction of suspicious region within the breast. Further, we propose a novel MWDAS algorithm to efficiently localize the suspicious region with high resolution.

2.2 Beamforming methods for image reconstruction

2.2.1 Confocal microwave imaging

Confocal microwave imaging (CMI) is one of the robust approaches for radar based microwave imaging. [33]. CMI originally employed a simple data-independent beamformer Delay-And-Sum (DAS) for microwave image reconstruction [31, 37]. In CMI, multistatic configuration is used by exciting each antenna with a short ultra-wideband (UWB) pulse in turns and other antennas collecting the backscattered signals. Assuming M antennas are used in an array, multistatic configuration can form a $M \times M$ matrix of received pulses. By using this multistatic matrix, it is possible to obtain the information of strong scatterers so that tumor location can be localized.

Although DAS is able to reconstruct image of the strongest scatterer such as breast tumor, its capability will be reduced if interferences from dispersive fibroglandular breast tissues are present. To overcome this, many variants of DAS have appeared [33, 42, 46]. Microwave imaging via space-time (MIST) [34] beamforming applies different signal processing filters to compensate the effects of the tissue artifacts to improve the performance of DAS. An alternative delay-multiply-and-sum (DMAS) reconstruction method [46] uses pairing multiplications to enhance the summation of energy at a confocal point. Another version known as improved delay-and-sum (IDAS) [41] incorporated a quality factor into DAS to adaptively increase the energy focused at the confocal point. The authors have widely employed this method with experimental data [42, 45]. For data-dependent beamforming technique, multistatic adaptive microwave imaging (MAMI) [47] was proposed using robust capon beamforming (RCB) [65] to

minimize the effects of clutter at various confocal points and obtained a reconstructed tumor image that has higher resolution than that of DAS.

The potential antenna array configurations that are used for breast cancer detection are shown in Figure 2.2.1. Figure 2.2.1(a) shows a circular arc array with 22 ideal antenna elements which are placed surrounding a 2D breast model. Figure 2.2.1(b) shows a circular cylindrical array with 90 antenna elements which we will use for 3-D heterogeneously dense breast phantom in Chapter 3. Figure 2.2.1(c) illustrates a hemispherical array with 32 elements which can be used with 3-D hemispherical breast phantom. We employ this 3-D hemispherical array with experimental UWB microwave imaging system as will be discussed in Chapter 5.

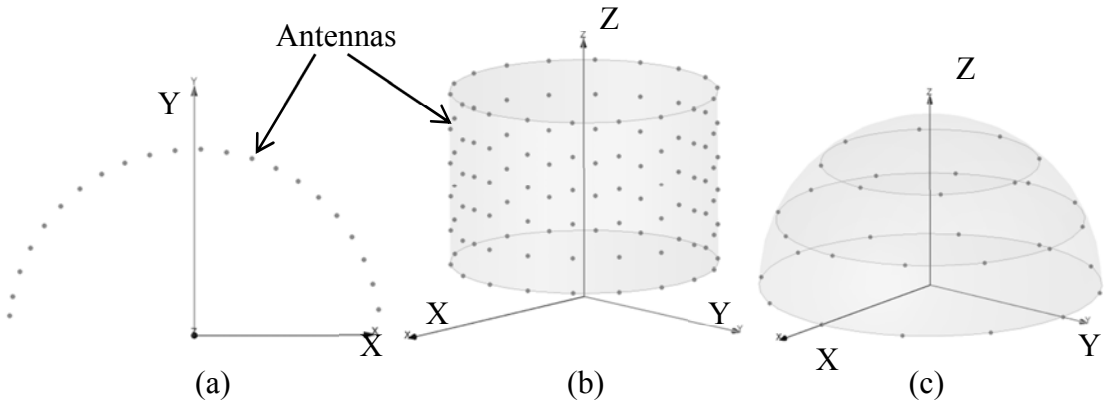

Figure 2.2.1 Antenna array configuration (a) simple circular array used in simulation in Chapter 2 (b) cylindrical array used in simulation in Chapter 3 (c) hemispherical array used in measurement in Chapter 5

Without loss of generality, consider M UWB antennas in the array. Each antenna transmits a UWB signal to the breast and all the other antennas receive the backscattered signals. Then $L = M \times M$ multistatic matrix is established using the received data $E_{i,j}(t)$, $i = 1, \cdots, M,\ j = 1, \cdots, M$, where $E_{i,j}(t)$ is the recorded the

backscattered fields from i th transmitting antenna to j th receiving antenna. The recorded signals are synthetically focused at one confocal point r_0 whose position is varied to cover the entire breast volume. Thus, the image of backscattered energy can be formed.

Before employing any beamforming technique to reconstruct the image of the strongest scatterer within the breast, unwanted content including skin reflections and incident excitation should be removed [31, 34]. Conventional methods to remove those unwanted contents uses a "calibration" signal E^{cal} that is obtained by averaging all the received signals that have approximately similar levels of unwanted contents[31]. The "calibrated" signals are then obtained using:

$$E^{\text{cal}}(t) = \frac{1}{L}\sum_{i=1}^{M}\sum_{j=1}^{M} E_{i,j}(t) \tag{2. 1a}$$

$$x_{i,j}(t) = E_{i,j}(t) - E^{\text{cal}}(t), \quad t = 1, \cdots, N \tag{2. 1b}$$

where $E^{\text{cal}}(t)$ is the calibration signal. $x_{i,j}(t)$ is the calibrated signal. CMI uses time shift to align the calibrated signal $x_{i,j}(t)$ coherently [31]. The time-shifted calibrated signal then becomes:

$$x^{s}{}_{i,j}(t) = x_{i,j}\left(t + n_{i,j}(\boldsymbol{r}_0)\right) \tag{2. 2}$$

$$n_{i,j}(\boldsymbol{r}_0) = \frac{\|\boldsymbol{r}_i - \boldsymbol{r}_0\| - \|\boldsymbol{r}_j - \boldsymbol{r}_0\|}{C/\sqrt{\varepsilon_{r,\text{avg}}}} \tag{2. 3}$$

where $\boldsymbol{r}_i$ denotes the location of i th transmitting antenna and $\boldsymbol{r}_j$ denotes the location of j th transmitting antenna, and C is the speed of light. $n_{i,j}(\boldsymbol{r}_0)$ is the

time delay used to shift the time to confocal point $\boldsymbol{r}_0$ using the average dielectric property $\varepsilon_{r,\text{avg}}$ of the breast model, $\|\cdot\|$ denotes the Euclidean norm to calculate the distance between confocal point to antenna location. To help CMI remove the interference due to the breast tissue background that has fatty, glandular tissues as well as chest wall, a time window is also used[31, 47] given by:

$$\mathrm{w}_t = \begin{cases} 1, & \Delta t < t < N \cdot \Delta t \\ 0, & \text{otherwise} \end{cases} \tag{2. 4}$$

where Δt is the time interval of sampling the time-domain signal, N is the number of time sampling. After multiplying with the time window, the time-shifted and windowed signal is processed by the weight of a beamformer W_{BF}:

$$y_{i,j}(t) = {W^H}_{\text{BF}} \cdot {x^s}_{i,j}(t) \cdot \mathrm{w}_t \tag{2. 5}$$

Where the superscript "*H*"denotes the complex conjugate transpose. Hence, the choice of the beamformer weight W_{BF} is crucial. W_{BF} can adaptively enhance the energy from the target (tumor) while suppressing the energy from the background tissues. The output out of the beamformer $y_{i,j}(t)$is used to calculate energy intensity p at the confocal point $\boldsymbol{r}_0$:

$$p(\boldsymbol{r}_0) = \sum_1^N \left(y_{i,j}(t)\right)^2 \tag{2. 6}$$

This reconstructed energy is calculated for all the confocal points within the breast. Then, the image of energy intensity is formed so that the location of maximum intensity can identify the tumor.

For simple DAS[33], the beamformer weight can be equal to 1 without any scaling. DMAS beamformer uses calibrated signal itself as a beamforming weight to multiply another signal[46]. In this chapter, we propose a novel beamforming algorithm named as Modified-Weighted-Delay-and-Sum (MWDAS) method. In this method, we first use a modified weight factor to adaptively increase the synthetically focused intensity for the strong scatterer. Further, we multiply signals between time snapshots at every confocal point. In the next section, we will demonstrate the performance of MWDAS method using FDTD simulations on a planar block-shaped breast phantom mainly containing fatty tissues and malignant lesion model [46]. In this thesis, FDTD simulation was conducted by using a FDTD software package available at UTS. The block breast phantom is useful for testing the capabilities of the reconstruction methods.

2.2.2 The 3-D planar block-shaped numerical breast phantom

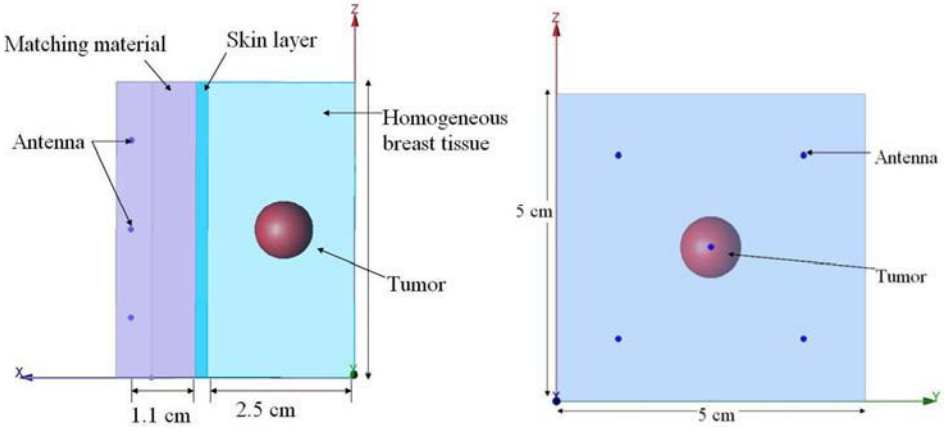

(a) (b)

Figure 2.2.2 Planar block breast phantom using FDTD. (a) View from y-axis. (b) View from x-axis. A spherical tumor is placed in the centre of breast tissue background.

A three-dimensional (3-D) planar block-shaped breast phantom is plotted in Figure 2.2.2 which has a width of 2.5cm, depth of 5cm and height of 5cm, with a skin layer of thickness of 2mm placed only on one side. A spherical tumor model with a known diameter (minimum=2mm and maximum=10mm) is embedded in the centre of the block model which is filled with model of homogeneous healthy (fatty) breast tissues. Five receiving antennas are placed at a distance of 1 cm from the skin layer as shown in Figure 2.2.2(b) and they are immersed in a coupling medium that has the same dielectric properties to those of the healthy breast tissues. Two-pole Debye equation is used to assign dielectric properties to normal breast tissues and the tumor. The parameters of normal breast tissues used are: $\varepsilon_\infty = 2.68$, $\varepsilon_{s1} = 5.01$, $\varepsilon_{s2} = 3.85$, $\tau_1 = 15.84\text{ps}$, $\tau_2 = 0.1\text{ns}$. For breast tumor, the parameters used are: $\varepsilon_\infty = 11.05$, $\varepsilon_{s1} = 51.67$, $\varepsilon_{s2} = 43.35$, $\tau_1 = 8.56\text{ps}$, $\tau_2 = 0.23\text{ns}$, and skin layer: $\varepsilon_\infty = 4.62$, $\varepsilon_{s1} = 37.1$, $\varepsilon_{s2} = 41.22$, $\tau_1 = 7.51\text{ps}$, $\tau_2 = 0.31\text{ns}$, which are similar to those given in [46].

A modulated Gaussian pulse with a maximum bandwidth of 13.5 GHz and 3-dB bandwidth of 4GHz is used as incident signal transmitted into the breast from each antenna. When the size of the tumor is large i.e. dia=10mm, a FDTD mesh of Δx=Δy=Δz=3mm is used to divide the block model into 20×26×26 cells with a time step of Δt=4.67ps. For a smaller tumor i.e., dia=2mm, a fine mesh is applied to FDTD to guarantee that the response from smaller tumor is properly captured in FDTD simulation with a time step Δt =0.81ps. Perfect matched layer (PML) absorbing boundary condition is used at 10 cells away from the simulation area. Since beamforming is used with FDTD simulation, the "Δt" requires for deciding the width of beamforming window given by equation (2.4) will be taken to be the smallest FDTD time step.

2.2.3 Reconstruction using MWDAS algorithm

2.2.3.1 Calibration

MWDAS algorithm helps to improve the confocal microwave imaging by enhancing the energy focused at a confocal point and simultaneously minimising the energy received from the clutters. The flowchart of MWDAS is shown in Figure 2.2.3.

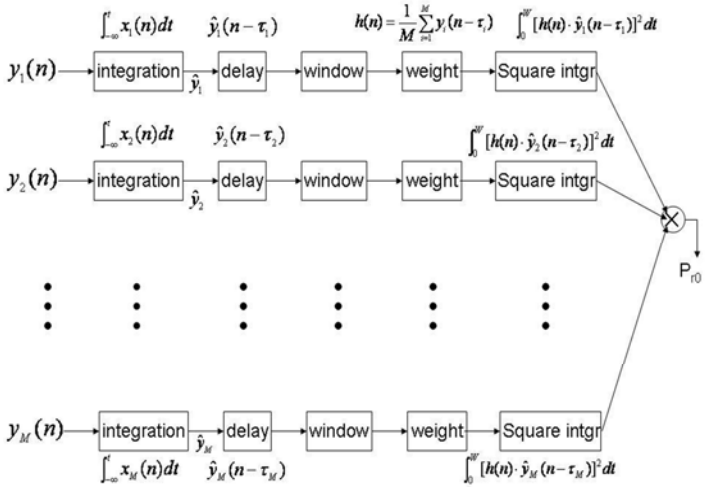

Figure 2.2.3 Block diagram depicting the procedures of MWDAS.

Here, we use a tumor-free template to obtain calibration signal $E^{\text{cal}}(t)$ to remove incident pulse and skin backscatter, assuming that signals recorded at various antenna positions have similar early-time content. The tumor-free template $E^{\text{free}}{}_{i,j}(t)$is obtained from the planar block-shaped phantom when the tumor model is removed. Thus in our case, $E^{\text{cal}}(t) = E^{\text{free}}{}_{i,j}(t)$. Then the calibrated signal is obtained by:

$$x_{i,j}(t) = E_{i,j}(t) - E^{\text{free}}{}_{i,j}(t) + e(t) \quad i = 1, \cdots, M, j = 1, \cdots, M, \tag{2. 7}$$

where $i =$ transmitting antenna index and $j =$ receiving antenna index. $x_{i,j}(t)$ is the calibrated time response, $E_{i,j}(t)$ is raw recorded backscattered data from ith transmitting antenna received at jth receiving antenna. $e(t)$ is residual signal containing interference from unwanted reflections and noise. By subtracting this calibration signal ${E^{\text{free}}}_{i,j}(t)$ from the raw data $E_{i,j}(t)$ at each antenna, the early-time content which includes excitation and skin backscatter, can be suppressed.

2.2.3.2 Integration

Now we use integration [32] to process the calibrated signal. The integration helps with synthetic focusing. Following the procedure given by [32], we integrate $x_{i,j}(t)$ at the zero-crossing point so that the coherent addition of local maxima occurs after time-shifting. After the integration over time for MWDAS, one obtains:

$$\hat{x}_{i,j}(t) = \int_{-\infty}^{t} x_{i,j}(u)du,\ u = 1,2,\cdots,\mathrm{N} \tag{2. 8}$$

where $\hat{x}_{i,j}(t)$ is the integrated signal. We assume that a number of confocal points exist inside the breast at locations $\boldsymbol{r}_k(x_k, y_k, z_k), k = 1,\cdots,K$. At each confocal point, we calculate the round trip distance for each antenna to the confocal point and convert it into time delay by propagation velocity in breast medium which is calculated using average dielectric constant of the breast tissues as given in (2.3). Now we shift the integrated signals $\hat{x}_{i,j}(t)$ by time delay at each confocal point to get:

$${\hat{x}^{\text{shift}}}_{i,j}(t) = \hat{x}_{i,j}\left(t + n_{i,j}(\boldsymbol{r}_k)\right) \tag{2. 9}$$

2.2.3.3 Image reconstruction

The key contribution of the proposed MWDAS method over the existing DAS [33]and DMAS[46] methods is the inclusion of the interaction between tumor responses

from different time snapshots to enhance the resolution and accuracy of tumor localization and at the same time offering high rejection to clutter interference. This interaction is implemented in MWDAS by cross multiplying the squared tumor responses. Before the cross-multiplication, a weight factor $h(t)$ is used to increase the energy intensity by averaging all the shifted signals at every antenna:

$$h(t) = \frac{1}{L}\sum_{i=1}^{L}\left[\hat{x}_{i,j}\left(t + n_{i,j}(\boldsymbol{r}_0)\right)\cdot \mathrm{w}_t\right] \quad (2.10)$$

where $L = M \times M$= size of the multistatic matrix, $\mathrm{w}_t$is time window as given in (2.4). The weight factor $h(t)$ can enhance the amplitude of the strong scatterers while helping to reduce that from other weak scatterers.

Finally the energy intensity that will be synthetically focused at any confocal point $\boldsymbol{r}_k$ as given by:

$$P(\boldsymbol{r}_k) = \prod_{i=1}^{M}\left\{\int_0^{W_t}\left[h(n)\cdot \hat{x}^{\mathrm{shift}}{}_{i,j}(t)\cdot \mathrm{w}_t\right]^2 \cdot dt\right\} \quad (2.11)$$

The 3-D breast phantom is divided into a number of voxels and the intensity given by equation (2.11) will be repeated at each voxel within the breast. The tumor will be localized at position whose intensity is the maximum. Since MWDAS method is based on energy, the region of maximum intensity can only reconstruct suspicious region. It is difficult to decide whether the maximum intensity is due to tumor or benign tissue. However, the information on suspicious region can be used to further process the signals which will be discussed in later chapters.

2.2.4 FDTD simulation using planar block breast phantom

In FDTD simulations, we use planar block phantom as shown in Figure 2.2.2. Then we employ DAS [33], DMAS[46], and the proposed MWDAS algorithms on FDTD data for comparison. The normalized intensity scales have been added on the figure. DAS and DMAS showed the absorbed backscattered field intensity. However, for MWDAS, the distribution of the image only shows pseudo-intensity due to backscattered signal at a focal point.

In this simulation, we consider signal-to-noise ratio (SNR) to be very high. We first consider a larger tumor (dia=10mm), for which the reconstructed images are shown in Figure 2.2.4. It can be seen that the proposed MWDAS method outperforms DAS and DMAS on resolution and clutter rejection. DAS has more interferences from clutters (fatty tissues) as shown in Figure 2.2.4(a). Figure 2.2.4(b) and (c) show the reconstructed image using DMAS which has a larger location uncertainty, while MWDAS estimates accurate location with reduced interference from clutters. In the second example, we consider a smaller tumor of dia=2mm. Comparison of the reconstructed images is shown in Figure 2.2.5. All the simulated results have also demonstrated that the proposed MWDAS improves the existing methods with better clutter rejection and can provide more accurate reconstruction of suspicious tumor location.

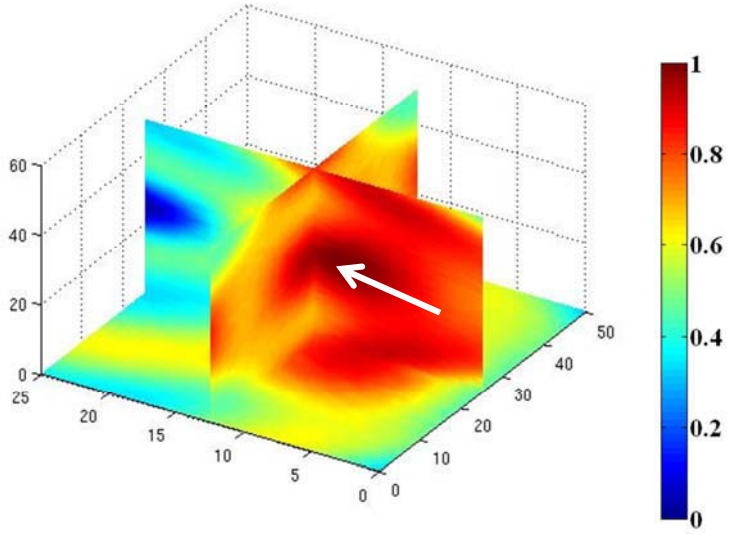
60
40
20
0
25
20
15
10
5
0
0
10
20
30
40
50
1
0.8
0.6
0.4
0.2
0

(a)

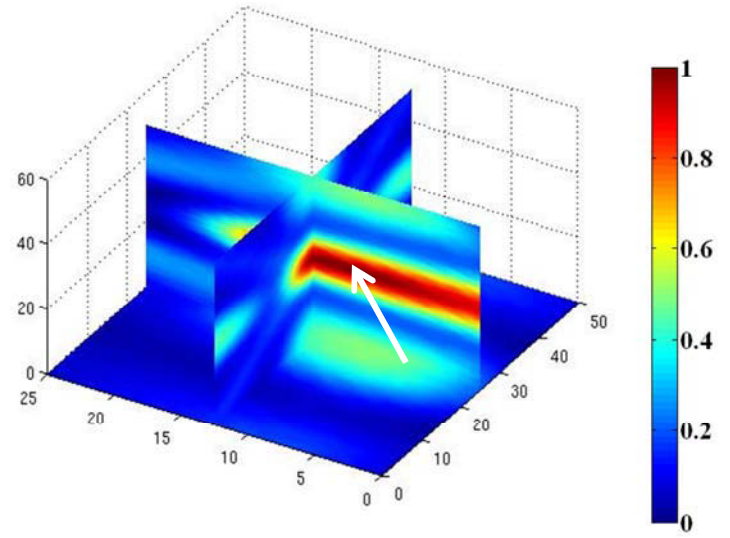
60
40
20
0
25
20
15
10
5
0
0
10
20
30
40
50
1
0.8
0.6
0.4
0.2
0

(b)

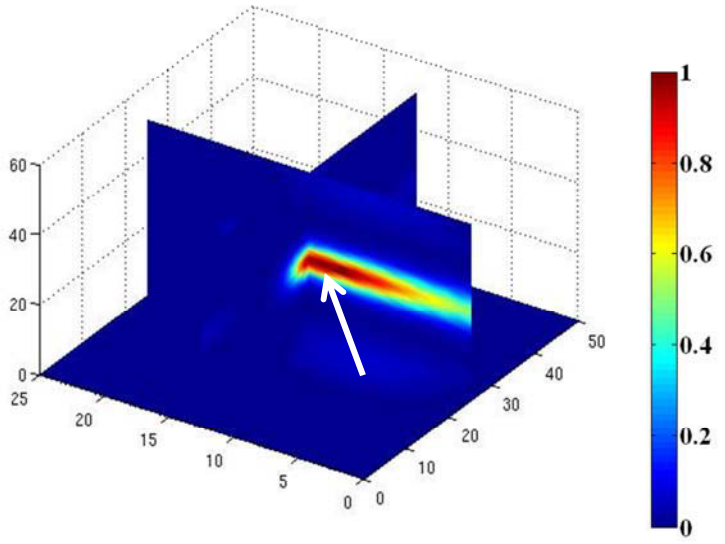

(c)

Figure 2.2.4 Comparison of the microwave reconstructed images for a 10mm embedded tumor in planar block phantom filled with only fatty tissues. (a) DAS. (b) DMAS. (c) Proposed MWDAS.

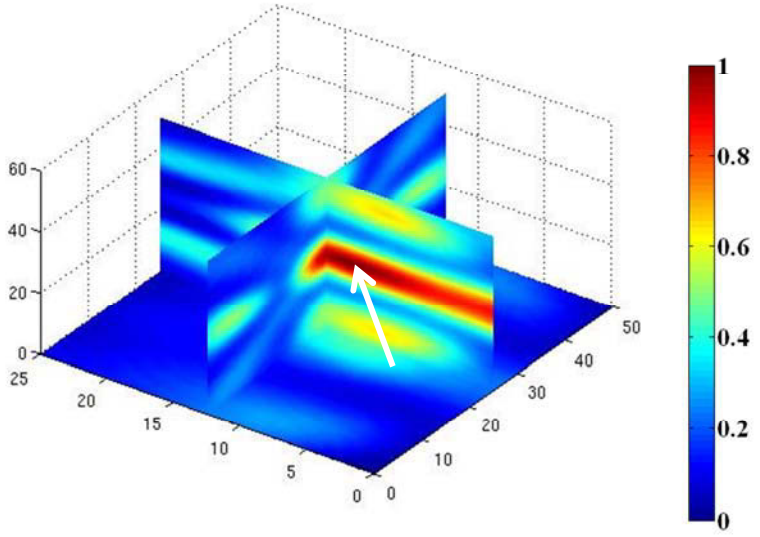

(a)

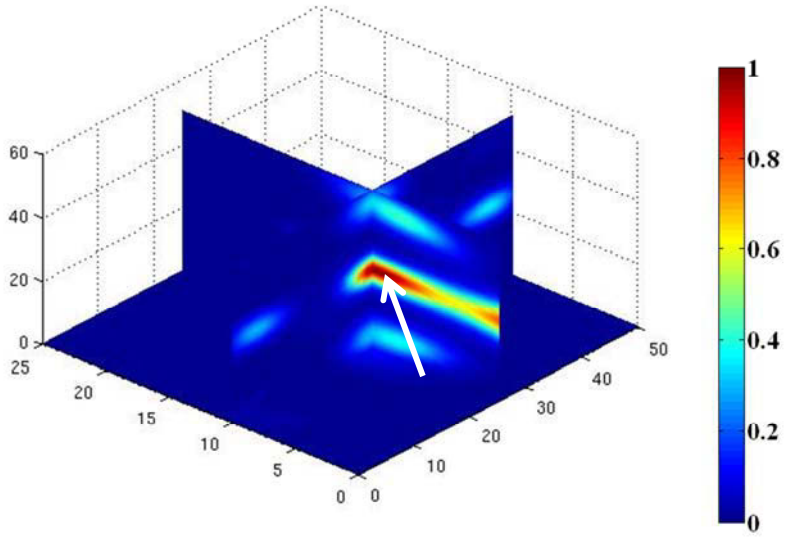

(b)

Figure 2.2.5 Comparison of microwave reconstructed images for a 2mm embedded tumor. (a) DMAS (b) Proposed MWDAS.

We have observed from the FDTD simulation that the performances of clutter rejection and reconstruction can be significantly affected by the window sizes as given by equation (2.4). In simulation, we have investigated four different window sizes viz., $440\Delta t$, $400\Delta t$, $350\Delta t$ and $300\Delta t$ with $\Delta t = 1.5ps$. Using MWDAS as shown in Figure 2.2.6, it can be observed that selection of window size is critical for the improved reconstruction and particularly when the size of the tumor is small. A larger window size may increase the clutter response whereas a smaller window may lead to localization bias as indicated in Figures 2.2.6(a) and (d). By comparing all the four reconstructed images of suspicious tumor locations, it can be concluded that when the window size is in the range of $400\Delta t$-$350\Delta t$, best results are obtained as shown in Figures 2.2.6 (b) and (c).

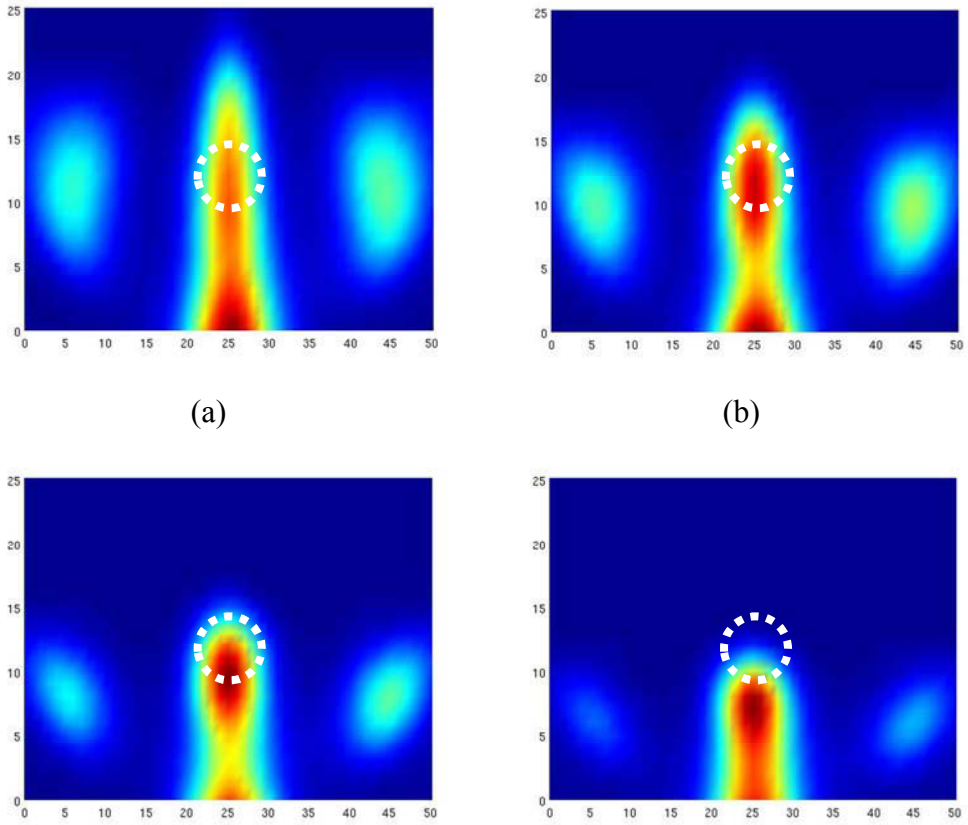

Figure 2.2.6 Comparison of microwave reconstructed images using MWDAS with different window sizes. (a) Window size=440$\Delta \boldsymbol{t}$ (b) Window size=400$\Delta \boldsymbol{t}$. (c) Window size=350$\Delta \boldsymbol{t}$. (d) Window size=300$\Delta \boldsymbol{t}$. The dashed circle indicates the true location of tumor in the phantom.

2.3 Data-dependent beamformer for image reconstruction

In this section, we describe the use of data-dependent beamformer such as robust capon beamformer (RCB) for breast image reconstruction using numerical phantoms. RCB was proposed by Stoica et al [65] and has been used for breast cancer detection [42, 47] due to its superior adaptive signal processing capacity. One such imaging method is multistatic adaptive microwave imaging (MAMI) which uses two stages of

RCB and demonstrated superior performances on a 3D breast phantom [47]. However, the phantom used in contain mostly fatty breast tissues and little fibroglandular tissues. Further, Xie et al [47] assumed high dielectric contrast between tumor and the heterogeneous breast fibroglandular tissues which deviate from the realistic breast tissue environment [52]. Our aim here is to demonstrate that the proposed MWDAS can also achieve high resolution of reconstructed image even for realistic dense glandular breast phantom.

2.3.1 Robust Capon Beamformer

The robust capon beamformer is derived from the original standard capon beamforming (SCB)[103]. For using SCB, first consider an antenna array that is receiving the backscattered signals from the target of interest. Here, we consider a semicircular array as shown in Figure 2.2.1(a) with number of antenna elements M=22. The adjacent elements have spacing d and array radius R. The array response vector (also known as steering vector) (θ), $i = 1, \cdots, K$, is formed in terms of to a narrow band signal $s(t)$ of wavelength λ impinging on the antenna elements from an angle θ, which is given by:

$$\mathbf{a}(\theta) = \left[e^{j\frac{2\pi R}{\lambda}\cos(\theta)} \; e^{j\frac{2\pi R}{\lambda}\cos(\theta - \frac{2\pi}{M})} \; \cdots \; e^{j\frac{2\pi R}{\lambda}\cos(\theta - \frac{2\pi(i-1)}{M})} \right]^T \qquad (2.12)$$

where superscript *T* denotes transpose. Then the received signal at ith antenna is given by:

$$\boldsymbol{x}_i(t) = \mathbf{a}(\theta)s(t) + \boldsymbol{e}(t) \qquad (2.13)$$

where $s(t)$ denotes the narrow frequency band signal. $\mathbf{a}(\theta)$ is steering vector of the receiving antenna array. $e(t)$ is residual contents that contain interference from

undesired reflections and additive white Gaussian noise. To use SCB for signal processing, the cross-spectral density matrix of the received signal is calculated using:

$$\mathbf{R}_X = E(\boldsymbol{x}\boldsymbol{x}^H) \tag{2. 14}$$

where E denotes expectation and superscript H denotes complex conjugate transposition. The power spectral density at output is given by[103]:

$$E(|\boldsymbol{y}|^2)=\boldsymbol{W}^H{}_{\mathrm{BF}}\mathbf{R}_X\boldsymbol{W}_{\mathrm{BF}} = \sigma^2 \tag{2. 15}$$

where $\boldsymbol{y}$ denotes the output of beamforming, $\boldsymbol{W}_{\mathrm{BF}}$ is the weight of beamforming, σ^2 is the signal strength of incident signal that impinges on the array. $\mathbf{R}_X$ can be decomposed into signal of interest and noise components by[103]:

$$\mathbf{R}_X = \sigma^2{}_s\mathbf{a}\mathbf{a}^H + \sigma^2{}_n Q \tag{2. 16}$$

where Q is the noise cross-spectral density matrix, $\sigma^2{}_s$ denotes the signal power, $\sigma^2{}_n$ denotes the noise power. The array gain G that helps to improve the signal-to-noise ratio (SNR) for beamforming is given as[103, 104]:

$$G = \frac{|\boldsymbol{W}^H{}_{\mathrm{BF}}\mathbf{a}|^2}{\boldsymbol{W}^H{}_{\mathrm{BF}}\boldsymbol{Q}\boldsymbol{W}_{\mathrm{BF}}} \tag{2. 17}$$

The aim of adaptive beamforming is to maximize array gain G given in (2.17). The maximizing problem can be formulated as:

$$\max_W \frac{|\boldsymbol{W}^H{}_{\mathrm{BF}}\mathbf{a}|^2}{\boldsymbol{W}^H{}_{\mathrm{BF}}\boldsymbol{Q}\boldsymbol{W}_{\mathrm{BF}}} \tag{2. 18}$$

The maximization in (2.18) is equivalent to minimization of [105]:

$$\min_W \boldsymbol{W}^H{}_{\mathrm{BF}} \boldsymbol{R}_X \boldsymbol{W}_{\mathrm{BF}} \quad \text{subject to} \quad \boldsymbol{W}^H{}_{\mathrm{BF}}\mathbf{a}=1 \tag{2. 19}$$

The solution of (2.19) can be obtained as [105]:

$$\boldsymbol{W}^{\mathrm{SCB}} = \frac{\boldsymbol{R}_X{}^{-1}\mathbf{a}}{\mathbf{a}^H \boldsymbol{R}_X{}^{-1}\mathbf{a}} \tag{2. 20}$$

The SCB is also known as minimum variance distortless response (MVDR) beamformer. SCB provides maximized SINR for output signal power, but it suffers from the steering vector bias due to the presence of errors in forming the steering vector.

To overcome the bias due to uncertainty of steering vector, RCB method was derived which gives an estimation for the steering vector using covariance fitting approach [64]:

$$\max_{\sigma^2{}_s,\, \mathbf{a}} \sigma^2{}_s \text{ subject to } \boldsymbol{R}_X - \sigma^2{}_s \mathbf{a}\mathbf{a}^H \geq 0, \left\|\mathbf{a}\text{-}\bar{\mathbf{a}}\right\|^2 \leq \partial \tag{2. 21}$$

where $\left\|\mathbf{a}\text{-}\bar{\mathbf{a}}\right\|^2 \leq \partial$ is constraint on the steering vector. By maximizing the objective function given in (2.21), an accurate estimation of steering vector can be obtained so that the beamformer $\boldsymbol{W}^{\mathrm{SCB}}$ in (2.20) can estimate an accurate waveform of signal $s(t)$ with maximized SINR. Since SCB and RCB both require the knowledge of steering vector, they are categorized as data-dependent beamformers. On the other hand, DAS, DMAS and the proposed MWDAS do not require steering vector information and thus are known as data-independent beamformers.

In the application of breast cancer detection, the calibrated signals $\boldsymbol{x}_{i,j}(t)$ from ith transmitting antenna to jth antenna is obtained after removal of the early-time content [32, 47]. Next, similar to other confocal microwave imaging methods such as DAS and MWDAS, the domain of interest within the breast phantom is divided into a number of confocal points so that RCB can scan for every confocal point repeatedly. At each confocal point $\boldsymbol{r}_k$, the calibrated signals $\boldsymbol{x}_{i,j}(t)$ are steered to this confocal point by using time shift [47] given by (2.9). Thus, the steering vector $\mathbf{a}$ will be made equal to a unit vector $1_{M\times 1}$ if a confocal point $\boldsymbol{r}_k$ falls at the true location of a scatterer so that the output of the RCB beamformer is the response from this scatterer. Otherwise, if the confocal point is not at a scatterer, a large bias will exist in steering vector and the output signal from this point will be suppressed by RCB. For implementing SCB or RCB, one has to divide the recorded UWB signal into a number of narrow subbands using FFT. Then, each subband signal can be processed by SCB or RCB.

In practice, steering vector after time shift at one confocal point can be approximately unity $1_{M\times 1}$ due to the uncertainties arising out of bias. The parameter ∂ in equation (2.21) is the uncertainty parameter that is sufficiently small[47, 65]. The problem of (2.21) can be reduced to following quadratic optimization [106] given by:

$$\min_{\widehat{\boldsymbol{a}}} \mathbf{a}^H \boldsymbol{R}_X{}^{-1}\mathbf{a} \text{ subject to } \|\mathbf{a}-\bar{\mathbf{a}}\|^2 \le \partial \qquad (2.22)$$

Once the steering vector $\widehat{\boldsymbol{a}}$ using (2.22) is estimated, RCB weight can be obtained by substituting the estimated $\widehat{\boldsymbol{a}}$ into equation (2.20). Thus, the output signal $\boldsymbol{y}_{i,j}(t)$ of the RCB will become the response from the target given by:

$$\boldsymbol{y}_{i,j}(t) = \boldsymbol{W}^{\mathrm{RCB}} \cdot \boldsymbol{x}^{\mathrm{shift}}{}_{i,j}(t) \qquad (2.23)$$

Then, the energy intensity of estimated target response $\boldsymbol{y}_{i,j}(t)$ can be calculated using (2.6) at a confocal point. By synthetically scanning this confocal point within the breast, reconstructed image can be formed for localization of suspicious region.

2.4 Comparison of image reconstruction using 2-D heterogeneously dense numerical breast phantom

For comparing the performances of data-independent versus data-dependent beamformers for image reconstruction, we employ a two-dimensional heterogeneous numerical breast phantom as shown in Figure 2.4.1. Healthy breast tissues including fibroglandular and fatty tissues are modeled as elliptical shapes and positioned randomly within the 2-D breast region [99, 102]. Chest wall is assumed to 30mm thick. A circular breast lesion with 10mm diameter is embedded at (12, 15)mm within the phantom. The dielectric properties for breast tissues including breast lesion are allocated using the two-pole Debye parameters [55] [52, 53]. FDTD grid size is 0.1mm×0.1mm and 10 layers of convolutional perfectly matched layer (CMPL) are used having 15 cells away from the simulation region. The incident Gaussian pulse has 3-dB bandwidth of 2.5GHz with frequency up to 7.4 GHz and transmits into the breast using all 22 ideal antennas which are placed 10mm away from the 2mm thick skin layer. The antennas are employed in a multistatic configuration, meaning that while one antenna transmits, all the other receive the backscattered signals. For employing SCB and RCB, the received UWB signals have to be transformed into narrow frequency subbands.

Pre-processing uses target-free template (2.1) to remove the early-time contents. It is worth noting that the backscattered signals including target response and responses from other healthy tissues are nonlinear. Thus, target response after subtracting the

target-free template still has residual signals from healthy tissues such as fatty and glandular tissues. The calibrated signals are then processed by time-shift, time-window, (2.2)-(2.4) for processing both the data-dependent and data-independent beamformers. We compare DAS, DMAS, SCB, RCB and the proposed MWDAS using this 2D breast phantom.

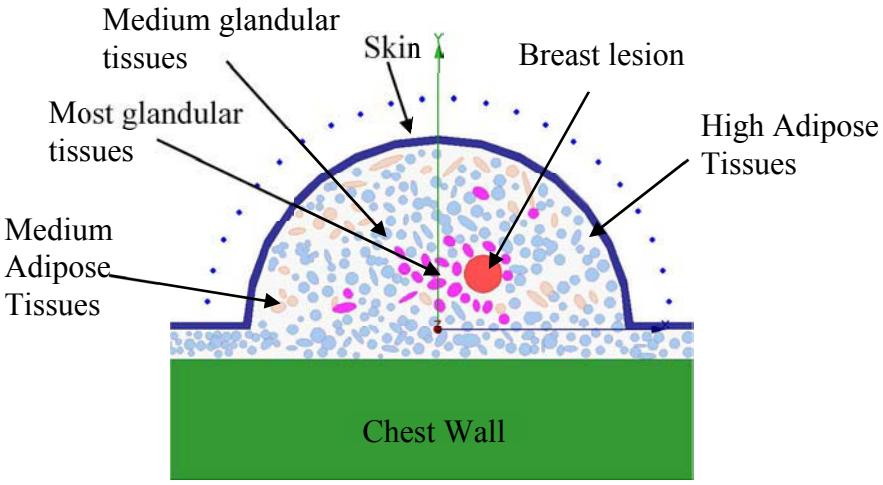

Figure 2.4.1 Two-dimensional FDTD breast model with heterogeneously breast tissues. A 10mm breast lesion is placed at (12, 15)mm.

The comparison of different reconstructed methods is shown in Figure 2.4.2. The suspicious tumor location is indicated by the position with the highest intensity. Based on the observation, as shown in Fig. 2.4.2, the brightest red color region would indicate the tumor position and lighter red and yellow colors may only represent the artifacts due to the reconstruction algorithm. This was also observed in Fig. 5.4.3 and Fig. 5.4.6 in chapter 5.

When using DAS [33], the beamformer weight is taken to be equal to 1 using (2.5) and the focused energy at confocal point is obtained using (2.6). The resulting image within the breast is shown in Figure 2.4.2 (a). It can be seen that clutter effect is significant and breast lesion (as indicated in white color dashed circle) is difficult to identify. On the other hand, DMAS appears to segregate the clutter region from the suspicious tumor region (white color dashed circle) within the breast as shown in Figure 2.4.2(b). However, the intensity of energy from clutter response for DMAS is still very high. In Figure 2.4.2(c), reconstructed image using SCB has reduced the clutter effects and also indicate correct position of breast lesion (white color dashed circle). But the energy from clutter is still higher than reconstructed energy from breast lesion. Reconstructed image using RCB provides better reconstructed image as shown in Figure 2.4.2(d). Compared with DAS, DMAS and SCB, RCB offers superior suppressing of clutter effects and thus breast lesion can be clearly identified (white color dashed circle). Finally, we show the resulted image reconstructed using proposed MWDAS in Figure 2.4.2(e). It can be seen that MWDAS can achieve higher resolution than the RCB. In addition, clutter effects can be well suppressed. To assess the resulted image quantitatively, we also calculate the signal-to-clutter ratio (SCR) as used in literature [44, 47]. The calculated SCR using (3.35) is given in Table 2.3.1.

Table 2.4.1 Signal-to-Clutter Ratio (dB) for 2D Breast Phantom at SNR=30dB

DAS	DMAS	SCB	RCB	MWDAS
-0.2	-0.4	-0.3	4.0	5.2

Table 2.4.2 Performance Comparison of Different Beamforming Techniques

	Advantages	Disadvantages
DAS	Low computation cost; Robust to breast tissue heterogeneity ; No steering vector required.	Low resolution; Difficult to detect under clutters.
DMAS	Low computation cost; Slightly better than DAS; No steering vector required.	Low resolution; Difficult to detect under clutters.
SCB	Higher resolution than DAS	High computation cost; Suffer from steering vector bias; Difficult to detect under clutter; Knowledge of accurate steering vector information required
RCB	Higher resolution; Easy to detect	High computation cost; Knowledge of accurate steering vector information required; Need to solve optimization to obtain steering vector.
MWDAS	Low computation cost; Higher resolution; Easy to detect; No steering vector required.	Obtains pseudo-energy of backscattered signal at a confocal point; Cannot directly obtain waveform.

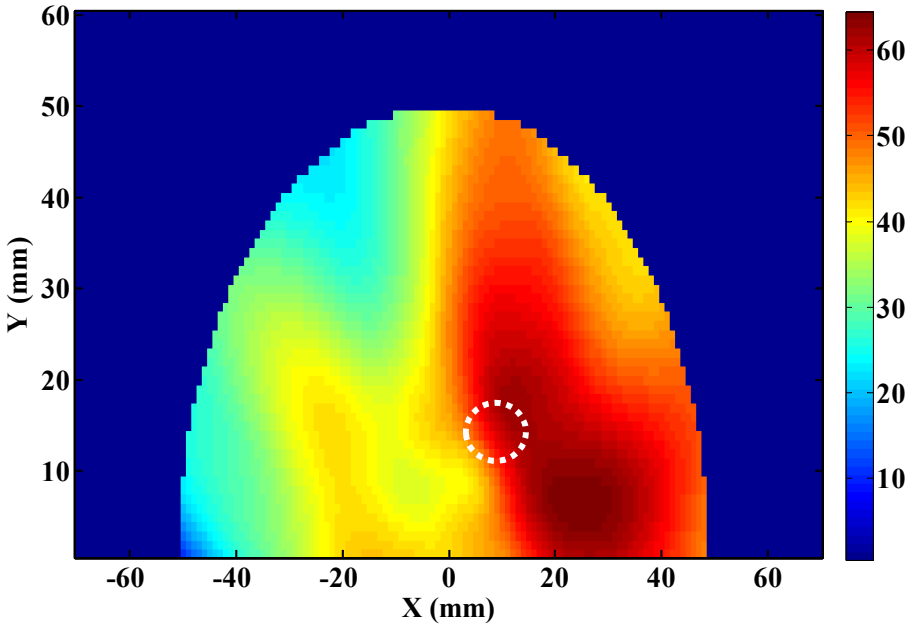
60
50
40
30
20
10
Y (mm)
-60
-40
-20
0
20
40
60
X (mm)
60
50
40
30
20
10

(a) DAS

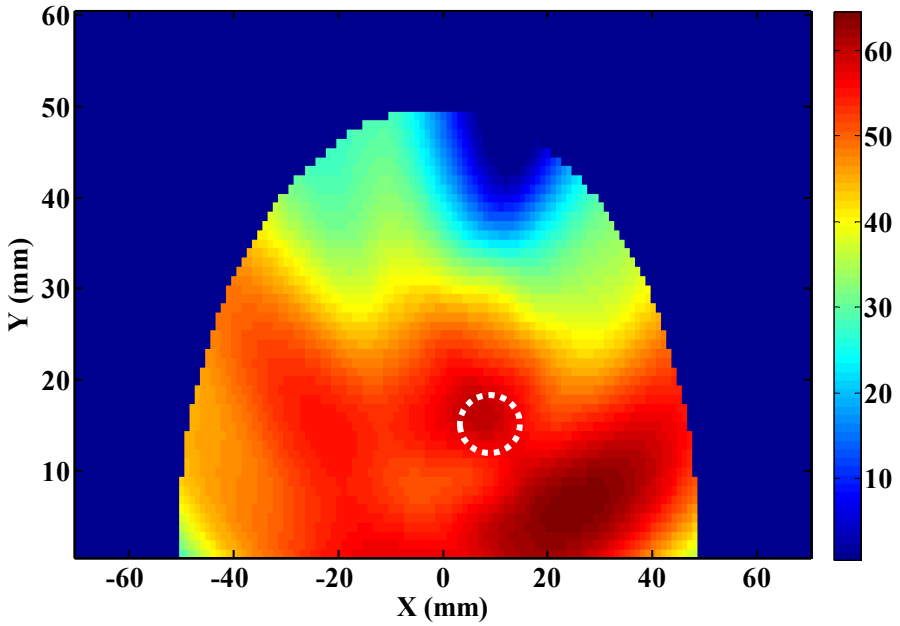
60
50
40
30
20
10
Y (mm)
-60
-40
-20
0
20
40
60
X (mm)
60
50
40
30
20
10

(b) DMAS

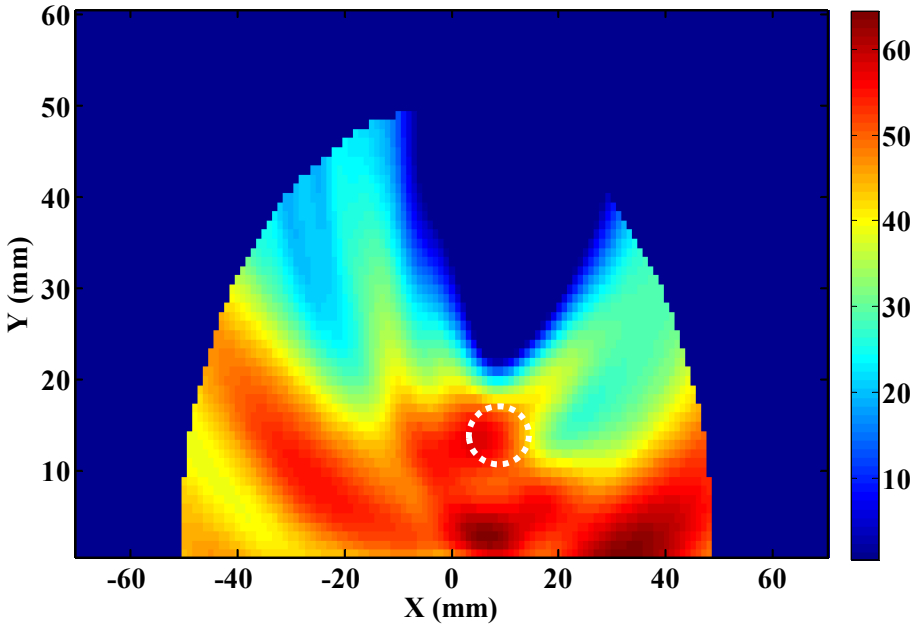
60
50
40
30
20
10
Y (mm)
-60
-40
-20
0
20
40
60
X (mm)
60
50
40
30
20
10

(c) SCB

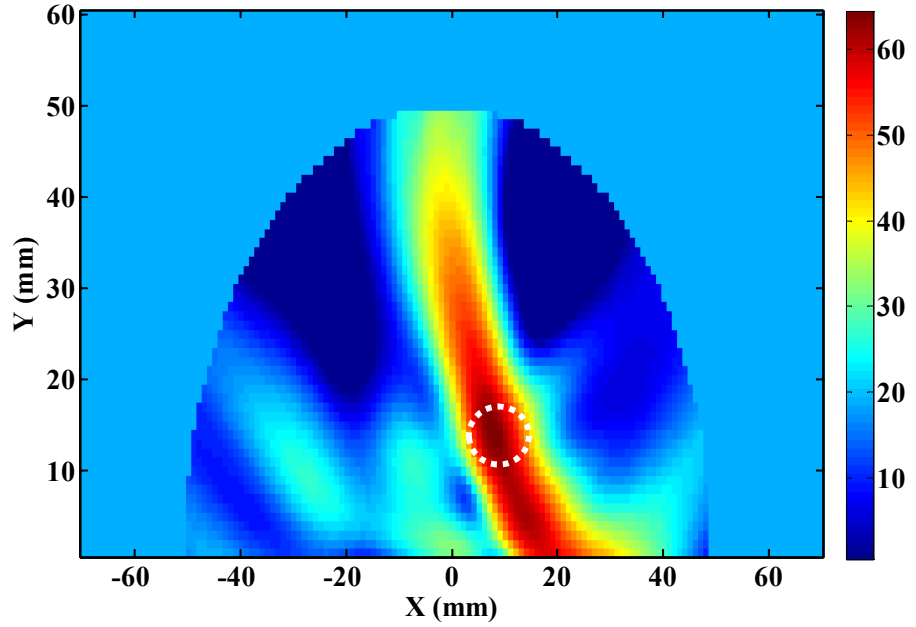
60
50
40
30
20
10
Y (mm)
-60
-40
-20
0
20
40
60
X (mm)
60
50
40
30
20
10

(d) RCB

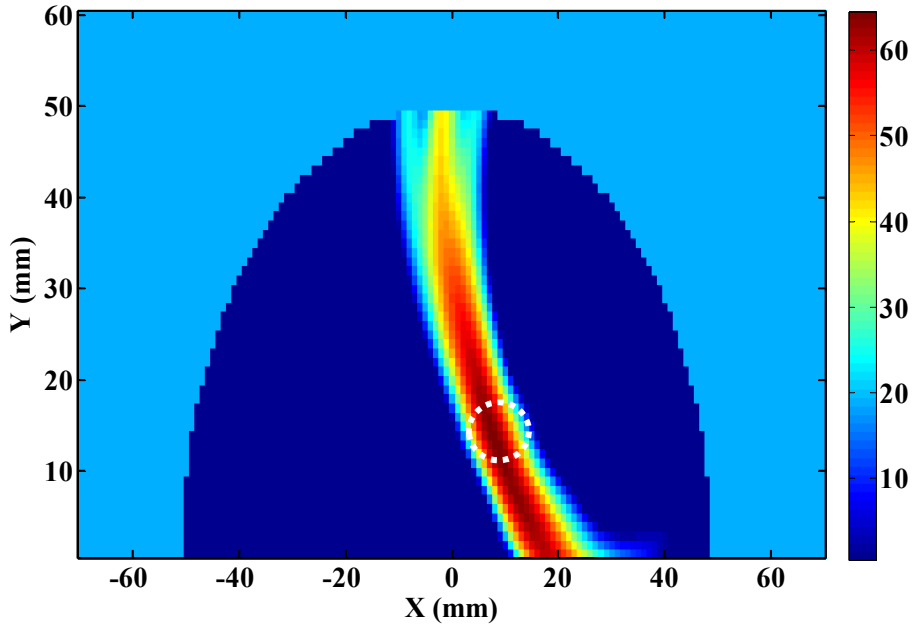

(e) MWDAS

Figure 2.4.2 Reconstructed images of suspicious tumor locations (a) DAS (b) DMAS (c) SCB (d) RCB (e) MWDAS

2.5 Discussion

This chapter presents the proposed MWDAS beamforming for localizing the suspicious region within the breast where malignant lesion could be located. We proposed MWDAS and demonstrate its performance using a simple 3D planar block phantom as well as 2D heterogeneous breast phantom. The smallest dielectric contrast employed between the tumor model and healthy fibroglandular tissues is 1.2:1 in the 2D phantom. Simulated results have demonstrated that our MWDAS can suppress the clutter effects significantly and also give accurate location of breast lesion.

It must be pointed here that MWDAS only provides pseudo-energy focused at a confocal point which may correspond to the location of the tumor within the breast,

however, it is difficult to estimate the time-domain waveform of the target response from the reconstructed suspicious region. Therefore, like other energy-based reconstruction methods such as DAS and DMAS, MWDAS also cannot identify whether the target tissue within the suspicious region is malignant or benign. However, it estimates the suspicious region within heterogeneous breast phantoms accurately.

Despite its limitation, MWDAS can be still very useful due to its focusing ability at a confocal point within the breast. Hence it will be employed for the breast tumor discrimination as will be discussed in Chapter 3. MWDAS can effectively perform as a filter to spatially remove the clutter effects effectively and thus helps to pre-process for the estimation of the late-time target response accurately. These will be discussed in later chapters.

Chapter 3
Discrimination of Malignant and Benign Tumors via Complex Natural Resonances

3.1 Introduction

The microwave imaging techniques reported in the literature have successfully established great potential to localize the malignant tissue inside the breast. [32, 35, 42, 107, 108]. However, for the clinical diagnosis, the detection of the suspicious tumor location alone is not enough. It is important to be able to distinguish malignant lesion from benign tumors from the location of suspicious region. The main factor that may hinder the success of any technique that seeks to identify the malignancy is the interference from fibroglandular tissue which usually acts a strong scatterer [53]. The inhomogeneity of the breast tissue usually results in blurred images when employing the existing radar based microwave imaging techniques. To overcome the limitations of radar based imaging techniques, tomographic microwave imaging techniques have been proposed which seek to produce dielectric property map to identify the malignant tissue

[24, 25, 109]. However, the performance of microwave tomography can also be severely degraded when dense glandular tissues dominate the breast tissue composition. This is due to the fact that tomography seeks to solve the complex ill-posed inverse problem and the presence of fibroglandular dense tissue may lead to false detection because the dielectric property of fibroglandular tissue is quite similar to that of the malignant tissue.

A new direction for the breast cancer detection has appeared recently which seeks to investigate the shape characteristics in addition to the electromagnetic properties of the malignant breast lesions [98]. It has been revealed that the resonance spectra of malignant breast lesions depend on the shape as well as the dielectric properties[98]. One way of identifying the resonant characteristics of a target is by obtaining complex natural resonance (CNR). CNRs associated with the size and dielectric properties of breast lesions have been studied [97] by using Prony's method [110] for extracting CNRs. Morphology-dependent temporal and spectral characteristics have also been used to distinguish benign and malignant masses [99] based on the distinct morphological features of benign and cancerous masses as obtained by MRI and mammographic images [4, 84-86]. In this thesis, we follow a two-stage microwave imaging in which we seek to identify the suspicious tumor location followed by the extraction of complex natural resonances to discriminate the morphological features of the breast lesions.

We propose a general pair-matching preprocessing to analyze the received time-domain microwave backscatter data and to remove the unwanted data by using root-mean-square error (RMSE) criterion. We then employ autocalibration of time-of-arrival (TOA) to estimate TOA due to unknown propagation paths within inhomogeneous breast phantom. As the early-time response and antenna ringing can result in spurious CNRs, we have developed a new method to suppress them by using the fundamental

resonance extracted from the target response. To achieve a high quality of the extracted CNR from time-domain data, practical calibration techniques have also been presented using smooth shaped and spiculated shaped PEC spheres. We follow three main steps of calibration:

1) Obtain CNRs for perfect electrically conducting (PEC) spheres using FDTD simulated scattered fields on numerical phantoms. The results will be compared with CNRs obtained using closed-form exact expression as well as measured data for the same size PEC spheres so as to confirm their authenticity of extracted CNRs. This is the first step of our CNR calibration.

2) Investigate the CNRs extracted from dielectric lesions that have spiculated surface geometries (morphology) using FDTD on numerical phantoms and compare the results with the CNRs extracted from PEC objects having the same morphological features. This helps to confirm the external mode of CNR for embedded dielectric lesion.

3) Apply normalized CNR estimation error (NCR) to estimate any errors in extracted CNRs.

Our FDTD based investigations for CNR extraction use realistic C3-class MRI-derived numerical breast phantom taken from UWCEM phantom repository[63], which contains dense fibroglandular tissues. Our results based on FDTD simulation have shown: 1. higher mode of CNR poles have increased potential for discriminating the malignant breast lesion from benign tissue based on CNR signatures; 2. the discrimination is possible in breast model with dense fibroglandular tissues within the frequency ranging from 4GHz to 10GHz if the diameter of the lesion is 10mm.

3.2 Complex natural resonance (CNR)

Complex natural resonance (CNR) is obtained from late-time target response which is generated after the target is excited by a transient signal. Fields are scattered initially from the target and then multiple scattering also occurs. Subsequently, the late-time radiated fields associated with the scattering decay and radiate away from the target [94, 99, 111]. The late-time response can be parameterized in terms of the well-known singularity expansion method (SEM) developed by Baum [112]. After SEM expansion, each nonzero singularity will correspond to a complex natural resonance (CNR) mode. Along with late-time target response, early-time nonresonant response also appears which only contains singularities due to the excitation source. It has been shown that CNR is closely related to the geometric signature[94] or burial depth [90] of a target. In particular, CNRs associated with dielectric sphere can be separated into internal and external modes [89]. The internal resonances are caused by the internal waves that experience multiple internal reflections, whereas the external modes are caused by the surface creeping waves [89]. The physical mechanism associated external resonances has shown that the external mode of CNR is related to surface propagating waves (creeping waves) and such creeping waves are determined by the surface geometry instead of the interior material property [113]. The same mechanism of the creeping wave can be explained by acoustic scattering in fluids[114]: the creeping waves propagate along the surface of water droplet with attenuation due to the continuous radiation in the tangent direction. Hence, by studying the extracted resonances, dielectric objects can be characterized [115, 116].

It is hypothesized that the internal and external modes of dielectric sphere can be extended to arbitrary shapes [96]. The external CNRs are independent of the target's internal material and only depend on the target's surface geometry[89]. Furthermore,

the external CNRs have much higher damping factors than the internal ones. Therefore, we propose to utilize the external mode of CNR to potentially discriminate malignant and benign breast lesions based on their morphological differences. It is worth noting that it is quite challenging to separate external and internal CNRs from the late-time response [96, 117].

To formulate the problem for extracting complex natural resonances, let us assume that the late-time target response is $f(t)$. It can be represented by a sum of complex exponentials by using singularity expansion method (SEM) [112]. SEM method has been investigated extensively for radar target recognition by extracting the complex natural resonances [118]. In essence, SEM models the late-time target response of a target excited by a burst of electromagnetic pulse as a sum of complex poles. Since the extracted complex poles are intrinsic to the geometry of the target, they can be utilized to characterize the target.

After applying SEM to the target response, $f(t)$ is represented by:

$$f(t-t_0) = \sum_{m=1}^{N} C_m e^{S_m(t-t_0)} \tag{3. 1}$$

where $S_m = \alpha_m + j2\pi f_m$ are called s-plane poles of CNR. α_m, f_m and C_m are damping factor, resonant frequency, and complex amplitude of CNR, respectively. t_0 is the start of the late-time target response. $f(t-t_0)$ can be sampled by time interval δt:

$$f\big((k-1)\delta t\big) = \sum_{m=1}^{N} C_m e^{S_m(k-1)\delta t} \quad \mathrm{k} = 1, \cdots, L \tag{3. 2}$$

If we define $Z_m = e^{s_m \delta t}$ as the natural resonances in Z-plane, for convenience, equation (3.2) is changed to:

$$f_k = f\big((k-1)\delta t\big) = \sum_{m=1}^{N} C_m Z_m^{k-1},\ \mathrm{k} = 1, \cdots, L \qquad (3.3)$$

Thus, damping factor and resonant frequency can represent the CNR signatures of late-time target response. The unit of damping factor is neper per second: Np/s. In the thesis, damping factor is normalized to neper, and hence does not correspond to the frequency [96]. The damping factor describes how fast the decaying exponential damped when it radiates away from the target for each resonant mode and thus must be negative. A high value of damping factor (absolute value) means it damps faster. For the target recognition using short pulse microwave illumination, damping factor is closely related to the geometric properties and dielectric properties of the target. Targets with different shape or conductivity will show varied damping factors.

To approximate a function $f(t)$ as a sum of complex exponentials, two popular singularity expansion methods are used: "polynomial" method and "matrix pencil" method[119]. The polynomial method was first developed by Prony [110] and further improved by many variants such as total least square (TRL) Prony's methods [94, 120]. On the other hand, matrix pencil method [121, 122] is more robust to noise and has no practical limitation on the number of poles compared to Prony's method. In this thesis, matrix pencil method (MPM) is used to explore the CNRs from the late-time target response [119].

3.2.1 CNR extraction from conducting spheres

From the time-domain late-time target response, we propose to extract CNRs by using matrix pencil method[119]. To obtain the time-domain scattered field of a target,

we use FDTD method to simulate scattering from a PEC sphere in free space excited by Gaussian pulse as shown in Figure 3.2.1. The reason to choose a PEC sphere is that the conducting spheres can be considered as reference objects to study the complex resonances. Further, the resonances extracted from PEC spheres with different sizes have been experimentally investigated in the literature [123] which can be used for comparison. By comparing our simulated results of extracted resonant frequencies with the experimental results and the resonant frequencies given by closed form expressions [124], we can calibrate the extraction method we used. Theoretical natural resonant frequency of PEC sphere in free space can be calculated by [124]:

$$f_n = \frac{p_n C}{\pi d} \tag{3. 4}$$

where C is speed of light, d is diameter of PEC sphere, p_n is imaginary part of pole location as given in literature [124].

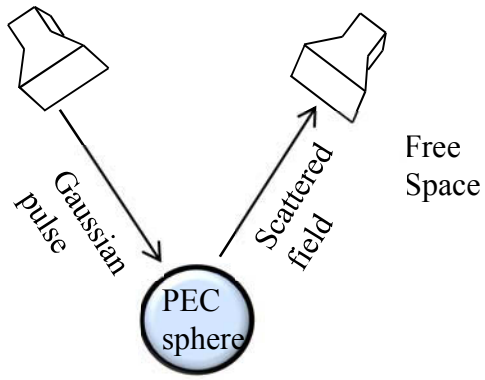

Figure 3.2.1 FDTD simulation to obtain scattered field from a PEC sphere in free space.

In the FDTD simulation, ideal antennas are used to receive the scattered field and the conducting sphere is illuminated by plane wave in the form of Gaussian pulse which has frequency up to 20GHz with 3dB bandwidth of 6GHz. Boundary condition uses

convolutional perfectly matched layer (CPML) with 6 layers. Mesh grid uses 1mm × 1mm grid size.

3.2.2 CNR extraction from embedded conducting spheres

We also simulate the backscattered field from conducting sphere immersed in dielectric half-space as shown in Figure 3.2.2. Baum's transform has linked the extracted CNRs of a PEC sphere when it is immersed in homogeneous lossy medium to the CNRs in free space [125]. Thus, we can obtain CNRs of PEC sphere immersed in a lossy medium from its free space CNRs. Baum's transform has been used to identify the objects such as anti-tank mine and unexploded ordnance buried underground by predicting their CNRs in lossy underground based on CNRs in free space [94]. The equation of Baum's transform is given by [125]:

$$S = -\frac{\sigma}{2\varepsilon_0\varepsilon_r} + \left[\left(\frac{\sigma}{2\varepsilon_0\varepsilon_r}\right)^2 + \frac{\left(S^{(0)}\right)^2}{\varepsilon_r}\right]^{1/2} \tag{3. 5}$$

where $S = \alpha + j2\pi f$ is the transformed s-plane pole in the dielectric medium with permittivity of ε_r and conductivity of σ. α and f are damping factor and resonant frequency of transformed CNR signatures respectively. $S^{(0)} = \alpha_0 + j2\pi f_0$ is the free space CNR pole and α_0 and f_0 are damping factor and resonant frequency in free space.

Baum's transform has two important restrictions: 1). It is only valid for a perfectly conducting sphere 2). The immersing medium is assumed to be isotropic and homogeneous but lossy medium. Here, we immerse conducting spheres in homogeneous dielectric half-space and simulate the scattered field using FDTD method.

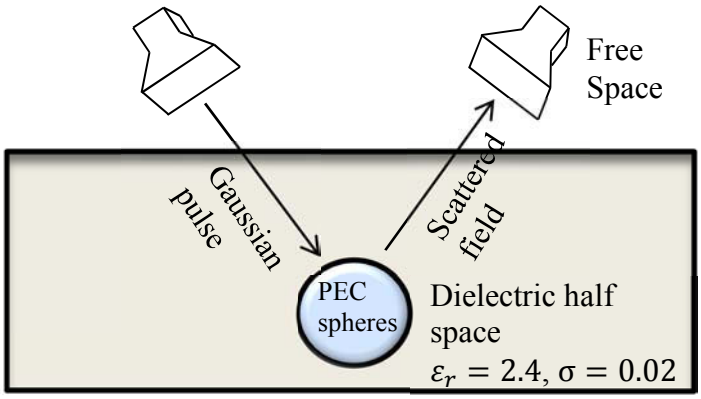

Figure 3.2.2 FDTD simulation to obtain scattered field from a PEC sphere in dielectric half-space

Table 3.2.1 COMPARISON OF RESONANT FREQUENCY OF PEC SPHERE (dia=1 inch)

Resonant frequency (GHz)	Pole 1	Pole 2	Pole 3	Pole 4	Pole 5
Theoretical [124] (Free Space)	3.26	6.79	10.37	13.97	17.58
Measured [123](Free Space)	*	6.8	10.6	13.6	*
Simulated (Free Space)	3.34	6.31	10.35	13.61	18.17
Baum's Transformed (in dielectric medium)	1.58	3.39	5.18	6.98	8.79
Simulated (in dielectric medium)	1.75	*	5.56	6.30	9.07

Table 3.2.2 COMPARISON OF RESONANT FREQUENCY OF PEC SPHERE (dia= $\mathbf{1\,^{1}/_{8}}$INCH)

Resonant frequency (GHz)	Pole 1	Pole 2	Pole 3	Pole 4	Pole 5
Theoretical [124](Free Space)	2.89	6.04	9.22	12.42	15.63
Measured [123](Free Space)	*	6.40	9.50	13.0	*
Simulated (Free Space)	2.85	5.83	9.40	12.58	15.96
Baum's Transformed (in dielectric medium)	1.44	3.02	4.61	6.21	7.81
Simulated (in dielectric medium)	*	3.08	4.22	6.18	8.26

Table 3.2.3 COMPARISON OF RESONANT FREQUENCY OF PEC SPHERE (dia= $\mathbf{1\,^{5}/_{16}}$INCH)

Resonant frequency (GHz)	Pole 1	Pole 2	Pole 3	Pole 4	Pole 5
Theoretical [124] (Free Space)	2.48	5.18	7.90	10.64	13.39
Measured [123](Free Space)	*	*	7.8	10.7	*
Simulated (Free Space)	2.62	*	7.45	*	13.17
Baum's Transformed (in dielectric medium)	1.24	2.59	3.95	5.32	6.69
Simulated (in dielectric medium)	*	2.51	3.04	*	7.44

Table 3.2.4 COMPARISON OF RESONANT FREQUENCY OF PEC SPHERE (dia= $\mathbf{1\,^{1}/_{2}}$INCH)

Resonant frequency (GHz)	Pole 1	Pole 2	Pole 3	Pole 4	Pole 5
Theoretical [124] (Free Space)	2.17	6.91	9.31	11.72	16.57
Measured [123](Free Space)	*	6.8	9.7	*	*
Simulated (Free Space)	2.35	6.8	*	11.51	16.22
Baum's Transformed (in dielectric medium)	1.08	3.45	4.65	5.86	8.28
Simulated (in dielectric medium)	*	*	4.50	5.74	8.78

The symbol $*$ refers to unavailable data in extracted poles, because some poles for complex natural resonance may not be extracted both in numerical extraction or experimental measurements [123, 126]. The reasons could be: (a) the late-time signal could not be extracted accurately. (b) the missing resonant mode could have been corrupted by the residual early-time nonresonant signal or imperfection due to antenna reception.

To get the simulated data, the same UWB pulse with 3-dB bandwidth of 6GHz illuminates the embedded PEC sphere. The dielectric medium chosen to immerse spheres has $\varepsilon_r = 4$, $\sigma = 0.02$. The calculated late-time responses are processed by Matrix Pencil method [119] to obtain the resonances. The numerical results obtained in free space are compared with theoretical [124] and published measured data [123] as tabulated from Table 3.2.1 to Table 3.2.4. The theoretical data in free space are transformed using Baum's equation (3.5) to obtain CNRs in embedded medium.

We then compare our CNRs extracted using FDTD simulation with the Baum transformed theoretical data as shown from Table 3.2.1 to Table 3.2.4. It can be observed from the four tables that: (1) the simulated data from free space are close to theoretical and measured data in free space; (2) the simulated data for embedded dielectric medium are close to those predicted by Baum's transformed theoretical data[124].

3.3 CNR extraction for numerical breast phantom

The above results on extracted CNRs show encouraging results of our FDTD simulations. However, our main aim here is to demonstrate that breast lesion can be discriminated (malignant versus benign) using CNRs which are extracted from the late-time target response and Matrix Pencil method. Therefore, obtaining accurate time-

domain late-time target response is important. To get the target response from breast lesions embedded in breast tissue background, we firstly localize the suspicious region within breast where it is possible for a malignant lesion to exist. For this, we employ MWDAS to suppress clutter response from background tissues which can affect the accuracy of extracted CNR. However, MWDAS, like other existing beamforming techniques [34, 42, 47], cannot estimate an accurate waveform from the suspicious region. Hence, we then propose another two-sage waveform estimation technique to estimate the late-time target response from the suspicious region. Using this waveform, we extract CNRs.

To effectively localize the suspicious region of breast lesion, early-time artifacts including antenna excitation and skin reflections must be removed. Hence, we propose a general preprocessing technique to remove the early-time artifacts. In addition, the varying tissue composition (fibroglandular and fatty tissues) within breast are dispersive and can result in different propagation velocities for the backscattered signals to propagate within the breast. This makes it difficult to focus on the lesion location when using only conventional confocal imaging method [34, 47]. To address this dispersive effect, we propose a time-of-arrival (TOA) autocalibration method that can further help the MWDAS to accurately localize the suspicious tissue region.

We use FDTD simulations to test our proposed methods. Here we first build simple 3D FDTD numerical breast phantoms having hemispherical shapes. Figure 3.3.1 shows two hemispherical numerical breast models. The diameter of the model is 100mm. Skin layer also has hemispherical shape with 2mm thickness and chest wall on the bottom is 20mm thick. Figure 3.3.1(a) is homogeneous breast model which only contains homogeneous fatty tissues.

On the other hand, Figure 3.3.1(b) is an inhomogeneous breast model which contains all the three main categories of normal breast tissues [52]: low adipose (mostly fibroglandular or fibroconnective tissues), medium adipose (31%-84% adipose tissues), and high adipose tissues (mostly fatty tissues). Dielectric properties of breast tissues are adopted from literature [55]. Phantom is immersed in a coupling liquid having the same dielectric property as that of the fatty tissues.

Breast lesion is constructed by using Gaussian random sphere model that generates random surface geometries [127-129]. The Gaussian random sphere can generate a family of distinct but related shapes which may follow the morphological features of breast lesions[130]. Malignant lesion normally has spiculated shape while benign lesion corresponds to smooth shape [130]. By setting the mean and covariance function of the radius, random geometries can be formed from smooth to uneven and spiculated shapes. By controlling different combination of mean radius and covariance, spiculated and smooth breast lesions are shown in Figure 3.3.2.

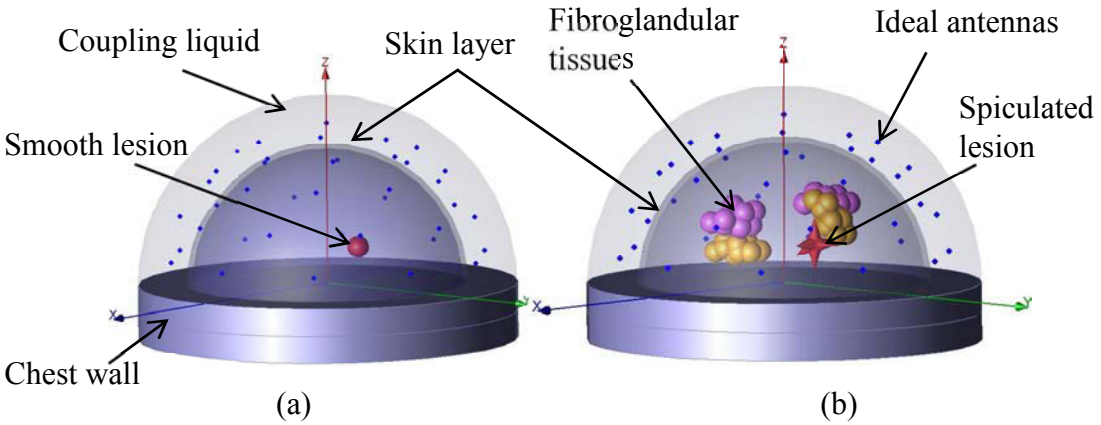

Figure 3.3.1 FDTD hemispherical breast models. (a) Homogeneous breast phantom (b) Inhomogeneous breast phantom.

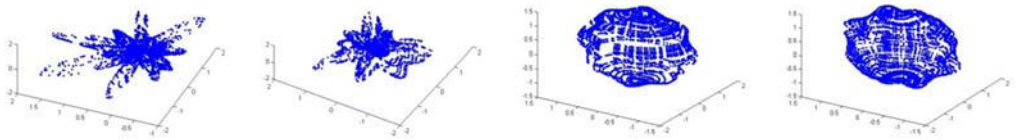

Figure 3.3.2 Spiculated and smooth breast lesions constructed using Gaussian random sphere

In our FDTD breast model, spiculated lesion is built by using a number of random spicules mounted on a smooth base [130] having an equivalent diameter of 10mm as shown in Figure 3.3.3 (a). For a smooth lesion, we first use a simple sphere model that has a diameter of 10mm as shown in Figure 3.3.3 (b). Fibroglandular tissue is modeled a clustered-chain pattern as shown in Figure 3.3.3 (c). Later, we show our results based on C3 heterogeneously dense phantom obtained from UWCEM phantom repository[63]. In C3 phantom, we employ spiculated and smooth lesions with different morphological features[130].

(a) (b) (c)

Figure 3.3.3 3D breast lesions in FDTD models (a) spiculated lesion. (b) smooth lesion. (c) healthy tissues in cluster pattern.

A hemispherical antenna array with 40 ideal antenna elements is placed around the breast model placed 10mm away from the skin. The antenna array is also immersed in the coupling liquid. In FDTD simulation, time-domain source is modulated Gaussian pulse having frequency up to 11GHz with 3dB bandwidth of 4GHz and excites the breast model using plane wave. Ideal antennas will then collect the scattered fields. The grid size of FDTD simulation is$0.4\text{mm} \times 0.4\text{mm} \times 0.7\text{mm}$. For spiculated lesion, sub-

grid technique is used to generate fine mesh in order to provide sufficiently mesh to model small spicules.

3.3.1 General pre-processing and TOA autocalibration

3.3.1.1 Pair-matching pre-processing method for removal of early-time content

The normal method to remove the early-time contents is subtracting a calibration signal that is obtained by averaging all the recorded signals. In literature, for experimental data collection, array rotation was suggested to remove the antenna excitation [42]. It is worth noting that subtraction of tumor-free signals to obtain the ideal tumor response is applicable only for ideal theoretical models and difficult to be implemented in practice. Although it is not practical for diagnosis, this ideal response can be used as a reference to calibrate the image reconstruction method.

Antennas at different locations receive different levels of early-time contents due to the uneven skin layer and dispersive medium. Hence, simple averaging of different levels of early-time signals [31, 33] may not accurate results. To improve the accuracy, we propose a pair-matching method of pre-processing utilizing the root mean square error (RMSE). RMSE is used to measure the difference between two vectors which in this case are time-domain raw data received at different antennas. RMSE is defined by:

$$U_{\mathrm{RMSE}} = \sqrt{\frac{\sum_{t=1}^{N}\left(u_{i,j}(t)-\tilde{u}_{i,j}(t)\right)^2}{N}} \tag{3. 6 a}$$

$$\min_{u^m{}_{i,j},\, \tilde{u}^m{}_{i,j}} U_{\mathrm{RMSE}} \tag{3. 6 b}$$

$$y_{i,j}(t) = u^m{}_{i,j} - \tilde{u}^m{}_{i,j} \tag{3. 6 c}$$

where $u_{i,j}(t)$ is a received time-domain pulse from ith transmitting antenna to jth receiving antenna and $\tilde{u}_{i,j}(t)$ is another time-domain signal at any receiving antenna. N is the width of the pulse and is equal to 1ns.

Use of RMSE criterion as given in (3.6a) will select pair-matched received signals ${u^m}_{i,j}(t)$and ${\tilde{u}^m}_{i,j}(t)$ as given in (3.6b) which give a minimized RMSE value. Then, calibrated signal $y_{i,j}(t)$can be obtained by subtracting ${u^m}_{i,j}(t)$ and ${\tilde{u}^m}_{i,j}(t)$ with each other as given in (3.6c) to remove the early-time contents.

The received raw data are shown in Figure 3.3.4 (a). All the received raw data are aligned to the major zero-crossing point which represents the dominant early-time contents [31, 34]. This alignment of early-time is necessary for effective reduction using RMSE criterion, because antennas are located at different positions [30]. It can be seen in Figure 3.3.4(a) the aligned raw data have significant different levels of amplitudes which make the conventional pre-processing [30, 47] using only averaging of the raw data very difficult to process.

In our RMSE pair-matching pre-processing, a matrix of RMSE results using equation (3.6 b) is shown in Figure 3.3.4 (b). X and Y axles are antenna elements. A pixel with high value represents a low RMSE value between two received pulses ${u^m}_{i,j}(t)$and ${\tilde{u}^m}_{i,j}(t)$ as given in equation (3.6 b) and such two pulses become pair-matched pulses. It can be observed from Figure 3.3.4 (b) that the pair-matched elements (high values of pixels) shown on RMSE matrix can be divided into four parts by the number of antenna elements: 1-10, 11-20, 21-30, and 31-40. It is interesting to note that antenna elements in each part are close to the transmitting antenna. It means that the pair-matched pulses come from antennas whose locations are close to transmitting antenna.

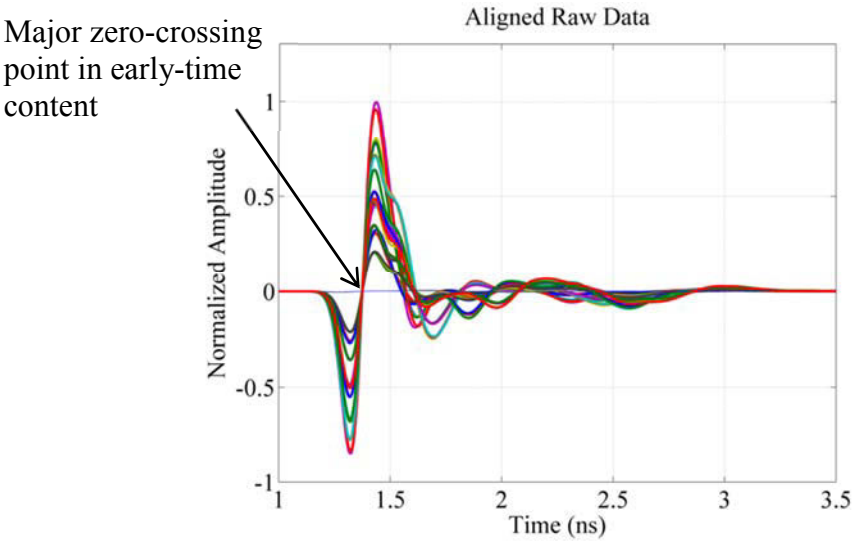

(a)

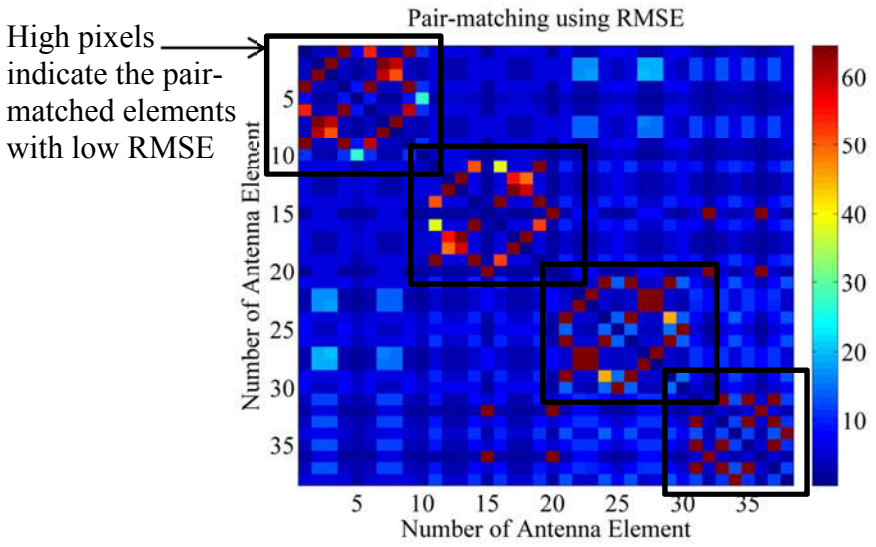

(b)

Figure 3.3.4 Aligned received signals and RMSE matrix for pair-matching pre-processing(a) simulated scattered fields after alignment to zero-crossing point (b) pair-matched elements using RMSE matrix.

This finding agrees with the pre-processing method used in literature [44], where only antennas that lie within close angular approximation to the transmitting antenna will be selected to record the measured signals. Further, this method is a special case of pair-matching generalized pre-processing when the breast phantom is symmetric and assuming that skin reflections are similar to different antennas.

3.3.1.2 Time-of-arrival (TOA) autocalibration

Time-of-arrival information is important for confocal microwave imaging[34]. In confocal microwave imaging, received signals are processed coherently by shifting the signals from the focal point [31, 34, 47] before using image reconstruction method and the signals are shifted according to the approximate TOA. The approximate TOA using an average dielectric constant given by:

$$n_{i,j}(\boldsymbol{r}_0) = \frac{D_{i,j}(\boldsymbol{r}_0)}{C/\sqrt{\varepsilon_{r,0}}} \tag{3. 7}$$

where $n_{i,j}(\boldsymbol{r}_0)$ and $D_{i,j}(\boldsymbol{r}_0)$are the TOA and round trip distance from ith transmitting antenna to jth receiving antenna respectively for a confocal point at $\boldsymbol{r}_0$. C is the speed of light and $\varepsilon_{r,0} = 4.32$ is the average dielectric constant for normal breast tissues [45]. For inhomogeneous breast, use of average dielectric constant will usually result in bias in the reconstructed tumor image [131]. To estimate reliable TOA information for accurate tumor reconstruction, we propose a novel TOA autocalibration using early-time contents.

Firstly, we introduce a TOA compensation factor μ. An initial TOA is determined using equation (3.7). For the initial TOA, compensation factor μ is made equal to 1. The raw data of received pulses which contain early-time information (see Figure 3.3.4(a))

are integrated to transform the zero-crossing point to the peak so that the highest peak will correspond to the antenna excitation that dominates the early-time content [31, 33]. The integration is given by:

$$\hat{u}_i = \int_{-\infty}^{t} u_i(t)dt,\ i = 1,2,\cdots,\mathrm{N} \tag{3. 8}$$

where $u_i(t)$ is the recorded raw data at ith antenna. The integrated signals $\hat{u}_i$ are then aligned to the antenna positions $r_{a,i}$, according to the initial TOA using equation (3.7). After aligning, signals are time shifted and become $\hat{u}_i(t-\mu\cdot n_{i,j}(\boldsymbol{r}_0))$. These time-shifted signals are passed through a time-window:

$$w(t) = \begin{cases} 1, & 0<t<t_w \\ 0, & \text{otherwise} \end{cases} \tag{3. 9}$$

where the size of time-window is the duration of early-time content. In this case of simulation, $t_w = 0.5ns$. Then the time shifted signal after time-window becomes:

$$\hat{u}_i(t)\cdot w(t) = \begin{cases} \hat{u}_i(t) = 0 & \text{for } t < \mu\cdot n_{i,j}(\boldsymbol{r}_0), \text{ or } t > \mu\cdot n_{i,j}(\boldsymbol{r}_0) + t_w \\ \hat{u}_i = \hat{u}_i\left(t-\mu\cdot n_{i,j}(\boldsymbol{r}_0)\right) & \text{for } \mu\cdot n_{i,j}(\boldsymbol{r}_0) \le t \le \mu\cdot n_{i,j}(\boldsymbol{r}_0) + t_w \end{cases} \tag{3. 10}$$

Equation (3.10) establishes that the time-windowing keeps the signal of interest. Then, the early-time content $\hat{u}_i$without removal of antenna excitation and skin reflection is processed by a simple DAS beamformer. Since the true antenna positions are assumed to be known apriori, DAS is expected to reconstruct the antenna excitation signal to the known antenna locations. The energy $p(r_{a,i})$ at true antenna location $r_{a,i}$ is calculated using DAS beamformer based on time-shifted and time-windowed signal:

$$p(r_{a,i}) = \sum_{t=1}^{M} \left(w_{\mathrm{DAS}} \cdot \hat{u}_i \left(t - \mu \cdot n_{i,j}(\boldsymbol{r}_0) \right) \right)^2 \quad (3.11)$$

Once the antenna excitation is reconstructed using equation (3.11), we can then calculate the objective function $\sigma_{r,i}$ which is the standard deviation of the reconstructed image (as shown in Figure 3.3.5(a)) of antenna excitation at ith transmitting antenna. By minimizing the objective function, TOA compensation factor μ_i can be optimized to a proper value that can correct the initial TOA information. The objective function is defined as:

$$\sigma_{r,i}(k) = \mathrm{std}\left(p(r_{a,i}, k) \right) \quad (3.12)$$

$$\mu_i(k+1) = \mu_i(k) + \Delta\mu \quad (3.13)$$

$$p(r_{a,i}, k+1) = \sum_{t=1}^{M} \left(w_{\mathrm{DAS}} \cdot \hat{u}_i \left(t - \mu_i(k+1) \cdot n_{i,j}(\boldsymbol{r}_0) \right) \right)^2 \quad (3.14)$$

where $\mathrm{std}(\cdot)$ is the operator to calculate the standard deviation of the reconstructed image of antenna excitation. $\sigma_{r,i}(k)$ is the calculated standard deviation of the reconstructed image of antenna excitation at i th transmitting antenna and at k-th iteration step. $p(r_{a,i}, k)$ is the reconstructed energy at true antenna location $r_{a,i}$ and at k-th iteration step.

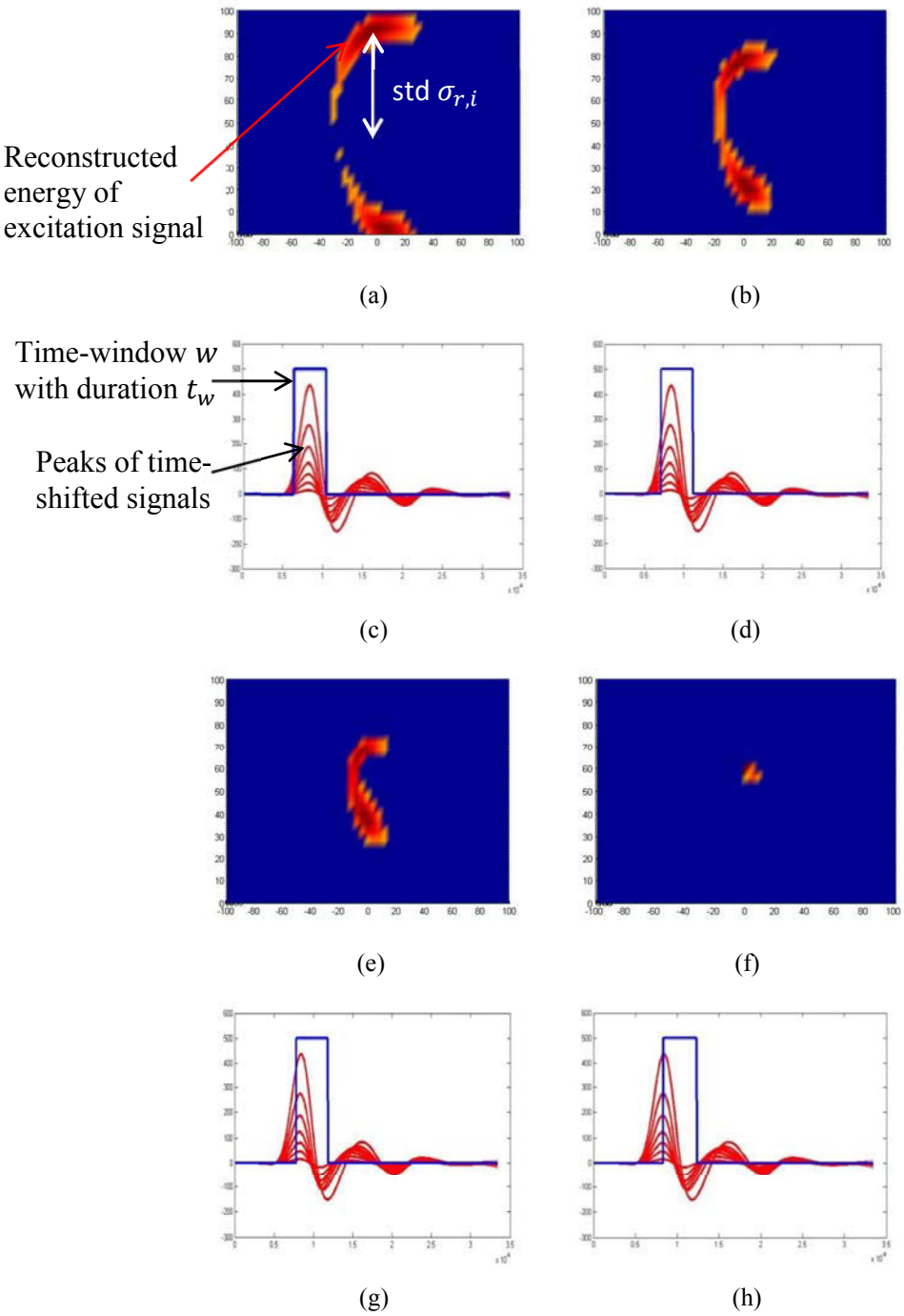

Figure 3.3.5 TOA autocalibration. (a), (b), (e), (f) show the focused energy of antenna excitation signal at (0, 0, 60)mm. (c), (d), (g), (h) show the time shifted signals and the time-window $\boldsymbol{w}$.

After calculating $\sigma_{r,i}(k)$at kth step of iteration, TOA compensation factor μ is updated at $(k+1)$th step as given by equation (3.13) by a small step $\Delta\mu$. We consider $|\Delta\mu| = 0.1$ in our simulated data. The reconstructed energy $p(r_{a,i}, k+1)$ is also updated at $(k+1)$th step as given in equation (3.14).

The TOA autocalibration process continues to run iteratively until a termination condition is fulfilled given by:

$$\left\| \mu \frac{D_{i,j}(\boldsymbol{r}_0)}{C/\sqrt{\varepsilon_{r,0}}} - t_{t\in(\hat{u}_i(t)=\max(\hat{u}_i)} \right\| < \rho \qquad (3.15)$$

where ρ is of the order of 0.1 to make sure the minimization process will terminate. Equation (3.15) is fulfilled when the peaks of the time-shifted signals match with the starting point of time-window in equation (3.9).

Now we describe our simulation using our proposed TOA autocalibration. Let an antenna is at (0, 0, 60)mm transmit an incident Gaussian pulse to illuminate the phantom in Figure 3.3.1(b). Figure 3.3.5-(a), (b), (e), (f) show the reconstructed energy of antenna excitation signal to the known location of transmitting antenna. It can be seen the energy is gradually focused to the correct antenna position at (0, 0, 60)mm while TOA is corrected by compensation factor.

Figure 3.3.5-(c), (d), (g), (h) show the corresponding time-shifted signals and time-window w using equation (3.9). More specifically, in Figure 3.3.5-(c), the time-window with duration t_w does not start from the peaks on time-shifted signals $\hat{u}_i = \hat{u}_i\left(t - \mu \cdot n_{i,j}(\boldsymbol{r}_0)\right)$. At this time, the corresponding reconstructed excitation signal is not focused as shown in Figure 3.3.5-(a), because the TOA compensation factor μ is not

optimum. As the estimated μ_i is changing iteratively, antenna position is becoming stable and compact. In Figure 3.3.5-(h), the time-window matches the peaks of time shifted signals so that the termination condition terminates the autocalibration iteration. At this time, the reconstructed excitation energy focuses on the correct transmitting antenna position at (0, 0, 60)mm as shown in Figure 3.3.5-(f). By relying on this autocalibration, the TOA compensation factor μ_i of ith transmitting antenna is obtained. The autocalibration also makes the image reconstruction algorithm patient specific, since in each case breast tissue inhomogeneities can differ from either pre-dominantly fatty or significantly fibroglandular (dense).

3.3.2 Late-time target response of breast lesion

Once the early-time content is removed, we need to obtain the late-time target response. For this, we propose a two-stage waveform estimation method to make sure the accuracy of waveform estimation for CNR extraction. In the two-stage waveform estimation, we incorporate robust Capon beamformer (RCB) [65]with minimum variance distortionless response (MVDR). Next, we utilize the minimum mean-square-error (MMSE) beamformer[132] to further reduce the bias.

MVDR (also known as standard Capon beamformer (SCB)[103]) minimizes SINR which only allows the backscattered signals of interest to pass through while suppressing interference from other scatters. It can provide waveform estimation by maximizing the SINR. However, it often results in a large estimation error[65, 132]. To estimate better amplitudes of waveform, MMSE beamformer obtains improvement over SCB. However, the uncertainty of steering vector in SCB must be solved. For this, we further incorporate RCB [47]to overcome the uncertainty of steering vector in the first stage of waveform estimation. In the second stage, we apply MMSE beamformer [132]to estimate the waveform from the suspicious region.

3.3.2.1 Steering vector estimation using RCB

Consider the pre-processed vector is:

$$\boldsymbol{y}_i(\mathrm{t}) = \mathbf{a}(t)s_i(t) + \boldsymbol{e}_i(t) \tag{3. 16}$$

where $\boldsymbol{y}_i(\mathrm{t}) = \left[y_{i,1}(t), \cdots y_{i,M}(t)\right]^T$ is the vector of preprocessed signals for 1 to M receiving antennas. The scalar $s_i(t)$denotes the backscattered signal from the confocal point at location$\boldsymbol{r}_0$. The vector $\mathbf{a}(t)$ is so called "steering vector" and is equal to$\mathbf{1}_{M\times 1}$ as all the preprocessed signals have been time-shifted temporally to a focal point. The vector $\boldsymbol{e}_i(t)$ denotes the residual term which contains noise and other possible interference.

When aligned to the target of interest, the steering vector $\mathbf{a}(t)$ is slightly different from 1, since it suffers from distorted waveform, imperfection of time-shift due to breast inhomogeneities, etc. RCB [47] improves SCB by minimizing the errors of steering vector using an uncertainty set. Let the true steering vector $\mathbf{a}(t_0)$ lie in the vicinity of the referenced steering vector $\bar{\mathbf{a}}(t) = [1, \cdots, 1]^T$ and force their difference under a condition in equation (3.17):

$$\|\mathbf{a}(t_0) - \bar{\mathbf{a}}(t)\|^{\mathbf{2}} \leq \partial \tag{3. 17}$$

where $\partial$is used to describe the uncertainty of steering vector $\mathbf{a}(t_0)$. In the literature [46], ∂ is around 3. In our simulation study, we choose $\partial = 3.4$. The covariance matrix is given by:

$$\mathbf{R}_Y(t_0) = \frac{1}{M}\mathbf{Y}(t_0)\mathbf{Y}^T(t_0) \tag{3. 18}$$

where $\mathbf{Y}(t_0) = [y_1(t_0), y_2(t_0), \cdots, y_M(t_0)]$

The objective function to optimize the unknown steering vector $\mathbf{a}(t_0)$ is given by[47]:

$$\min_{\mathbf{a}(t_0)} \mathbf{a}^T(t_0)\mathbf{R^{-1}}_Y(t_0)\mathbf{a}(t_0) \quad \text{subject to} \quad \|\mathbf{a}(t_0) - \bar{\mathbf{a}}(t)\|^2 \leq \partial \tag{3. 19}$$

To minimize equation (3.19), we have used We use particle swarm optimizer (PSO) [133, 134] to obtain the optimized steering vector $\mathbf{a}(t_0)$. Unlike the method used by [135], here we transform the equation (3.19) into:

$$\min_{\mathbf{a}(t_0)}(\mathbf{a}^T(t_0)\boldsymbol{R^{-1}}_Y(t_0)\mathbf{a}(t_0) + \xi \cdot \|\boldsymbol{a}(t_0) - \bar{\boldsymbol{a}}(t)\|^2) \tag{3. 20}$$

where a new parameter ξ is introduced to incorporate the condition given by (3.17) in addition to minimize the objective function. This parameter ξ can also be obtained during the PSO optimization.

After obtaining estimated steering vector $\mathbf{a}(t_0)$, the first stage of waveform estimation is complete. The array weight of RCB can be calculated for a confocal point at $\boldsymbol{r}_0$:

$$\mathbf{w}_{\text{RCB}} = \frac{\boldsymbol{R^{-1}}_Y(t_0)\mathbf{a}(t_0)}{\mathbf{a}^T(t_0)\mathbf{R^{-1}}_Y(t_0)\mathbf{a}(t_0)} \tag{3. 21}$$

The output of RCB beamformer is then obtained by:

$$\hat{\mathbf{s}}(t_0) = [\boldsymbol{w^T}_{\text{RCB}}(t_0)\mathbf{Y}(t_0)]^T \tag{3. 22}$$

3.3.2.2 MMSE beamformer

Although RCB also minimizes mean-square-error (MSE), it does not necessarily result in a good estimation of signal waveform[132]. Therefore, in the second stage of waveform estimation, we use MMSE beamformer [132]. Assuming $\hat{s}_i$(t) is the estimate of backscattered signal $s_i(t)$, the MSE between them is:

$$\mathrm{E}\{|\hat{s}-s|^2\} = \mathbf{w}^H\mathbf{R}_{\mathrm{Y}}\mathbf{w}+|s|^2|1-\mathbf{w}^H\mathbf{a}|^2 \tag{3. 23}$$

where $\mathbf{w}$ is the beamformer if properly designed will minimize the MSE. When s is a zero-mean random variable with variance$\sigma^2{}_s$, the term $|s|^2$is replaced by $\sigma^2{}_s$. The MMSE beamformer is derived by minimizing equation (3.23) [132] as given by:

$$\mathrm{w}_{\mathrm{MMSE}} = |s|^2(\mathbf{R}_{\mathrm{Y}}+|s|^2\mathbf{a}\mathbf{a}^H)^{-1}\mathbf{a}=\beta\cdot\mathbf{w}_{\mathrm{RCB}} \tag{3. 24}$$

$$\beta = \frac{|s|^2\cdot\mathbf{a}^H\boldsymbol{R}_{\mathrm{Y}}{}^{-1}\mathbf{a}}{1+|s|^2\cdot\mathbf{a}^H\boldsymbol{R}_{\mathrm{Y}}{}^{-1}\mathbf{a}} \tag{3. 25}$$

MSE of using MMSE beamformer in equation (3.24) is smaller than that of obtained by RCB beamformer given by(3.21). However, MMSE depends on $|s|$ which is unknown in practice. Instead, we may know the upper and lower bounds of $|s|$:

$$L \le |s| \le U \tag{3. 26}$$

where L and U are lower and upper bounds of $|s|$. Considering these, the MMSE beamformer can change to [132]:

$$\mathbf{w}_{\mathrm{MMSE}} = \beta_{\mathrm{MMSE}}\cdot\mathbf{w}_{\mathrm{RCB}} \tag{3. 27}$$

where scaling parameter β_{MMSE}becomes:

$$\beta_{\mathrm{MMSE}} = 1 - \frac{1}{\sqrt{(1+L^2\mathbf{a}^H\boldsymbol{R}^{-1}{}_Y\mathbf{a})(1+U^2\mathbf{a}^H\boldsymbol{R}^{-1}{}_Y\mathbf{a})}} \tag{3. 28}$$

Now the output of the second stage of waveform estimation is:

$$\hat{\mathbf{s}}(\mathrm{t}) = [\boldsymbol{w}^{\boldsymbol{T}}{}_{\mathrm{MMSE}}(t)\mathbf{Y}(t)]^T \tag{3. 29}$$

The method of estimating U and L are also given in the literature[132] as:

$$U = (1+\phi)^2 \cdot \sqrt{\frac{1}{N}\sum_1^N \hat{s}^2(t_0)} \tag{3. 30}$$

$$L = (1-\phi)^2 \cdot \sqrt{\frac{1}{N}\sum_1^N \hat{s}^2(t_0)} \tag{3. 31}$$

where ϕ is selected as equal to 5 in our simulations. $\hat{\mathrm{s}}(t_0)$ is a rough estimate using RCB in equation (3.22).

3.3.2.3 Simulation results

We employ FDTD simulations using the numerical hemispherical shaped breast models as shown in Figure 3.3.1. We first use MWDAS (as given in Chapter 2) to process the pre-processed signals to localize the suspicious locations of malignant lesions followed by two-stage waveform estimation as explained above. The smooth shaped and spiculated shaped lesions are embedded at (0, 20, 15)mm respectively in the model. The reconstructed suspicious lesion location is plotted in the 3D image as shown in Figure 3.3.6 on a hemispherical breast contour for the display of 3D image.

Figure 3.3.6(a) produces the suspicious location of breast lesion in homogeneous breast model of Figure 3.3.1(a), while Figure 3.3.6(b) gives the suspicious location in the inhomogeneous breast model of Figure 3.3.1(b). The reconstructed image is normalized to the highest focused energy and then a threshold 'ϑ' is chosen to remove the clutter effects as much as possible [42, 44]. Any normalized energy lower than 'ϑ' will be removed. In this simulation study, 'ϑ'is chosen as 0.9. It can be seen that reconstructed images can clearly indicate the suspicious lesion location. Hence, the target response can be estimated only from the suspicious location r_s.

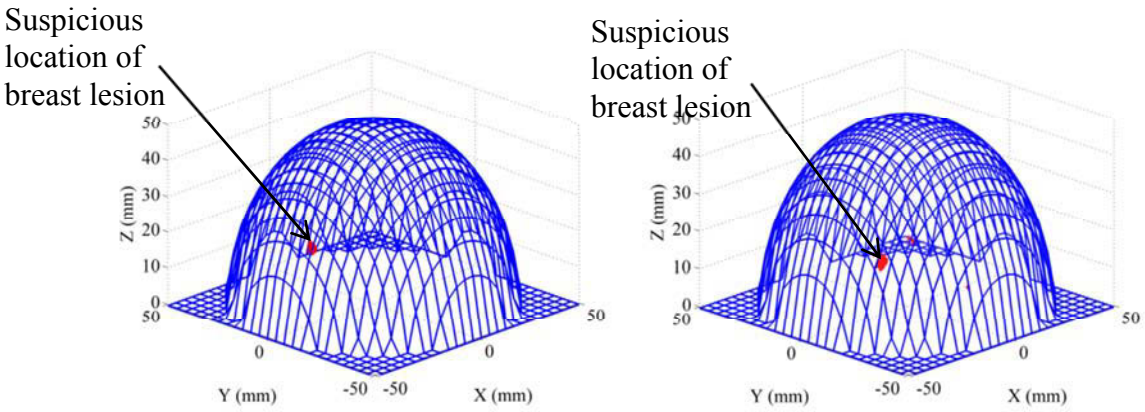

(a) (b)

Figure 3.3.6 Reconstructed suspicious region in hemispherical phantom: (a) homogeneous breast model in Figure 3.3.1-(a); (b) inhomogeneous breast model in Figure 3.3.1-(b)

Target response of breast lesion can be estimated using (3.20), (3.21) and (3.29) from pre-processed signals. In FDTD simulation, we estimate the target response $\hat{\mathbf{s}}(\mathrm{t})$ by transforming the received ultrawideband pulse into a number of frequency subbands. Here the number of subbands are chosen to be K_B=60 and each subband has a bandwidth of 166MHz. Time interval $\Delta \mathrm{t} = 0.96\mathrm{ps}$ and number of time

sampling N=2000 . For each narrow subband, we apply two-stage waveform estimation. Additive white Gaussian noise with zero-mean and variance $\sigma^2{}_0$is added to the scattered fields. Then the signal-to-noise ratio (SNR) is calculated by [47]:

$$\text{SNR}=10\log_{10}\left\{\frac{{}^{1}\!/_{M^2}\sum_{i=1}^{M}\sum_{j=1}^{M}\left[\frac{1}{N}\sum_{t=0}^{N-1}\hat{s}^2{}_{i,j}(t)\right]}{\sigma^2{}_0}\right\} \tag{3. 32}$$

For our simulation, we fix SNR to be 30dB. PSO uses 30 particles and 39 dimensions as the 39 receiving antennas record the scattered fields for each excitation. The steering vector is obtained using average of 100 runs of PSO and for each run, 500 times iteration are used. Figure 3.3.7 shows an example of calculated fitness of objective function (3.20) for a subband whose centre frequency is 5GHz. The uncertainties of steering vector as given (3.17) are calculated for the whole bandwidth and are shown in Figure 3.3.8. It can be seen that uncertainties are smaller than the given value$\partial = 3.4$ for every subband which satisfy the constraining condition given by (3.17).

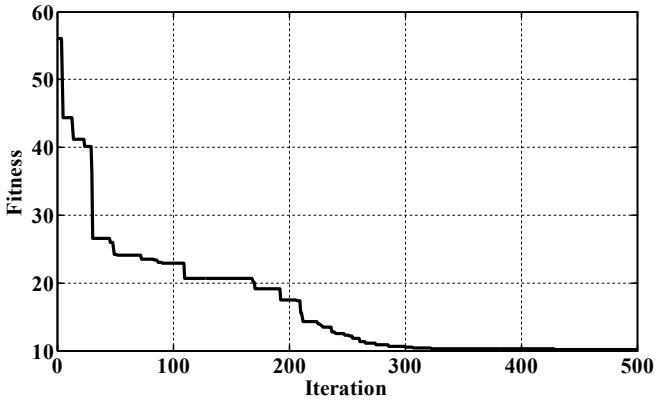

Figure 3.3.7 Calculated fitness value using PSO for steering vector estimation at 5GHz for hemispherical breast phantom.

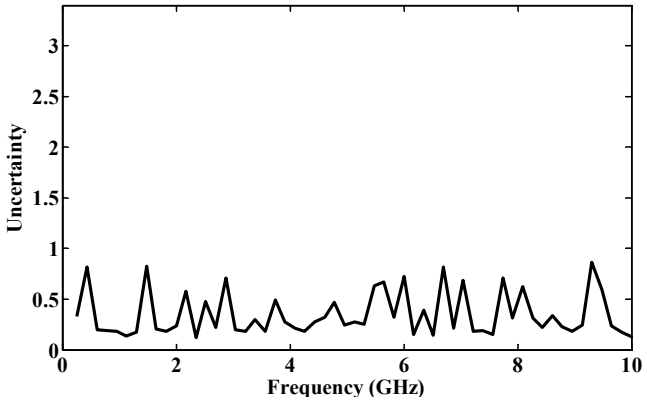

Figure 3.3.8 Uncertainties of steering vector for the whole bandwidth of backscattered signal

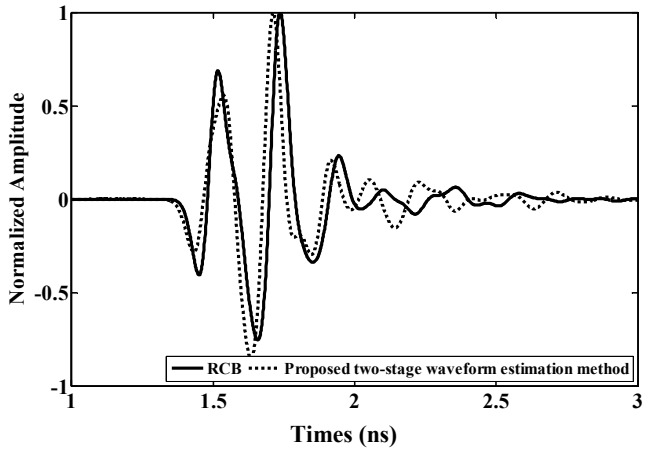

Figure 3.3.9 Estimated waveform using the proposed two-stage waveform estimation method.

After obtaining the steering vector using RCB, now we estimate the waveform of target using MMSE beamformer using equations from (3.27) to (3.31). The estimated waveform is illustrated in Figure 3.3.9 and the waveform of target response using RCB is also plotted. The proposed two-stage waveform estimation method can offer smaller mean-square-error (MSE) which helps to estimate waveform accurately when only robust Capon beamforming (RCB) as shown in equation (3.24) and (3.25) is used. It can be observed that during the late-time period of the both waveforms, amplitudes

and phases have significant differences which will certainly change the CNR values. However, it is worth noting that the discrepancy on the extracted CNR cannot tell as to how accurately one particular beamforming method can estimate the waveform, but MSE can provide better metric for accuracy of estimation. Thus, based on lower MSE criteria, the proposed two-stage waveform method can estimate the waveform much more accurately. This will then lead to more reliable CNR extraction. Now CNR of embedded target, which in our case is the breast lesion in the FDTD breast model, can be extracted based on the estimated waveform of target response.

3.3.3 Extraction of late-time resonant signal from target response

However, before extracting CNR by directly applying matrix pencil method on estimated waveform, we need to know from what time on the waveform the CNRs can be extracted[99]. In other words, we need to separate late-time resonant signal from early-time non-resonant signal which is only due to singularity of excitation[94]. Otherwise, spurious CNRs may be extracted if non-resonant signal is used for CNR extraction. In the literature related to CNR extraction [94], resonances are calculated as a function of time and are mapped as resonant frequency-time plane to examine the fundamental resonance and other higher mode resonances. Fundamental resonance corresponds to a complex resonant pole which has the lowest resonant frequency excited by the embedded target and it is found to be related to the physical length of a conducting object [94]. On the resonant frequency-time plane, the fundamental resonance is the lowest line which has non-fluctuating and nearly constant levels of resonant frequencies.

Here we propose to modify the resonances-time plane by forming only the resonances with dominant CNR poles. Dominant pole is the pole S_m having the highest amplitude of $|C_m|$ as given in equation (3.1). By forming this plane,

fundamental resonance can be clearly seen which also appears with relatively flat and non-fluctuating values of resonant frequencies over time. We construct such planes using the target responses from spiculated and smooth breast lesions respectively based on the FDTD models as shown in Fig 3.3.1-3.3.3.

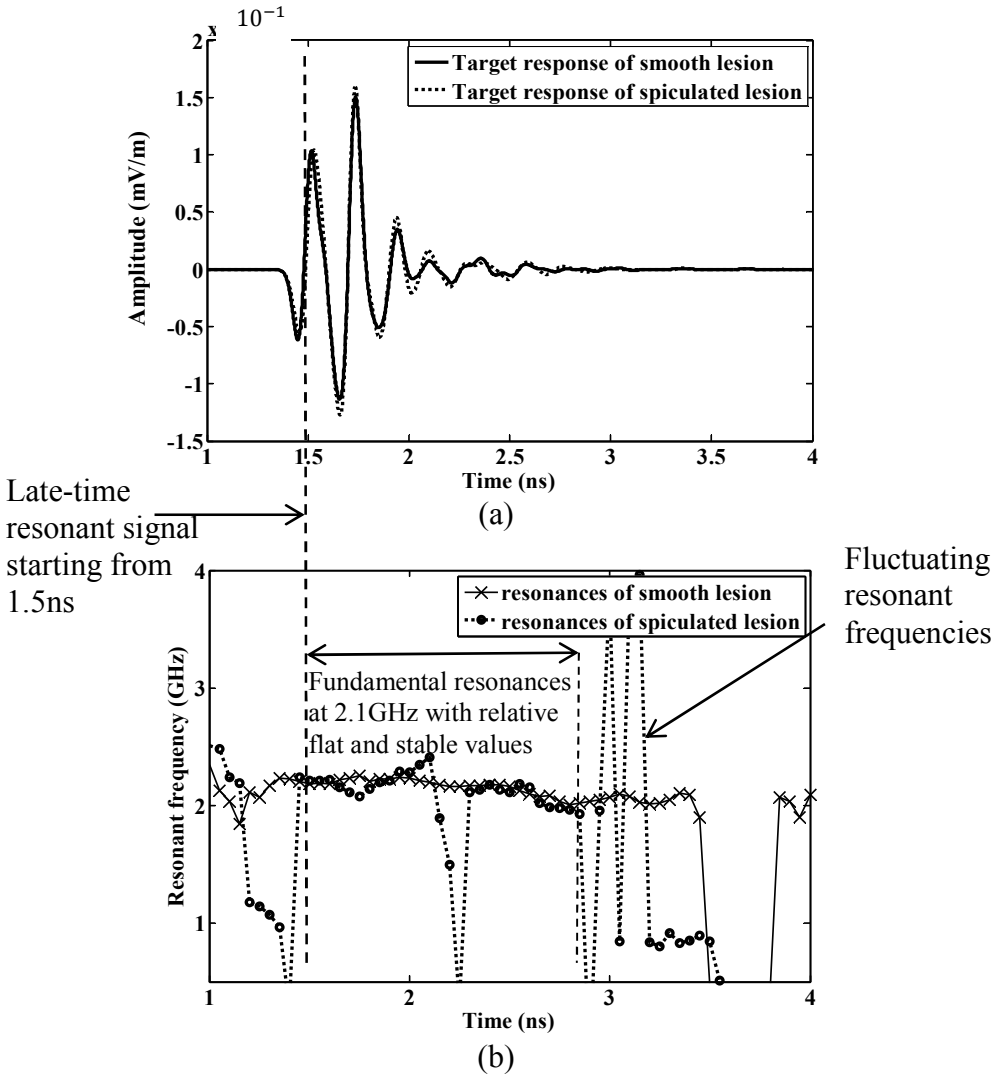

Figure 3.3.10 Localization of late-time resonant signal using hemispherical breast phantom (a) Target responses of smooth and spiculated lesions (b) resonant frequency-time planes

The target responses after two-stage waveform estimation are shown in Figure 3.3.10 (a) for both spiculated and smooth lesions, in which slight differences can be observed for the amplitudes of waveforms. Figure 3.3.10(b) shows the dominant resonant frequency-time plane corresponding to Figure 3.3.10(a). It can be seen that the dominant resonances appears stable and flat after about 1.5ns (indicated by dashed line on the figure) with averaged resonant frequency of 2.1GHz for both the lesions. This period indicates the late-time resonant signal. On the other hand, resonances before 1.5ns and after 2.9ns appear to have large fluctuating values ranging from 0.5GHz to 4GHz which correspond to nonresonant spurious CNRs. Therefore, for CNR extraction using matrix pencil method, only the late-time resonant signal should be applied.

3.3.4 Calibration techniques for CNR signatures

3.3.4.1 Calibration of CNR extraction using non-penetrable PEC objects

Before we extract CNRs from late-time target response, we need to make sure that the extracted CNRs correspond to the external mode (as discussed in section 3.2), as only the external mode of CNR can be related to morphological features of target geometries. Hence, we first employ non-penetrable PEC sphere and embed it inside the numerical hemispherical breast phantom. Since the PEC sphere has only external mode of CNRs [94], use of such PEC sphere can help to compare whether the extracted CNRs from dielectric breast lesions having the same size and shape correspond to external mode CNRs. In addition, PEC object with spiculated shape is also examined to compare the external mode of CNR of spiculated dielectric breast lesion having the same spiculated profile as PEC spiculated object.

We first examine the morphological features corresponding to the CNR signatures for smooth lesion by embedding the same sized PEC and dielectric spheres at (0, 20, 15)

inside the numerical hemispherical breast phantom (Figure 3.3.1) respectively. Both PEC sphere and spherical shaped dielectric lesion has dia=10mm. Their target responses and extracted CNRs are shown in Figure 3.3.11. It can be observed that CNRs for dielectric breast lesion and PEC sphere have similar pattern and also have close resonant frequencies and damping factors. Therefore, it is possible that CNRs from dielectric breast lesion correspond to be external mode CNRs. Then we examine the morphological features correspond to the CNR signatures for PEC and dielectric objects having the same spiculated profile. The target responses and extracted CNRs are plotted in Figure 3.3.12. The findings appear to be similar: extracted CNRs for both PEC and dielectric shapes have close resonant frequencies and damping factors.

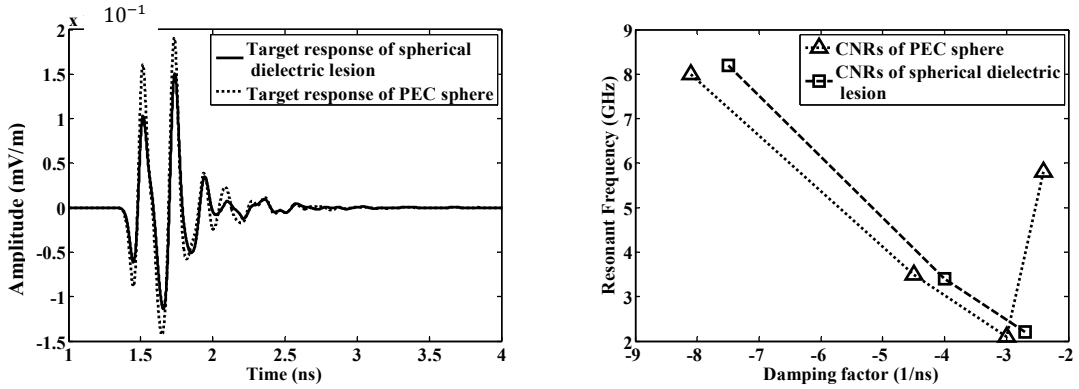

(a) (b)

Figure 3.3.11 (a) target responses from dielectric breast lesion and PEC object with the same spherical shapes. (b) extracted CNRs

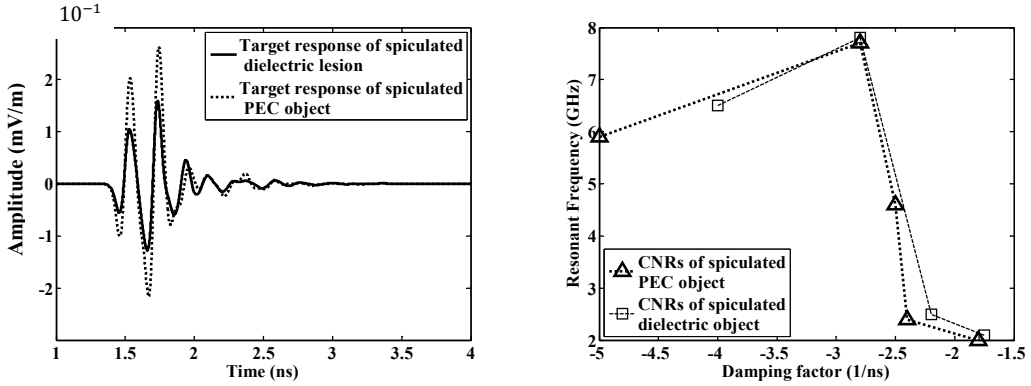

Figure 3.3.12 (a) target responses from dielectric breast lesion and PEC object with the same spiculated shapes. (b) extracted CNRs

3.3.4.2 Normalized CNR error (NCR)

To analyze the errors in extracted CNRs, a closed-form normalized estimation error (NCR) is applied following the method in the literature [136], which is given by:

$$n_{\text{norm}} = \frac{\left\| \left(\boldsymbol{I} - \boldsymbol{Z}(\boldsymbol{Z}^H \boldsymbol{Z})^{-1} \boldsymbol{Z}^H \right) \boldsymbol{y}_{\text{unknown}} \right\|}{\| \boldsymbol{y}_{\text{unknown}} \|} \tag{3. 33}$$

where Z is the matrix of CNR in Z-plane as given by equation (3.3) and is represented by:

$$\boldsymbol{Z} = \begin{bmatrix} Z_1 & Z_2 & \cdots & Z_k \\ \vdots & \vdots & \ddots & \vdots \\ {Z_1}^N & {Z_2}^N & \cdots & {Z_k}^N \end{bmatrix} \tag{3. 34}$$

where Z_i, $i = 1,2,\cdots,K$ is the i-th CNR pole (3.3). Here, CNRs in Z-plane are chosen as the reference for comparison. The signal $\boldsymbol{y}_{\text{unknown}}$ is the objective waveform and is in the form of the sum of complex exponentials using matrix pencil method[119].

In this thesis, we use NCR as a metric to measure the difference of CNRs which are extracted from different targets for discrimination of morphological features. The higher value of NCR is calculated, the larger difference of morphological features exists between the targets. The maximum value of NCR is equal to 1. For targets in Figure 3.3.11, NCR between dielectric and PEC spheres are only 0.12. NCR between dielectric and PEC objects with the same spiculated shapes is 0.04. Those small NCRs confirm that the extracted CNRs from dielectric breast lesions are external modes.

3.3.5 Extracted CNRs in hemispherical numerical breast models

Since our proposed two-stage waveform estimation method can give lower bias than RCB and DAS for extracted CNRs, we now extract CNRs from breast lesions using our proposed pre-processing given by (3.6), TOA autocalibration given by (3.12)-(3.15), extraction of late-time resonant signal from target response, and two-this stage estimation method given by (3.20)-(3.31). In FDTD simulations, spiculated and spherical lesions (as shown in Figure 3.3.3) has been placed at 20 random positions within the hemispherical models (as shown in Figure 3.3.1). The results are shown in Figure 3.3.13. Figure 3.3.13(a) shows the extracted CNRs in homogeneous breast phantom, where CNRs from spiculated lesion has larger damping factors than spherical lesion. In this homogeneous phantom only fatty tissues dominate the breast environment. Figure 3.3.13(b) shows the extracted CNRs in inhomogeneous hemispherical model. In this case, differences of damping factors between spherical and spiculated lesions reduce significantly, since the lesion is placed close to fibroglandular tissues which can cause interference to responses from target locations.

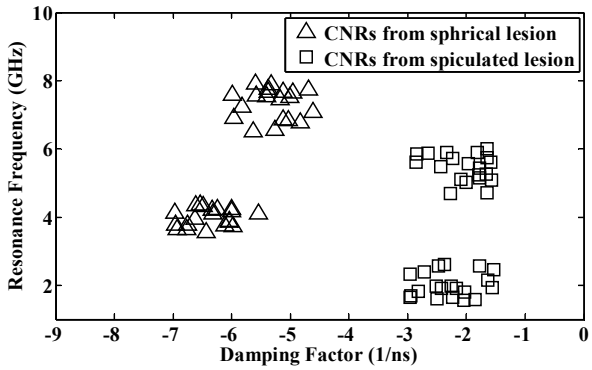

(a)

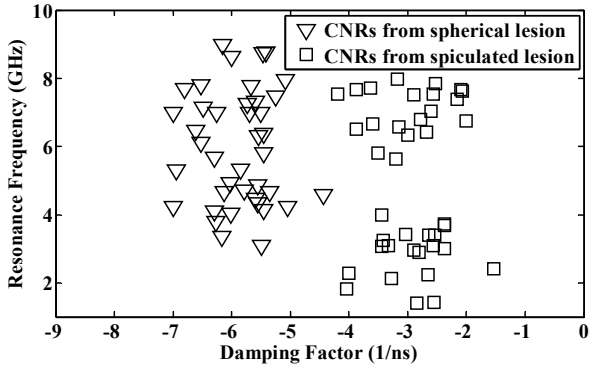

(b)

Figure 3.3.13 Extracted CNRs of spherical and spiculated dielectric lesions at 20 different locations in hemispherical breast phantom (a) in homogeneous hemispherical numerical breast phantom (b) in inhomogeneous hemispherical numerical breast phantom

3.4 CNR extraction for MRI-derived breast phantom with dense fibroglandular tissues (C3 breast phantom obtained from UWCEM phantom repository)

In this section, we uses a realistic C3 (heterogeneously dense phantom 1) breast phantom which has dense fibroglandular tissues which is provided by University of Wisconsin-Madison [63]. This dense breast phantom has pixels of 332×202×269 and the resolution is 0.5mm. 2D slices and 3D view of such C3 phantom are shown in Figure 3.4.1. This phantom contains fatty, fibroglandular, and connective tissues as well as a chest layer. Breast lesion of spiculated shape is modelled using a number of random spicules mounted on a smooth base to represent malignant breast lesion [130]. On the other hand, smooth shaped lesion is also modelled using Gaussian sphere[130] to represent benign breast lesion. We simulated four different sets of spiculated and smooth lesions as shown in Figure 3.4.1(d). Spiculated lesions have approximate diameters of 12mm and smooth lesions have averaged diameter of 10mm. In FDTD simulation, the whole breast is immersed in a coupling liquid that has the same dielectric property on that of the fatty tissue. 90 ideal antennas are placed surrounding the breast phantom to form a cylindrical array. A modulated Gaussian pulse with 3-dB bandwidth of 6GHz illuminates the breast from one antenna at a time while all the other antennas receive the scattered fields to form a multistatic matrix. FDTD simulation uses $0.5\text{mm} \times 0.5\text{mm} \times 0.5\text{mm}$ mesh size for the whole breast. Fine meshed are employed to model the small spicules of the spiculated lesion. Two-pole Debye model [55] is incorporated into FDTD simulations to incorporate dielectric properties for different tissues[57].

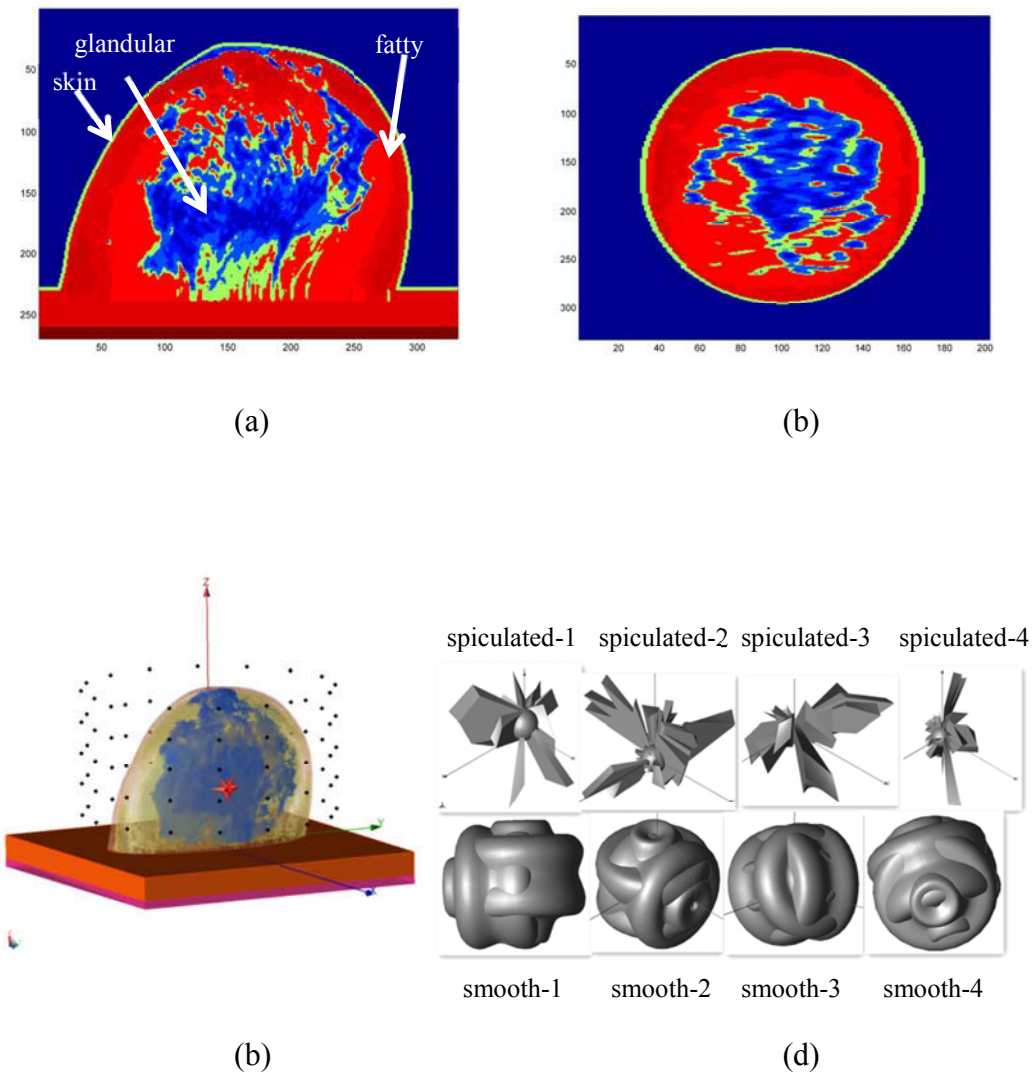

Figure 3.4.1 C3 heterogeneously dense breast phantom (a) 2D view of phantom in X-Z plane (b) 2D view of phantom in X-Y plane (c) 3D view of phantom (d) models of spiculated and smooth breast lesions

3.4.1 Localization of suspicious region of breast lesion in C3 phantom

3.4.1.1 Preprocessing and TOA autocalibration for C3 phantom

TOA autocalibration is applied with non-preprocessed data using equations from (3.8) to (3.15). The reconstructed antenna locations for 6 transmitting antennas at different positions are estimated as shown in Figure 3.4.2. By accurately reconstructing antenna locations, optimized TOA compensation factor μ is obtained which is used to correct the initial TOA given by (3.7) that is calculated using the averaged propagation velocity.

Now, we use pair-matching pre-processing method. Pair-matching given by (3.6) is used to form a map of RMSE matrix for removal of early-time content as shown in Figure 3.4.3. In Figure 3.4.3, spots of high intensity represent pair-matched received pulses with low RMSE. Calibrated signals are then obtained by subtraction of pair-matched signals using equations as given by (3.6).

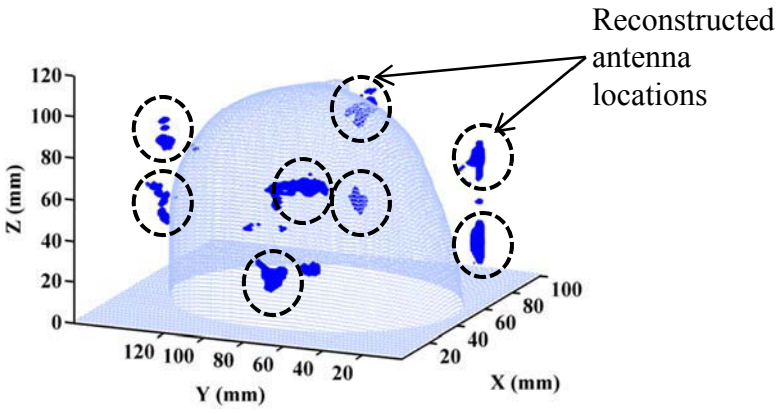

Figure 3.4.2 Reconstructed 6 antenna positions using C3 dense breast phantom

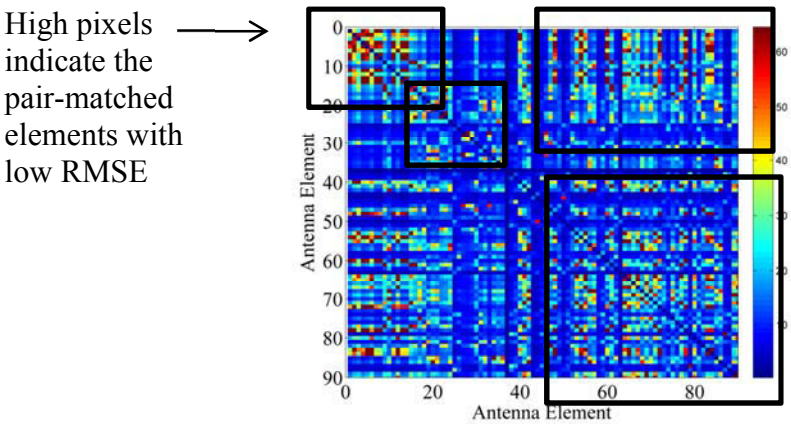

Figure 3.4.3 RMSE matrix for pair-matching preprocessing using C3 dense breast phantom

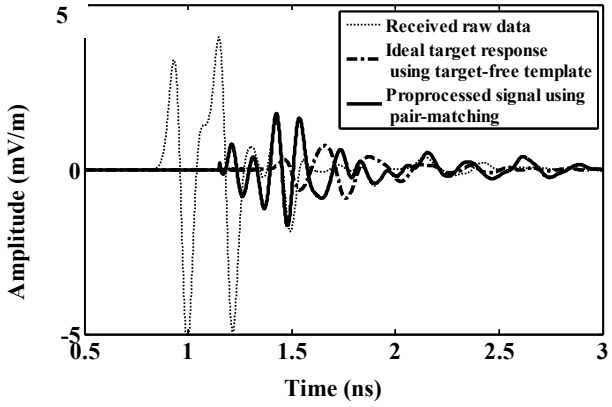

(a)

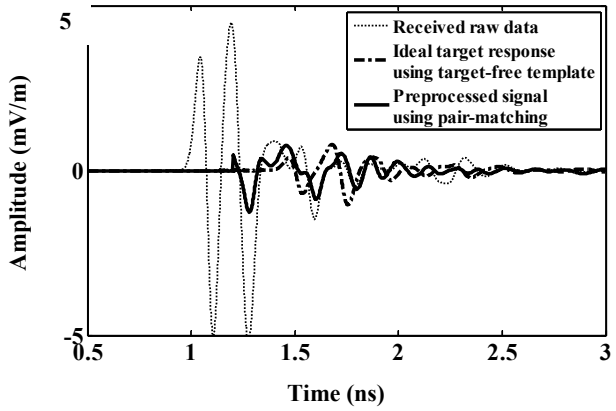

(b)

Figure 3.4.4 Two samples of pre-processed signals showing comparison of pre-processed signals using pair-matching and ideally obtained target responses.

We plot two pre-processed signals in Figure 3.4.4 and compare them with ideal target responses obtained by subtracting the target-free templates. As described previously, target-free template is the calculated signal obtained without including the target tissue. It can be seen that the preprocessed signals using RMSE pair-matching have close agreement with ideally obtained target responses.

3.4.1.2 Localization of suspicious regions in C3 phantom

Now we localize the suspicious region within the breast lesion when a dielectric lesion is placed at (84, 55, 38)mm in a C3 phantom (Figure 3.4.1). In this simulation, SNR level set to be 25dB calculated using equation (3.32). To calibrate the focused image, we first map a reference image as shown in Figure 3.4.5(a) which is formed by ideally obtained target responses using target-free template. The suspicious target location is indicated by arrow in the images. Delay-and-sum (DAS) beamformer is then used to form the image as shown in Figure 3.4.5(b). It can be seen that more clutter

interference appears in the image due to the limitations of DAS beamformer. The reconstructed energy from clutters has similar level with that arising from breast lesion.

We show the result obtained using our proposed MWDAS in Figure 3.4.5(c) which offers higher resolution in the localization of the suspicious region compared to DAS. MWDAS efficiently reduces effects from clutter interference. One can see that the reconstructed region can be identified clearly (arrow) and has similar performance to the reference ideal image. To quantitatively assess imaging results, we also use the measure of signal-to-clutter ratio (S/C) [42]to examine the detection quality: ratio of peak target energy to a peak of clutter energy. S/C is given by:

$$S/C = \frac{\text{Peak target energy}}{\text{Peak clutter energy}} \tag{3. 35}$$

The simulated S/C results are listed in Table 3.4.1. Results show that MWDAS improves DAS by several orders of magnitudes from a 10mm sized lesion.

Table 3.4.1 Signal-to-Clutter Ratio (dB) for C3 Breast Phantom

Reference	DAS	MWDAS
0.1	0.08	0.3

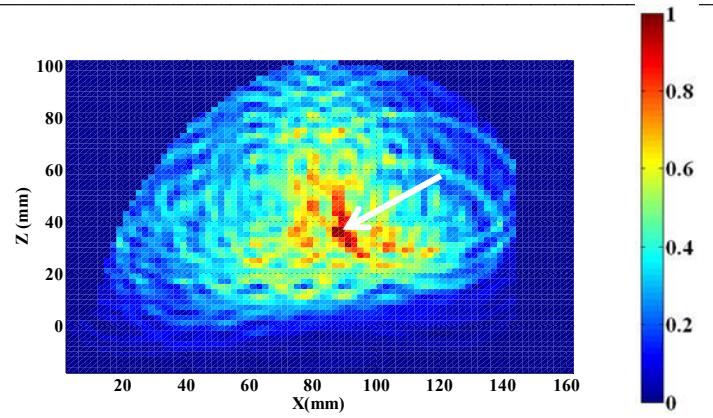

(a)

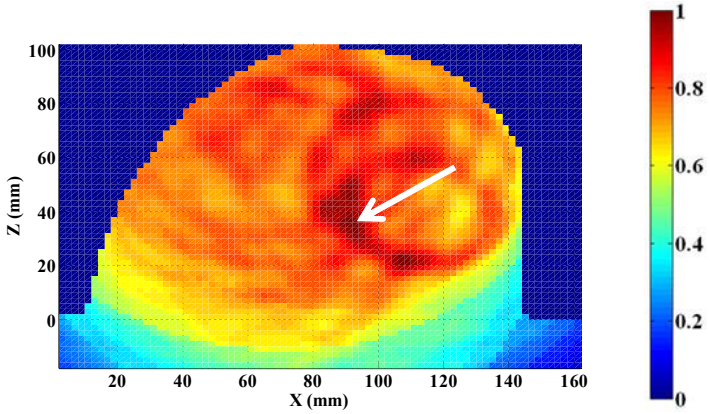

(b)

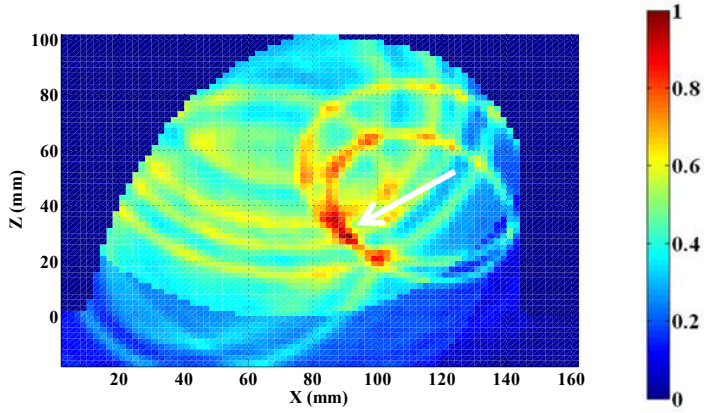

(c)

Figure 3.4.5 Reconstructed image of suspicious region in C3 dense phantom (a) reference image using target-free template (b) DAS (c) proposed MWDAS

3.4.2 Discrimination of lesion morphologies using CNR signatures in C3 phantom

In this section, CNRs are extracted from four sets of spiculated and smooth lesions (Figure 3.4.1 (d)) when they are embedded in C3 heterogeneously dense phantom (Figure 3.4.1) at a location (84, 55, 38)mm. For each lesion, two CNR poles are extracted and they are shown in Figure 3.4.6. A pole at higher frequency is called higher mode of CNR and a pole at lower frequency is lower mode CNR. It can be observed that the damping factors at higher mode of spiculated lesions are significantly lower than those of smooth lesions. On the contrary, the damping factors at lower mode are not separated for all lesions: except for smooth-3, all the other lesions have closely clustered damping factors at lower frequencies and thus are difficult to differentiate. The results of damping factors and resonant frequencies are also listed in Table 3.4.2.

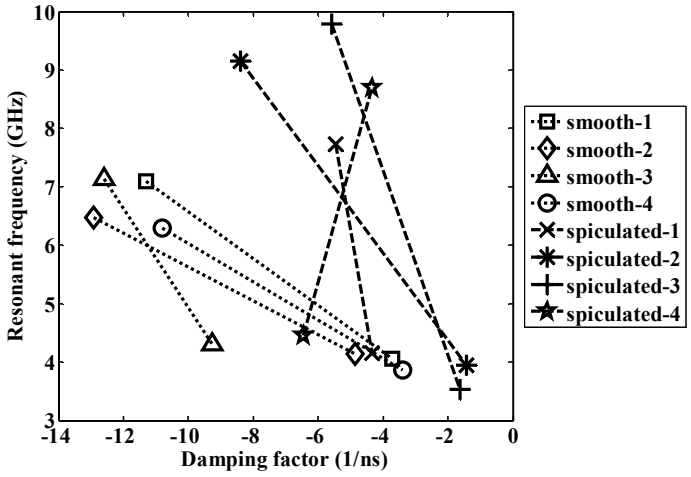

Figure 3.4.6 Extracted CNRs from simulated data using four sets of spiculated and smooth lesions in C3 phantom

Table 3.4.2 Extracted CNRs of Spiculated and Smooth Lesions in C3 Phantom

		Higher Mode	Lower Mode
Smooth Lesion-1	Resonant Frequency (GHz)	7.1	4.05
	Damping Factor (1/ns)	-11.3	-3.71
Smooth Lesion-2	Resonant Frequency (GHz)	6.47	4.14
	Damping Factor (1/ns)	-12.91	-4.87
Smooth Lesion-3	Resonant Frequency (GHz)	7.14	4.3
	Damping Factor (1/ns)	-12.6	-9.26
Smooth Lesion-4	Resonant Frequency (GHz)	6.29	3.86
	Damping Factor (1/ns)	-10.8	-3.4
Spiculated Lesion-1	Resonant Frequency (GHz)	7.73	4.15
	Damping Factor (1/ns)	-5.47	-4.35
Spiculated Lesion-2	Resonant Frequency (GHz)	9.15	3.94
	Damping Factor (1/ns)	-8.4	-1.44
Spiculated Lesion-3	Resonant Frequency (GHz)	9.78	3.53
	Damping Factor (1/ns)	-5.59	-1.62
Spiculated Lesion-4	Resonant Frequency (GHz)	4.45	8.7
	Damping Factor (1/ns)	-6.45	-4.33

To quantitatively analyze the CNR discrimination for the embedded lesions, we use normalized-CNR-error (NCR) (3.33) for the extracted CNRs. NCR results are shown in Figure 3.4.7. As expected, NCRs among smooth lesions are small (averaged value is equal to 0.2) as shown in Figure 3.4.7 (a), since smooth lesions have small transitions of surface geometries. On the other hand, NCRs between spiculated lesions are high (>0.6) as shown in Figure 3.4.7(b), as spiculated lesions have random sharp transitions of their surface shapes. It can also be seen from both Figure 3.4.7(a) and (b) that NCRs between smooth and spiculated lesions are considerably higher than those between smooth lesions. These simulated results have demonstrated that spiculated shaped lesions can be

used potentially to discriminate smooth lesion shapes from spiculated shapes using CNRs.

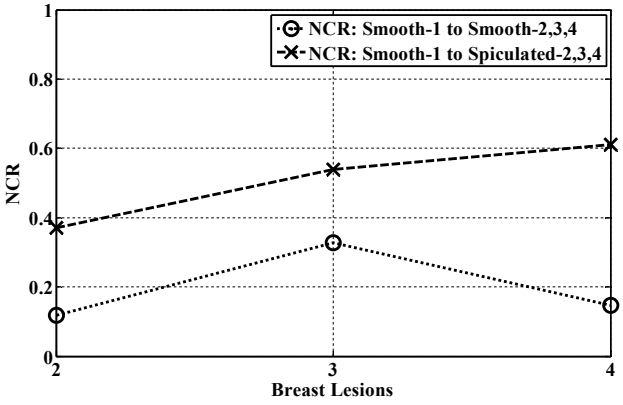

(a)

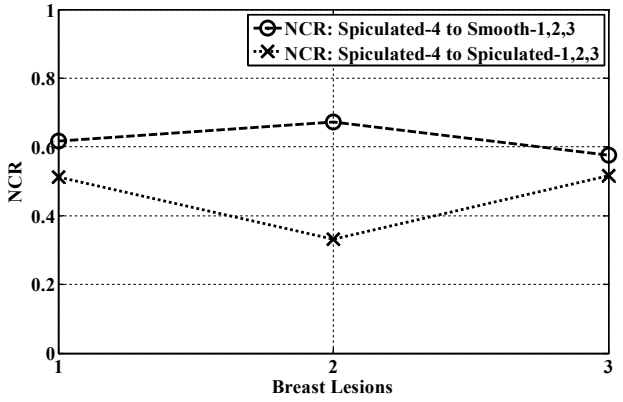

(b)

Figure 3.4.7 Normalized CNR errors between extracted CNRs from breast lesions in C3 phantom. (a) NCRs of smooth-1 to other lesions (b) NCRs of spiculated- to other lesions

3.5 Discussion

This chapter presents a new technique to discriminate breast lesions using complex natural resonances. We use MWDAS to spatially minimize the interferences from clutters followed by two-stage waveform estimation method. Numerical results using C3 heterogeneously dense breast phantom have demonstrated that MWDAS can achieve a high resolution image to identify the location of suspicious region inside dense breast phantom. To efficiently focus on the suspicious region within the breast, we develop a general pair-matching pre-processing technique using root-mean-square-error as a criterion to select the available pulses from which we can remove the early-time unwanted contents. We also develop a TOA autocalibration technique which can make the reconstruction method adapt to inhomogeneous breast. Numerical demonstrations have shown that TOA autocalibration is easy to implement and results in good reconstructed lesion image in both simple hemispherical model and C3 dense breast phantom.

The proposed two-stage waveform estimation combines a minimum-square-error based beamforming and steering vector estimation using RCB to estimate an accurate waveform of target response, since waveform is important for extraction of CNRs. We develop a method to make sure CNRs are extracted from late-time resonant signal on the obtained target response. This method separates late-time resonant signal from early-time non-resonant signal by forming a map of dominant resonances as a function of time. By using this method, spurious CNRs that may be extracted from early-time nonresonant signals can be reduced. Normalized-CNR-error (NCR) is used as a metric to measure the difference between CNRs extracted from different targets.

The extracted CNRs from four sets of breast lesions in C3 heterogeneously dense phantom have shown that CNRs extracted from spiculated lesions have significantly

lower damping factors than those from smooth lesions. This difference on CNR indicates that breast lesions with distinct surface shapes can be potentially discriminated. NCRs also confirm that spiculated and smooth lesions can be discriminated, since their calculated NCRs are considerably larger than those between smooth lesions.

Chapter 4
UWB Antennas for Microwave Breast Imaging

4.1 Introduction

Antenna is critical for the success of any practical microwave imaging system. Many ultrawideband (UWB) antennas have been reported [48, 73, 137, 138]. For breast cancer detection, the end-fire antennas have attracted special attention since they have good directivity and de-coupling capability [78, 80, 81, 139-141]. *Li et al* proposed a ridged pyramidal horn antenna having very low return loss over UWB bandwidth to perform both in free space and inside a coupling liquid [79]. A hemispherical wide-slot antenna array was developed for both radar imaging and tomography imaging applications [44], in which a wide-slot antenna was combined with a metallic cage to force the radiated energy into the breast phantom. Balanced antipodal Vivaldi antenna (BAVA) [80] incorporating a novel dielectric director was proposed by *Bourqui et al* to improve the antenna directivity and gain for breast cancer imaging [80]. A TEM horn antenna was reported in which high dielectric material was used to match with breast tissues so that use of coupling liquid can be avoided [81].

In this chapter, we examine three different types of end-fire directional UWB antennas by using FDTD simulations. The FDTD mesh size is 1/14 of the smallest wavelength and use of much smaller fine mesh is required to model fine geometrical features of the antenna. Convolutional perfectly matched layers (CPML) are used for absorbing boundary condition. Antennas are optimized to work efficiently when immersing into the coupling liquid. We employ iteratively empirical optimization that includes resizing and rescaling of the geometries and shapes of antennas based on FDTD simulations to obtain the best reflection and transmission performances in the frequency band of interest. We select our antennas based on a selection criterion as discussed in section 4.2.

Our aim is to design novel and efficient UWB antennas for use in experimental microwave breast imaging system. We first propose three novel designs and use FDTD based empirical optimization to obtain good characteristics for each proposed antenna. We then compare the simulated performances based on a set of criteria so that we pick one antenna that has satisfied all the criteria. We then fabricate the antenna that has satisfied our criteria and measure the performance. Once satisfactory measured performance is obtained, we then employ it in our proposed experimental microwave imaging system.

Our investigations have proven that the proposed BAHA antenna satisfied all the criteria and we fabricated this BAHA antenna. Both simulated and measured results have demonstrated that BAHA antenna has good antenna characteristics for microwave breast imaging. Then, we also examine the effects of antenna on the extraction of complex natural resonances from the embedded targets. The measured results using different antennas have also demonstrated that our proposed BAHA antenna has minimal effects on the CNRs extracted from the embedded target.

4.2 Criteria for antenna selection

To design an antenna with good characteristics for microwave breast imaging, we set up the following criteria for the three proposed end-fire directional antennas in this chapter. They are: (a) compact aperture size which is equivalent to a few centimeters (i.e., <4cm), (b) ultrawideband impedance bandwidth (<-10dB) which better covers the UWB range allowed by the Federal Communication Commission (FCC) for indoor applications, i.e., 3.1GHz to 10.6GHz, (c) superior transmission response which requires the magnitude of transfer function be as flat as possible and the magnitude is higher than -30dB when antennas are immersed in coupling liquid and have 100mm separation (d) high fidelity (>0.9) at 100mm separation when immersing antenna in coupling liquid used for imaging. These criteria are also included in Table 4.2.2. Whichever antenna of the three investigated in this chapter fulfills these metrics and outperforms others, it will be chosen for use in breast cancer detection.

4.2.1 Ultrawideband impedance bandwidth

For near-field microwave imaging applications, wide bandwidth can provide more information of interest from the imaged region that increases the chances of detecting breast cancer [33]. Further, since one of our key aims is to extract complex natural resonances (CNRs) from embedded breast lesion, antenna should be able to receive signals within the band that covers the natural resonant frequencies of the targets. The resonant frequencies for a smooth lesion (dia=10mm) embedded in breast tissues can be estimated using Baum's transform as given in (3.5)[125]. The breast medium referred in Table 4.2.1 can represent the average values of the permittivity of the breasts for both high fatty ($\varepsilon_r = 4$) and low fatty ($\varepsilon_r = 14$) tissue scenarios according to the MRI derived realistic breast phantom provided by UWCEM [57]. The permittivity of $\varepsilon_r = 4$ can represent the average permittivity of high adipose tissue dominated breast [57]. On

the other hand, $\varepsilon_r = 15$ can represent low adipose tissue dominated breast, and permittivity of heterogeneously dense breast can vary from 15.2 to 27.5 [131].

Only three CNR poles that fall in frequencies less than 11GHz are discussed, since poles falling at frequencies >11GHz are not useful due to inefficient penetration of microwaves into breast tissues at higher microwave frequencies. It can be seen from Table 4.2.1 that it is ideal to have an antenna that can have an impedance bandwidth from 2Ghz to 8.5GHz meaning that antenna can receive signals within the band for CNR extraction efficiently. The aperture size of the antenna needs to be increased if lower operating frequency is required to cover the natural resonant frequencies that fall at those low end microwave frequencies. For example, the first pole at 2GHz in low adipose tissue phantom as shown in Table 4.2.1. As a compromise between lower operating frequency and the antenna size, we have chosen the UWB frequency operating from 4GHz so that it covers band of natural resonant frequencies of some CNR poles while maintaining a compact size. We fixed the desirable aperture size to be 20mm so that the antenna is small and thus useful to form a large antenna array for microwave breast imaging.

Table 4.2.1 Resonant Frequencies of Embedded Spherical Tumor (dia=10mm) in Breast Phantoms

Low adipose tissue $\varepsilon_r = 15$			**High adipose tissue $\varepsilon_r = 4$**		
1st Pole	**2nd Pole**	**3rd Pole**	**1st Pole**	**2nd Pole**	**3rd Pole**
2GHz	4.4GHz	6GHz	4GHz	8.5GHz	13.1GHz

Table 4.2.2 Criteria Of Antenna Metrics

Metric	**Criteria**	**Dimension**
1	Compact aperture size	<4cm
2	Ultrawideband bandwidth	<-10dB
3	High transmission response	>-30dB
4	High fidelity	>0.9

4.2.2Transmission response

In order to achieve minimal distortion of UWB signals transmitted into the breast, it is desirable that the magnitude of the transfer function of the antenna is as flat as possible across the required frequency band [78]. Thus, antenna should have constant and high magnitude of S21 across the chosen bandwidth. We obtained S21 in both FDTD simulation or measurement using the setup as shown in Figure 4.2.1, where two antennas facing each other at bore sight while both immersed in coupling liquid having dielectric constant$\varepsilon_r = 2.5, \sigma = 0.04$ S/m at 100mm distance [78, 80].

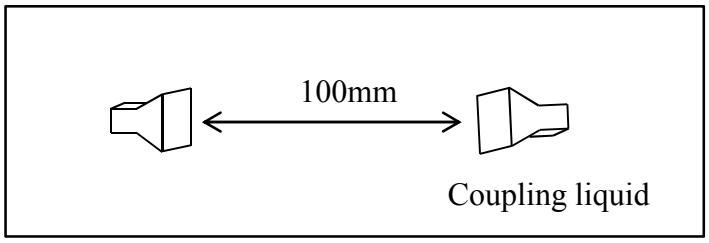

Figure 4.2.1 Antenna setup for S21 measurement or simulation immersed in coupling liquid. Two identical antennas face each other at boresight in coupling liquid and separated by 100mm.

4.2.3 Fidelity

When radiating narrow time-domain pulsed signal (UWB in frequency domain), it is important that antennas do not distort the pulse shape while in transmission. In order to study the level of distortion in the radiated pulse, fidelity is a critical metric. Maximum value of fidelity (fidelity=1) of an antenna means this antenna can radiate a negligibly distorted UWB pulse into imaging region. The fidelity parameter **F** is a measurement of how faithfully the pulse is transmitted and received by the antenna. It is calculated by the maximum magnitude of the cross-correlation between the normalized observed response and an ideal response derived from the source waveform, as given by [79]:

$$\mathbf{F} = \max_{\tau} \int_{-\infty}^{\infty} \boldsymbol{r(t-\tau) f(t) dt} \quad (4.1)$$

where the observed pulse is the received UWB pulse $r(t)$ and ideal response is the normalized time derivative of the source waveform $f(t)$. To calculate the fidelity using (4.1), use of antenna setup for simulation or measurement is the same as that shown in Figure 4.2.1 and the source UWB signal in our simulation has bandwidth from 2GHz to 10GHz with a 3-dB bandwidth of 2.1GHz.

4.3 Proposed antenna 1: UWB ridged horn antenna with straight launching plane

It has been noted that the bandwidth of waveguide horn antennas can be increased significantly by adding metallic ridges to waveguide and flared sections [142, 143]. Pyramidal horn antenna with double ridges was proposed to operate from 1-18GHz [144]. A modified version of pyramidal horn antenna was proposed by Li et al [79] that a curved metallic plane is terminated by two chip resistors. In this section, we propose a modified design for UWB ridged horn which has a straight ridge and a straight launching plane terminated with four chip resistors. The aperture dimension of the proposed straight ridged horn antenna is $20\text{mm} \times 15\text{mm}$ as shown in Figure 4.3.1. A metallic straight launching plane is connected to the central conductor of the coaxial feed. Four 200 Ω termination resistors are attached between the end of the launching plane and the side wall of the horn. The ridge is also straight which is attached to the wall opposite to the straight launching plane as shown in Figure 4.3.1. The straight shaped ridge and launching plane make both simulation and fabrication simple. The dimensions and shapes of the horn, ridge, launching plane, and the termination resistors are the main factors that influence the input impedance of the antenna. The optimized

dimensions and shapes of this antenna using FDTD simulation are shown in Figure 4.3.1.

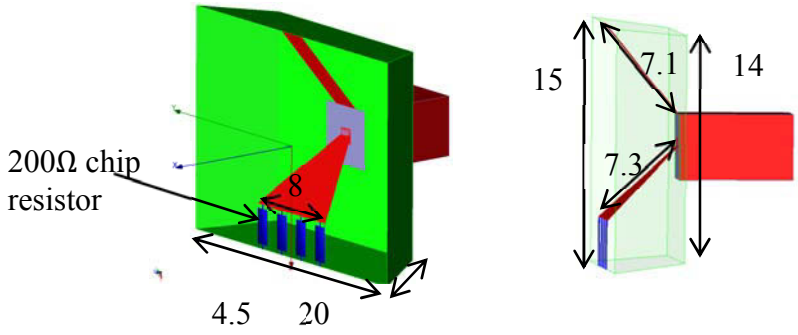

Figure 4.3.1 Proposed straight ridged horn antenna with straight launching plane, and four 200ohm chip resistors. (a) 3D view (b) another 3D view

S11 and S21 results for the straight ridged horn are obtained using FDTD simulations are shown in Figures 4.3.2 and 4.3.3, respectively. S11 results indicate that the proposed ridged horn antenna has very good impedance match up to 12GHz with S11 level lower than -15dB. S21 results are obtained by using the same setup as shown in Figure 4.2.1. The coupling liquid used in simulation has $\varepsilon_r = 2.5, \sigma = 0.04$ S/m. It can be seen from Figure 4.3.3 that the simulated S21 with magnitudes above -30dB ranges from 5GHz to 11GHz.

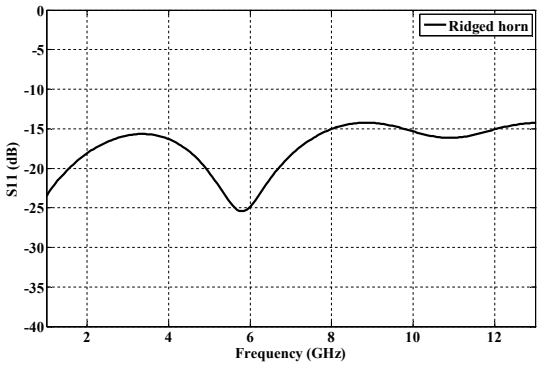

Figure 4.3.2 S11 of ridged horn antenna using FDTD simulation in coupling liquid

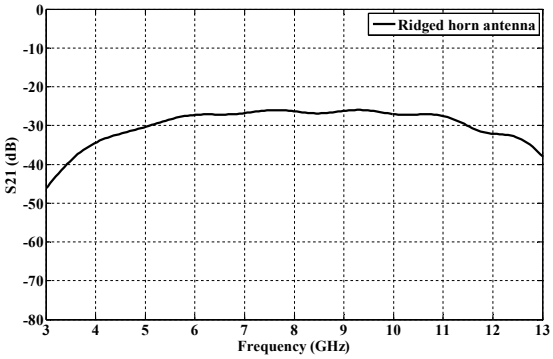

Figure 4.3.3 S21 of ridged horn antenna using FDTD simulation in coupling liquid

The fidelity of ridged horn antenna is also calculated using the procedure in section 4.2.3. The ideal and the observed responses are shown in Figure 4.3.4. The calculated fidelity using (4.1) is 0.995.

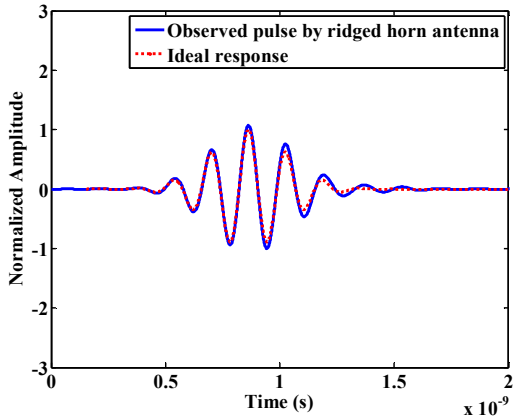

Figure 4.3.4 Ideal and observed responses using FDTD simulation for ridged horn antenna in coupling liquid

4.4 Proposed antenna 2: A modified Balanced Antipodal Vivaldi Antenna (mBAVA)

Balanced antipodal Vivaldi antenna (BAVA) was first introduced by Langley et al [145] with wideband and end-fire radiation. It was first modified for UWB breast imaging application by Bourqui et al [80, 140] by including a dielectric director. The main feature of dielectric directed BAVA is that it provides high fidelity for pulse radiation and the radiation characteristics are enhanced by the presence of dielectric director for energy radiation into the breast.

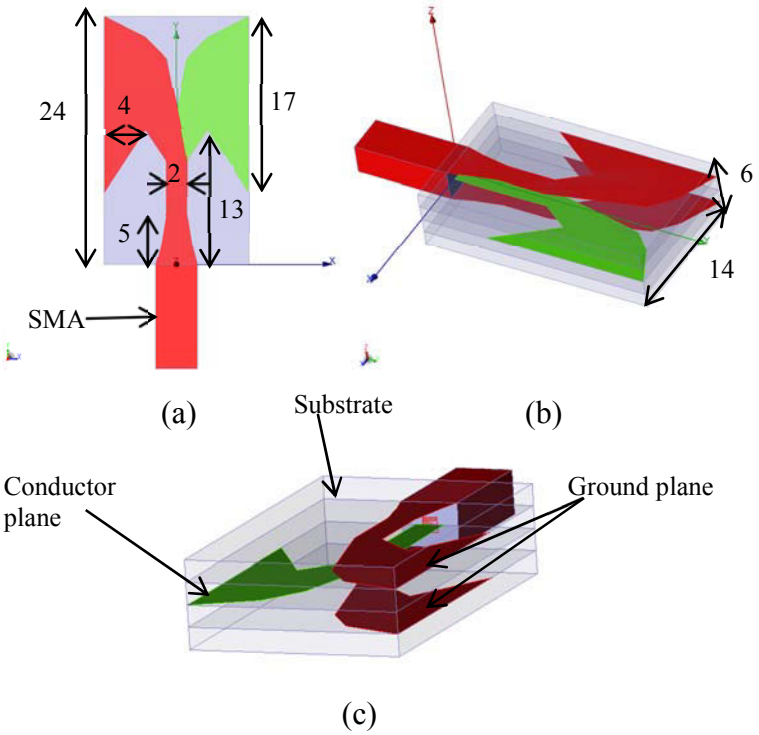

Figure 4.4.1 Dimensions of mBAVA. (a) Top view. (b) 3D view. (c) another 3D view

In this section, we further modify BAVA and propose another modified balanced antipodal Vivaldi antenna which we call "mBAVA". Our modified "mBAVA" has no dielectric director with reduced size to be able to accommodate in a large antenna array

for breast cancer detection. The resultant aperture size is $14\text{mm} \times 6\text{mm}$ as shown in Figure 4.4.1. The mBAVA uses four Rogers Duroid 6002 substrates having $\varepsilon_r = 2.94$, and $\sigma = 0.0027$ S/m. The four substrates support the three copper planes i.e., one conductor plane in the middle layer (green) and two ground planes (red) as shown in Figure 4.4.1 (c). Each layer of substrate is 1.524mm thick. Unlike Bourqui et al [80], we use tapered flares for ease of manufacture. This antenna is fed by an SMA coaxial connector.

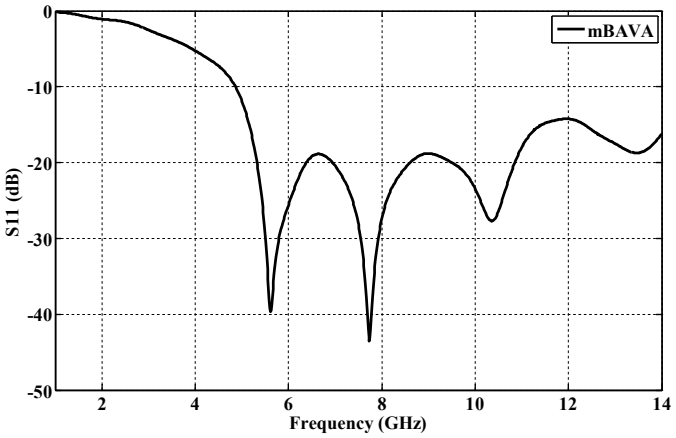

Figure 4.4.2 S11 of mBAVA using FDTD simulation in coupling liquid

The mBAVA is also designed to work when immersed in a coupling liquid with dielectric constant$\varepsilon_r = 2.5, \sigma = 0.04$ S/m. The FDTD simulated S11 results are plotted in Figure 4.4.2, which show that the -10dB impedance bandwidth is 11GHz in the band from 5GHz to over 14GHz. Simulated S21 results are shown in Figure 4.4.3, from which it can be observed that S21 values higher than -30dB level occur between 5.2GHz and 14GHz using the same setup shown in Figure 4.2.1. The S21 values have flat transmission response with high magnitudes over the band that demonstrates the superior transmission capability of mBAVA. Simulated fidelity for mBAVA is 0.98 at distance of 100mm in coupling liquid calculated using the setup given in Figure 4.2.1.

Both received pulse shape and ideal response (both simulated) are shown in Figure 4.4.4.

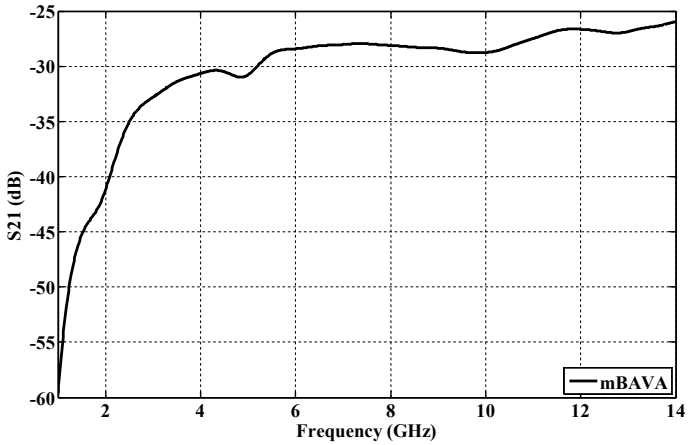

Figure 4.4.3 S21 of mBAVA using FDTD simulation in coupling liquid

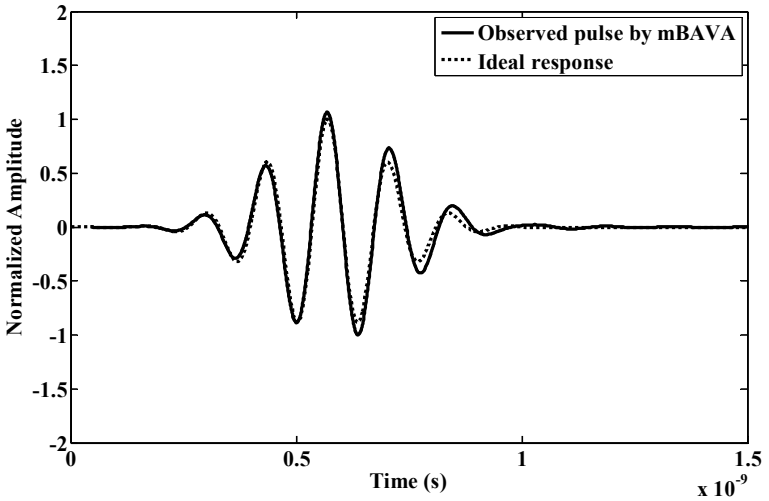

Figure 4.4.4 Observed and ideal responses in coupling liquid using FDTD simulation for mBAVA

4.5 Proposed antenna 3: UWB Balanced Antipodal Horn Antenna (BAHA)

In this section, we propose a new balanced antipodal Vivaldi type UWB horn antenna (BAHA). BAHA has similarities to the well-known balanced antipodal Vivaldi antenna [80]. BAHA is a horn type antenna whereas BAVA is a Vivaldi without any horn arrangement. The geometry of the BAHA is shown in Figure 4.5.1.

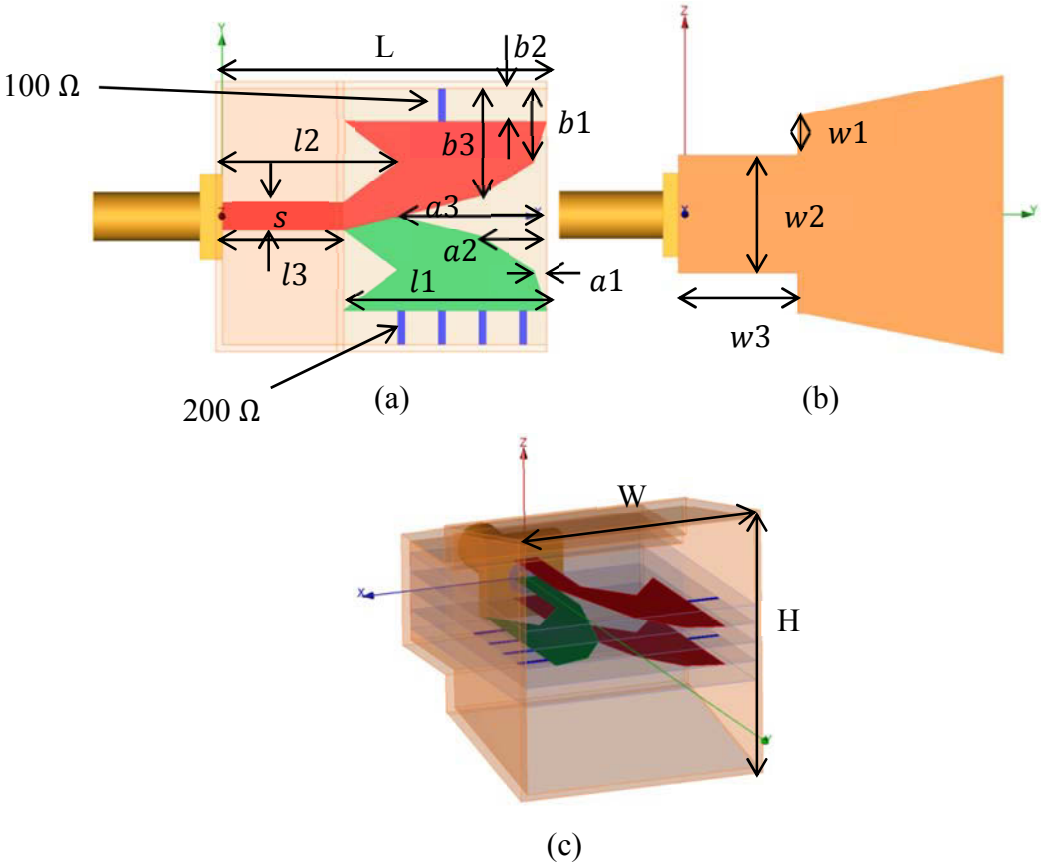

Figure 4.5.1 BAHA antenna geometry

The BAHA contains a metallic, tapered horn in which a dielectric-conductor sandwich is used similar to that used in Vivaldi [80], but with redesigned aspects. The dielectric-conductor sandwich has four dielectric substrates supporting three copper layers. Two external layers are the ground planes that are connected to the external horn structure terminated with two 100 Ω termination resistors. The central metallic layer connects to the central conductor of coaxial feed and its flare section is terminated to the external horn cavity through four 200 Ω resistors. The shapes and dimensions of three copper layers are redesigned and optimized by using FDTD simulation. A straight feed line is connected to the SMA connector as shown in Figure 4.5.1(a). Both the conductor and the ground have the same transition width. The copper layers are separated by two dielectric substrates (supportive substrates) and two additional dielectric layers are stacked on each side of the antenna which are in similar configuration in [80], and thus form the sandwich. Two dielectric substrates have been used viz., Taconic TLE-95 and Rogers RO3003 with 1.52mm thickness and dielectric constant $\varepsilon_r = 2.95$ for our fabrication. BAHA is also designed to work in coupling liquid that has approximate dielectric properties $\varepsilon_r = 2.5, \sigma = 0.04$ S/m. The parameters of antenna geometry and their FDTD optimized values are listed in Table 4.5.1. The overall antenna size is $20 \times 20 \times 24$mm.

Table 4.5.1 Parameters of BAHA Antenna Optimized by FDTD Simulation

Parameters	Optimized Values (mm)	Parameters	Optimized Values (mm)
W	20	***a*2**	5
H	20	***a*3**	11
L	24	***b*1**	3
***l*1**	15	***b*2**	2
***l*2**	13	***b*3**	5.5
***l*3**	9	***w*1**	3
s	2	***w*2**	7
***a*1**	1	***w*3**	9

4.5.1 Performance of BAHA using FDTD simulation

Simulated results S11 and S21 are shown in Figure 4.5.2 and Figure 4.5.3 respectively. It can be seen that BAHA has low S11 values up to 11GHz. By examining the simulated S21, it can be seen that the transmission response is flat over 14GHz. S21 with magnitudes higher than -30dB starts from 4.5GHz to 14GHz and the average magnitude has very high value of -23dB. The simulated observed and ideal response pulses can be seen in Figure 4.5.4 using the procedure given in section 4.2.3. The calculated fidelity using simulated data is 0.989.

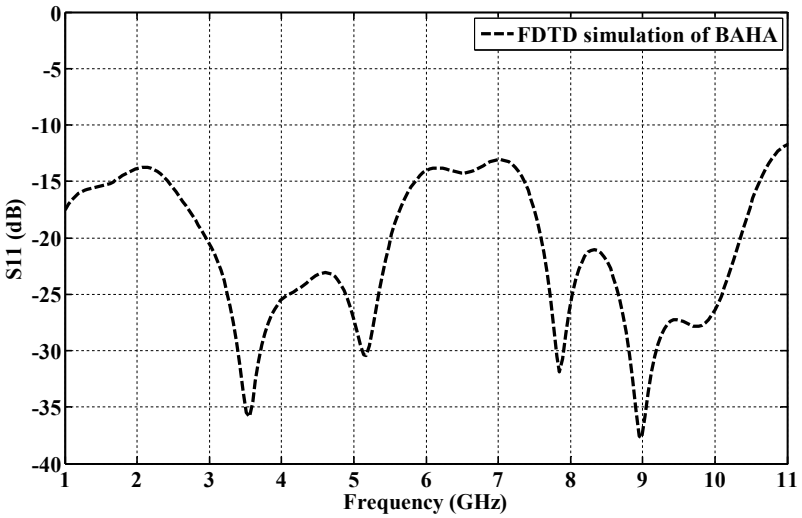

Figure 4.5.2 Simulated results of S11 for BAHA in coupling liquid

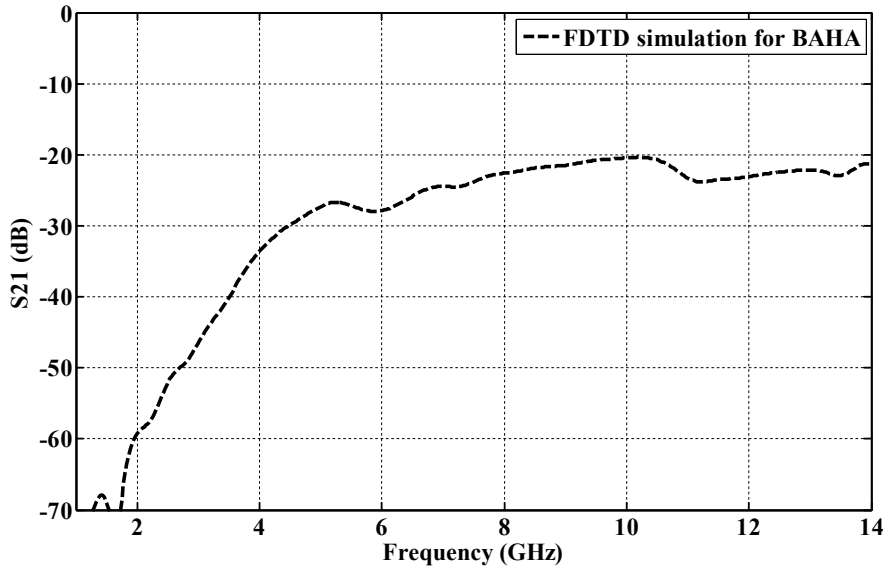

Figure 4.5.3 Simulated results of S21 for BAHA in coupling liquid

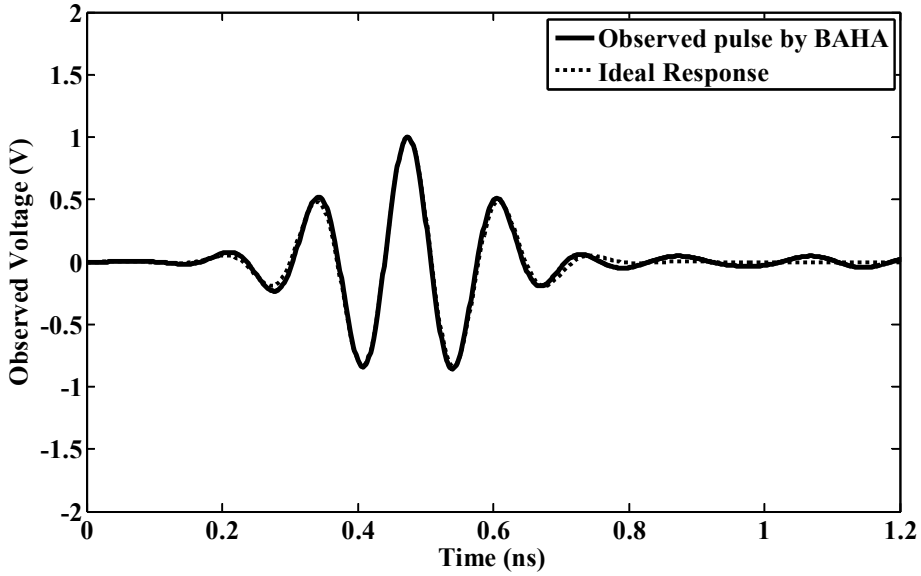

Figure 4.5.4 Simulated results of observed and ideal responses by BAHA in coupling liquid.

4.6 Selection of the best UWB antenna

Out of the three UWB antenna configuration investigations so far using FDTD simulations, now we choose the best configuration that satisfies the criteria and fabricate it for inclusion in the experimental microwave imaging system for breast cancer detection. As discussed in section 4.2, there are overall five criteria that are used to evaluate the antennas. The evaluation results for these three antennas are listed in Table 4.6.1. All the three end-fire UWB antennas as discussed in earlier sections have similar impedance bandwidth as shown in Table 4.6.1. It can be seen that among them BAHA has the highest S21 magnitude while maintaining high fidelity. The aperture size of BAHA is also compact. Further, BAHA has UWB band with starting frequency from 4.5GHz which falls within the resonant frequencies of CNR poles as given in Table 4.2.1. Although other antennas have smaller aperture size than BAHA, smaller antenna aperture size is not the only metric to influence the resolution. Other metrics such as fidelity and transmission response are more important for antenna. BAHA comes out with superior performance. BAHA provides over 4dB higher magnitude of transfer function than other antennas in comparison and has relative flat phase response over the band. Thus, we choose BAHA as the candidate antenna for our experimental microwave imaging system for the breast cancer detection.

Unfortunately, we could not get measured data for arrow slot antenna and hence this antenna was not presented in the thesis. The reason for not choosing the arrow slot antenna is that the arrow slot antenna requires higher dielectric material as coupling medium than other three antennas (BAHA, mBAVA, and ridged horn) and those materials were not available. Hence, simulation results of arrow slot antenna are incorporated in a report which is referred in the thesis [156].

Table 4.6.1 Antenna Characteristics of Proposed UWB Antennas using FDTD Simulation

Antenna Type	Aperture Size	Impedance Bandwidth	S11	Averaged S21	Fidelity
Arrow shaped slot antenna with modified fork feed [156]	10mm × 11mm	4.5-10.6GHz	<-10dB	-27dB	0.980
Ridged horn antenna	15mm × 20mm	5-11.4GHz	<-10dB	-28.5dB	0.995
mBAVA	16mm × 14mm	5-11GHz	<-10dB	-28dB	0.980
BAHA	20mm × 20mm	4.5-11GHz	<-10dB	-23.9dB	0.989

4.7 Measured Antenna Characteristics of BAHA

4.7.1 Fabrication of BAHA

As explained in the previous section, the internal sandwich Vivaldi structure of BAHA is first fabricated using Rogers RO3003 substrates. The flared part of the copper conductor layer soldered with four 200Ω termination chip resistors are shown in Figure 4.7.1(a). The fabricated internal Vivaldi structure of BAHA before connecting to the horn is shown in Figure 4.7.1(b). Later, the sandwich was inserted into the metallic horn as shown in Figure 4.7.1(c). The fabricated BAHA is shown in Figure 4.7.1(d) and (c) in different views.

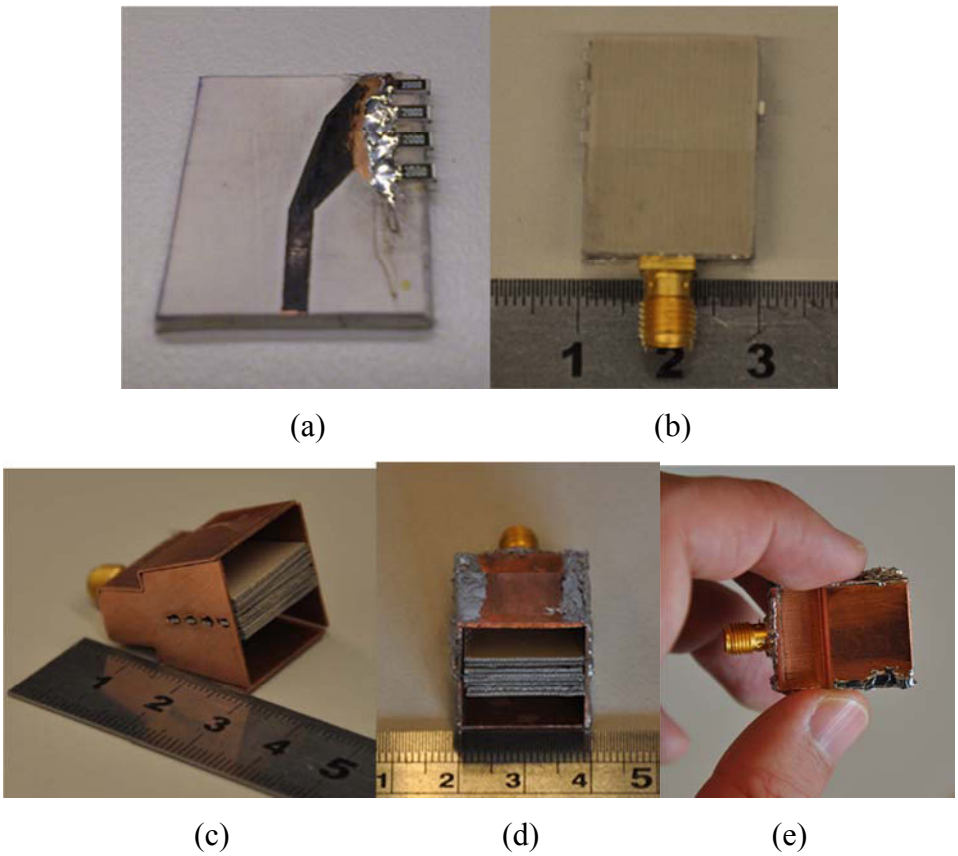

(a) (b)

(c) (d) (e)

Figure 4.7.1 Pictures showing fabrication of BAHA (a) The middle conductor layer of sandwich structure (b) fabricated sandwich Vivaldi structure (c) BAHA without soldering the termination of chip resistors (d) front view of fabricated BAHA (e) top view of fabricated BAHA

4.7.2 Measured S11

The measured S11 is compared with simulated S11 in Figure 4.7.2. It can be observed that both measured and simulated impedance bandwidth (-10dB) is 10GHz in the band 1-11GHz due to the chip resistors, which demonstrates superior input response performance. Moreover, the measured data also demonstrates that a very low S11< -15dB with frequency up to 9.6GHz. It can also be observed that measured S11 matches the main trend of the simulated data, although measured data appears to be shifted. The

shifted measured data with respect to FDTD simulation could be due to the fabrication imperfection and soldering of chip resisters and copper layers as well as gaps between the layers of the dielectric sandwich.

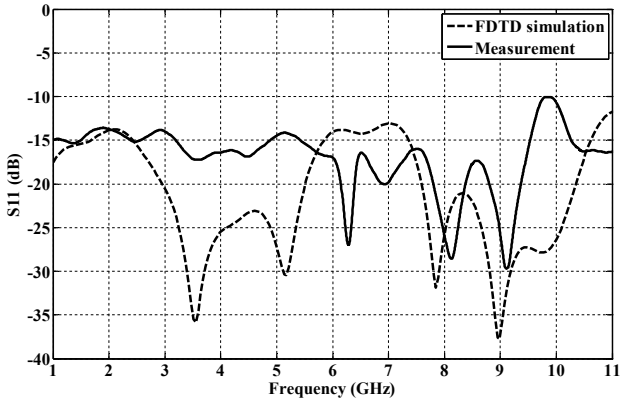

Figure 4.7.2 Measured and simulated S11 of BAHA when immersed in coupling liquid.

4.7.3 Investigation on effects of fabrication imperfections

During fabrication of BAHA, soldering of the resistors could not guarantee tight bonding of the substrates within the sandwich. Thus, the gaps may appear between the substrates. These gaps in the fabricated BAHA could have contributed to the discrepancies in the S11 result shown in Figure 4.7.2. To investigate the effect of gaps formed between layers of dielectric sandwich as shown in Figure 4.7.3, we undertake detailed FDTD simulations. Each chip resistor is modelled to have a size of of $2.5\text{mm} \times 1.5\text{mm} \times 1\text{mm}$ in FDTD model and the corresponding gaps as shown in Figure 4.7.4(a) are also modeled in FDTD. On the figure, we used three gap sizes viz. gap-1=0.4mm, gap-2=0.8mm and gap-3=1.2mm, and the ideal result assumes perfect bonding without any gap. From Figure 4.7.4 (b)-(d), one can observe that having the gap, worse are the S11 results. But for all the three gap sizes considered, the S11 over the band still did not exceed -10dB.

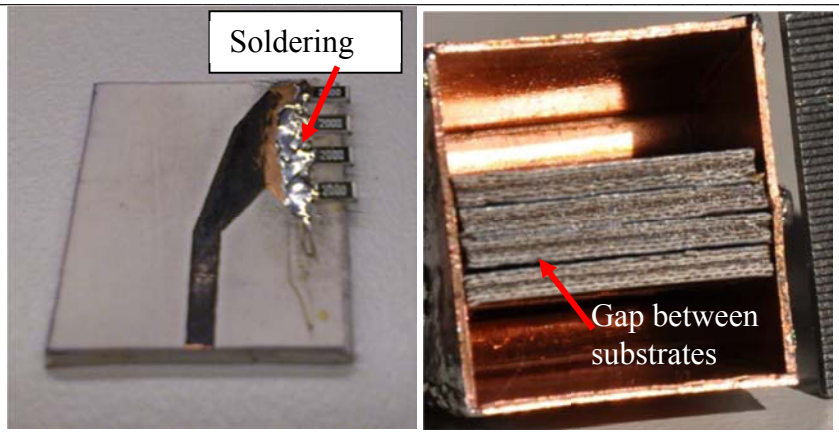

(a) (b)

Figure 4.7.3 Gaps between supportive substrates of BAHA (a) fabricated conductor layer with chip resistors (b) gaps appearing between substrate layers.

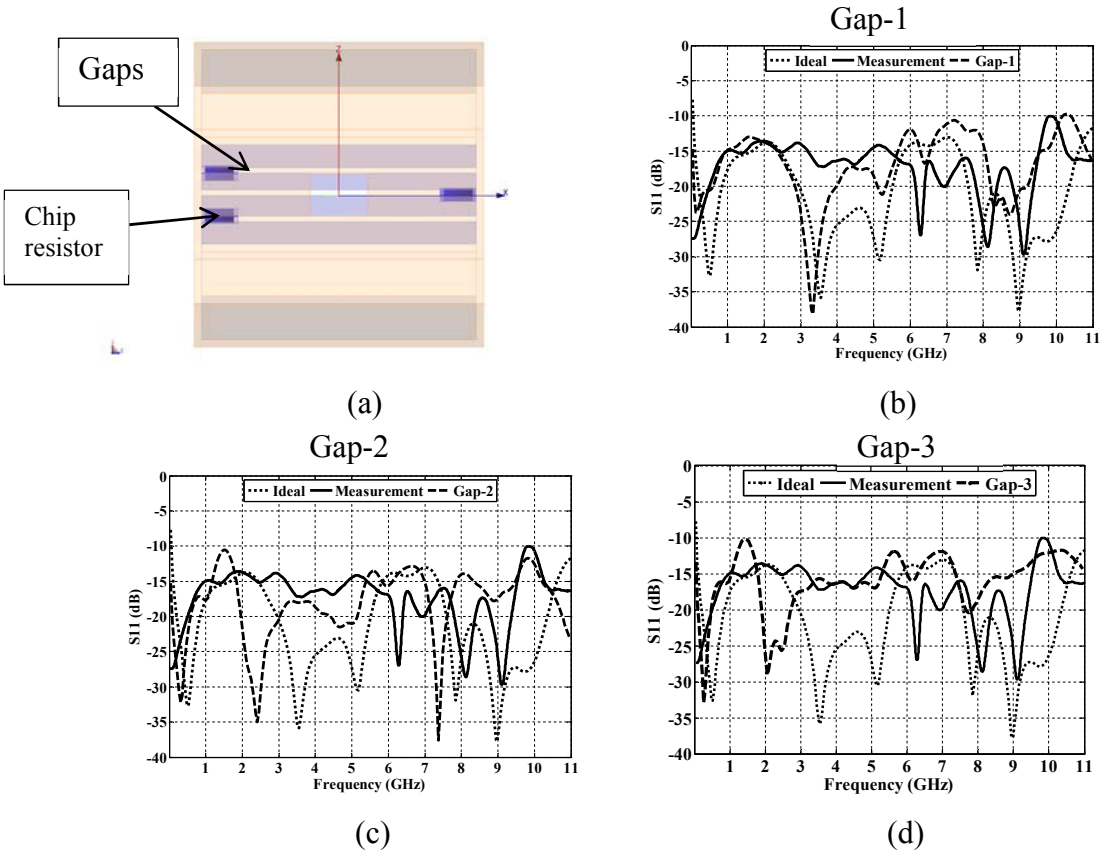

(a) (b) (c) (d)

Figure 4.7.4 Simulated S11 results showing the effects of gaps between substrates due to the fabrication imperfection (a) gaps modelled between substrates of BAHA antenna (b) s11 with gap-1 (c) s11 with gap-2 (3) s11 with gap-3

4.7.4 Measured S21

The transmission coefficient S21 was measured using the setup given in section 4.2.2 as shown in Figure 4.2.1. The coupling liquid used here is olive oil which has approximate dielectric constant $\varepsilon_r = 2.5, \sigma = 0.04$. The simulated and measured results are shown in Figure 4.7.5. Measured S21 results have shown that the magnitudes higher than -30dB are obtained from 4.1GHz to 14GHz and beyond. The measured S21 results have flat characteristics and their magnitudes are high demonstrating that the transmitted UWB pulse experience low distortion. When compared with other antennas discussed in this chapter (ridged horn with straight ridge and launching plane, and mBAVA), BAHA obtains superior performance with high S21 magnitude. Further, BAHA also has higher S21 magnitudes than the TEM horn and wide slot antennas reported in literature [78, 81].

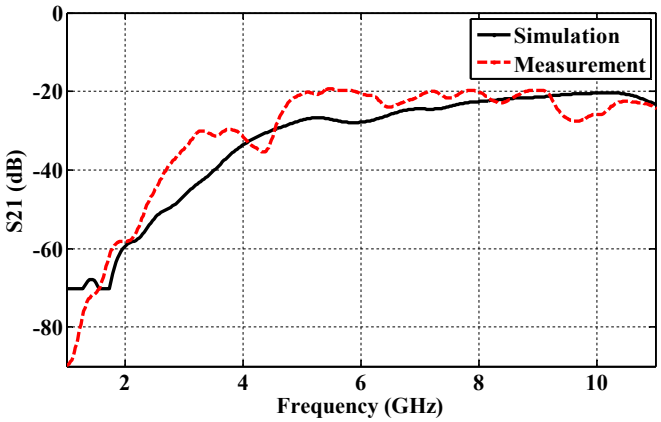

Figure 4.7.5 Measured and simulated S21 of BAHA immersed in coupling liquid.

4.7.5 Measurement of antenna fidelity for BAHA

The measured pulse is generated synthetically by using frequency swept mode of VNA over the band of 1-8GHz with 1600 frequency samples. Then the time-domain waveform is calculated by IFFT over the spectrum. The measured ideal response is

obtained from the measured data by directly connecting two ports of VNA using a low loss cable and its time-domain signal is plotted as solid line in Figure 4.7.6 (a).

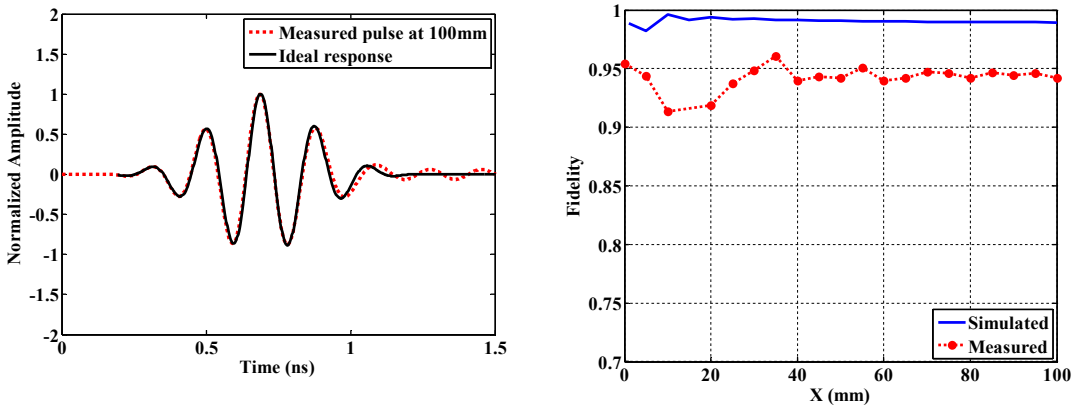

(a) (b)

Figure 4.7.6 Measured fidelity of BAHA (a) measured pulse and ideal response (b) measured and simulated fidelities at different distances

To measure the observed response, two BAHA are immersed in coupling liquid (olive oil) with 100mm separation. Then the observed pulse can be measured synthetically using VNA using the same frequency swept. The measured observed response is also shown in Figure 4.7.6 (a) in dotted line which shows low distortion compared to the waveform of the ideal response. Fidelity is also measured at different distances ranging from 0 to 100mm at a step of 5mm. Fidelity versus distance is shown in Figure 4.7.6(b) and compared with simulated data. Despite the reduced fidelity level, measured fidelity is still larger than 0.9 and is reasonably stable after a 40mm demonstrating robust fidelity of BAHA over distance. This stable fidelity is superior to that of TEM horn antenna reported in literature [81]. The measured result has demonstrated a low distorted UWB pulse can be radiated and received for obtaining good quality signals for microwave imaging of breast cancer and CNR extraction.

4.7.6 Coupling efficiency

Coupling efficiency is another measurable parameter that can approximately characterize the performance of the power coupling into the imaged region within breast[81]. To calculate the coupling efficiency, near field directivity (NFD) is first computed by the ratio of power integrated only from the aperture surface of the antenna to the total power integrated from all the six surfaces of the antenna. The power integrated is computed by the integration of the real part of the Poyning vector on the cuboid surface. This factor provides an approximate proportion of power radiated through the front aperture. The virtual cuboid structure that encloses the antenna can be viewed in Figure 4.7.7(a). The results of NFD are shown in Figure 4.7.7(b). The average NFD from 4.1GHz to 11GHz is larger than 0.9, which means that over 90% energy radiated only through aperture of BAHA will be coupled into the imaged region.

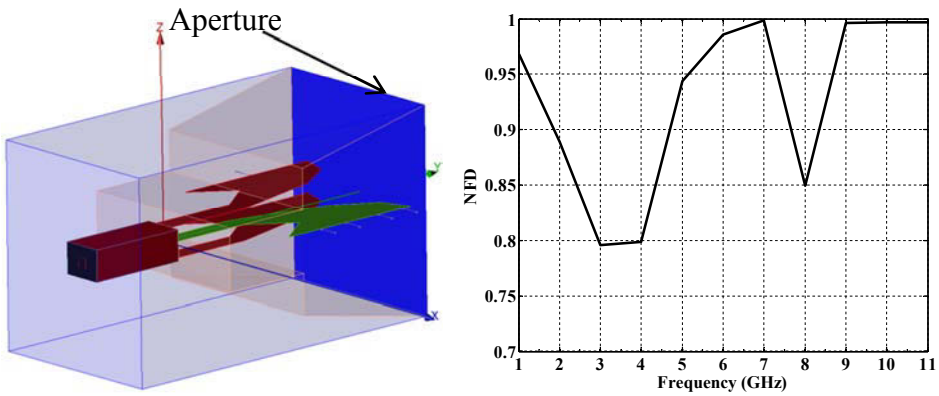

(a) (b)

Figure 4.7.7 Simulation of NFD (a) cuboid structure to simulate NFD (b) calculated NFD from simulated data

To measure the coupling efficiency, two BAHA antennas are positioned touching with each other and immersed in coupling liquid using the setup as shown in Figure 4.7.8(a). Coupling efficiency is defined by[81]:

$$e_c = \frac{|S_{21}|}{\sqrt{(1-|S_{11}|^2)\cdot(1-|S_{22}|^2)}\cdot \mathrm{NFD}} \tag{4. 2}$$

It should be noted that the calculated coupling efficiency is only an approximate metric, as NFD is calculated from simulated data.

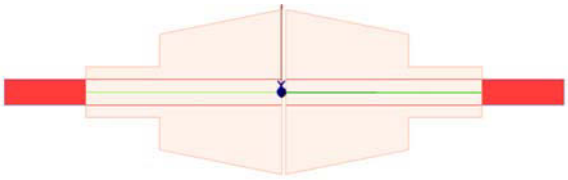

(a)

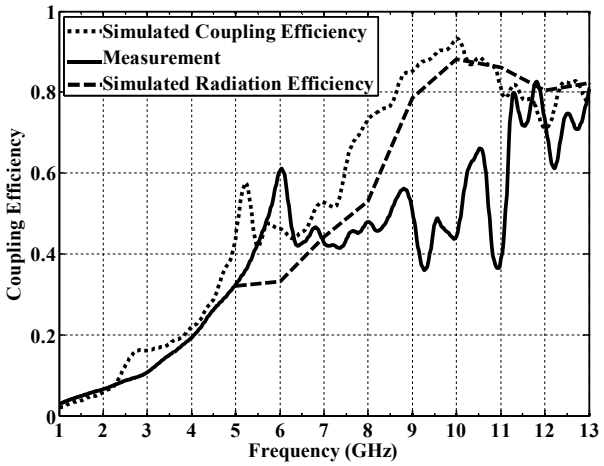

(b)

Figure 4.7.8 Measured and simulated coupling efficiencies (a) method of measuring coupling efficiency in coupling liquid(b) comparison of results

The measured coupling efficiencies (solid line) are shown in Figure 4.7.8 (b). The averaged measured coupling efficiency is 47% from 4.1GHz to 11GHz, while the simulated average coupling efficiency is 60%. BAHA has 15% higher coupling efficiency than the existing TEM horn antenna (e_c =32%) [81].

Radiation efficiency is the ratio of input power to output power of the antenna. It is normally measured in an anechoic chamber or using wheeler's cap [146, 147]. Since it is difficult to measure antenna radiation efficiency when antenna is immersed in coupling liquid, here we only present simulated radiation efficiency as shown in dashed line in Figure 4.7.8(b).

4.7.7 Radiation pattern

Due to difficulties in measuring the radiation pattern for BAHA antenna when immersed in coupling liquid, here we only show the simulated results of far field radiation patterns when antenna immersed in coupling liquid. Far-field or near field depends on the dimension of antenna and wavelength according to $R = 2d^2/\lambda$, where d is antenna dimension and λ is the wavelength. For near-field imaging antenna such as BAVA [80], d=44mm and the antenna was immersed in coupling liquid with $\varepsilon_r = 2.5$. Hence, the imaging region could be in the radiating near field. However, BAHA has dimension of 20mm and when immersed in the coupling liquid, the radiated fields within the breast region could be in the far field.

Radiation pattern is an important metric for microwave imaging, as a focused beam that illuminates into a small volume can increase the tumor-to-clutter ratio [80]. Moreover, symmetric radiation pattern is also important to radiate the pulses into the region of interest. Hence, the proposed BAHA with focused beam and symmetric pattern could be a good candidate antenna element for microwave imaging.

2D cuts of radiation patterns in X-Y plane are shown in Figure 4.7.9(a), while patterns in Y-Z plane are shown in Figure 4.7.9(b). 3D patterns are shown in Figure 4.7.10.

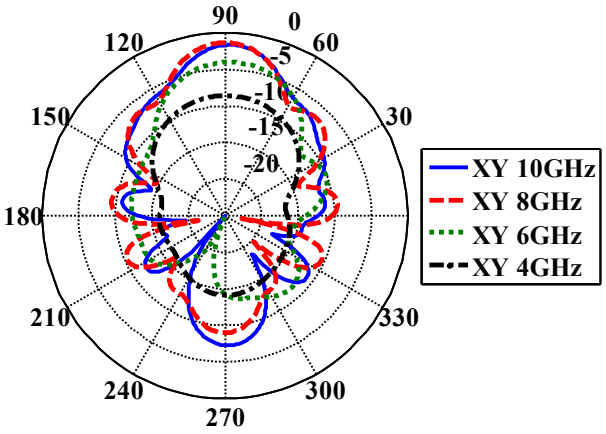

(a)

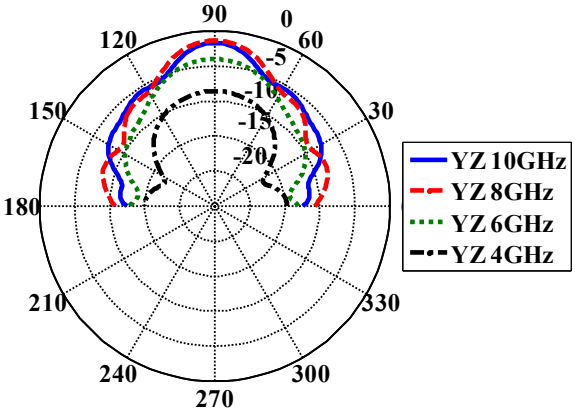

(b)

Figure 4.7.9 Simulated radiation pattern of BAHA at 4, 6, 8, and 10GHz when immersed in coupling liquid. (a) XY plane (b) YZ plane

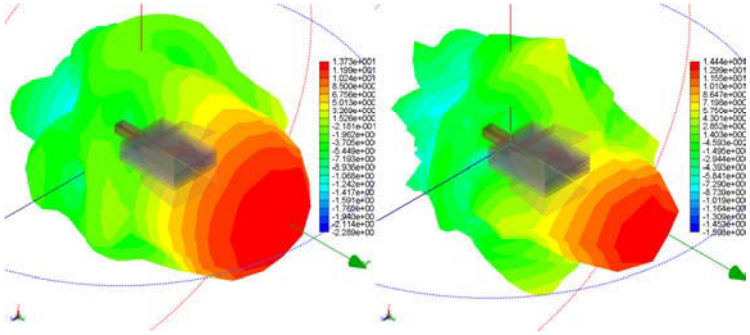

Figure 4.7.10 3D view of radiation pattern of BAHA at 7 and 9 GHz.

4.8 Effects of antenna in measurement of scattered fields for extracting CNRs from embedded targets

In this section, measurement is carried out to investigate effects of antenna on CNR extraction, since our aim is to extract CNRs from embedded targets using proposed BAHA antenna. For this, we used fabricated BAHA as explained earlier and also fabricated BAVA[80], and pyramidal ridged horn antenna given by [79]. BAVA and pyramidal ridged horn are reported having high fidelity (>0.95 at 100mm separation in coupling liquid).

When a transient pulse is radiated by the antenna, the antenna can introduce additional CNRs in the form of antenna ringing. For an ideal antenna, no ringing will be present which is equivalent to fidelity value of 100%. In addition to fabricated antennas, we also investigate the antenna effects using TEM horn antenna proposed by [81] using simulation, since fabrication can be relatively complex and it requires special dielectric materials and absorbing sheets. The reason to choose simulating TEM horn is that we tried to investigate how fidelity would affect the extracted CNRs, as TEM horn has low fidelity (<0.4 at 100mm separated by coupling medium) as reported in [81].

For the CNR extraction, backscattered signals from an embedded PEC sphere in a coupling liquid are collected when antennas for test are radiating or receiving. Once late-time response is separated from the record pulse, CNR are then extracted from the late-time target response that is obtained by subtracting a target-free template. Finally, the effects of antennas on those extracted CNRs are discussed by comparing them with theoretically estimated CNRs obtained using Baum's transform (3.5) given by [112].

4.8.1 Data collection using TEM horn in simulation

Firstly we use FDTD simulation to investigate the effects of using TEM horn antenna proposed in [81]. To test the effect of antenna for extracted CNR, simulation setup is shown in Figure 4.8.1. Two TEM horn antennas face each other and are separated by 17mm thick dielectric box ($\varepsilon_r = 10$). Here only a short distance of 17mm is used because the fidelity of TEM horn antenna is low and also decreases significantly with increased separation as reported in[81].

Before obtaining the target response, fidelity at this separating distance of 17mm is examined. The simulated fidelity (without the embedded object) is only 0.76 which is close to the value reported in [81] using similar arrangement and distance. The ideal response and the observed signal are shown in Figure 4.8.2. The radiated signal is significantly distorted due to the low fidelity even though the separation is only 17mm. These observations lead to the conclusion that TEM horn antenna proposed in [81] may not be the best choice for use for CNR extraction due to distorted received pulse.

Now we extract CNR from a PEC steel sphere with diameter of 15.875mm which is embedded in the centre of the dielectric box as shown in Figure 4.8.1. CNR has been extracted using matrix pencil method [122] from late-time target response which is obtained by subtracting a target-free signal. The extracted CNRs from simulation data are shown in Table 4.8.1.

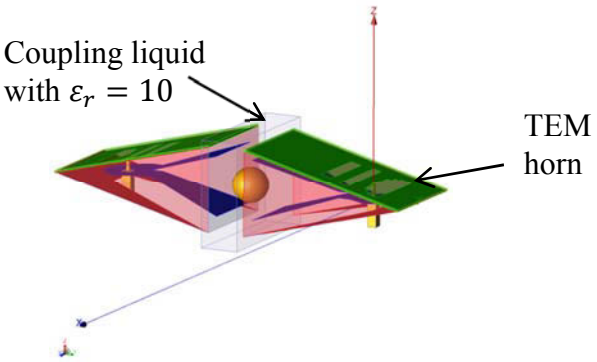

Figure 4.8.1 Simulation setup using TEM horn antennas [81]to collect reflected data from immersed PEC sphere (dia=15.875mm) for CNR extraction

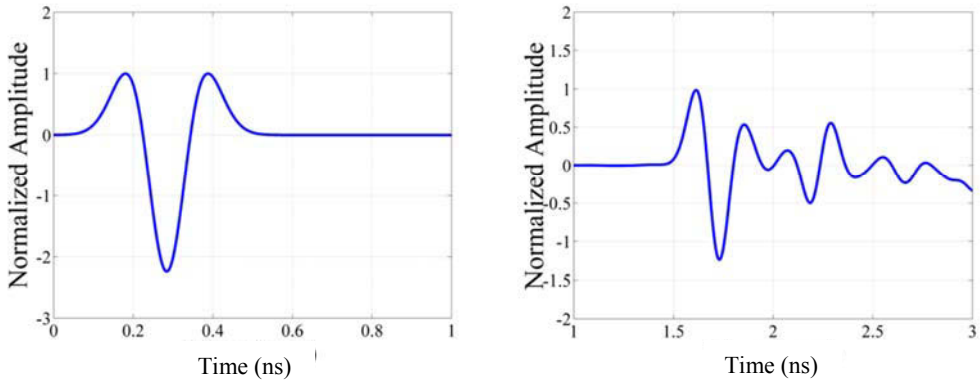

Figure 4.8.2 Simulated ideal and observed pulse responses from TEM horn [81] (a) ideal response (b) observed pulse

Table 4.8.1 CNRs of Steel Sphere (dia=15.875mm) Extracted from Simulated Data using TEM Horn in Coupling Liquid ($\boldsymbol{\varepsilon_r = 10}$)

Frequency (GHz)		Damping factor (1/ns)	
Higher mode	**Lower mode**	**Higher mode**	**Lower mode**
6.18	2.78	-7.14	-2.01

4.8.2 Data collection using BAVA in measurement

The balanced antipodal Vivaldi antenna (BAVA) [80] was fabricated as shown in Figure 4.8.3(a) to examine its effect for extracting CNR. The measured and simulated S11 values of a fabricated BAVA are shown in Figure 4.8.3 (b). It can be seen that simulated and measured S11 values have close agreement.

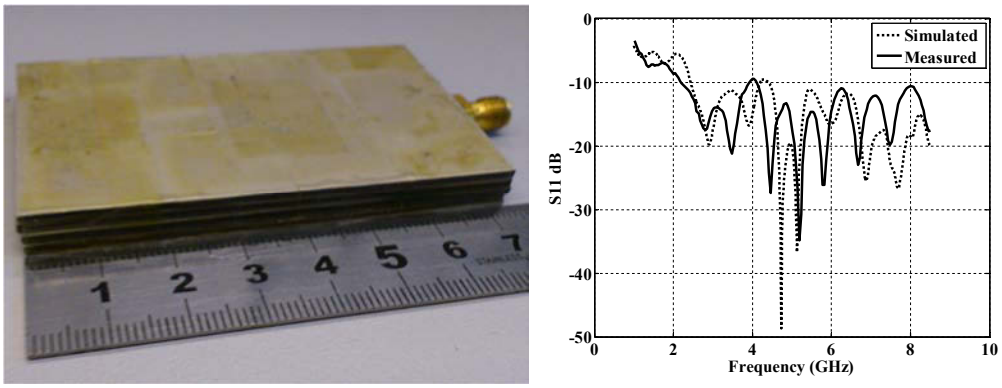

(a) (b)

Figure 4.8.3 Measurement S11 using BAVA [80](a) fabricated BAVA (b) measured S11

The comparison of S_{21} between mBAVA and BAVA was not presented, because: (a) mBAVA prototype was not fabricated as only BAHA was selected as the final antenna prototype for fabrication. (b) BAVA has larger aperture dimension thus it can cover lower frequency at about 2GHz. However, the lower frequency for mBAVA starts from 5GHz. Hence, in S21, differences can be expected. (c) from simulation, we know that BAVA would provide about 8dB higher in the magnitude of transfer function than mBAVA. The original BAVA and ridged horn antennas were fabricated because they were used to measure the backscattered signals from PEC spheres which were used for CNR extraction and compare with the CNRs extracted from spheres collected by the proposed BAHA antenna. Using this comparison, the effects of antenna on CNR extraction can be investigated. On the other hand, mBAVA and ridged horn with straight launching plane were not fabricated as they were not deemed good enough for CNR extraction based on simulations when compared to BAHA antenna. Hence, BAHA element was chosen for fabrication.

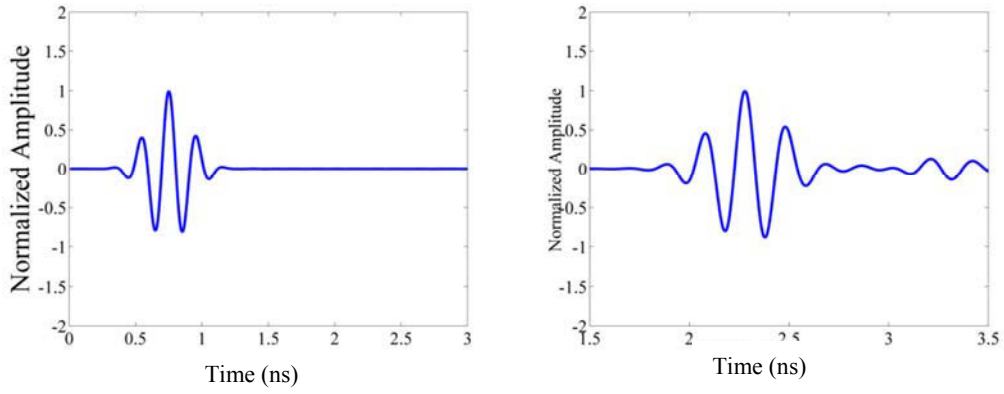

(a) (b)

Figure 4.8.4 Measured response using BAVA in coupling liquid (a) measured ideal response (b) measured received pulse at 100mm distance using BAVA

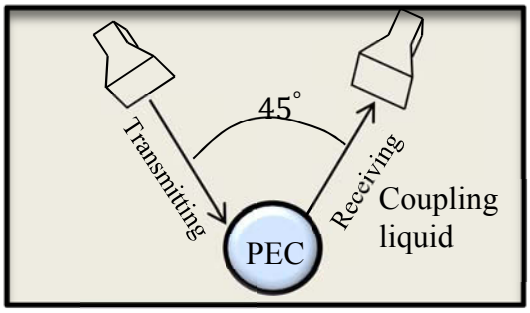

Figure 4.8.5 Measurement setup for CNR extraction from a PEC sphere in coupling liquid (dia=15.875mm)

The measured ideal and received pulses are illustrated in Figure 4.8.4. It can be observed that the radiated signal has reasonably close waveform shape with the ideal response. The measured results indicate that BAVA has high fidelity (0.98) which outperforms the TEM horn antenna. To extract the CNR from embedded PEC sphere (dia=15.875mm), two BAVA antennas are immersed in coupling liquid at an angle of 45 degrees with respect to each other and at a distance of 50mm to the immersed PEC sphere as shown in Figure 4.8.5. Olive oil is used as coupling liquid which has $\varepsilon_r = 2.5, \sigma = 0.04$ S/m.

CNRs are extracted from measured data of late-time target response obtained by subtracting target-free signal. The values of CNRs are listed in Table 4.8.2.

Table 4.8.2 CNRs of Steel Sphere (dia=15.875mm) Extracted from Measured Data using BAVA in Coupling Liquid ($\boldsymbol{\varepsilon_r = 2.5}$)

Frequency (GHz)		**Damping factor (1/ns)**	
Higher mode	**Lower mode**	**Higher mode**	**Lower mode**
6.83	3.40	-5.92	-3.99

4.8.3 Data collection using ridged pyramidal horn in measurement

Ridged pyramidal horn antenna given by [79] is fabricated for measurement to examine its effects for the extracted CNR. The fabricated ridged pyramidal horn is shown in Figure 4.8.6. The measured ideal response and observed pulse are shown in Figure 4.8.7 using the same setup in Figure 4.2.1. Olive oil is used as a coupling liquid with $\varepsilon_r = 2.5, \sigma = 0.04$ S/m. The measured fidelity is 0.965 which indicates that this antenna has small level of distortion for the radiated pulse shape. CNRs for the same PEC sphere (dia=15.875mm) are extracted and listed in Table 4.8.3.

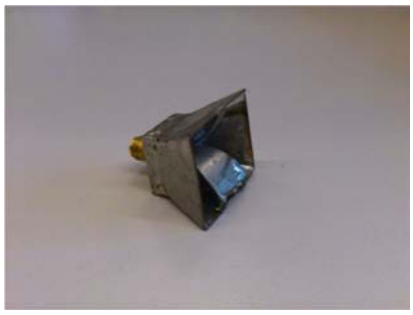

Figure 4.8.6 Fabricated ridged pyramidal horn antenna.

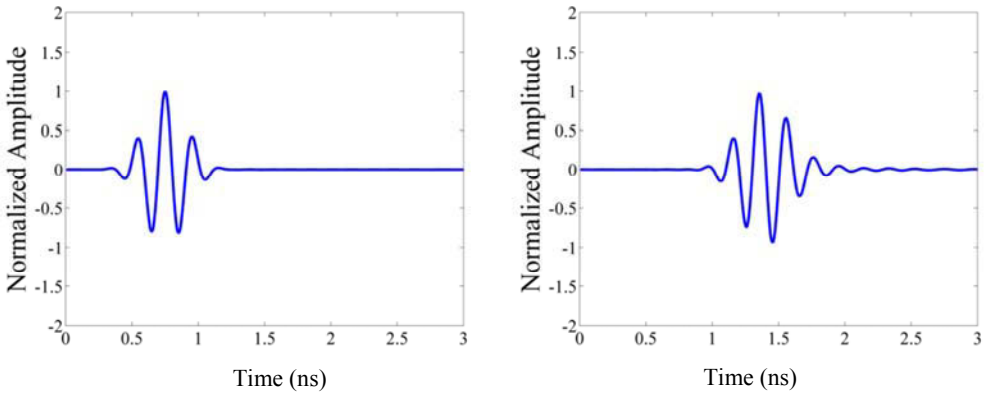

Figure 4.8.7 Measured ideal and observed responses using ridged pyramidal horn[79] in coupling liquid (a) measured ideal response (b) measured received pulse

Table 4.8.3 CNRs of Steel Sphere (dia=15.875mm) Extracted from Measured Data using Ridged Pyramidal Horn in Coupling Liquid ($\boldsymbol{\varepsilon_r = 2.5}$)

Frequency (GHz)		**Damping factor (1/ns)**	
Higher mode	**Lower mode**	**Higher mode**	**Lower mode**
6.10	3.53	-13.3	-3.88

4.8.4 Effects of antenna on extracted CNRs

Now we discuss the effects to CNRs using different antennas. Extracted CNRs using Baum's transform [125] given in (3.5) for the same PEC sphere (dia=15.875mm) are used as a reference to compare the CNRs extracted from measured data when using different antennas. The measurement of characteristics for CNR extraction using BAHA is reported in the Chapter 5. We first examine the extracted CNRs from the embedded PEC sphere in coupling medium ($\boldsymbol{\varepsilon_r = 10}$) where TEM horns are immersed. The results are shown in Figure 4.8.8. It can be seen that the CNRs extracted from simulated data using TEM horn have large discrepancy with the theoretically estimated CNRs using Baum's transform[125]. This is probably due to large pulse distortion introduced by TEM horn antenna.

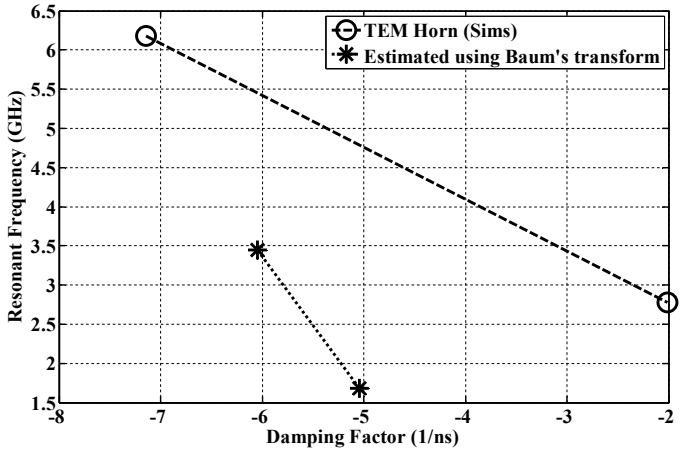

Figure 4.8.8 Extracted CNRs from simulated data for PEC sphere (dia=15.874mm) using TEM horn [81].

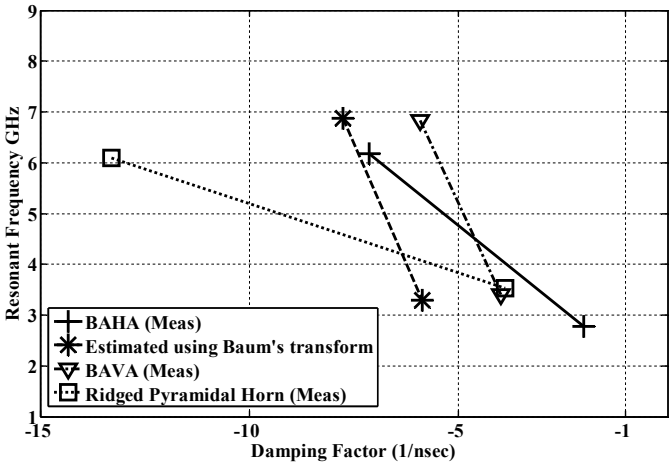

Figure 4.8.9 Extracted CNRs from measured data for PEC sphere (dia=15.874mm) using BAHA, BAVA[80], and ridged pyramidal horn[79].

Next, we compare the extracted CNRs from measured data for the same PEC sphere (dia=15.875mm) using different antennas including BAVA, ridged pyramidal horn and BAHA as shown in Figure 4.8.9. For comparison, we also plot the CNRs obtained by using Baum's transform (3.5). It can be seen from Figure 4.8.9 that BAHA gives most close value of the extracted damping factor at higher order mode compared with the

theoretically estimated value. However, at lower CNR mode, BAHA gives large bias for damping factor, as BAHA works from 4.5GHz as shown in measurement data in the earlier section. BAVA gives accurate resonant frequencies for both higher and lower mode. However, their damping factors have a large shift with reduced values. Ridged pyramidal horn gives significantly large discrepancy on damping factor values at higher CNR mode, although the extracted resonant frequencies are similar to the theoretically estimated values. As discussed in Chapter 3, damping factors are most important to differentiate CNR signatures so that the objects with different shapes can be discriminated. Therefore, estimation of accurate damping factors is critical. As discussed above, use of proposed BAHA is able to provide accurate estimation of damping factor at frequency higher than 4.5GHz. Thus, once again it is demonstrated that BAHA could be a good candidate for microwave imaging system and thus may help to discriminate breast lesions with different morphological features.

4.9 Discussion

In this chapter, three UWB antennas have been investigated for use in experimental microwave imaging for breast cancer detection. Firstly we modified ridged pyramidal horn [79]and propose a modified ridged horn with straight ridge and launching plane. Subsequently, we propose a mBAVA by using tapered flares and straight transition. Finally, we propose a novel UWB antenna called BAHA. BAHA combines an internal Vivaldi structure and an external horn. By comparing antenna characteristics between these three antennas, it appears that BAHA has superior characteristics on high fidelity and S21 and thus is selected as a candidate for microwave breast cancer imaging.

Measured results have shown that BAHA has high fidelity (>0.9) and high S21 magnitudes (-23dB) that help to radiate a low distorted UWB pulse into breast tissues. In particular, we also examine the effects of antenna for extracted CNRs using different

antennas including TEM horn[81], BAVA[80], ridged pyramidal horn [79] and BAHA. Through measurement demonstration, BAHA is superior to other antennas in terms of accurate extraction of damping factor. Therefore, we choose BAHA element for the UWB antenna array in the experimental microwave imaging system for breast cancer detection and discrimination which will be dealt in the next chapter.

Chapter 5
Experimental Investigation on CNR based Tumor Discrimination using Chemical Phantoms

5. 1 Introduction

Recently many studies have appeared that used chemical as well as numerical breast phantoms and some preclinical experiments. All have successfully demonstrated the potential of microwave imaging for breast cancer detection [27, 35, 38, 42, 45, 148, 149]. However, when employing radar based microwave imaging, still problems exist regarding the discrimination of malignant and benign breast lesions. It is desirable to have a technique that compliments the existing approaches and in addition is capable to identify whether the localized suspicious target is malignant or benign. The main factors that significantly hinder the process of identification of malignant tissues are the interferences from fibroglandular tissues in the background as well as the presence of benign lesions. Furthermore, the inhomogeneity of the breast can result in blurred

images when using existing radar based techniques. However, microwave tomography can avoid this ambiguity by reconstructing the dielectric property map [24, 107, 109, 150] so that the malignant and benign lesions can be discriminated based on dielectric properties. However, tomography can be significantly affected by severely ill-posed inverse problem, particularly in dense breasts.

The main focus of the radar based microwave imaging for breast cancer detection appears to be the identification of the suspicious tumor location. This is because the energy-based detection methods employed by almost every researcher that worked on microwave imaging for breast cancer detection can only identify the strong scatterers, but cannot discriminate whether the identified scatterer is malignant or benign. Li has reported the first experimental work using 3D beamforming on low dielectric contrast (1.5:1) breast phantom [35]. Klemm et al have presented fast ultrawideband (UWB) imaging system to accurately collect data for imaging [17, 42, 44, 45]. Others, e.g., Amineh et al [81] reported a new TEM horn antenna with high coupling efficiency and directivity to raster scan the breast. A preclinical prototype has been reported in [151] for thermal therapy using time-reversal to focus the possible tumor location. However, these imaging systems have not addressed the discrimination of breast tissues based on their microwave signatures so that microwave imaging can be truly useful for clinical diagnosis of early stage breast cancer.

To discriminate whether the breast tissue is malignant or benign, electromagnetic properties related to tumor shape and material have been explored using radar cross section (RCS) and complex natural resonances [97, 98]. The surface geometry of the dielectric lesion influences the external mode of CNR which was investigated for detecting the tissue [99, 100]. Notably, most of the analyses to distinguish morphological features of tumor lesions that are reported in literatures are based on 2D

numerical phantoms [72, 99, 152]. Further, so far no studies are reported on measuring the external mode CNRs of the embedded dielectric targets in a lossy medium.

In this chapter, we report experimental investigations for distinguishing of morphological features of breast tumors using complex natural resonances (CNRs) using breast tissue mimicking chemical phantoms. The proposed method combines the radar based microwave imaging technique for detecting the suspicious locations and CNR identification for discriminating the features of the embedded dielectric targets. The experimental setup employs a UWB array that uses with 32 BAHA antennas which have been addressed in chapter 4. The proposed experimental imaging system is used to collect time domain backscattered data so that the image of suspicious region within the breast phantom is reconstructed. Next we use the proposed two-stage waveform estimation from the suspicious region to recover the resonant signal for the calculation of complex natural resonances. The CNRs are calculated using matrix pencil method[119]. For the experiments, we employ two types of targets: a 12 mm-diameter dielectric inserts (made of chemicals) that have irregular border profiles to mimic the malignant lesions and an approximately spherical dielectric body with smooth profile to mimic benign lesions. The existence of differences on tumor morphologies has been well established by MRI and X-ray images [4, 84-86]. These dielectric inserts are embedded in both homogeneous and inhomogeneous tissue mimicking chemical phantoms. The CNRs have been extracted for both irregular shaped as well as smooth shaped dielectric insertions so as to investigate their relationship with the morphological features so that they can be used for discriminating the breast tumors. The resonant frequency-time plane effectively localizes the late-time resonant response to help CNR extraction. Further, a two-step calibration procedure for the extracted CNR is employed to reject spurious CNRs from nonresonant signals. Moreover, normalized CNR error (NCR) also helps to evaluate the morphological differences between the malignant and benign tumors. It has been demonstrated that the proposed experimental microwave

imaging system that employs 32 BAHA antenna elements has potential to: (a). localize the suspicious region in breast phantoms with high dielectric and low dielectric contrast; (b). distinguish malignant and benign tumors based on the extracted CNR signatures.

5. 2 Tissue Mimicking Chemical Breast Phantoms

5.2.1 Inhomogeneous chemical breast phantom

Use of tissue mimicking chemical phantoms have been reported by numerous research groups for making microwave measurements [40, 45, 58, 59, 61, 153-155]. We made oil-gelatin tissue mimicking phantoms [58, 59]. Figure 5.2.1 shows our phantom fabrication system. First, we have developed our own mold to fabricate the hemispherical shaped breast phantom in which we have developed arbitrary shaped tissue mimicking glandular tissues. Our hemispherical mold has radius of 70mm which is made of nylon to support the phantom. In addition, it can also be used to mold a nipple of 1cm size. On our fabrication process, skin layer was firstly molded and let it solidified for 2 days. Later, the fabrication of fatty and glandular tissues was made. The procedures are shown in Figure 5.2.2. Skin layer has approximate thickness from 2 to 4mm as shown in Figure 5.2.3(a) which was fabricated by pouring the skin mimicking chemical material into the gap between nylon mold and inner hemispherical wheat flour mold. Figure 5.2.3 (b) and (c) illustrates patterns of glandular tissues which are surrounded by fatty tissues. A 1cm nipple can be seen in Figure 5.2.3(d). The dielectric properties of fabricated tissues at 6GHz are listed in Table 5.2.1.

Table 5.2.1 Dielectric Properties of Tissue Mimicking Chemical Phantom at 6GHz

Tissue Type	**Dielectric Property**
Skin	$\varepsilon_r = 30, \sigma = 5$
Fatty tissue	$\varepsilon_r = 11, \sigma = 1.5$
Glandular tissue	$\varepsilon_r = 26, \sigma = 4$
Tumor	$\varepsilon_r = 45, \sigma = 7$

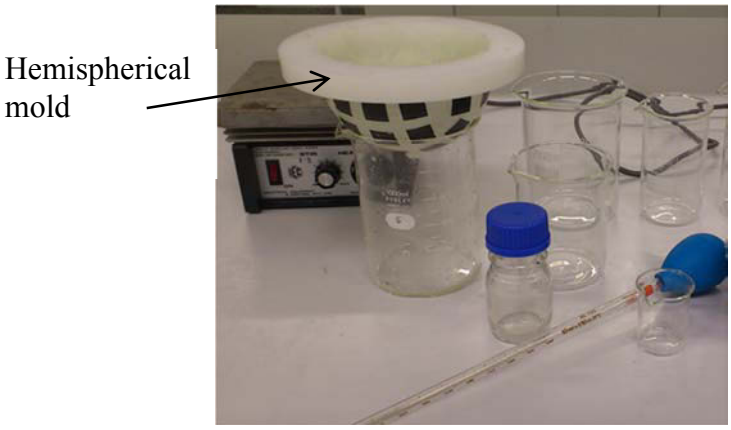

Figure 5.2.1 Methods employed for phantom fabrication

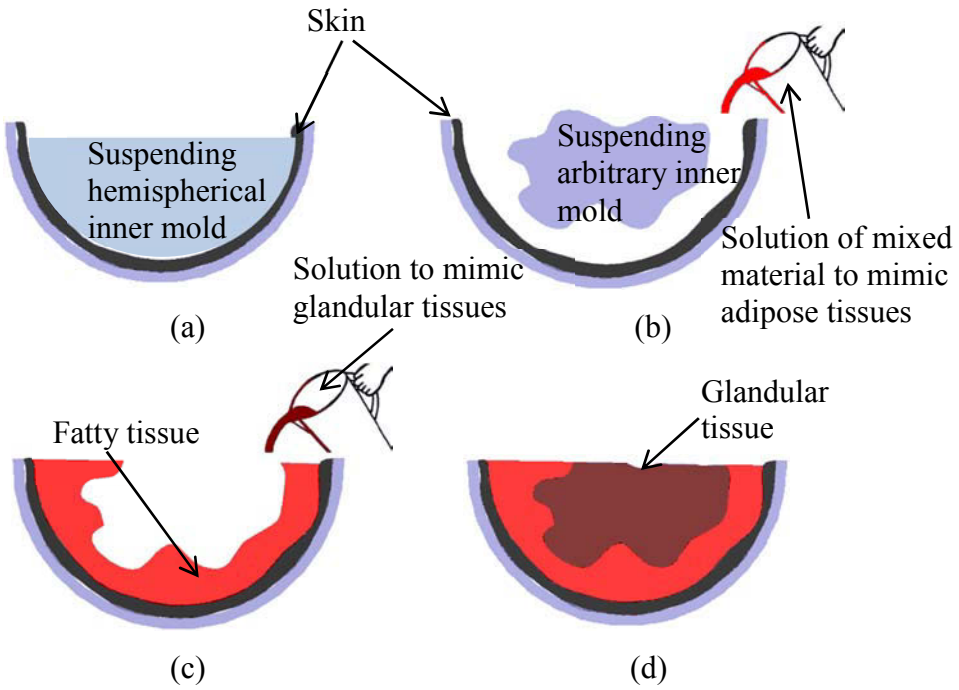

Figure 5.2.2 Procedures employed to make tissue mimicking heterogeneous breast phantom. (a) suspending hemispherical inner wheat flour mold to make skin layer (b) filling fatty tissue mimicking material into wheat flour mold (c) fill glandular tissue mimicking material (d) resultant multilayer heterogeneous breast phantom

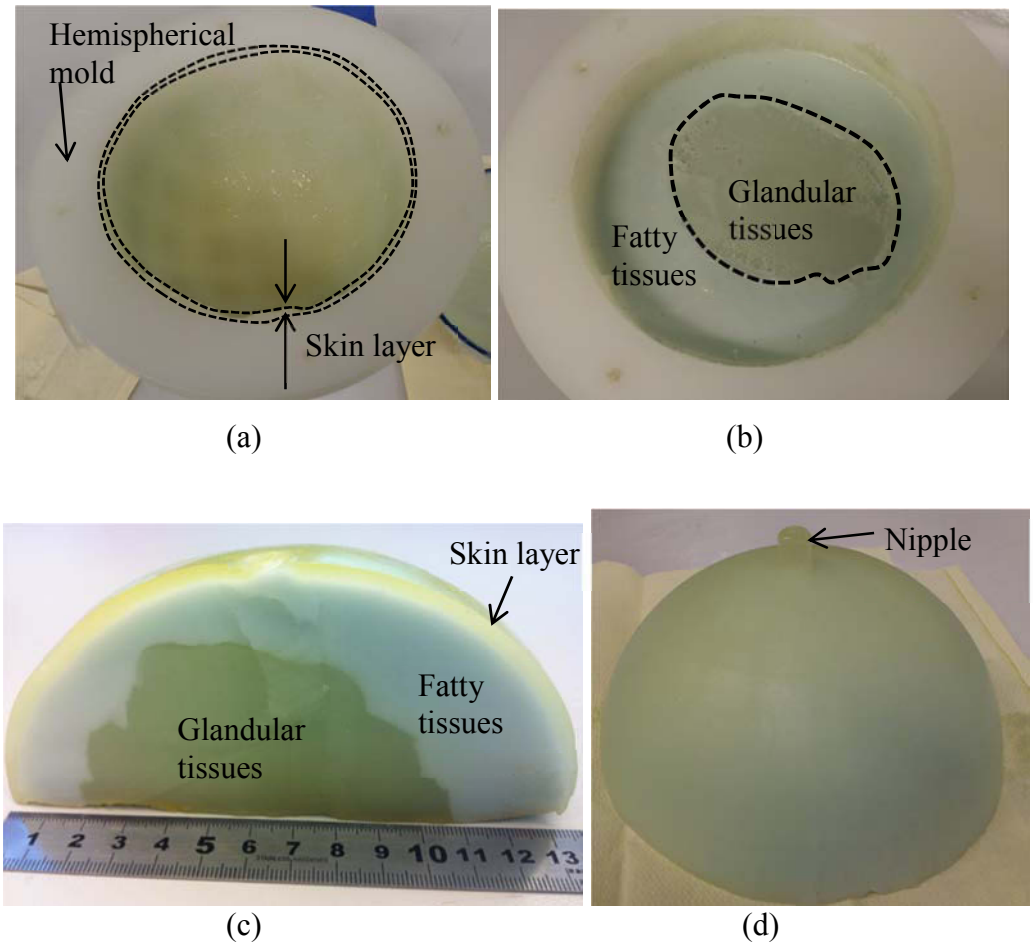

Figure 5.2.3 Fabricated inhomogeneous breast phantom. (a) skin layer (b) bottom view (c) cross section of inhomogeneous phantom (d) side view

5.2.2 Smooth and spiculated dielectric inserts

A number of dielectric inserts have been fabricated as shown in Figure 5.2.4 including spiculated and smooth oil-gelatin inserts to mimic malignant and benign tumors respectively. These dielectric inserts have the same dielectric properties as shown in Table 5.2.1 to mimic breast tumors. Spiculated inserts (Figure 5.2.4 (a)) are fabricated following the method described in [130] that a number of random spicules

are mounted on a central smooth base. On the other hand, smooth inserts are made so that they have no sharp transitions on surface (Figure 5.2.4 (b)). Both spiculated and smooth inserts have average diameter of approximately 12mm.

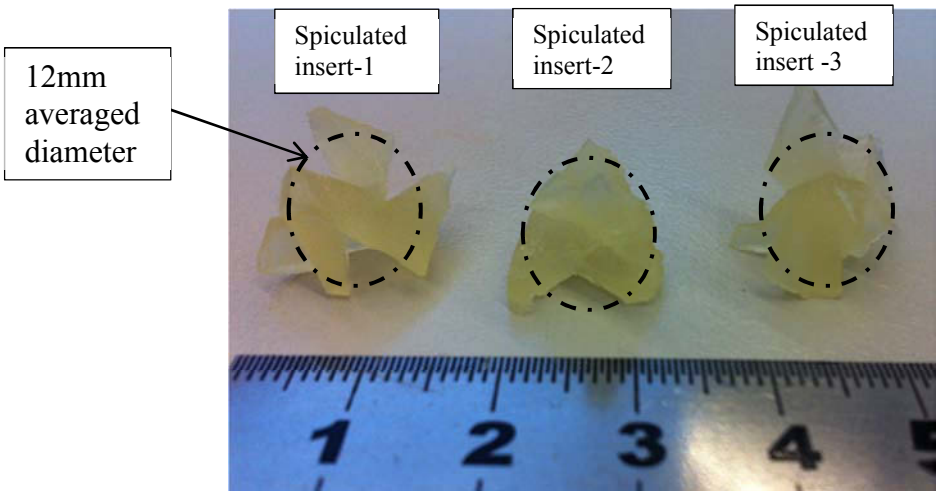

(a)

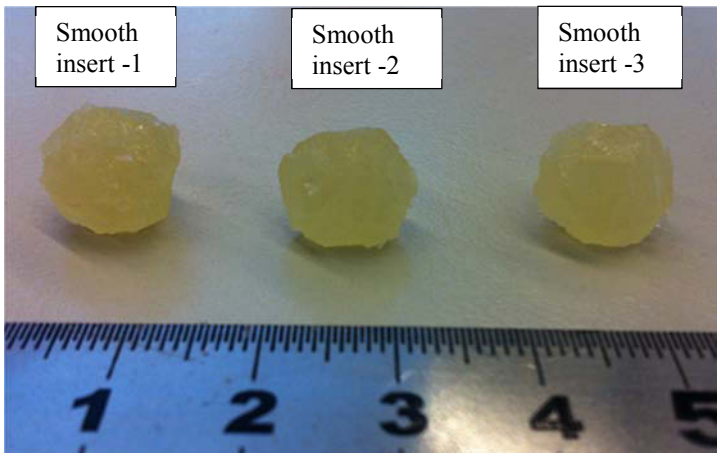

(b)

Figure 5.2.4 Fabricated oil-gelatin dielectric inserts to mimic breast lesions (a) spiculated inserts (b) smooth inserts

5.3 Development of microwave imaging system using hemispherical antenna array of 32 BAHA elements

We have developed a UWB multistatic experimental microwave imaging system that employs 32 BAHA elements. BAHA was proposed in Chapter 4 and it was also demonstrated that it offers superior performance. Since BAHA is compact in size, it is useful to form a compact but large array placed surrounding the breast. 32 BAHA antenna elements form a hemispherical array and antennas are held by a plastic holder as shown in Figure 5.3.1. This hemispherical array is formed of three circular rings: the top and middle rings have 12 BAHA elements; lower ring has 8 BAHA elements. Figure 5.3.1 (a) and (b) also show different views of the antenna array and Figure 5.3.1 (c) zoom the antenna element. All the antennas are made to radiate towards the centre of the phantom so that more phantom area can be covered.

5.3.1 Measured data acquisition

The UWB microwave imaging system using BAHA array is used with vector network analyzer (VNA HP8510C) for experimental investigations as shown in Figure 5.3.2. Short-open-load-through (SOLT) calibration on VNA is conducted for 2-ports calibration at the measurement planes using low loss coaxial cables from 50MHz to 15GHz. After calibration, the two ports of the VNA and S-parameter test set (Agilent 8517B) are connected to the BAHA array for the measurement of the breast mimicking chemical phantom. The UWB pulse for radiation is synthetically generated [44, 94]. Firstly, frequency domain transmission measurement is conducted by sweeping signals using VNA from 1GHz to 10GHz with 1600 frequency samples. After both the two-port complex S parameters were measured over the frequency band, the time domain response was then obtained by taking the inverse Fourier transform. The 1600

frequency samples are over 3 times more than the measured samples reported in [126] and thus we deem they are sufficient for CNR measurement. The phantom and BAHA array are both immersed in a coupling liquid (normal olive oil). We have manually switched the connection from transmitting and receiving antennas to VNA to obtain multistatic configuration. Transmitting antenna is excited with input signal up to 10GHz and the scattered fields collected by different receiving antennas are recorded by VNA. Not all antennas are used to receive the backscattered signals in the measurement, eliminating those antennas that only receive very low levels of signal amplitudes. We use the method described in [44], where only antennas that can see the transmitting antenna are selected to receive the backscattered signals. For our measurement setup, five antenna elements that have closet positions to transmitting antenna are selected to record the measured data. Thus, the recorded raw data can be represented by: $E_{i,j}(t)$,($i = 1, \cdots, 32$ is the index of transmitting antenna), $j = 1, \cdots, 5$ (j is the index of receiving antenna). Pulses from other antennas will be eliminated based on their received low amplitudes due to backscattered signals. Hence, the total recorded raw data only have $M = 32 \times 5 = 160$ pulses instead of the full multistatic configuration having 992 pulses from 32 antennas.

Early-time content including antenna excitation and skin reflected artifacts are removed using a simple procedure that was suggested by Klemm et al [42] in which the measured raw data was removed by mechanically rotating the array. As there are 32 elements positioned in the array, mutual coupling can be present between antenna elements. The mutual coupling of antennas can be suppressed in the pre-processing. In pre-processing recorded signals subtracted with similar level of signal magnitude in early-time, which will remove the unwanted signal contents including mutual coupling. In addition, antennas with focused beam such as BAHA antenna can avoid the mutual coupling between adjacent positioned antennas. In practical measurements,

mechanically array rotation also will suppress the mutual coupling between antennas. In reports [43], antenna elements are increased up to 60 and array rotation can still effectively suppress the mutual coupling effects.

Only a small rotation about 10 degrees was used. After the rotation, a twin-signal $\tilde{E}_{i,j}(t)$ (after IFFT) was recorded. Thus, another group of pulses having $M = 32 \times 5 = 160$ are recorded as the twin signals, which are used for calibration. Now the artifact-removed calibrated signal was obtained using:

$$x_{i,j}(t) = E_{i,j}(t) - \tilde{E}_{i,j}(t), \;\; i = 1, \cdots, 32, \;\; j = 1, \cdots, 5 \tag{5. 1}$$

A sample of the time-domain received pulse obtained from measured data is shown in Figure 5.3.3(a). The twin signal obtained by mechanically rotating the array by a small angle (10 degree) is also shown as dotted line in Figure 5.3.3(a). It can be seen that twin signals have similar levels of amplitudes of early-time signals, since skin reflections do not differ at small angular separation. Then, target response can be obtained using (5.1) to remove the early-time contents as much as possible which are plotted in Figure 5.3.3(b). This calibrated signal is then processed using time-shift and time-window processing given by (2.2)-(2.4) and later processed by MWDAS algorithm given by (2.8)-(2.11) proposed in Chapter 2, to form the image for the suspicious region for embedded dielectric insert (lesion).

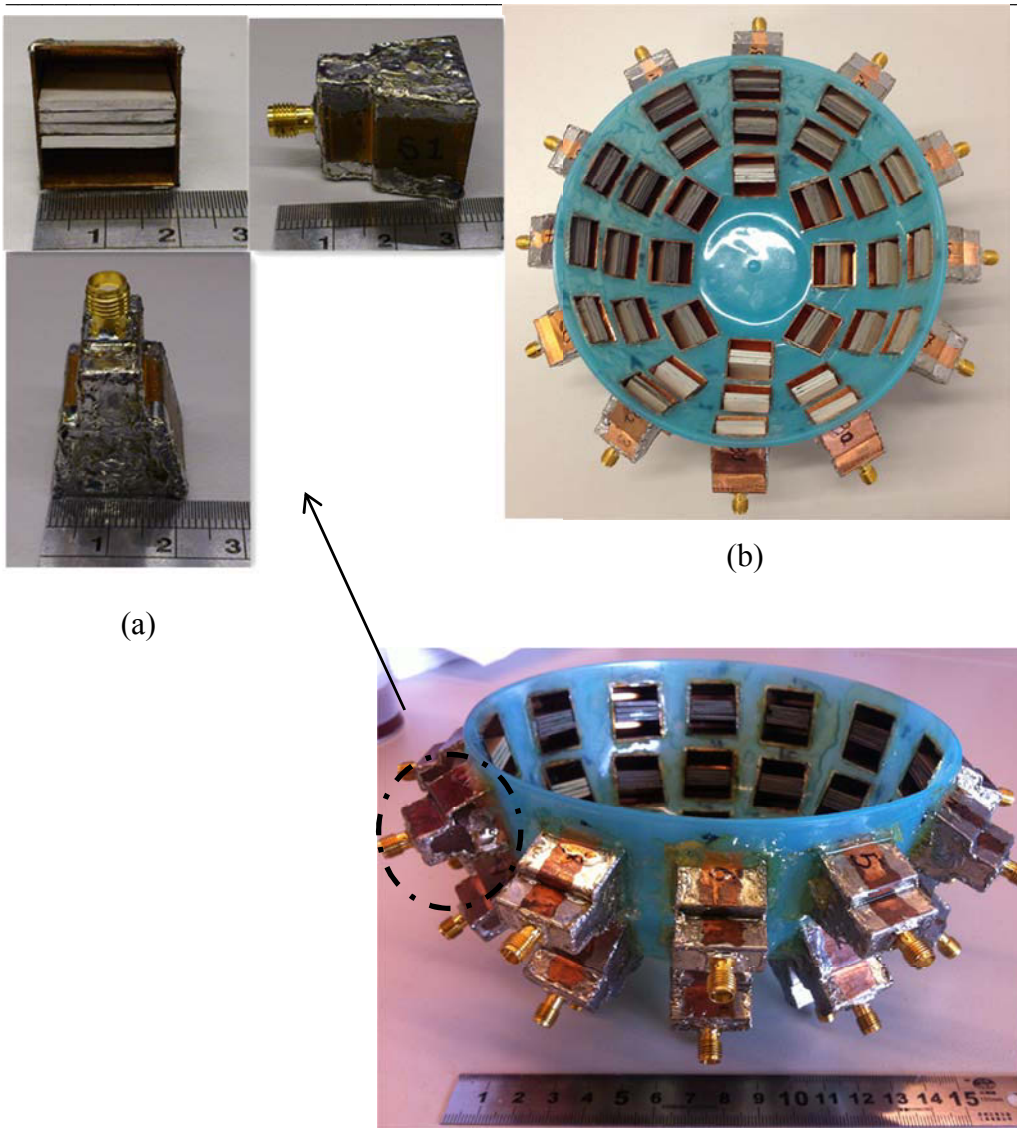

(a)

(b)

(c)

Figure 5.3.1 Hemispherical UWB array with 32 proposed BAHA antennas. (a) zoomed view of individual BAHA element (b) top view of the array held by the plastic holder (c) side view

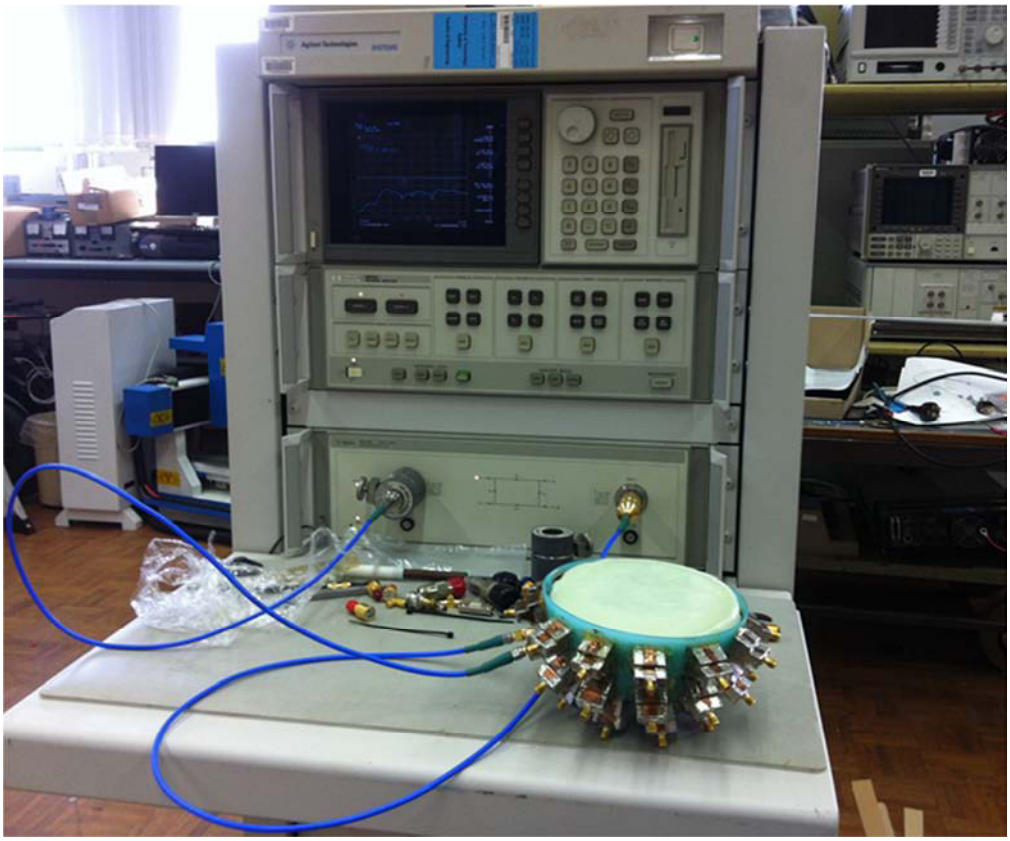

Figure 5.3.2 Experimental microwave imaging system for breast cancer detection and discrimination

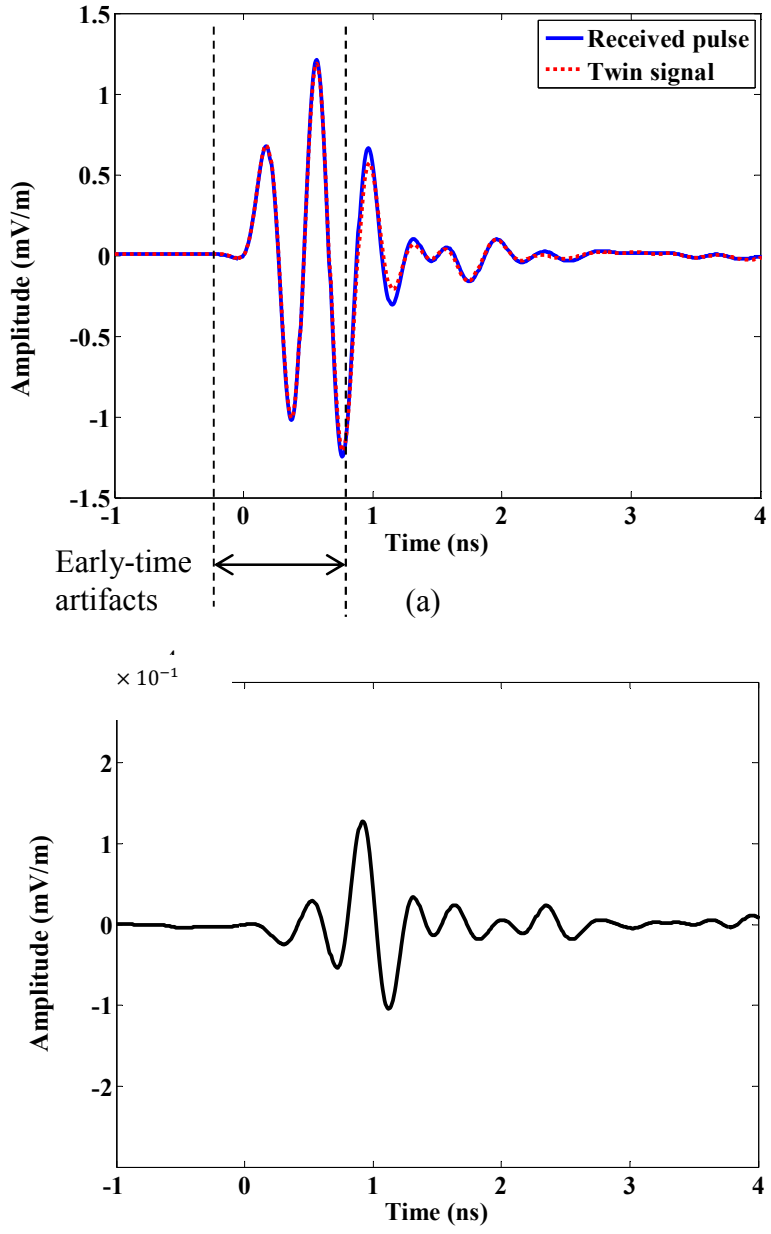

Figure 5.3.3 Measured pulse and its twin signal (a) time-domain pulse obtained from measured data and its twin signal obtained by a small angle rotation(b) late-time response obtained after subtraction of the early-time contents shown in(a)

It is worth noting that the pair-matching preprocessing using RMSE given by (3.6) proposed in Chapter 3 is not used here in our experiments. Instead, we employ a simple mechanical array rotation [42] to remove early-time contents. The reason is that RMSE based pair-matching requires a large number of antenna elements and will be highly suitable for heterogeneously dense breast phantom such as C3 or C4 phantoms. Usually, a large number of antenna elements (>90) may be required to form the RMSE matrix, but due to the hardware, fabrication and switching limitation, we employed only 32 antenna elements and used manual switching for preliminary experiments reported here.

5.4 Breast imaging in homogeneous and inhomogeneous breast mimicking chemical phantoms

5.4.1 TOA autocalibration based on measured data

Time-of-arrival (TOA) autocalibration is conducted based on the measured raw data that contain antenna excitations. Knowing the actual antenna positions, the TOA compensation factor μ, using (3.11)-(3.15) as described in Chapter 3 was optimized by estimating the locations of the transmitting antenna so that we can match the estimated known positions. The antenna positions which are estimated by optimizing the TOA compensation factor are plotted in Figure 5.4.1. From Figure 5.4.1, it can be observed that the estimated positions fit well with the known true locations of transmitting antennas at (0, -72, -20)mm, (55, 0, -45)mm, (0, 72, -20)mm, and (-55, 0, -45)mm. This guarantees that the TOAs are properly calibrated which ensures the accuracy of tumor reconstruction process. In particular, we will demonstrate the TOA autocalibration as proposed in Chapter 3 by reconstructing the suspicious region for both homogeneous and inhomogeneous tissue mimicking chemical breast phantoms.

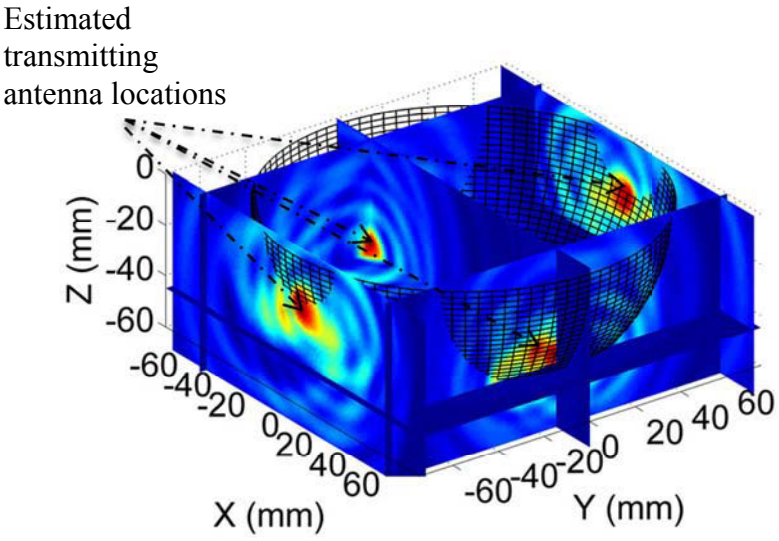

Figure 5.4.1 Estimated antenna positions for TOA autocalibration based on measured data.

5.4.2 Reconstructed image in homogeneous breast phantom with large amounts of adipose tissue equivalents

In this case, we embedded a 12mm smooth shaped dielectric insert (tumor) in homogeneous phantom that was filled with large amounts of adipose breast tissue equivalents and having tumor-to-background dielectric contrast of 4:1. This smooth dielectric insert is embedded at location (30, 0, -10)mm inside the breast phantom. Each antenna in the experimental imaging system is excited to radiate microwave signal using the frequency sweep facility offered by VNA with bandwidth up to 6.5GHz. The magnitudes of recorded S21 by VNA are shown in Figure 5.4.2 (a) and the IFFT transformed time-domain pulses $E_{i,j}(t)$ and its twin signals $\tilde{E}_{i,j}(t)$are plotted in Figure 5.4.2(b).

The measured results in Figure 5.4.2, Figure.5.4.5, and Figure 5.4.7 showed multiple recorded frequency domain results. The jitter noise came in the results when the received antenna is separated at large separation from the transmitting antenna. As the BAHA produces relatively focused radiation, a large angular distance will result in low fidelity. Hence, jitter noise may appear in the recorded result. The dynamic range of transmission measurement of the VNA is 106dB and the maximum power at the port is 11dBm. Thus, any signal up to -90dB of magnitude has can be measured without much problem.

The reconstructed 3D tumor image using simple data-independent delay-and-sum (DAS) (2.6) is shown in Figure 5.4.3 (a). It can be observed that the 12mm smooth dielectric insert is successfully localized (white arrow) with high resolution. Due to the dominant content of high adipose tissue equivalents (dielectric properties listed in Table 5.2.1) and the phantom homogeneity, the effect of clutter interference is very small, and hence accurate localization could be achieved. Another 2D view using DAS is also shown in Figure 5.4.3 (b). On the other hand, proposed MWDAS (2.11) as described in Chapter 2 further improves the resolution of the suspicious region of embedded dielectric insert as shown in Figure 5.4.3(c). Signal-to-clutter ratio (SCR) (3.37) is defined by the ratio between the energy of the strongest response from tumor to the strongest response from clutter within the breast [42]. Here, SCR for image of 12mm smooth dielectric insert inside homogeneous phantom using DAS and MWDAS is 1.65dB and 2.75dB respectively at a SNR level of 15dB.

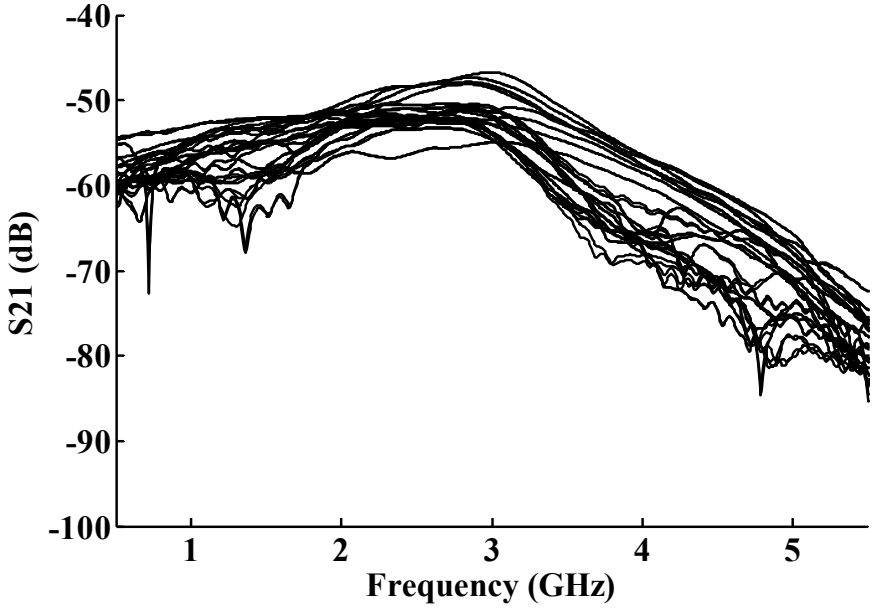

(a)

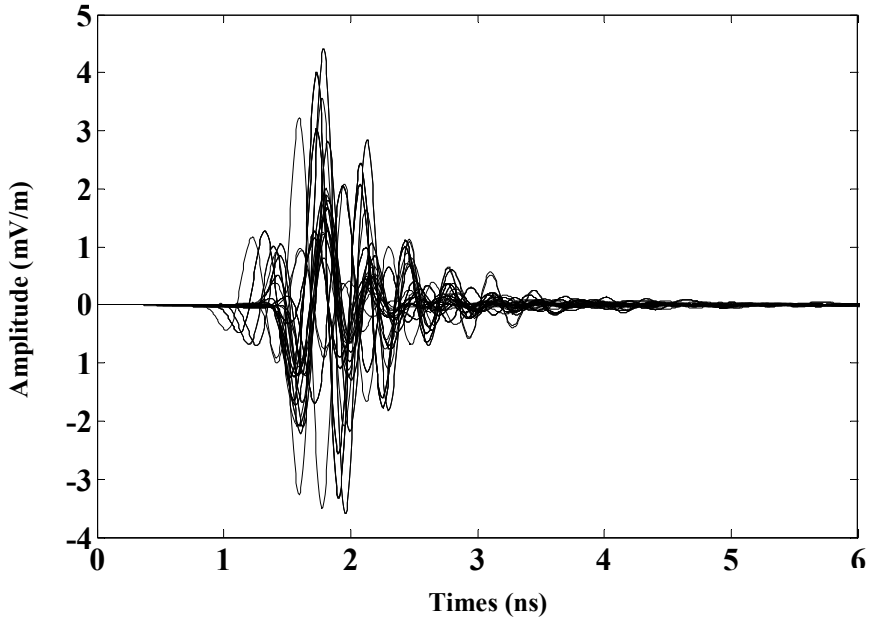

(b)

Figure 5.4.2 Recorded data from UWB BAHA array for homogeneous breast phantom. (a) magnitudes of S21 (b) transformed time-domain pulses by iFFT

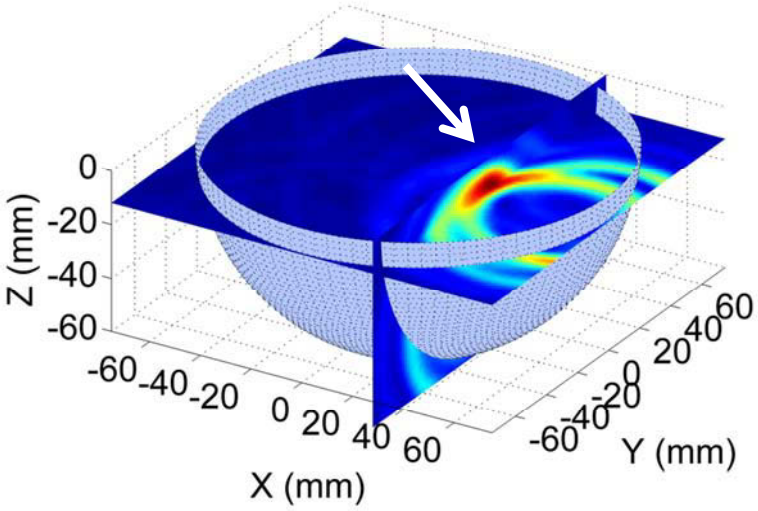
0
-20
-40
-60
Z (mm)
-60 -40 -20 0 20 40 60
X (mm)
60 40 20 0 -20 -40 -60
Y (mm)

(a)

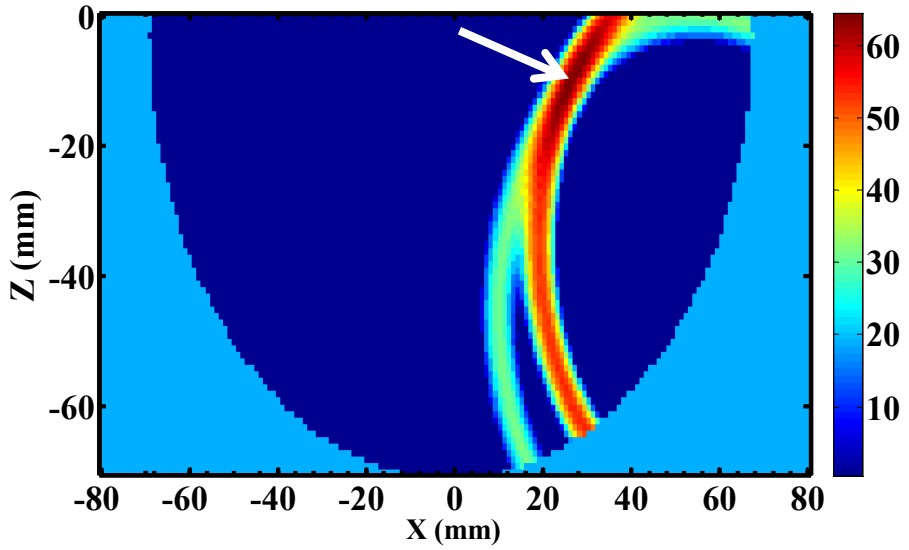
0
-20
-40
-60
Z (mm)
-80 -60 -40 -20 0 20 40 60 80
X (mm)
60
50
40
30
20
10

(b)

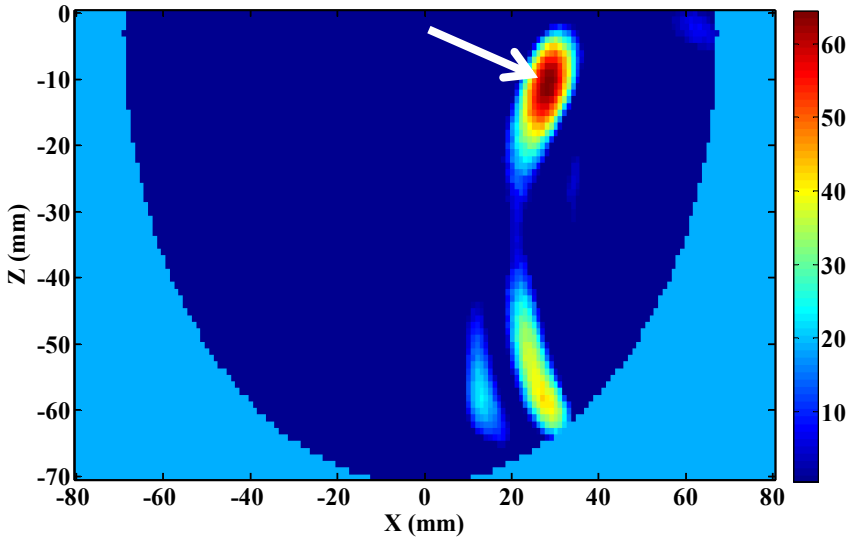

(c)

Figure 5.4.3 Reconstructed tumor image in homogeneous phantom (a) 3D image of 12mm smooth lesion at (30, 0, -10)mm (b) 2D view using DAS (c) 2D view using MWDAS

5.4.3 Reconstructed image in inhomogeneous breast phantom containing dense tissues

In this case, we embedded the same smooth shaped dielectric insert in inhomogeneous breast phantom. The inhomogeneous breast phantom contains dense fibroglandular tissue equivalents. The smooth insert is embedded inside the region where dense fibroglandular tissues are present at the position-1: (20, 0, -20) mm marked as a 'black circle' symbol in Figure 5.4.4. The dielectric contrast in this case between tumor to breast medium is 1.7:1 at 6GHz. Time-domain signals are obtained by using the frequency sweep from 50MHz to 8GHz employing VNA. The recorded magnitudes of S21 values are shown in Figure 5.4.5 (a) and transformed time-domain pulses are plotted in Figure 5.4.5 (b).

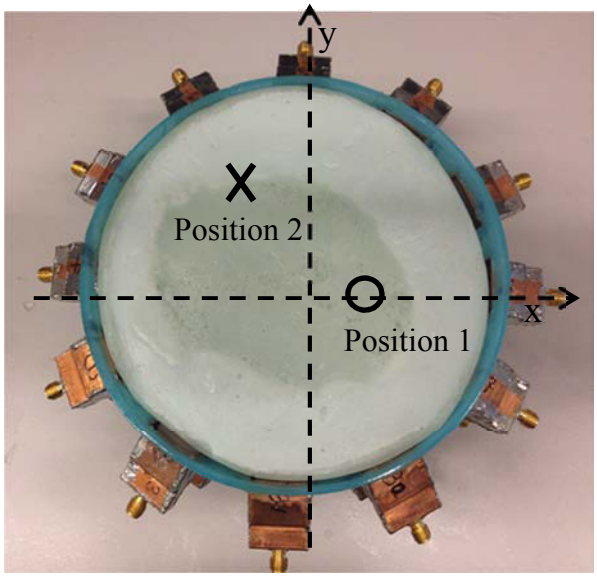

Figure 5.4.4 Inhomogeneous breast phantom with fibroglandular tissue content. Position-1: (20, 0, -20)mm marked by black circle. Position-2: (-20, 36, -20)mm marked by black cross.

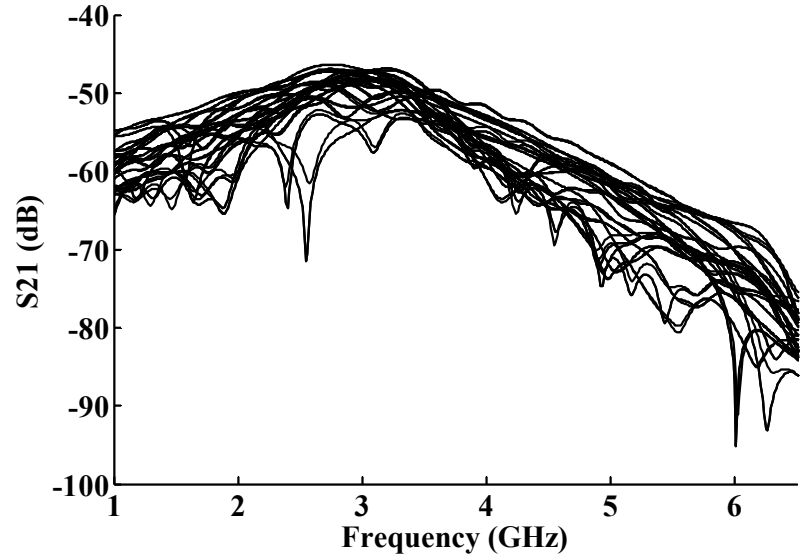

(a)

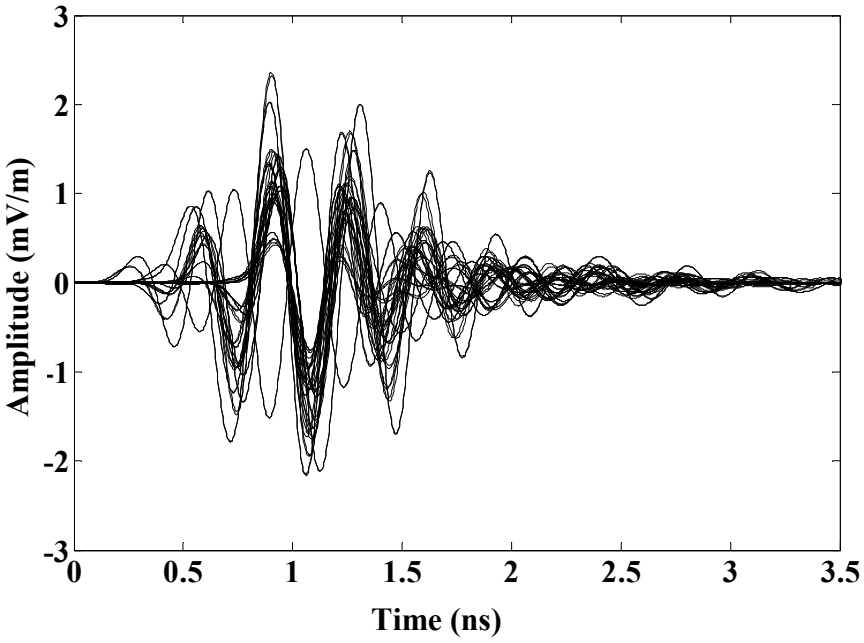

(b)

Figure 5.4.5 Recorded data when dielectric insert is embedded in position-1 in a inhomogeneous breast phantom. (a) magnitudes of S21 (b) transformed time-domain pulses by iFFT

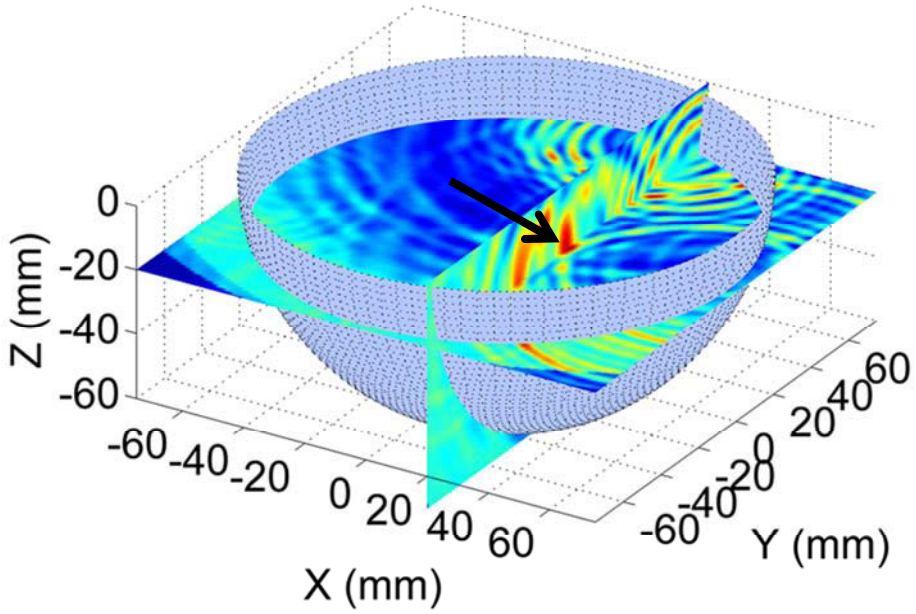
0
-20
-40
-60
Z (mm)
-60
-40
-20
0
20
40
60
X (mm)
60
40
20
0
-20
-40
-60
Y (mm)

(a)

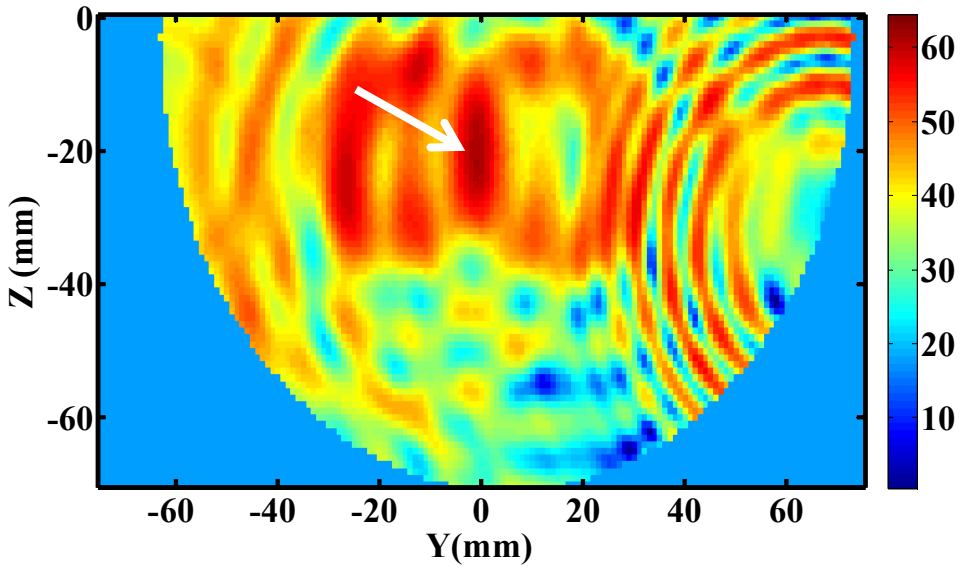
0
-20
-40
-60
Z (mm)
-60
-40
-20
0
20
40
60
Y(mm)
60
50
40
30
20
10

(b)

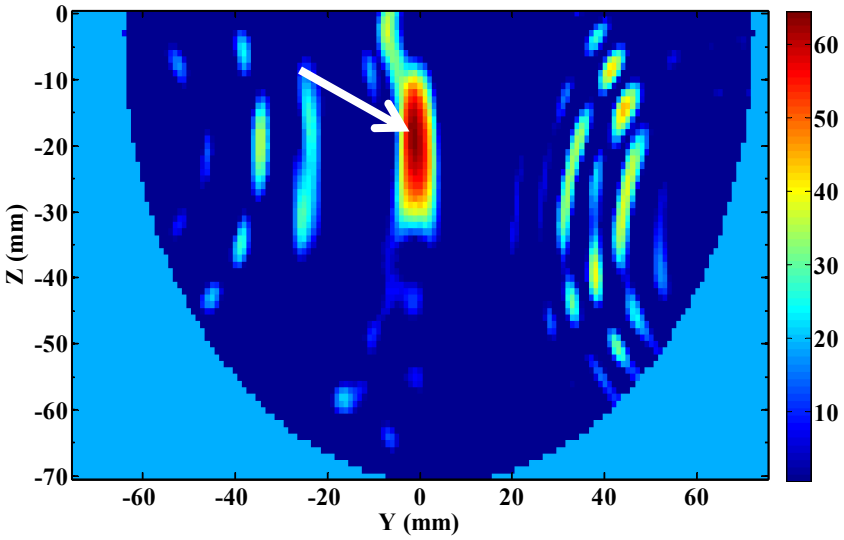

(c)

Figure 5.4.6 Reconstructed suspicious region when dielectric insert is placed in position-1 in inhomogeneous phantom (a) 3D image of 12mm smooth dielectric insert at (20, 0, -20)mm (b) 2D view using DAS (c) 2D view using MWDAS

Tumor (suspicious region) is reconstructed (arrow) using DAS (2.6) as shown in 3D view of Figure 5.4.6 (a) and in 2D view is also plotted in Figure 5.4.6 (b). As expected, DAS cannot perform satisfactory and more clutters appear in the reconstructed image due to the high dielectric properties of fibroglandular tissues (Table 5.2.1) and breast inhomogeneity. This can be improved by our proposed MWDAS which reconstructs the embedded dielectric insert accurately as shown in Figure 5.4.6 (c). It can be seen that MWDAS improves the quality of suspicious region of embedded insert (white colour arrow) and suppress the clutter effects significantly. SCR obtained for image obtained using DAS and MWDAS is 0.38dB and 1.58dB respectively for the same embedded insert.

To test the robustness of the experimental microwave imaging system, the smooth tumor mimicking dielectric insert is also placed at a location where transition between glandular and fatty tissues occur at position-2 (-20, 36, -20) mm which is marked as black cross symbol in Figure 5.4.4. Measured magnitudes of S21 are recorded using VNA from 50MHz to 8GHz as illustrated in Figure 5.4.7 (a) and the inverse Fourier transformed time-domain pulses are plotted in Figure 5.4.7 (b).

The reconstructed 3D suspicious region of embedded dielectric insert (arrow) using DAS is shown in Figure 5.4.8 (a) and its 2D view is plotted in Figure 5.4.8 (b). Further, reconstructed suspicious location using MWDAS is shown in Figure 5.4.8 (c). It can be clearly seen that MWDAS improves DAS significantly with higher resolution and locates the suspicious location accurately (white colour arrow). These images have shown that the location of embedded dielectric insert is accurately imaged despite its position inside the inhomogeneous phantom.

Signal-to-clutter ratio (SCR) for image of the embedded dielectric insert using DAS and MWDAS inside inhomogeneous breast phantom at position-2 is 2.21dB and 2.60dB respectively at SNR level of 15dB. The results of SCR for homogeneous and inhomogeneous phantoms are also tabulated in Table 5.4.1.

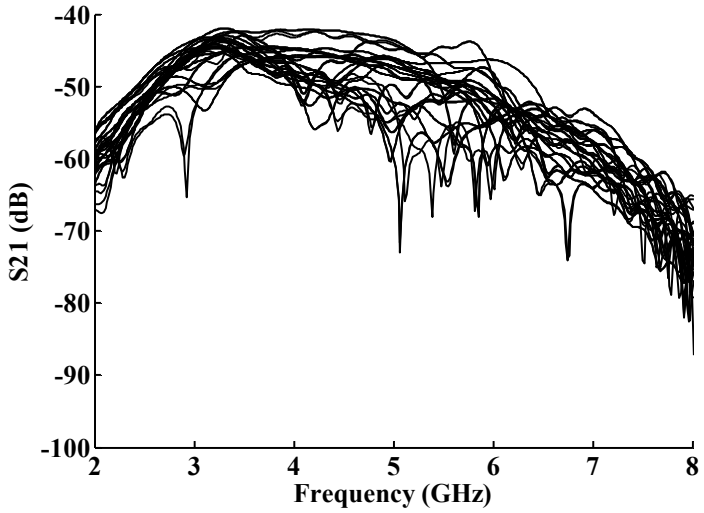

(a)

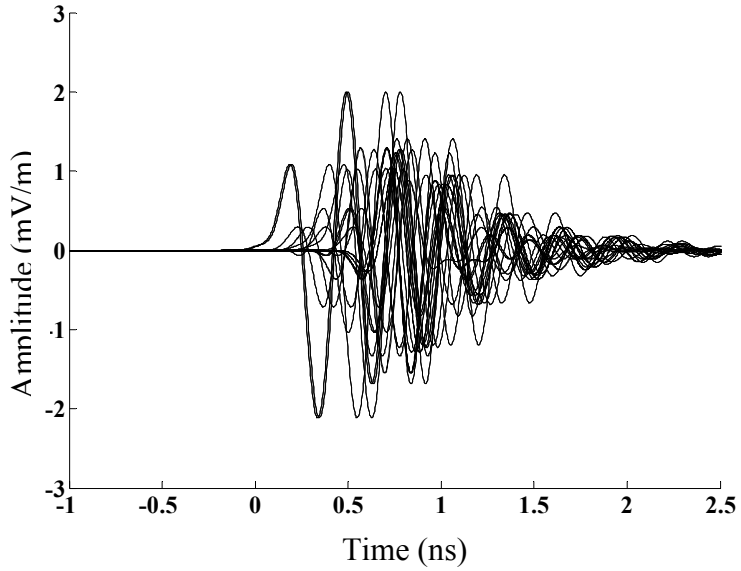

(b)

Figure 5.4.7 Recorded data when dielectric insert is embedded in position-2 in a inhomogeneous breast phantom shown in Figure 5.4.4. (a) magnitudes of S21 (b) transformed time-domain pulses by iFFT

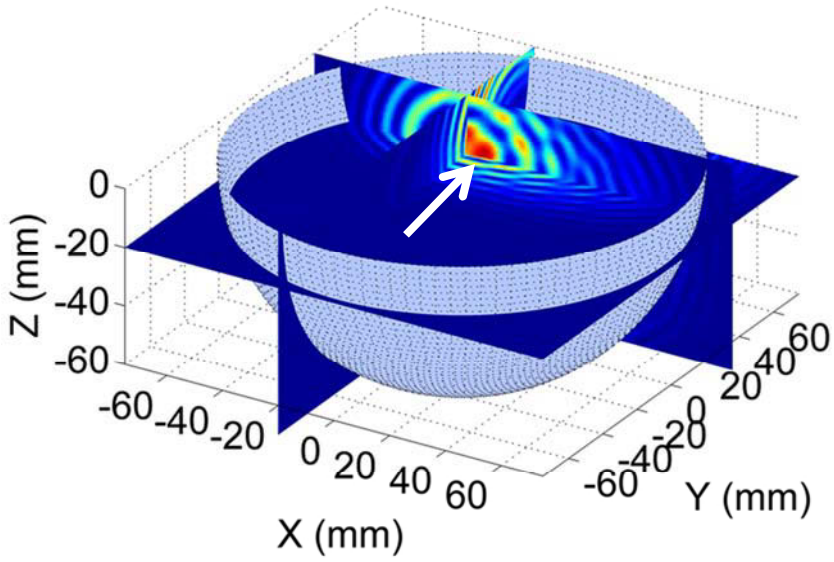
0
-20
-40
-60
Z (mm)
-60 -40 -20 0 20 40 60
X (mm)
60 40 20 0 -20 -40 -60
Y (mm)

(a)

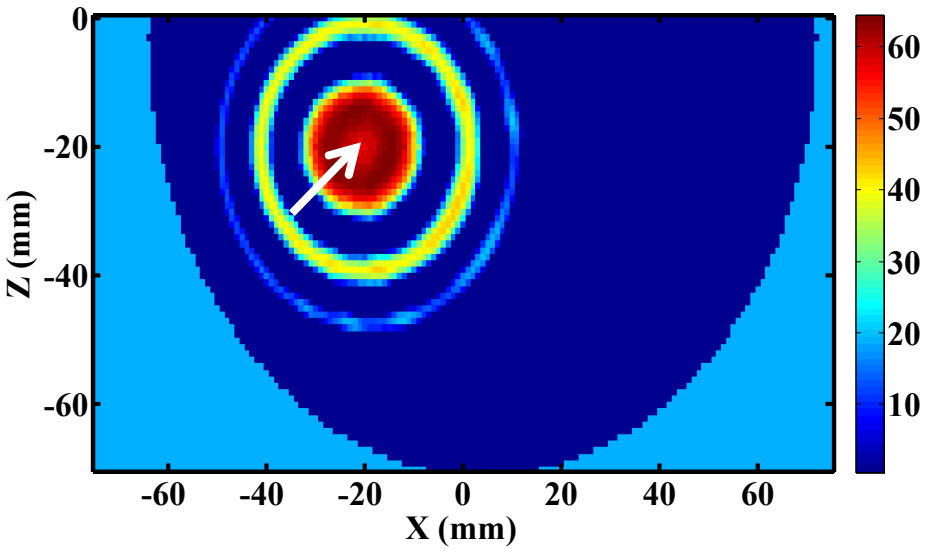
0
-20
-40
-60
Z (mm)
-60 -40 -20 0 20 40 60
X (mm)
60
50
40
30
20
10

(b)

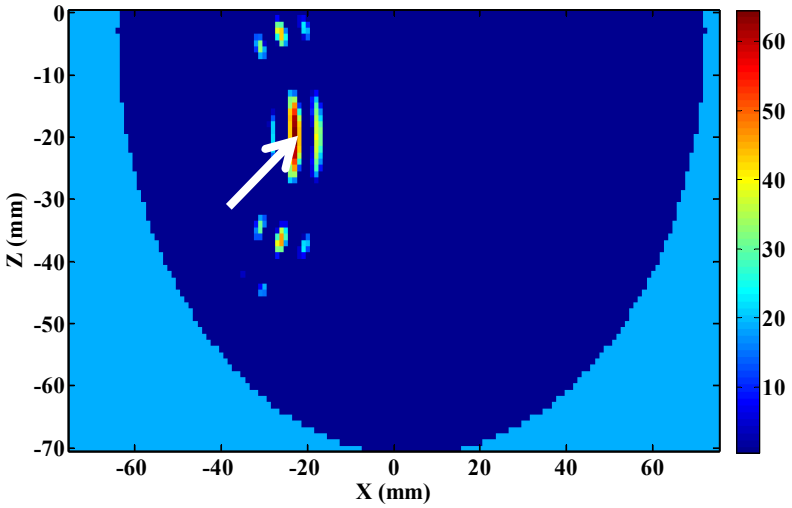

(c)

Figure 5.4.8 Reconstructed suspicious region when dielectric insert is placed in position-2 in inhomogeneous phantom (a) 3D image of 12mm smooth dielectric insert at (-20, 36, -20)mm (b) 2D view of DAS result (c) 2D view of MWDAS result

Table 5.4.1 Signal-to-clutter ratio for images of embedded targets located at different position inside the chemical breast phantom at SNR=15dB

Locations in Breast Phantoms	SCR obtained with DAS (dB)	SCR obtained with MWDAS (dB)
(30, 0, -10)mm in homogeneous high adipose phantom	1.65	2.75
Position-1 in inhomogeneous dense phantom at (20, 0, -20)mm	0.38	1.58
Position-2 in inhomogeneous dense phantom at (-20, 36, -20)mm	2.21	2.60

Here, we only compared the results using DAS and MWDAS, because: (a) DAS and MWDAS both are data-independent beamformers. RCB is a data-dependent method. So comparing between data-independent methods is appropriate. (b)DAS is simple but more popular data-independent beamforming method that has been reported in the

literature for image reconstruction [62], although it can introduce more clutter contamination on the reconstructed image. MWDAS can reduce the clutter contamination. Hence, when comparing DAS, MWDAS, one can clearly see the improvement offered by MWDAS. (c) DAS has been used as a reference for image comparison in clinical diagnosis [18], where DAS images were compared with mammogram images for the same patients to establish successful detection. Hence, comparison of MWDAS with DAS can demonstrate the superior performance of MWDAS for clinical application.

5.5 CNR extraction calibration using PEC objects

Once the suspicious region is accurately reconstructed, we will estimate the waveform using our proposed two-step approach. This waveform will be used for CNR extraction. However, before we extract CNRs of dielectric inserts, it is necessary to extract CNRs of embedded PEC inserts inside chemical phantoms. This is important since the PEC objects have only external mode CNRs [89]which can be used to discriminate target shape, etc. Thus, CNR extraction using PEC inserts can be considered to be equivalent to CNR calibration.

5.5.1 Measurement setup for calibration

To evaluate the capacity of the proposed experimental microwave imaging system for CNR extraction, firstly we employ conducting objects with different surface geometries to calibrate the extracted CNRs. Two typical PEC objects are used: (i) a steel sphere and (ii) a copper insert with some small random spicules as shown in Figure 5.5.1. The PEC spiculated insert is fabricated by soldering copper spicules on a smooth copper base using Gaussian sphere method [127, 130]. The two metallic objects are immersed in olive oil. For PEC target, we employ the procedures as shown in Figure 5.5.2. Here, one BAHA antenna illuminates the embedded target using VNA with

frequency swept from 1 to 10GHz and another BAHA antenna that is positioned at 45 degree angle and separated at 50mm away from the target will receive the scattered field. Time domain pulse is obtained by using iFFT. The received scattered filed will then be subtracted from signal obtained for target-free scenario to ideally obtain the late-time target response to extract CNRs. The measured results will be compared with available published data [123] on CNRs and theoretical predictions obtained by using Baum's transform [125].

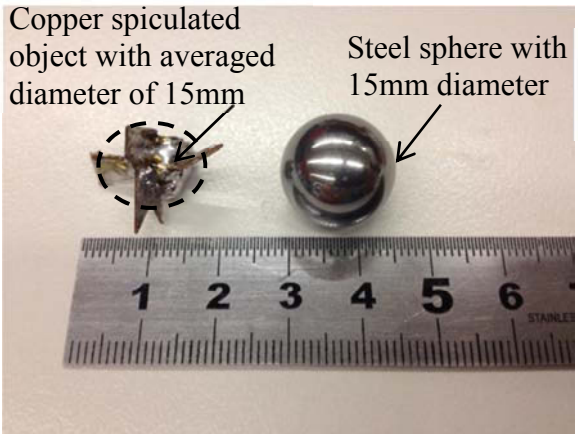

Figure 5.5.1 Spiculated and spherical metallic objects.

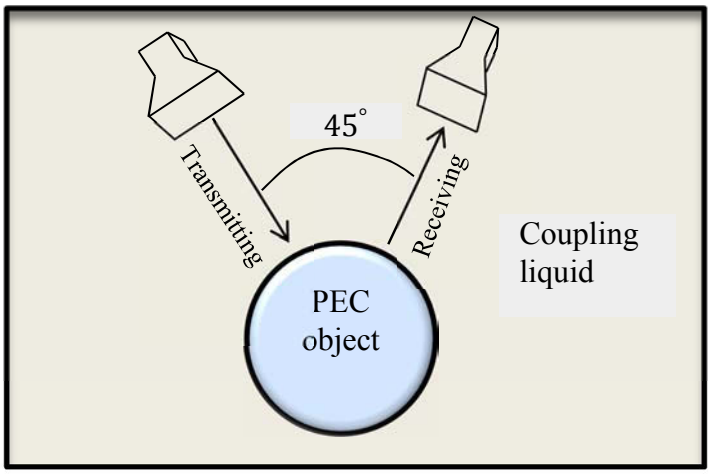

Figure 5.5.2 Experimental setup for calibration of CNR extraction using PEC objects embedded inside coupling liquid

5.5.2 Methods for detecting late-time resonant signal for CNR extraction

CNRs are extracted based on late-time responses. For the embedded objects in dielectric medium, CNRs can be affected by non-resonant early-time signal and antenna ringing, as well as spurious CNRs due to clutters. In fact, it is difficult to differentiate late-time resonant signal with other nonresonant signals. The existing solution for discrimination of late-time and early-time signal is based on an empirical time window [99] which is not straight forward to implement. Hence, it is desirable to develop a method that can accurately pinpoint the period of late-time resonant signal.

We propose a time-resonant frequency method to find out the late-time response to extract CNRs. It should be noted that here the term "late-time" is used with regard to resonant signals. Time-resonant frequency is conventionally used to find out the fundamental resonant frequency of an embedded object in GPR applications [89, 94], where resonant frequencies are plotted as the function of time to obtain a time-frequency plane. On this resonant frequency-time plane, the longest stable line with the lowest frequency indicates the fundamental resonant frequency[94]. On the other hand, higher order mode of resonant frequencies usually result in short and instable lines[94]. Hence, fundamental resonant frequency can be easily identified to determine the embedded object, as this fundamental frequency corresponds to the physical length of the embedded metallic PEC objects[94].

Here, we have modified this resonant frequency-time plane to localize the starting time of late-time resonant signal, for which a stable and non-fluctuating resonant frequency can be expected. On the contrary, non-resonant frequencies including early-

time and antenna ringing do fluctuate. Our method differs from the conventional method[94], as we only plot the dominant poles as a function of time. This is because the dominant poles are certainly due to the resonant signal and other spurious poles with lower magnitudes can be suppressed on this plane. The extracted CNRs of the dominant poles will have highest magnitudes. The dominant poles will form stable and non-fluctuating resonant frequencies on this time-freq plane. Thus, the starting time of resonant signal which coincides with the starting time of dominant poles can be clearly displayed on the resonant frequency-time plane. To get late-time response, a target-free reference signal is firstly obtained without immersing any object in the coupling liquid. Then, the signal is measured by immersing the object back to the coupling liquid. Then both signals are subtracted with each other to get calibrated signal.

5.5.3 Calibration using metallic spheres

We firstly employed two spherical PEC smooth targets with diameter of 15.875mm and 11.11mm respectively. The late-time target response of measured data from 15.875mm steel sphere and its time-resonant frequency planes are shown in Figure 5.5.3. Figure 5.5.3 (a) shows the target response of 15.875mm PEC sphere. Figure 5.5.3 (b) shows the resonances on time-resonant frequency plane. From this data, it appears that fundamental resonance with lowest resonant frequency is around 3GHz with stable period that is short and starts from 0.91ns as indicated in the dashed line in Figure 5.5.3. This time starting gives the starting point of the late-time resonant signal and CNR will then be extracted by using matrix pencil method [119] from that starting time. It should be noted that in this plot, the stable period is short and difficult to identify. Other fluctuating results shown in the figure may be due to erroneous CNR poles that are caused by early-time nonresonant signals and antenna ringing and thus must be eliminated. Figure 5.5.3 (c) shows a plane using conventional method for localizing fundamental resonant frequency [94].

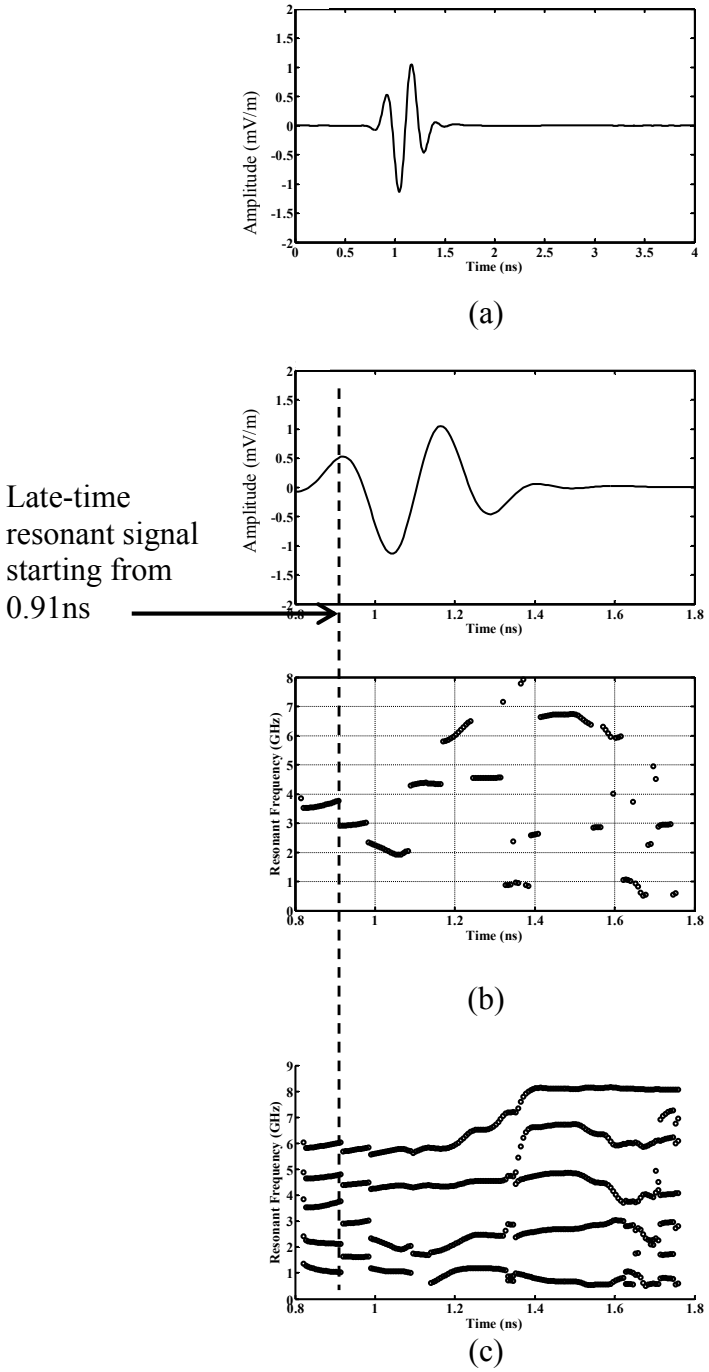

Figure 5.5.3 Localization of late-time resonant signal for PEC sphere of 15.875mm immersed in coupling liquid. (a) target response signal (b) localization of late-time resonant signal using proposed time-resonant frequency plane (c) localization of late-time resonant signal using conventional method[94].

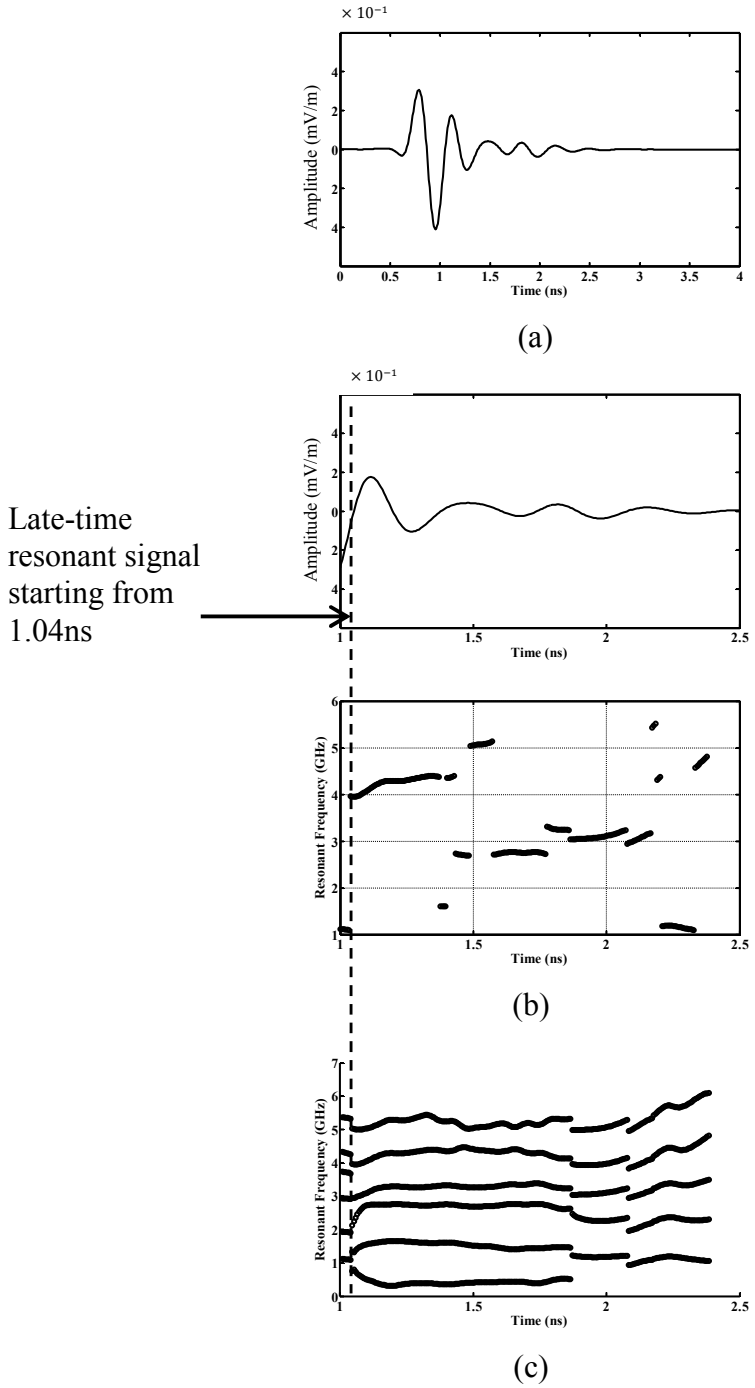

Figure 5.5.4 Localization of late-time resonant signal for PEC sphere of 11.11mm immersed in coupling liquid. (a) target response signal (b) localization of late-time resonant signal using proposed time-resonant frequency plane (c) localization of late-time resonant signal using conventional method [94].

It can be seen the resonant frequency-time plane plotted using the conventional method gives the unwanted resonances from 1 to 6GHz. It also obtains flat and stable resonances along the whole time which makes it difficult to discriminate the late-time resonant frequencies from early-time nonresonant frequencies. However, by using our proposed method, most of the spurious resonances can be suppressed and in addition it helps to identify late-time resonant frequency accurately. For steel sphere of 11.11mm diameter, target response and the localization of late-time resonant signal are plotted in Figure 5.5.4. Fundamental frequency appears to be around 4.5 GHz starting from 1.04ns. It can also be observed that the proposed method can suppress many spurious resonant frequencies. Therefore, CNRs can be extracted based on these localized stable periods.

The measured CNRs from immersed steel spheres are listed in Table 5.5.1. For comparison, we theoretically calculate the CNRs from spheres located in free space using equation (3.4). These CNRs are transformed using Baum's transform (3.5) [125]to obtain CNRs in lossy medium.

Table 5.5.1 Measured Resonant Frequency of PEC (Steel) Spheres

Size (mm)	mode	Resonant Frequency in Free Space (GHz)	Predicted Resonant Frequency in Coupling Liquid (GHz)	Measured Resonant Frequency (GHz)
15.875	1	5.21	3.29	3.18
	2	10.87	6.87	6.75
11.11	1	7.44	4.7	4.79

It can be observed from Table 5.5.1 that the measured resonant frequencies are very close to the values predicted by Baum's transform[125]. This demonstrates that our proposed late-time localization method can accurately localize reliable late-time response for CNR extraction. This procedure will be used in later sections as a method of calibration when extracting CNRs of dielectric inserts embedded in tissue mimicking chemical phantoms.

5.5.4 Calibration using metallic spiculated objects

Since the CNRs extracted for metallic (PEC) objects have only external mode of CNRs, they reflect the morphological characteristics of PEC objects [89]. Hence, we can extract external mode CNRs of dielectric objects. Then we can correlate the CNRs with the geometrical features of the object. However, dielectric objects have both external and internal CNRs. So, to identify the external mode CNRs of dielectric objects, we require CNRs of PEC objects. Thus, by comparing the external mode of CNRs, objects with distinct surface geometries can be identified [94]. Here, we employ PEC inserts with spiculated shapes and extract the CNRs from them to discriminate the CNRs from smooth inserts in terms of external mode of CNRs.

In our experiment, we embed PEC spiculated inserts (shown in Figure 5.5.1) in the coupling liquid and measure the scattered field from the object using the experimental setup as shown in Figure 5.5.2. CNRs extracted from measured data from PEC spiculated insert are plotted in Figure 5.5.5, and compared with CNRs extracted from measured data for smooth steel inserts of diameter 15.875mm. It can be seen that at a higher order mode around 6GHz, the damping factor from a PEC spiculated insert is distinct (having much lower damping factor) from that of the smooth PEC insert. Higher order mode of CNR is the pole with higher resonant frequency. However, as can be seen, at lower order modes, CNR poles have similar values of damping factors, then

making it difficult to discriminate. Also, since BAHA antenna element is designed to work above 4GHz when immersed in coupling oil (as discussed in Chapter 4), resonant frequency lower than 4GHz may not be adequately detected.

From the above measured experiments, we can discriminate PEC spiculated and smooth objects using CNRs when they are immersed in coupling liquid. Now we examine their extracted CNRs by embedding them in homogeneous adipose-content dominant phantom. Two additional metallic spiculated objects are fabricated each with equivalent diameter of 15mm (in Figure 5.5.6) and both are embedded at the same location. We use the same experimental setup as shown in Figure 5.5.2. The breast phantom is also immersed in coupling liquid for matching purpose. The results on CNRs are shown in Figure 5.5.7, from which the following findings can be observed: a) damping factors can be distinguished at higher order modes of CNR poles; b) at lower order modes, CNR damping factors have similar values and so are difficult to differentiate due to BAHA antenna characteristics.

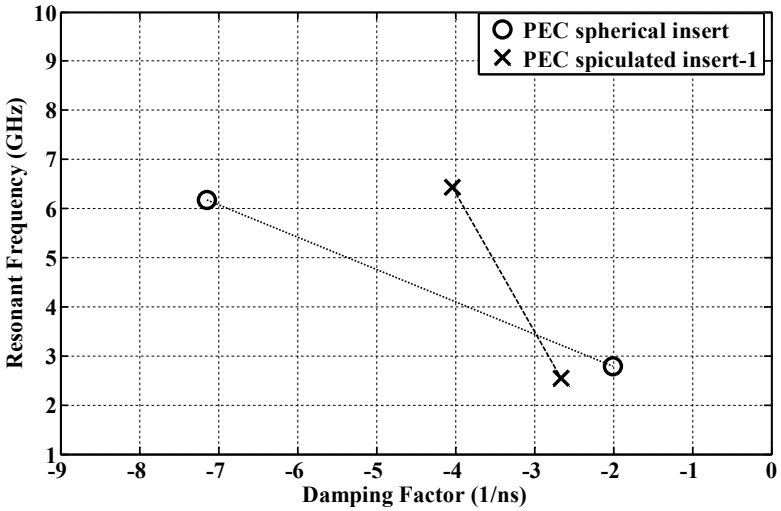

Figure 5.5.5 CNRs from metallic PEC spiculated and spherical inserts in coupling liquid

The extracted CNRs are tabulated in Table 5.5.2. By using PEC spherical and spiculated inserts, external mode of CNRs can be calculated. These external mode CNRs correspond to the target's morphological features and thus offers promising potential for discriminating breast lesions. The reason that damping factors at lower order mode are difficult to discriminate may lie in the design of BAHA antenna as it starts radiating efficiently from 4.1GHz.

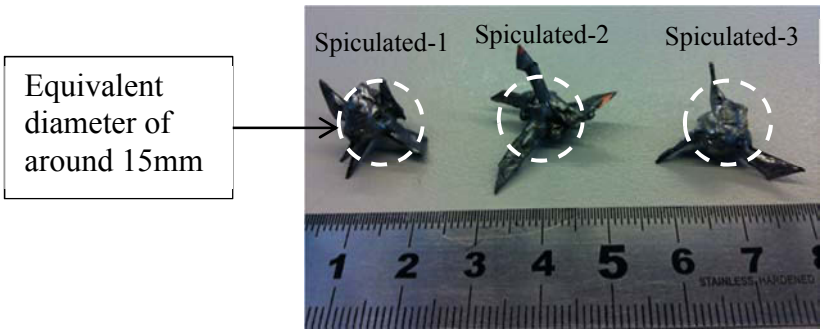

Figure 5.5.6 Fabricated spiculated copper inserts

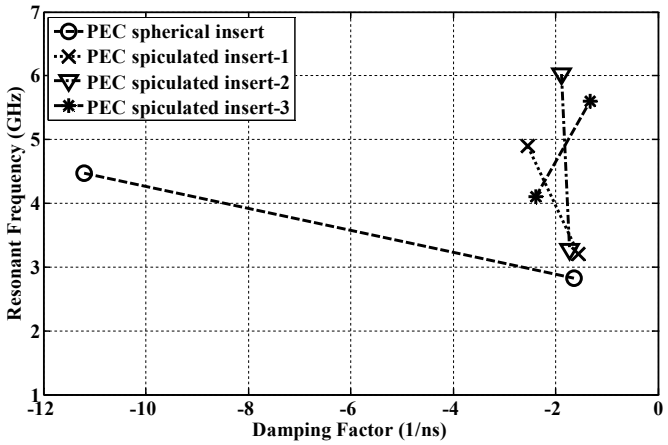

Figure 5.5.7 CNRs from PEC spiculated and spherical inserts embedded in homogeneous adipose tissue dominant breast phantom.

Table 5.5.2 Extracted CNRs for PEC Inserts

Object Type	Embedded Dielectric Medium			
	Coupling Liquid		High Adipose Phantom	
	Frequency (GHz)	Damping factor (1/ns)	Frequency (GHz)	Damping factor (1/ns)
Sphere of 15.875mm diameter	6.18 2.78	-7.14 -2.01	4.47 2.83	-11.2 -1.64
Spiculated lesion-1	6.44 2.55	-4.04 -2.66	4.9 3.2	-2.55 -1.56
Spiculated lesion-2			6.03 3.27	-1.88 -1.73
Spiculated lesion-3			4.1 5.6	-2.38 -1.33

5.6 Discrimination of tumor mimicking dielectric inserts using CNR signatures

5.6.1 Methods of CNR extraction

For embedded dielectric inserts in tissue mimicking breast phantoms, we employ the proposed UWB microwave imaging system with BAHA antenna array to collect the backscattered pulses for extraction of CNR signatures. We have employed general preprocessing given by (3.6) and TOA autocalibration given by (3.11)-(3.15) to process the measured data. Then we used two-stage beamforming given by (3.20)-(3.31) to reconstruct time-domain target response from the embedded dielectric inserts. After localizing the late-time resonant signal on resonant frequency-time plane, CNRs are extracted by using Matrix Pencil method [122].

5.6.2 Estimated late-time resonant signals

Three sets of tumor mimicking dielectric inserts (spiculated and smooth as shown in Figure 5.2.4) are first embedded within the homogeneous breast phantom containing high adipose tissue content, all three at the same position (30, 0, -10) mm, respectively. The dielectric properties of adipose tissue and dielectric insert (tumor) are shown in Table 5.2.1.

Plots of CNR on resonant frequency-time planes for the smooth dielectric insert-1 and spiculated dielectric insert-1 are plotted in Figure 5.6.1, and Figure 5.6.2, respectively. For smooth dielectric insert-1, the lowest resonant frequency appears at 3GHz with starting time at 1.25ns meaning that CNRs can be extracted after 1.25ns. On the other hand, spiculated dielectric insert-1 has fundamental resonant frequency at 3.5GHz with time starting from 1ns.

5.6.3 Extracted CNRs for dielectric inserts in homogeneous breast phantom

CNRs extracted for the three sets of spiculated and smooth shaped dielectric inserts (as shown in Figure 5.2.4) are illustrated in Figure 5.6.3. Resonant frequencies range from 3GHz to 6GHz with fundamental resonant frequency at 3GHz. For each complex pole, both spiculated and smooth dielectric inserts have similar level of resonant frequencies.

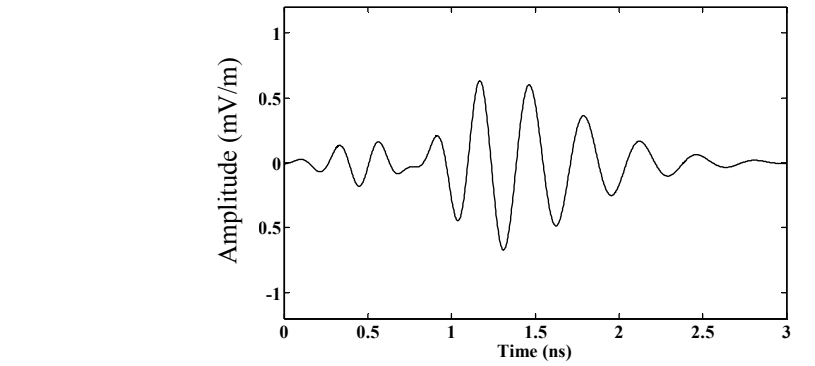

(a)

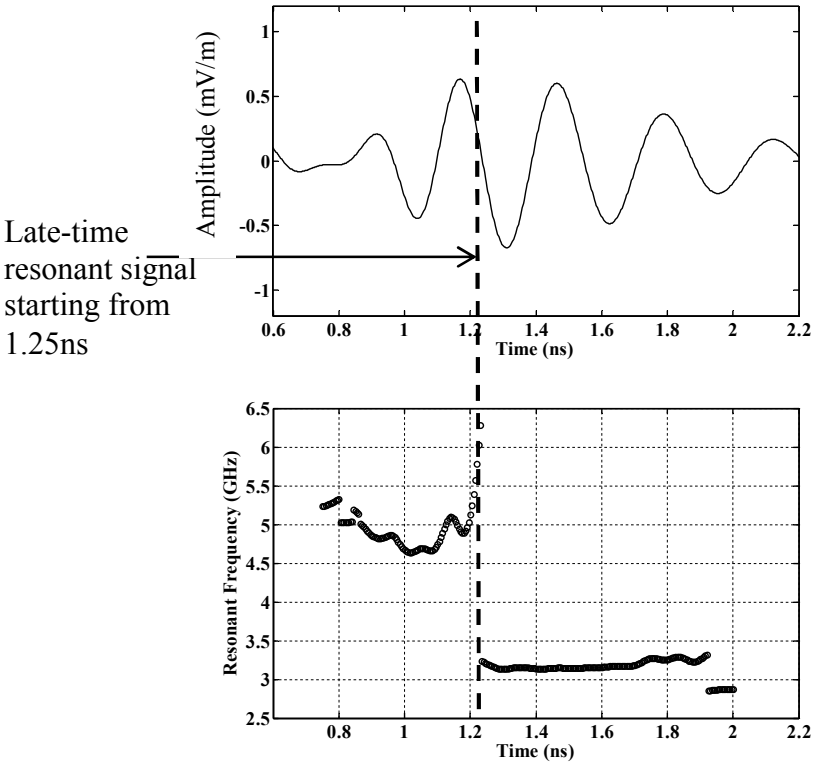

(b)

Figure 5.6.1 Localization of late-time resonant signal for smooth shaped dielectric insert-1 in homogeneous adipose-dominated phantom. (a) tumor response signal (b) localization of late-time resonant signal using proposed time-resonant frequency plane

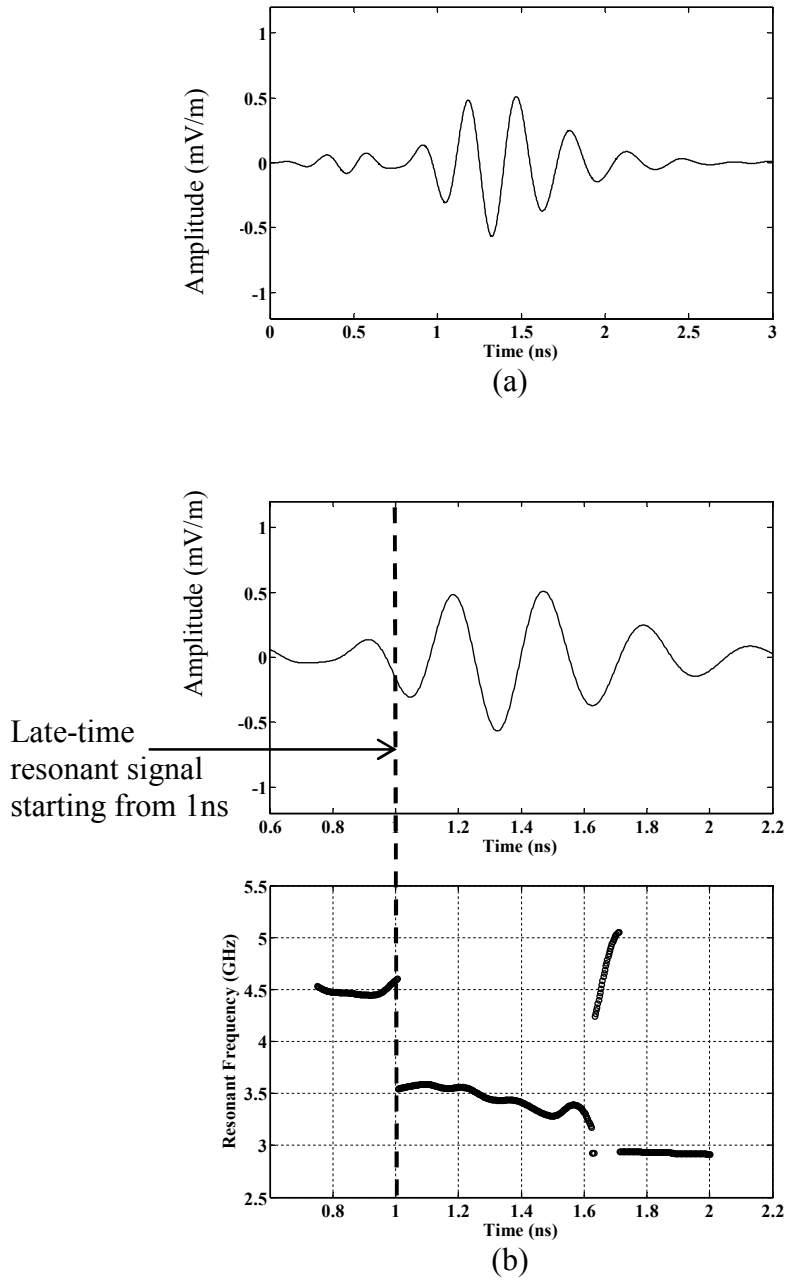

Figure 5.6.2 Localization of late-time resonant signal for spiculated shaped dielectric insert-1 in homogeneous adipose-dominated phantom. (a) tumor response signal (b) localization of late-time resonant signal using proposed time-resonant frequency plane

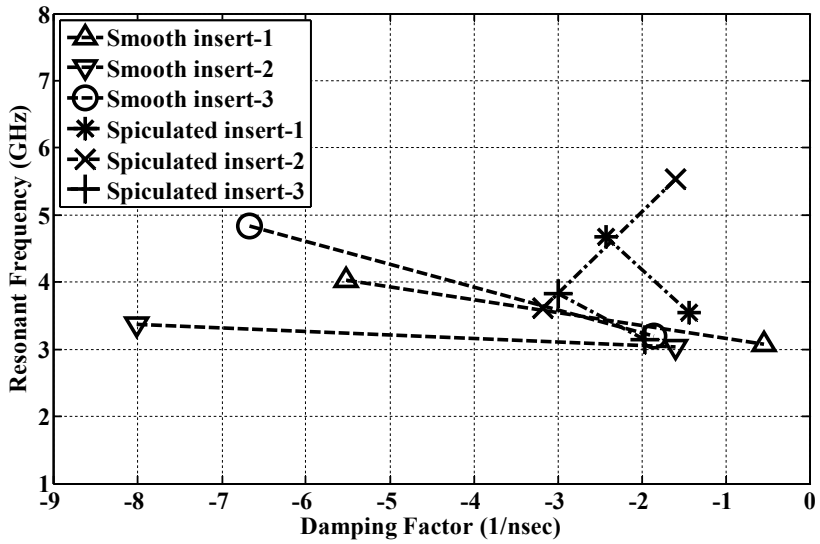

Figure 5.6.3 Extracted CNRs from measured data for three sets of tumor mimicking dielectric inserts in homogeneous adipose-dominated breast phantom.

Table 5.6.1 Extracted CNRs for Dielectric Inserts Embedded in Homogeneous Phantom

Tumor Mimicking Inserts	Extracted CNRs			
	Frequency (GHz)		Damping Factors (1/ns)	
	Higher mode	Lower mode	Higher mode	Lower mode
Smooth dielectric insert-1	4.03	3.07	-5.52	-0.54
Smooth dielectric insert-2	3.37	3.04	-8.02	-1.60
Smooth dielectric insert-3	4.84	3.2	-6.67	-1.85
Spiculated dielectric insert-1	4.68	3.54	-2.42	-1.44
Spiculated dielectric insert-2	5.53	3.61	-1.60	-3.18
Spiculated dielectric insert-3	3.83	3.14	-2.99	-1.96

It can be observed that CNRs corresponding to higher mode have differences in their values for spiculated and smooth shaped dielectric inserts. One can observe that the damping factors are different for smooth and spiculated dielectric inserts. On the

contrary, CNRs at lower mode have very similar values of damping factors and hence are difficult to discriminate. This establishes that the damping factor of higher order modes of CNRs for spiculated dielectric inserts have distinct differences with smooth inserts as shown in Table 5.6.1. It should be mentioned that the lack of distinct difference in lower mode of CNR could be due to the BAHA antenna element which works above 4 GHz when immersing in coupling liquid ($\varepsilon_r = 2.5$) as discussed in Chapter 4 so that resonant frequency lower than 4GHz may not be collected properly. Estimation of late-time resonant signal is limited by the lossy medium, breast inhomogeneity, as well as the SNR of measured system. Although our proposed method improves resonant frequency-time plane, it still strongly depends on the accurately estimated time-domain signals.

One cannot measure CNRs directly. They are obtained by using Matrix Pencil Method on measured scattered field data. Furthermore, there is no standard method to calibrate CNRs for dielectric inserts that have either smooth or spiculated peripheries. Therefore, we have employed indirect calibration methods by using PEC spheres and Baum's transform (3.5) by estimating CNR values for PEC spheres embedded in homogeneous dielectric medium. Another indirect calibration method we have employed is to use the external mode of CNRs of PEC inserts to compare and identify external mode CNRs of dielectric inserts. This is possible because PEC targets have external mode CNRs only[94]. Extracted CNRs from measured data have shown that spiculated objects have much lower damping factors than smooth shaped objects as shown in Table 5.5.2.

5.6.4 Extracted CNRs for dielectric inserts in inhomogeneous breast phantom

CNRs are extracted from the measured data using the same three sets of tumor mimicking dielectric inserts as reported in the earlier section. Here, these dielectric

inserts are embedded in inhomogeneous dense breast phantom at (20, 0, -20) mm. The dielectric contrast between dielectric inserts and ambient medium (glandular tissues) is 1.7:1 and their dielectric properties are shown in Table 5.2.1. CNRs extracted from measured data are shown in Figure 5.6.4. A similar trend can be observed from Figure 5.6.4 that the differences of damping factors for higher order modes is distinct, whereas at lower modes (about 3GHz) differences in damping factors values is not distinct. Then, one can use damping factors of higher mode CNRs to differentiate between smooth and spiculated shaped dielectric inserts. The CNR results are also tabulated in Table 5.6.2.

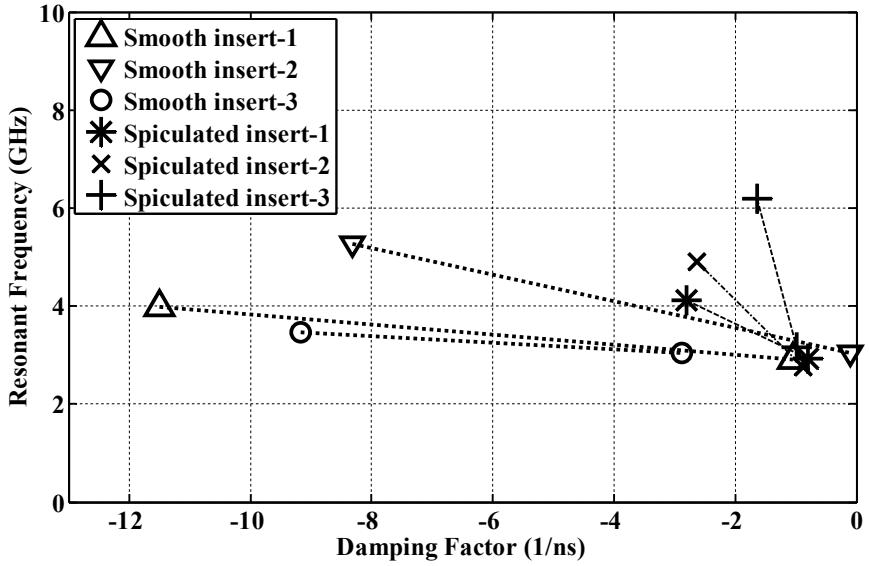

Figure 5.6.4 Extracted CNRs from measured data for three sets of dielectric inserts embedded in inhomogeneous dense breast phantom.

Table 5.6.2 Extracted CNRs for dielectric inserts in inhomogeneous phantom

Tumor Mimicking Inserts	Extracted CNRs			
	Frequency (GHz)		Damping Factors (1/ns)	
	Higher mode	Lower mode	Higher mode	Lower mode
Smooth shaped insert-1	3.98	2.90	-11.50	-1.05
Smooth shaped insert-2	5.27	3.04	-8.31	-0.10
Smooth shaped insert-3	3.46	3.05	-9.17	-2.88
Spiculated insert-1	4.11	2.93	-2.80	-0.80
Spiculated insert-2	4.91	2.75	-2.64	-0.87
Spiculated insert-3	6.19	3.15	-1.64	-0.99

5.6.5 Normalized CNR error (NCR)

Since CNRs are closely associated to morphological features of the targets, a standard to evaluate the obtained CNRs is critical. Normalized CNR error (NCR) given by (3.33) as discussed in Chapter 3 is used to measure the differences between the extracted CNRs from two objects[136]. Values of NCR lie between 0 and 1. For a large NCR, the two targets can be discriminated indicating that they have distinct morphological features. On the other hand, targets that have similar morphological features are possible to have small NCR. NCR for the three sets of dielectric inserts placed in homogeneous phantom is illustrated in Figure 5.6.5. As expected, errors among smooth shaped inserts have smallest NCR, since their shapes have gradual transitions at the borders. Spiculated inserts have shown distinct NCR with respect to each other due to their irregular random sharp transitions. This is useful in identifying spiculated breast tissues as they have random irregular morphologies. We have calculated NCR between smooth and spiculated inserts: 1) smooth insert-1 and

spiculated insert-2 have the largest NCR of 0.86; 2) smooth insert-1 and spiculated insert-3 gives a low NCR, because they have relative close damping factors at higher mode CNR.

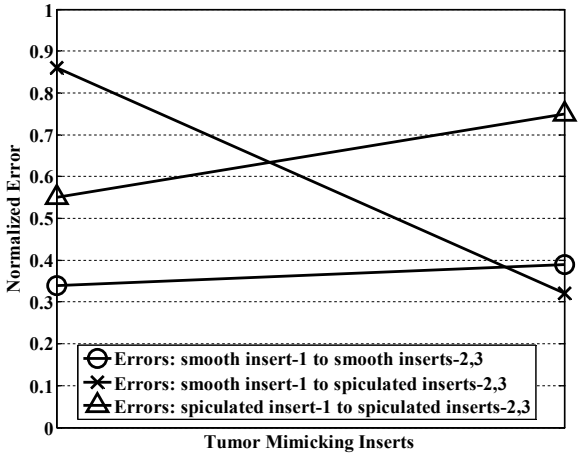

Figure 5.6.5 Normalized CNR errors of dielectric inserts in homogeneous adipose-dominated breast phantom

NCR for the same three sets of dielectric inserts placed in inhomogeneous phantom is illustrated in Figure 5.6.6. NCR between smooth insert-2 and spiculated insert-1 and 3 are 0.75 and 0.69, respectively. On the other hand, NCR between smooth insert-2 and smooth inserts-1 and 3 are decreased by 0.21 and 0.29 due to their smooth border transitions. In this experiment, the highest NCR (0.94) appears between spiculated inserts 1 and 3 because of the highly random spiculated shapes.

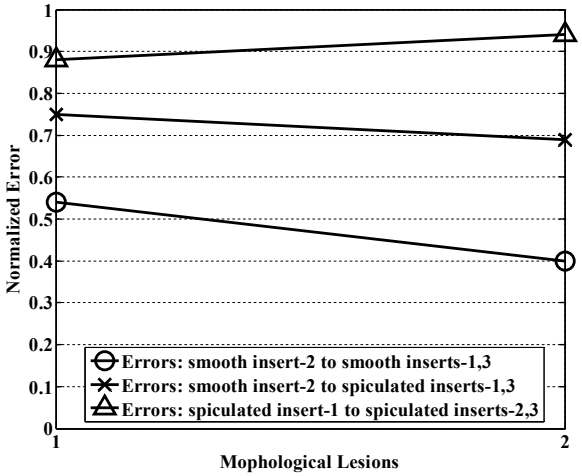

Figure 5.6.6 Normalized CNR errors of dielectric inserts in inhomogeneous dense breast phantom

NCR helps to discriminate the shapes of unknown embedded targets. It is difficult to judge the difference between CNR poles only by examining their contrasts between damping factors (Table 5.6.1 and Table 5.6.1). Smooth inserts have large damping factor contrasts with respect to each other, but they have shown small NCR value indicating that they have similar surface shapes. On the other hand, spiculated inserts have small damping factor contrast but has large NCR value indicating that they have distinct morphological features. Therefore, NCR could offer to identify difference between morphological features based on CNR poles and is preferable to be a metric to discriminate target shape.

5.7 Discussion

We develop an experimental microwave imaging system using the 32 BAHA elements. By using this system, we have demonstrated that tumor mimicking dielectric inserts with diameter of 12mm can be successfully detected in both high homogeneous and inhomogeneous tissue mimicking breast phantoms. Furthermore, we have also

fabricated three sets of dielectric inserts with smooth and spiculated shapes which represent benign and malignant breast tumors respectively. By extracting their CNRs from measured data when they are embedded in breast phantoms, spiculated dielectric inserts can be discriminated from smooth dielectric inserts. The significant contrast of calculated NCRs for these dielectric inserts also demonstrates that spiculated inserts can be differentiated from smooth inserts. This discrimination between smooth and spiculated shaped dielectric inserts have demonstrated the potential of breast tumor discrimination by using CNR.

Our preliminary experiments reported in this chapter are the first experimental attempt to discriminate morphological features of dielectric inserts. The fabricated tissue mimicking chemical phantoms and dielectric inserts can be further improved to mimic denser breast phantoms such as C3 or C4 dense phantom models [57]and more realistic body profiles of breast lesions.

BAHA antenna elements used in microwave imaging system is designed to collect the backscattered signals with frequency from 4GHz as reported in Chapter 4 when immersed in coupling liquid ($\varepsilon_r = 2.5$). The antenna response at frequency lower than 4GHz may not be optimal. Thus, due to this, we have emphasized that use of higher resonant mode which usually has frequency greater than 4GHz or 5GHz can be more appropriate for CNR discrimination. On the other hand, higher resonant mode shows distinct contrast between damping factors which further re-conforms that use of higher mode is helpful. Hence, although the current BAHA antenna's performance is sub-optimal at lower frequency, it can still be used for CNR discrimination.

Based on the experimental experiences in this thesis, we observed that it is possible to develop a six element BAHA imaging system with a mechanical rotation device. This system can avoid the complex high frequency microwave switch system which can be

very expensive. However, use of rotation device can increase the total time for data collection which may lead to increase in the measurement uncertainty. For example, the patient may move if the measurement time is longer.

Experimental results have shown that dielectric inserts can be discriminated by their distinct damping factors. However, the values of damping factors depend on ambient breast tissue background and also the size of the lesion. Hence, reference damping factors are required to identify the difference between damping factors of breast lesions. Otherwise, it is difficult to interpret the obtained damping factor data from extracted CNRs. Therefore, our proposed breast lesion discrimination method can be used as a complementary method with other techniques such as mammography. Once the ambient background of the suspicious lesion location is obtained from mammogram, an initial dielectric property of ambient medium can be known from which we estimate the possible range of damping factor values that the suspicious lesion may have. By using this knowledge obtained apriori using mammography, the proposed discrimination method will help to find out whether the extracted CNRs are from smooth or spiculated lesions.

Chapter 6
Conclusions

6.1 Overview

This chapter presents the conclusions based on the contributions made in this thesis. It is organized by firstly presenting the major chapters summaries and then the key contributions from the thesis are reported. Finally, scope for future work is briefly addressed

6.2 Summary of the thesis

This thesis presents a novel microwave imaging technique for early stage breast tumor detection and discrimination by proposing a novel TOA autocalibration and a novel data-independent beamforming, and extraction of complex natural resonances. Based on the detected suspicious region of breast tumor, a method for CNR extraction and calibration techniques are presented to discriminate the shapes of embedded breast lesions. To validate the proposed methods, this thesis also reports experimental microwave imaging system that uses a UWB antenna array connected to VNA. A new and efficient UWB antenna for microwave imaging is also proposed in this thesis. Measurements on microwave imaging have been carried out using tissue mimicking chemical breast phantoms as well as tumor mimicking dielectric inserts which have

been fabricated. Using the measured data, complex natural resonances (CNR) of tumor-mimicking dielectric lesion have been extracted and compared with CNRs of metallic objects. Our results have shown that it is possible to discriminate malignant and benign lesions based on their complex natural resonances. In this chapter, the main conclusions incorporated in each chapter are highlighted.

Chapter 2

This chapter presents the use of array beamforming technique for early stage breast tumor detection. We propose data-independent beamformer known as MWDAS method for localizing suspicious regions. Using FDTD simulation on 2D and 3D numerical breast phantoms, it has been demonstrated that MWDAS method is capable of focusing to the strongest scatterer within the breast thereby effectively localizing suspicious regions. When compared to existing methods viz., DAS and DMAS, the proposed MWDAS could offer higher resolution even for inhomogeneous breasts. The importance of TOA information has also been addressed showing as to how TOA can affect the final reconstruction of tumor location. FDTD simulations have revealed that data-independent method (such as DAS) with proper TOA calibration is able to achieve the similar level of reconstruction accuracy that has been reported with RCB, which is a data-dependent method.

Chapter 3

This chapter presents the techniques for discriminating whether the tumor malignant or benign by using the morphological features of breast tissues in term of complex natural resonances (CNRs). Since CNR is an approximate metric extracted from the time-domain signal by singularity expansion method (SEM), the quality of the extracted CNR is vital. To guarantee the high quality of CNR extraction, this chapter presents a number of novel procedures:

1) TOA autocalibration: use early-time artifacts to estimate TOA information for different propagation paths by reconstructing the antenna positions initially as a calibration step since they are known apriori.
2) General pre-processing: remove early-time artifacts based on backscattered signals
3) Two-stage of scaled beamforming: in the first stage, array steering vector is estimated by using stochastic method-PSO; in the second stage, time-domain waveform of target response is estimated.
4) CNR calibration: in the first case, calibrate the CNR extraction by employing PEC spheres with different sizes and the extracted CNRs are examined by predicted values by using Baum's transform. In the second case, calibrate external mode of CNR by employing spiculated and spherical PEC objects and compare with their corresponding dielectric counterparts having the similar shapes. The results have shown that external mode of CNR for dielectric objects can be extracted which are useful for discriminating the surface morphological features of tissues.
5) Method of identifying late-time resonant signal: we improved the conventional resonant frequency-time plane to obtain the resonances as function of time. This method helps to find out the starting time of late-time resonant signal from which CNR can be extracted by using matrix pencil method.

To test the above techniques, FDTD simulations have been carried out using MRI-derived C3 class dense breast phantom which is obtained from online repository provided by University of Wisconsin-Madison[57]. Computational results from the C3 dense breast phantom have demonstrated that:

1) TOA can be well calibrated based on received raw data by using simple DAS beamformer. As a test, a number of transmitting antenna positions have been

accurately estimated, then providing optimized TOA information, for use with breast phantoms.

2) Suspicious tumor location within dense breast phantom can be identified. The performance has been evaluated by ideally reconstructed tumor location that is obtained when subtracting tumor-free signal, obtained from ideal tumor-free template.
3) Extracted CNRs of PEC spheres from simulated data have very close agreement with those extracted from measured data given in literature[123] as well as the available theoretically predicted results. Extracted CNRs from embedded PEC spheres also fit well with Baum's transformed data.
4) Discrimination of tumor shapes by using CNRs has been observed at higher order mode of CNR poles. The poles of higher order mode CNR have much smaller damping factors for spiculated breast lesion than those from smooth lesion. However, damping factors of corresponding lower order mode CNR have too close values to differentiate.

Extracted CNRs from simulated data have obvious limitation: firstly, CNR extraction is limited by waveform estimation, as the applied two-stage waveform estimation can only reduce the interference from clutters, but the errors still exist; secondly, late-time resonant signal is difficult to differentiate form early-time nonresonant signal. Thus, erroneous CNRs could also be introduced. This may lead to the unsuccessful discrimination of damping factors at lower order mode.

Chapter 4

This chapter focuses on UWB antenna design. We exclusively focus on end-fire compact UWB antennas as they could radiate higher energy into the imaged tissues than other antennas such as monopole and slot antennas. Firstly, modified ridged horn and Vivaldi antennas are reported. They also have compact size and could form a large

antenna array. Finally, we have developed a modified ridged horn antenna with straight ridge and launching plane using FDTD simulations. A modified balanced antipodal Vivaldi antenna is also investigated in this chapter using FDTD simulation. Finally, we proposed a BAHA antenna element that has a size of $20\text{mm} \times 20\text{mm}$ and selected this antenna as the candidate for experimental breast imaging setup. Measured results have shown that BAHA has low return loss (<-15dB) and high fidelity (>0.9) and S21 levels (around -25dB) at 100mm distance in a coupling liquid. BAHA resonates from 4.1GHz to 11GHz covering sufficient UWB bandwidth for our proposed microwave imaging.

Chapter 5

In this chapter, we investigated methods to determine whether the breast tissue is malignant or benign using tumor mimicking dielectric inserts embedded inside chemical breast phantoms. The phantoms are categorized into two types: homogeneous phantom which consists of manly fatty tissue equivalents and inhomogeneous phantom which has dense glandular tissues and fatty tissues. For tumor mimicking inserts, both smooth and spiculated dielectric inserts have been fabricated with 12mm equivalent diameters to represent benign and malignant breast tumors respectively.

We have built an imaging system for breast tumor detection and tumor shape discrimination. As a critical component in this system, a hemispherical antenna array is formed by 32 BAHA antennas. Antennas in the array are excited by VNA to radiate UWB microwave to the breast which is immersed in coupling liquid. Time-domain signals at the receiving antennas are obtained synthetically by employing wideband frequency scan using VNA. To investigate breast tumor detection and tumor morphology discrimination, chemical breast phantoms with radius of 68mm have been fabricated to mimic breast tissue equivalents including homogeneous and inhomogeneous breast tissues. Fabricated tumor mimicking dielectric inserts (with

equivalent diameter of 12mm) which correspond to benign and malignant breast tumors have been inserted into breast phantom for measurements. Based on measured data, we have successfully localized the regions where the inserts have been placed in both homogeneous and inhomogeneous breast phantoms. The measured data has been processed to extract waveforms for CNR extraction.

To calibrate CNR extraction from measured data, two steel spheres with 15.875mm and 11.11mm diameters respectively are employed into the coupling liquid and their CNRs are extracted from measured data using BAHA antenna elements. The extracted CNRs fit well with the estimated values calculated by Baum's transform. Furthermore, calibration using PEC spiculated objects is also carried out in both coupling liquid and inside the homogeneous chemical phantom. Finally, extracted CNRs from the measured data have revealed that smooth inserts can be discriminated from spiculated inserts, thus providing a very promising potential for early stage breast cancer detection.

6.3 Summary of original contributions

The following is the summary of the contributions made is this thesis.

1. Novel end-fire UWB antennas for near-field microwave imaging

The thesis has proposed different novel UWB antenna elements that have compact sizes. Modified ridged horn is proposed with good impedance bandwidth (-10dB) from 5 to 14GHz by using straight ridge and launching plane. These modifications improve the ease of fabrication. We have also proposed a modified Vivaldi antenna (mBAVA) with aperture size only of $14\text{mm} \times 6\text{mm}$.

2. Study of BAHA antenna for microwave imaging

One of the key contributions of this thesis is the design of novel BAHA antenna for UWB imaging. Measured results have shown that BAHA antenna offers good performance for near-field breast imaging. Of having high level of fidelity, BAHA can

radiate low distorted UWB pulse demonstrated through measurements using VNA. Minimized pulse distortion is important for accurately recording the measured tumor response, as tumor response has very small amplitudes and are dominated early-time by early-time artifacts. Moreover, BAHA has flat S21 characteristics over the band.

3. Experimental microwave imaging setup with hemispherical BAHA antenna array using on tissue mimicking breast phantoms

We have built a microwave imaging system for experimental study of breast tumor detection. This system used our proposed UWB BAHA antennas to form a hemispherical antenna array. Due to the superior performances of the proposed BAHAs, experimental results have shown that tumor mimicking inserts (with diameter of 12mm) can be identified when the dielectric contrast is both high (4:1) and low (1.7:1) for the breast phantoms.

We also developed multilayered chemical phantoms for experimental tests. The tissue mimicking phantom has 68mm radius and has a 10mm nipple. By controlling the amount of the inner mold made of flour, we can fabricate both high-adipose-dominated phantom as well as dense glandular-tissue-dominated phantom. In addition, the arbitrary shaped glandular tissues can also be controlled by the inner mould during the phantom fabrication.

4. Experimental investigation for discrimination of tumor mimicking inserts using CNR

Measured results on three tissue mimicking dielectric inserts have revealed that their morphological features can be discriminated by their extracted CNRs. As expected, damping factors of CNR poles extracted from smooth shaped inserts are significantly higher than those from spiculated shaped inserts. These experimental findings have demonstrated that CNR extraction for breast tumor discrimination can be highly useful.

We have also proposed some empirical metrics for measuring the effectiveness of the proposed techniques.

5. Investigation of antenna effects for extracted CNR

The effects of antenna itself for extracted CNR have been investigated for four UWB antennas: BAHA, BAVA, pyramidal ridged horn antenna, and TEM horn antenna. Only for TEM horn antenna, the effects are evaluated by only FDTD simulations. Other three antennas have been fabricated and the backscattered signals from a standard steel sphere immersed in coupling oil are measured for CNR extraction.

Late-time target response is obtained by subtracting a target-free signal which is measured when the steel sphere is not present. The results of extracted CNRs from measured data are listed in Table 6.1. All the antennas, BAHA, BAVA and pyramidal ridged horn have high fidelities with values above 0.9 and thus provide close levels of resonant frequencies compared to the CNRs obtained by Baum's transform[125]. However, when compared with other antennas, BAHA obtains the best measured results for the estimation of damping factor at higher order mode CNR. BAVA results are also reasonable as the estimation of resonant frequencies is accurate but there is a shift on extracted damping factors. Data from pyramidal ridged horn causes a large bias on extracted damping factor. The extracted CNRs of simulated data by TEM horn are also listed in Table 6.2. As TEM horn has very low fidelity which is only 0.76 even at a near distance of 17mm, extracted CNRs have large bias compared to CNRs obtained by Baum's transform.

Table 6.1 CNRs of steel sphere (diameter=15.875mm) extracted from measured data in coupling liquid ($\boldsymbol{\varepsilon_r = 2.5}$)

CNR obtained from	Frequency (GHz)		Damping factor (1/ns)	
	Higher mode	Lower mode	Higher mode	Lower mode
Measured data by BAHA	6.18	2.78	-7.14	-2.01
Measured data by BAVA	6.83	3.40	-5.92	-3.99
Measured data by Pyramidal ridged horn	6.1	3.53	-13.30	-3.88
Baum's transform	6.87	3.29	-7.77	-5.87

Table 6.2 CNRs of steel sphere (diameter=15.875mm) extracted from simulated data in coupling liquid ($\boldsymbol{\varepsilon_r = 10}$)

CNR obtained from	Frequency (GHz)		Damping factor (1/ns)	
	Higher mode	Lower mode	Higher mode	Lower mode
Simulated data by TEM horn	6.18	2.78	-7.14	-2.01
Baum's transform	3.45	1.68	-6.05	-5.04

6. Novel MWDAS method for reconstruction of tumor suspicious region

We have proposed a new MWDAS method and demonstrated both by numerical simulation and phantom experiments that MWDAS can very accurately localize the suspicious region within the breast phantom and reject clutter interferences effectively, when compared to other existing methods in literature[31, 46].

7. TOA autocalibration for inhomogeneous breast

We proposed a novel TOA autocalibration and demonstrated it both by both numerical simulation and phantom experiments that it is capable to estimate accurate

TOA for different propagation paths within heterogeneous breast phantoms. The proposed TOA autocalibration can enhance the localization of suspicious regions and it is adaptive to any types of breast environment varying from homogeneous adipose-dominant to heterogeneously dense breast phantoms.

Thus, the work reported in this thesis, has for the first time, experimentally demonstrated that morphological features of tissue mimicking dielectric inserts can be differentiated using CNRs.

6.4 Future Work

1. There is a need to extend our method to highly dense breast phantoms viz., C4 type phantoms.

2. As BAHA only radiate from 4 GHz, the CNR corresponding to lower resonant frequency cannot be obtained. Hence, it is desirable to develop a new antenna that can work from lower frequency such as 2GHz while maintaining high fidelity and relatively smaller aperture. It is also expected to obtain lower mode CNR poles by improving the discrimination of tissue morphologies.

3.Only 10mm breast tumors have been studied. Smaller tumor size will bring significant challenges for radar based detection due to limits on resolution. For tumor discrimination, a smaller size requires higher resonant frequency. Hence, more studies on CNR extraction of small dielectric inserts are necessary.

References

[1] N. Irishina, "Microwave medical imaging using level set techniques," PhD, Departamentao De Ciencia Eingenieria De Materiales Eingenieria Quimica, Universidad Carlos III De Madrid, Spain, 2009.

[2] A. G. R. Lynn, L. Carol, B. Kosary, and F. Hankey, "SEER cancer statistics review:1973-1994," vol. NIH Pub. 2789, ed. Bethesda, MD: Nat. Cancer Inst., 1997.

[3] "Guide for women with early breast cancer," ed: National Breast and Ovarian Cancer Centre, 2012.

[4] P. T. Huynh, A. M. Jarolimek, and S. Daye, "The false-negative mammogram," *Radiographics,* vol. 18, pp. 1137-1154, 1998.

[5] E. C. Fear, P. M. Meaney, and M. A. Stuchly, "Microwave for breast detection?," *IEEE Potencials,* pp. 12-18, Feb-Mar 2003.

[6] L. E. Larsen and J. H. Jacobi, *Medical Applications of Microwave Imaging*. New York: IEEE Press, 1986.

[7] J. C. Bolomey, L. Jofre, and G. Peronnet, "On the possible use of microwave-active imaging for remove thermal sensing," *IEEE Transactions on Microwave Theory and Techniques,* vol. 31, pp. 777-781, Sept 1983.

[8] J. C. Lin, "Frequency optimization for microwave imaging of biological tissues," *Proc. IEEE,* vol. 73, pp. 374-375, Feb 1985.

[9] N. C. Haslam, A. R. Gillespie, and C. G. T. Haslam, "Aperture synthesis thermography-A new approach to passive microwave temperature measurements in the body," *IEEE Transactions on Microwave Theory and Techniques,* vol. 32, pp. 829-835, Aug 1984.

[10] A. Franchois and C. Pichot, "Microwave imaging-complex permittivity reconstruction with a Levenberg-Marquardt method," *IEEE Transactions on Antennas and Propagation,* vol. 45, pp. 203-215, 1997.

[11] F. J. Paoloni, "Implementation of microwave diffraction tomography for measurement of dielectric constant distribution," *IEEE Proc. Microwave, Antennas Propagt.,* vol. 134, pp. 25-29, 1987.

[12] L. Jofre, M. S. Hawley, A. Broquetas, E. d. l. Reyes, M. Ferrando, and A. R. Elias-Fuste, "Medical imaging with microwave tomographic scanner," *IEEE Transactions on Biomedical Engineering,* vol. 37, pp. 303-312, Mar 1990.

[13] A. H. Barrett, P. C. Myers, and N. L. Sadowsky, "Detection of breast cancer by microwave radiometry," *Radiol. Sci.,* vol. 12, pp. 167-171, 1977.

[14] K. L. Carr, "Microwave radiometry: Its importance to the detection of cancer," *IEEE Transactions on Microwave Theory and Techniques,* vol. 37, pp. 1862-1869, Dec 1989.

[15] A. Rosen, M. A. Stuchly, and A. V. Vorst, "Applications of RF/Microwaves in Medicine," *IEEE Transactions on Microwave Theory and Techniques,* vol. 50, pp. 963-974, Mar 2002.

[16] E. C. Fear, S. C. Hagness, P. M. Meaney, M. Okoniewski, and M. A. Stuchly, "Enhancing Breast Tumor Detection with near-field imaging," *IEEE Microwave Magazine,* pp. 48-56, Mar 2002.

[17] M. Klemm, I. J. Craddock, J. A. Leendertz, A. Preece, D. R. Gibbins, M. Shere*, et al.*, "Clinical trials of a UWB imaging radar for breast cancer," presented at the Antennas and Propagation (EuCAP), 2010 Proceedings of the Fourth European Conference on, Barcelona, 2010.

[18] E. C. Fear, J. Bourqui, C. Curtis, D. Mew, B. Docktor, and C. Romano, "Microwave breast imaging with a monostatic radar-based system: a study of application to patients," *IEEE Transactions on Microwave Theory and Techniques,* vol. 61, pp. 2119-2128, May 2013.

[19] B. Bocquet, J. C. v. d. Velde, A. Mamouni, Y. Leroy, G. Giaux, J. Delannoy*, et al.*, "Microwave radiometric imaging at 3GHz for the exploration of breast tumors," *IEEE Transactions on Microwave Theory and Techniques,* vol. 38, pp. 791-793, 1990.

[20] S. Mouty, B. Bocquet, R. Ringot, N. Rocourt, and P. Devos, "Microwave radiometric imaging for the characterisation of breast tumors," *Eur. Phys. I.: Appl. Phys.,* vol. 10, pp. 73-78, 2000.

[21] R. A. kruger, K. K. Kopecky, A. M. Aisen, D. R. Reinecke, G. A. Kruger, and j. W. L. Kiser, "Thermoacoustic CT with radio waves: a medical imaging paradigm," *Radiology,* vol. 211, pp. 275-278, 1999.

[22] A. Mashal, J. H. Booske, and S. C. Hagness, "Toward contrast-enhanced microwave-induced thermoacoustic imaging of breast cancer: an experimental study of the effects of microbubbles on simple thermoacoustic targets," *Phys Med Biol,* vol. 54, pp. 641-50, Feb 7 2009.

[23] A. E. Bulyshev, S. Y. Semenov, A. E. Souvorov, R. H. Svenson, A. G. Nazarov, Y. E. Sizov*, et al.*, "Computational modeling of three-dimensional microwave tomography of breast cancer," *IEEE Transactions on Biomedical Engineering,* vol. 48, pp. 1053-1056, Sep 2001.

[24] Q. Fang, P. M. Meaney, and K. D. Paulsen, "Viable three-dimensional medical microwave tomography: theory and numerical experiments," *IEEE Transactions on Antennas and Propagation,* vol. 58, pp. 449-458, February 2010.

[25] C. Gilmore and J. LoVetri, "Enhancement of microwave tomography through the use of electrically conducting enclosures," *Inverse Probl,* vol. 24, p. 035008, 2008.

[26] C. Pichot, L. Jofre, G. Peronnet, and J.-C. Bolomey, "Active microwave imaging of inhomogeneous bodies," *IEEE Transactions on Antennas and Propagation,* vol. 33, pp. 416-425, Apr 1985.

[27] T. M. Grzegorczyk, P. M. Meaney, P. A. Kaufman, R. M. D. Alexander, and K. D. Paulsen, "Fast 3-D tomographic microwave imaging for breast cancer detection," *IEEE Transactions on Medical Imaging,* vol. 31, pp. 1584-1592, August 2012.

[28] J. Johnson, T. Takenaka, K. Ping, S. Honda, and T. Tanaka, "Advances in the 3-D forward-backward time-stepping (FBTS) inverse scattering technique for breast cancer detection," *IEEE Transactions on Biomedical Engineering,* vol. 56, pp. 2232-2243, 2009.

[29] P. Mojabi and J. LoVetri, "A novel microwave tomography system using a rotatable conductive enclosure," *IEEE Transactions on Antennas and Propagation,* vol. 59, pp. 1597-1605, May 2011.

[30] M. J. Burfeindt, N. Behdad, B. D. V. Veen, and S. C. Hagness, "Quantitative microwave imaging of realistic numerical breast phantoms using an enclosed array of multiband, miniaturized patch antennas," *IEEE Antennas and Wireless Propagation Letters,* vol. 11, pp. 1626-1629, 2012.

[31] E. Fear, X. Li, S. C. Hagness, and M. A. Stuchly, "Confocal microwave imaging for breast cancer detection: localization of tumors in three dimensions," *IEEE Transactions on Biomedical Engineering,* vol. 49, pp. 812-822, August 2002.

[32] S. C. Hagness, A. Taflove, and J. E. Bridges, "Two-dimensional FDTD analysis of a pulsed microwave confocal systems for breast cancer detection: fixed-focus and antenna-array sensors," *IEEE Transactions on Biomedical Engineering,* vol. 45, pp. 1470-1479, December 1998.

[33] S. C. Hagness, A. Taflove, and J. E. Bridges, "Three-dimensional FDTD analysis of a pulsed microwave confocal system for breast cancer detection: design of an antenna-array element," *IEEE Transactions on Antennas and Propagation,* vol. 47, pp. 783-791, May 1999.

[34] E. J. Bond, X. Li, S. C. Hagness, and B. D. V. Veen, "Microwave imaging via space-time beamforming for early detection of breast cancer," *IEEE Transactions on Antennas and Propagation,* vol. 51, pp. 1690-1705, August 2003.

[35] X. Li, S. K. Davis, S. C. Hagness, D. v. d. Weide, and B. D. V. Veen, "Microwave imaging via space-time beamforming: experimental investigation of tumor detection in multi-layer breast phantoms," *IEEE Transactions on Microwave Theory and Techniques,* vol. 52, pp. 1856-1865, August 2004.

[36] X. Li and S. C. Hagness, "A confocal microwave imaging algorithm for breast cancer detection," *IEEE Microwave and Wireless Components Letters,* vol. 11, pp. 130-132, March 2001.

[37] R. Nilavalan, A. Gbedemah, I. J. Craddock, X. Li, and S. C. Hagness, "Numerical investigation of breast tumour detection using multi-static radar," *Electronics Letters,* vol. 39, p. 1787, 2003.

[38] E. C. Fear and M. A. Stuchly, "Microwave detection of breast cancer," *IEEE Transactions on Microwave Theory and Techniques,* vol. 48, pp. 1854-1863, November 2000.

[39] J. M. Sill and E. C. Fear, "Tissue sensing adaptive radar for breast cancer detection-experimental investigation of simple tumor models," *IEEE Transactions on Microwave Theory and Techniques,* vol. 53, pp. 3312-3319, Nov. 2003.

[40] J. M. Sill and E. C. Fear, "Tissue sensing adaptive radar for breast cancer detection-experimental investigation of simple tumor models," *IEEE Transactions on Microwave Theory and Techniques,* vol. 53, pp. 3312-3319, November 2005.

[41] M. Klemm, I. J. Craddock, J. A. Leendertz, A. Preece, and R. Benjamin, "Improved Delay-and-Sum Beamforming Algorithm for Breast Cancer Detection," *International Journal of Antennas and Propagation,* vol. 2008, pp. 1-9, 2008.

[42] M. Klemm, I. J. Craddock, J. A. Leendertz, A. Preece, and R. Benjamin, "Radar-based breast cancer detection using a hemispherical antenna array-experimental results," *IEEE Transactions on Antennas and Propagation,* vol. 57, pp. 1692-1704, June 2009.

[43] M. Klemm, D. Gibbins, J. Leendertz, T. Horseman, A. W. Preece, R. Benjamin*, et al.*, "Development and testing of a 60-element UWB conformal array for breast cancer imaging," presented at the Proc. 5th European Conf. Antennas and Propagation (EuCAP), 2011.

[44] M. Klemm, J. A. Leendertz, D. Gibbins, I. J. Craddock, A. Preece, and R. Benjamin, "Microwave radar-based differential breast cancer imaging: imaging in homogeneous breast phantoms and low contrast scenarios," *IEEE Transactions on Antennas and Propagation,* vol. 58, pp. 2337-2344, July 2010.

[45] M. Klemm, J. A. Leendertz, D. Gibbins, I. J. Craddock, A. Preece, and R. Benjamin, "Microwave radar-based breast cancer detection: imaging in inhomogeneous breast phantoms," *IEEE Antennas and Wireless Propagation Letters,* vol. 8, pp. 1349-1352, 2009.

[46] H. B. Lim, N. T. T. Nhung, E. Li, and N. D. Thang, "Confocal microwave imaging for breast cancer detection: delay-multiply-and-sum image reconstruction algorithm," *IEEE Transactions on Biomedical Engineering,* vol. 55, pp. 1697-1704, June 2008.

[47] Y. Xie, B. Guo, L. Xu, J. Li, and P. Stoica, "Multistatic adaptive microwave imaging for early breast cancer detection," *IEEE Transactions on Biomedical Engineering,* vol. 53, pp. 1647-1657, August 2006.

[48] M. A. Hernandez-Lopez, M. Quintillan-Gonzalez, S. Gonzalez Garcia, A. Rubio Bretones, and R. Gomez Martin, "A rotating array of antennas for confocal microwave breast imaging," *Microwave and Optical Technology Letters,* vol. 39, pp. 307-311, 2003.

[49] V. D. Santis, M. Feliziani, and F. Maradei, "Safety assessment of UWB radio systems for body area network by the FD2TD method," *IEEE Transactions on Magnetics,* vol. 46, pp. 3245-3248, 2010.

[50] Q. Wang and J. Wang, "SA/SAR analysis for multiple UWB pulse exposure," presented at the Proceedings of Asia-Pacific Symposium on EMC, Singapore, Japan, 2008.

[51] E. Zastrow, S. K. Davis, and S. C. Hagness, "Safety assessment of breast cancer detection via ultrawideband microwave radar operating in pulsed-radiation mode," *Microwave and Optical Technology Letters,* vol. 49, pp. 221-225, Jan 2007.

[52] M. Lazebnik, L. McCartney, D. Popovic, C. B. Watkins, M. J. Lindstrom, J. Harter*, et al.*, "A large-scale study of the ultrawideband microwave dielectric properties of normal breast tissue obtained from reduction surgeries," *Phys Med Biol,* vol. 52, pp. 2637-56, May 21 2007.

[53] M. Lazebnik, D. Popovic, L. McCartney, C. B. Watkins, M. J. Lindstrom, J. Harter*, et al.*, "A large-scale study of the ultrawideband microwave dielectric properties of normal, benign and malignant breast tissues obtained from cancer surgeries," *Phys Med Biol,* vol. 52, pp. 6093-115, Oct 21 2007.

[54] C. Gabriel, S. Gabriel, R. W. Lau, and E. Corthout, "The dielectric properties of biological tissues: Part I, II, and III," *Phys Med Biol,* vol. 41, pp. 2231-2249, 1996.

[55] M. Lazebnik, M. Okoniewski, J. H. Booske, and S. C. Hagness, "Highly accurate Debye models for normal and malignant breast tissue dielectric properties at microwave frequencies," *IEEE microwave and Wireless Components Letters,* vol. 17, pp. 822-824, Dec 2007.

[56] B. Guo, L. Jian, and H. Zmuda, "A new FDTD formulation for wave propagation in biological media with Cole-Cole model," *IEEE microwave and Wireless Components Letters,* vol. 16, pp. 633-635, Dec 2006.

[57] E. Zastrow, S. Davis, M. Lazebnik, F. Kelcz, and S. C. Hagness, "Development of anatomically realistic numerical breast phantoms with accurate dielectric properties for modeling microwave interations with the human breast," *IEEE Transactions on Biomedical Engineering,* vol. 55, pp. 2792-2800, 2008.

[58] M. Lazebnik, E. Madsen, G. Frank, and S. C. Hagness, "Tissue-mimicking phantom materials for narrowband and ultrawideband microwave applications," *Phys Med Biol,* vol. 50, pp. 4245-4258, 2005.

[59] E. Porter, J. Fakhoury, R. Oprisor, M. Coates, and M. Popovic, "Improved tissue phantoms for experimental validation of microwave breast cancer detection," presented at the 2010 Proceedings of the Fourth European Conference on Antennas and Propagation, Spain, 2010.

[60] E. Porter, A. Santorelli, D. Coulibaly, M. Coates, and M. Popovic, "Time-domain microwave breast screening system: testing with advanced realistic

breast phantoms," presented at the Proc. 6th European Conference on Antennas and Propagation (EUCAP 2012), 2012.

[61] E. Porter, A. Santorelli, A. Bourdon, D. Coulibaly, M. Coates, and M. Popovic, "Time-domain microwave breast cancer detection: experiments with comprehensive glandular phantoms," presented at the Proceedings of the Asia-Pacific Microwave Conference 2011, Melbourne, Australia, 2011.

[62] D. Byrne, M. O'Halloran, M. Glavin, and E. Jones, "Data independent radar beamforming algorithms for breast cancer detection," *Progress in Electromagnetics Research,* vol. 107, pp. 331-348, 2010.

[63] E. Zastrow, S. K. Davis, M. Lazebnik, F. Kelcz, B. D. V. Veen, and S. C. Hagness. Database of 3d grid-based numerical breast phantoms for use in computational electromagnetics simulations [Online]. Available: http://uwcem.ece.wisc.edu/home.htm

[64] J. Li, P. Stoica, and Z. Wang, "On robust Capon beamforming and diagonal loading," *IEEE Transactions on Signal Processing,* vol. 51, pp. 1702-1715, July 2003.

[65] P. Stoica, Z. Wang, and J. Li, "Robust Capon beamforming," *IEEE Signal Processing Letters,* vol. 10, pp. 172-175, Jun 2003.

[66] A. J. Surowiec, S. S. Stuchly, J. R. Barr, and A. Swarup, "Dielectric properties of breast carcinoma and the surrounding tissues," *IEEE Transactions on Biomedical Engineering,* pp. 257-263, 1988.

[67] A. S. Swarup, S. S. Stuchly, and A. Surowiec, "Dielectric properties of mouse MC A1 fibrosarcoma at different stages of development," *Bioelectromagnetics,* vol. 12, pp. 1-8, 1991.

[68] W. T. Joines, Y. Z. Dhenxing, and R. L. Jirtle, "The measured electrical properties of normal and malignant human tissues from 50-900 MHz," *Med. Phys.,* vol. 21, pp. 547-550, April 1994.

[69] C. Gabriel, R. W. Lau, and S. Gabriel, "The dielectric properties of biological tissues: II. measured in the frequency range 10Hz to 20GHz," *Phys Med Biol,* vol. 41, pp. 2251-2269, Nov. 1996.

[70] D. Byrne, M. O'Halloran, E. Jones, and M. Glavin, "Transmitter-grouping robust capon beamforming for breast cancer detection," *Progress in Electromagnetics Research,* vol. 108, pp. 401-416, 2010.

[71] N. Nikolova, "Microwave imaging for breast cancer," *IEEE Microwave Magazine,* vol. 12, pp. 78-94, December 2011.

[72] P. Kosmas, S. Laranjeira, J. H. Dixon, X. Li, and Y. Chen, "Time reversal microwave breast imaging for contrast-enhanced tumor classification," presented at the 32nd Annual International Conference of the IEEE EMBS, Buenos Aires, Argentina, 2010.

[73] A. Lazaro, D. Girbau, and R. Villarino, "Simulated and experimental investigation of microwave imaging using UWB," *Progress in Electromagnetics Research,* vol. 94, pp. 263-280, 2009.

[74] J. Bourqui, J. M. Sill, and E. C. Fear, "A prototype system for measuring microwave frequency reflections from the breast," *International Journal of Biomedical Imaging,* vol. 2012, 2012.

[75] J. Bourqui, J. Garrett, and E. Fear, "Measurement and analysis of microwave frequency signals transmitted through the breast," *International Journal of Biomedical Imaging,* vol. 2012, 2012.

[76] T. T. Wu and W. P. King, "The cylindrical antenna with nonreflecting resistive loading," *IEEE Transactions on Antennas and Propagation,* vol. 13, pp. 369-373, May 1965.

[77] R. Nilavalan, I. J. Craddock, A. Preece, J. Leendertz, and R. Benjamin, "Wideband microstrip patch antenna design for breast cancer detection," *IET Microwave Antennas and Propagation,* vol. 1, pp. 277-281, 2007.

[78] D. Gibbins, M. Klemm, I. J. Craddock, J. A. Leendertz, A. Preece, and R. Benjamin, "A comparison of a wide-slot and a stacked patch antenna for the purpose of breast cancer detection," *IEEE Transactions on Antennas and Propagation,* vol. 58, pp. 665-674, March 2010.

[79] X. Li, S. C. Hagness, M. K. Choi, and D. W. v. d. Weide, "Numerical and experimental investigation of an ultrawideband ridged pyramidal horn antenna with curved lauching plane for pulse radiation," *IEEE Antennas Wireless Propagation Letters,* vol. 2, pp. 259-262, 2003.

[80] J. Bourqui, M. Okoniewski, and E. C. Fear, "Balanced antipodal Vivaldi antenna with dielectric director for near-field microwave imaging," *IEEE Transactions on Antennas and Propagation,* vol. 58, pp. 2318-2326, July 2010.

[81] R. K. Amineh, M. Ravan, A. Trehan, and N. K. Nikolova, "Near-field microwave imaging based on aperture raster scanning with TEM horn antennas," *IEEE Transactions on Antennas and Propagation,* vol. 59, pp. 928-940, March 2011.

[82] K. Moussakhani, R. K. Amineh, and N. K. Nikolova, "High-efficiency TEM horn antenna for ultra-wide band microwave tissue imaging," in *Antennas and Propagation (APSURSI), 2011 IEEE International Symposium on*, 2011, pp. 127-130.

[83] B. J. Mohammed, D. Ireland, and A. M. Abbosh, "Experimental investigations into detection of breast tumour using microwave system with planar array," *IET Microwave Antennas and Propagation,* vol. 6, pp. 1311-1317, 2012.

[84] E. A. Sickles, "Nonpalpable, circumscribed, noncalcified solid breast masses: likelihood of malignancy based on lesion size and age of patient," *Radiographics,* vol. 192, pp. 439-442, 1994.

[85] K. Kinkel, T. H. Helbich, L. J. Esserman, J. Barclay, E. H. Schwerin, E. A. Sickles*, et al.*, "Dynamic high-spatial-resolution MR imaging of suspicious breast lesions: diagnostic criteria and interobserver variability," *American Journal of Roentgenology,* vol. 175, pp. 35-43, July 2000.

[86] L. W. Nunes, M. D. Schnall, E. S. Siegelman, C. P. Langlotz, S. G. Orel, D. Sullivan*, et al.*, "Diagnostic performance characteristics of architectural features revealed by high spatial-resolution MR imaging of the breast," *American Journal of Roentgenology,* vol. 169, pp. 409-415, Aug. 1997.

[87] J. Tang, R. M. Rangayyan, J. Xu, I. E. Naqa, and Y. Yang, "Computer-aided detection and diagnosis of breast cancer with mammography: recent advances," *IEEE Transactions on Information Technology in Biomedicine,* vol. 13, pp. 236-251, March 2009.

[88] S. Vitebiskiy and L. Carin, "Resonance of perfectly conducting wires and bodies of revolution buried in a lossy dispersive half-space," *IEEE Transactions on Antennas and Propagation,* vol. AP-44, pp. 1575-1583, Dec 1996.

[89] C.-C. Chen, "Electromagnetic resonances of immersed dieletric spheres," *IEEE Transactions on Antennas and Propagation,* vol. 46, pp. 1074-1083, July 1998.

[90] N. Geng, D. R. Jackson, and L. Carin, "On the resonances of a dielectric BOR buried in a dispersive layered medium," *IEEE Transactions on Antennas and Propagation,* vol. AP-47, pp. 1305-1313, 1999.

[91] E. J. Rothwell, D. P. Nyquist, K. Chen, and B. Drachman, "Radar target discrimination using the extinction-pulse technique," *IEEE Transactions on Antennas and Propagation,* vol. Ap-33, pp. 929-936, Sep 1985.

[92] D. Blanco, D. P. Ruiz, E. Alameda, and M. C. Carrion, "An asymptotically unbiased E-pulse-based scheme for radar target discrimination," *IEEE Transactions on Antennas and Propagation,* vol. 52, pp. 1348-1350, May 2004.

[93] H.-S. Lui and N. V. Z. Shuley, "Detection of depth changes of a mettalic target buried in a frequency-dependent lossy halfspace using the E-pulse technique," *IEEE Transactions on Electromagnetic Compatibility,* vol. 49, pp. 868-874, Nov 2007.

[94] C.-C. Chen and J. Leon Peters, "Buried unexploded ordnance identification via complex natural resonances," *IEEE Transactions on Antennas and Propagation,* vol. 45, pp. 1645-1654, Nov 1997.

[95] C. E. Baum, *Detection of Identification of Visually Obscured Targets*: New York: Taylor & Francis, 1999.

[96] Y. Wang, I. D. Longstaff, and C. J. Leat, "Measurement of complex natural resonances of targets in free space and lossy media," *Progress in Electromagnetics Research,* vol. 29, pp. 221-230, 2000.

[97] Y. Huo, R. Bansal, and Q. Zhu, "Modeling of noninvasive microwave characterization of breast tumors," *IEEE Transactions on Biomedical Engineering,* vol. 51, pp. 1089-1094, 2004.

[98] M. El-Shenawee, "Resonant spectra of malignant breast cancer tumors using the three-dimensional electromagnetic fast multipole," *IEEE Transactions on Biomedical Engineering,* vol. 51, pp. 35-44, 2004.

[99] Y. Chen, E. Gunawan, K. S. Low, S.-C. Wang, C. B. Soh, and T. C. Putti, "Effect of lesion morphology on microwave signature in 2-D ultra-wideband

breast imaging," *IEEE Transactions on Biomedical Engineering,* vol. 55, pp. 2011-2021, Aug 2008.
[100] Y. Chen, I. J. Craddock, P. Kosmas, M. Ghavami, and P. Rapajic, "Multiple-input multiple-output radar for lesion classification in ultrawideband breast imaging," *IEEE Journal of Selected Topics in Signal Processing,* vol. 4, pp. 187-201, Feb. 2010.
[101] Y. Chen, I. J. Craddock, and P. Kosmas, "Feasibility study of lesion classification via contrast-agent-aided UWB breast imaging," *IEEE Transactions on Biomedical Engineering,* vol. 57, pp. 1003-1007, May 2010.
[102] Y. Chen, E. Gunawan, K. S. Low, S.-c. Wang, C. B. Soh, and T. C. Putti, "Time-reversal ultrawideband breast imaging: pulse design criteria considering multiple tumors with unknown tissue properties," *IEEE Transactions on Antennas and Propagation,* vol. 56, pp. 3073-3077, September 2008.
[103] J. Capon, "High resolution frequency-wavenumber spectrum analysis," *Proceedings of the IEEE,* vol. 57, pp. 1408-1418, August 1969.
[104] H. Cox, R. M. Zeskind, and M. M. Owen, "Robust adaptive beamforming," *IEEE Transactions on Acoustics Speech and Signal Processing,* vol. 35, pp. 1365-1376, October 1987.
[105] R. A. Monzingo and T. W. Miller, *Introduction to Adaptive Arrays* New York: Wiley, 1980.
[106] J. Li and P. Stoica, *Robust Adaptive Beamforming*: New York: Wiley, 2005.
[107] P. M. Meaney, M. W. Fanning, D. Li, S. P. Poplack, and K. D. Paulsen, "A clinical prototype for active microwave imaging of the breast," *IEEE Transactions on Microwave Theory and Techniques,* vol. 48, pp. 1841-1853, November 2000.
[108] M. H. Shenouda and E. C. Fear, "Design of dielectric immersed tapered slotline antenna for radar-based microwave breast imaging," *Microwave and Optical Technology Letters,* vol. 51, pp. 633-638, 2009.
[109] C. Yu, M. Yuan, J. Stang, E. Bresslour, R. T. George, G. A. Ybarra*, et al.*, "Active microwave imaging II: 3-D system prototype and imaging reconstruction from experimental data," *IEEE Transactions on Microwave Theory and Techniques,* vol. 56, pp. 991-1000, 2008.
[110] R. Prony, "Essai experimental et analytique..." *Paris J. I'Ecola Polytechnique,* vol. 1, pp. 24-76, 1795.
[111] M. A. Morgan, "Singularity expansion representations of fields and currents in transient scattering," *IEEE Transactions on Antennas and Propagation,* vol. AP-32, pp. 466-473, May 1984.
[112] C. E. Baum, "On the singularity expansion method for the solution of electromagnetic interaction problems," Air Force Weapons Laboratory, Kirkland Air Force Base, New MexicoDecember 11 1971.
[113] W. Franz, "Uber die Greenschen funktionen des zylinders und der kugel," *Z. Naturforsch,* vol. A-9, pp. 705-716, 1954.

[114] T. S. Fahlen and H. C. Bryant, "Direct observation of surface waves on water droplets," *J. Optical Soc. Amer.,* vol. 56, pp. 1635-1636, Nov 1966.
[115] L. C. Chan, D. L. Moffatt, and L. Peters, "A characterization of subsurface radar targets," *Proc. IEEE,* vol. 67, pp. 991-1000, July 1979.
[116] P. Barber, J. F. Owen, and R. K. Chang, "Resonant scattering for characterization of axisymmetric dielectric objects," *IEEE Transactions on Antennas and Propagation,* vol. AP-30, pp. 168-172, Mar 1982.
[117] P. R. Conwell, P. W. Barber, and C. K. Rushforth, "Resonant spectra of dielectric spheres," *J. Acoust. Soc. Amer.,* vol. 1, pp. 62-67, Jan 1984.
[118] D. L. Moffatt and R. K. Mains, "Detection and discrimination of radar target," *IEEE Transactions on Acoustics Speech and Signal Processing,* vol. 23, pp. 358-367, May 1975.
[119] T. K. Sarkar and O. Pereira, "Using the matrix pencil method to estimate the parameters of a sum of complex exponentials," *IEEE Antennas and Propagation Magazine,* vol. 37, pp. 48-55, Feb. 1995.
[120] M. D. A. Rahman and K.-B. Yu, "Total least squares approach for frequency estimation using linear prediction," *IEEE Transactions on Acoustics Speech and Signal Processing,* vol. ASSP-35, pp. 1440-1454, Oct 1987.
[121] Y. Hua, "On techniques for estimating parameters of exponentially damped/undamped sinusoids in noise," PhD PhD dissertation, Syracuse University, NY, 1988.
[122] Y. Hua and T. K. Sarkar, "Matrix pencil method for estimating parameters of exponentially damped/undamped sinusoids in noise," *IEEE Transactions on Acoustics Speech and Signal Processing,* vol. 38, pp. 814-824, May 1990.
[123] F. Tseng and T. K. Sarkar, "Experimental determination of resonant frequencies by transient scattering from conducting spheres and cylinders," *IEEE Transactions on Antennas and Propagation,* vol. 32, pp. 914-918, 1984.
[124] L. Marin, "Natural-mode representation of transient scattering from rotationally symmetric bodies," *IEEE Transactions on Antennas and Propagation,* vol. 22, pp. 266-274, March 1974.
[125] C. E. Baum, "The SEM representation of scattering from perfectly conducting targets in simple lossy media," Phillips Laboratory, Kirkland Air Force Base, New MexicoApril 21 1993.
[126] S. K. Padhi and N. V. Shuley, "Resonance Behavior of a Dielectric Target in a Half-Space Using the CNR (Complex Natural Resonance) Method," in *Ultra-Wideband Short-Pulse Electromagnetics 8*, C. Baum, A. Stone, and J. S. Tyo, Eds., ed: Springer New York, 2007, pp. 187-193.
[127] K. Muinonen, "Introducing the Gaussian shape hypothesis for asteroids and comets," *Astronomy and Astrophysics,* vol. 332, pp. 1087-1098, 1998.
[128] K. Muinonen, E. Zubko, J. Tyynelä, Y. G. Shkuratov, and G. Videen, "Light scattering by Gaussian random particles with discrete-dipole approximation,"

Journal of Quantitative Spectroscopy and Radiative Transfer, vol. 106, pp. 360-377, 2007.

[129] K. Muinonen, T. Nousiainen, H. Lindqvist, O. Muñoz, and G. Videen, "Light scattering by Gaussian particles with internal inclusions and roughened surfaces using ray optics," *Journal of Quantitative Spectroscopy and Radiative Transfer,* vol. 110, pp. 1628-1639, 2009.

[130] S. K. Davis, B. D. V. Veen, S. C. Hagness, and F. Kelcz, "Breast tumor characterisation based on ultrawideband microwave backscatter," *IEEE Transactions on Biomedical Engineering,* vol. 55, pp. 237-246, Jan 2008.

[131] D. J. Kurrant and E. C. Fear, "An improved technique to predict the time-of-arrival of a tumor response in radar-based breast imaging," *IEEE Transactions on Biomedical Engineering,* vol. 56, pp. 1200-1208, April 2009.

[132] Y. C. Eldar, A. Nehorai, and P. S. L. Rosa, "A competitive mean-squared error approach to beamforming," *IEEE Transactions on Signal Processing,* vol. 55, pp. 5143-5154, Nov 2007.

[133] R. C. Eberhart and J. Kennedy, "Particle swarm optimization," presented at the Proc. IEEE Conf. Neural Networks IV, NJ, 1995.

[134] T. Huang and A. S. Mohan, "A hybrid boundary condition for robust particle swarm optimization," *IEEE Antennas and Wireless Propagation Letters,* vol. 4, pp. 112-117, 2005.

[135] Y. Chen and V. K. Dubey, "Ultra-wideband source localization using a particle-swarm-optimized capon estimator from a frequency-dependent channel modeling viewpoint," *EURASIP Journal on Applied Signal Processing,* vol. 12, pp. 1854-1866, 2005.

[136] J.-H. Lee and H.-T. Kim, "Radar target recognition based on late time representation: closed-form expression for criterion," *IEEE Transactions on Antennas and Propagation,* vol. 54, pp. 2455-2462, Sep. 2006.

[137] A. M. Abbosh, "Directive Antenna for Ultrawideband Medical Imaging Systems," *International Journal of Antennas and Propagation,* vol. 2008, pp. 1-6, 2008.

[138] W. C. Khor, M. E. Bialkowski, A. Abbosh, N. Seman, and S. Crozier, "An ultra wideband microwave imaging system for breast cancer detection," *IEICE Transactions on Communications,* vol. E90-B, pp. 2376-2381, September 2007.

[139] R. K. Amineh, A. Trehan, and N. K. Nikolova, "TEM horn antenna for ultra-wide band microwave breast imaging," *Progress in Electromagnetics Research B,* vol. 13, pp. 59-74, 2009.

[140] J. Bourqui, M. Okoniewski, and E. C. Fear, "Balanced antipodal Vivaldi antenna for breast cancer detection," presented at the Proc. 2nd Eur. Conf. Antennas Propag., Edinburgh, U.K., 2007.

[141] J. Zhang, E. C. Fear, and R. H. Johnston, "Cross-Vivaldi antenna for breast tumor detection," *Microwave and Optical Technology Letters,* vol. 51, pp. 275-280, 2009.

[142] K. L. Shlager, G. S. Smith, and J. G. Maloney, "Accurate analysis of TEM horn antennas for pulse radiation," *IEEE Transactions on Electromagnetic Compatibility,* vol. 38, pp. 414-423, August 1996.
[143] K. L. Walton and V. C. Sundberg, "Broadband ridged horn design," *Microwave Journal,* vol. 4, pp. 96-101, April 1964.
[144] B. M. Notaros, C. D. McCarrick, and D. P. Kasilingam, "Two numerical techniques for analysis of pyramidal horn antennas with continuous metallic ridges," presented at the Proc. IEEE Int. Symp. Antennas Propagation Dig., Boston, MA, 2001.
[145] J. Langley, P. Hall, and P. Newham, "Novel ultrawide-bandwidth Vivaldi antenna with low crosspolarisation," *Electronics Letters,* vol. 29, pp. 2004-2005, 1993.
[146] H. A. Wheeler, "The radiansphere around a small antenna," *Proc. IRE, S,* pp. 1325-1331, August 1959.
[147] P. Miskovsky, J. M. Gonzalez-Arbesu, and J. Romeu, "Antenna radiation efficiency measurement in an ultrawide frequency range," *IEEE Antennas and Wireless Propagation Letters,* vol. 8, pp. 72-75, April 2009.
[148] S. K. Davis, H. Tandradinata, S. C. Hagness, and B. D. V. Veen, "Ultrawideband microwave breast cancer detection: A detection-theoretic approach using the generalized likelihood ratio test," *IEEE Transactions on Biomedical Engineering,* vol. 52, pp. 1237-1250, July 2005.
[149] D. Li, P. M. Meaney, and K. D. Paulsen, "Conformal microwave imaging for breast cancer detection," *IEEE Transactions on Microwave Theory and Techniques,* vol. 51, pp. 1179-1186, April 2003.
[150] J. D. Shea, P. Kosmas, S. C. Hagness, and B. D. Van Veen, "Three-dimensional microwave imaging of realistic numerical breast phantoms via a multiple-frequency inverse scattering technique," *Medical Physics,* vol. 37, p. 4210, 2010.
[151] J. Stang, M. Haynes, P. Carson, and M. Moghaddam, "A preclinical system prototype for focused microwave thermal therapy of the breast," *IEEE Transactions on Biomedical Engineering,* vol. 59, pp. 2431-2438, Sept 2012.
[152] J. Teo, Y. Chen, C. B. Soh, E. Gunawan, K. S. Low, T. C. Putti*, et al.*, "Breast lesion classification using ultrawideband early time breast lesion response," *IEEE Transactions on Antennas and Propagation,* vol. 58, pp. 2604-2613, August 2010.
[153] J. C. Y. Lai, C. B. Soh, E. Gunawan, and K. S. Low, "Homogeneous and heterogeneous breast phantoms for ultra-wideband microwave imaging applications," *Progress in Electromagnetics Research,* vol. PIER 100, pp. 397-415, 2010.
[154] G. Bindu, S. J. Abraham, A. Lonappan, V. Thomas, C. K. Anandan, and K. T. Mathew, "Active microwave imaging for breast cancer detection," *Progress in Electromagnetics Research,* vol. PIER 58, pp. 149-169, 2006.

[155] A. Mashal, F. Gao, and S. C. Hagness, "Heterogeneous anthropomorphic phantoms with realistic dielectric properties for microwave breast imaging experiments," *Microwave and Optical Technology Letters,* vol. 53, pp. 1896-1902, 2010.

[156] Fan Yang " Investigations on arrow slot antenna for breast cancer detection", Internal Research Report, Faculty of Engineering and IT, University of Technology, Sydney, March, 2013.